Cryogenic phonon-scintillation detectors with PMT readout for rare event search experiments and characterisation of a PMT at milli-Kelvin temperatures

Junsong Lin

St Catherine's College

University of Oxford

A thesis submitted for the degree of

Doctor of Philosophy

Trinity 2016

Abstract

Reliable, robust, efficient, and scalable light detectors operated at milli-Kelvin temperature that can resolve individual photons in a scintillation event are required by the cryogenic phonon-scintillation detectors (CPSD) for next generation rare-event search experiments. This thesis demonstrates a cryogenic detector with a scintillating crystal as the absorber, equipped with a Neutron Transmutation Doped Germanium (NTD-Ge) phonon sensor and a Hamamatsu R8520-06 photomultiplier tube (PMT) with platinum underlay as the light detector. The PMT is powered by a Cockcroft-Walton generator. In this experiment, two CPSD modules are successfully tested, one with $CaWO_4$ and the other with $CaMoO_4$ as the scintillating absorber. The detector modules were cooled down to ~ 18 milli-Kelvin inside a dilution refrigerator. The CPSD modules are demonstrated to be able to measure signals from the phonon channel and light channel simultaneously, which is critical for particle identification. The full-width-at-half-maximum (FWHM) energy resolutions at 122.1 keV for the phonon channel are 2.17 keV (1.8%) for $CaWO_4$ and 0.97 keV (0.79%) for $CaMoO_4$. The FWHM resolutions at 122.1 keV γ excitation for the scintillation/photon channel are 19.9% for $CaWO_4$ and 29.7% for $CaMoO_4$. At milli-Kelvin temperatures, the dark count rate of the PMT is determined to be less than 5 Hz while the gain of the PMT is found to be 3.3×10^6. These characteristics of the CPSD in this work compare favourably to conventional CPSDs with cryogenic calorimeter-based light detectors currently de-

ployed in cryogenic rare-event search experiments, especially in the energy region of interest for dark matter direct detection. The PMT is demonstrated to have low dark count rate and high gain at milli-Kelvin temperatures, thus it remains an effective single photon detector. From the radioactivity of a similar model of PMT as input to a Geant4 simulation, the radioactivity introduced by the PMT contributes only minorly (<10%) to the overall radioactive background of a hypothetical CPSD module for WIMP searches. The CPSD module with PMT readout benefits a reliable, well-tested and commercially available apparatus, while the PMT as a photon detector at milli-Kelvin temperatures offers a much better time resolution than cryogenic light detectors, allowing to resolve individual photons. The technology in this study can potentially revolutionise the science reach of rare event search experiments using CPSD (e.g. the CRESST experiment), by offering an alternative light detector solution which is much more scalable and more consistent in performance than conventional CPSDs with cryogenic calorimeter-based light detectors, addressing two major issues that the present techniques face.

Acknowledgment

I would like to thank Prof. Hans Kraus first and foremost. His patience and dedication to students, his skilful guiding of students into research roles, and his passion for research make him a role model for me.

I also want to thank Xiaohe Zhang, with whom I collaborated closely for this thesis work. Together we shared many exciting moments in research work, and I learned persistence and thoroughness besides practical experimental skills from her.

Thanks to Paul Scovell and Kathryn Boast for offering suggestions and help with my written English on many occasions.

I thank Vitaliy Mikhailik, Sam Henry, Babak Abi and Mark Pipe for their help and useful advice to me about experiments.

Also thanks to other graduate students in our group, Alice Lynch, Philip Coulter, Amy Cottle, FengTing Liao, Cees Carels and Theresa Fruth for making the group a pleasant place to work in.

Thanks to Paul Pattison, Martin Scott, Robert Storey and Mike Tacon for their technical support of this thesis work.

I would also like to thank China Scholarship Council for funding my D.Phil. study along with the University of Oxford.

I thank my family for their consistent support. I thank especially my mother Lifang Mai, who received only a primary school education (not uncommon back

in 1970s China) but is still devoted to the education of her children. One of my childhood memories is her saying firmly to me “No matter what, I will support you financially all the way through doctoral level as long as you like it.” She has kept her promise over the past 20 years. Together with my father, she has sent both of her children abroad to obtain degrees. It is amazing to see from personal experience that in modern China, the education people get changes so dramatically in a single generation.

Finally, I would like to thank my partner Shishi Liao, for the delicious food she cooks daily with effort, and for her understanding and support of my pursuit of an academic career.

Contents

1 Introduction **10**

1.1 Evidence of dark matter in the Universe 10

1.2 Dark matter candidates 30

1.3 Direct detection of WIMPs - signal model 34

1.4 Neutrinoless double-beta decay - signal model 40

1.5 Radioactive backgrounds in rare event search experiments 42

1.5.1 Background external to the detector 42

1.5.2 Radioactive background from detector materials 43

1.5.3 Common radioactive isotopes 45

1.5.3.1 U/Th chains 46

1.5.3.2 Other radioactive isotopes 53

1.5.4 Neutrino background 54

1.6 Direct detection of WIMPs - a survey to experiments 54

1.6.1 Liquid noble gas detector experiments 56

1.6.1.1 Detector medium 56

1.6.1.2 Dual-phase noble gas detector experiments 57

1.6.1.3 Single-phase noble gas detector experiments . . . 61

1.6.2 Cryogenic detector experiments 62

1.6.2.1 Cryogenic germanium detector experiments . . . 63

1.6.2.2 Cryogenic phonon-scintillation detector experiments 66

1.7 Overview of cryogenic phonon-scintillation detectors 68

2 Experimental apparatus **73**

2.1 Overview of the experiment setup 73

2.2 Calorimeter setup 78

2.2.1 Heat capacity 81

2.3 Light detector setup 81

2.4 Detector assembly 86

2.5 Data acquisition 88

2.5.1 Phonon channel DAQ 88

2.5.2 Light channel DAQ 88

2.6 Light detection optimisation 90

2.7 Helium permeation and cryostat cooldown procedure 97

2.8 ^{57}Co source 101

3 Data analysis **103**

3.1 Phonon channel analysis 106

3.1.1 Demodulation 106

3.1.2 Pulse finding 114

3.1.3 Data quality cuts 120

3.1.3.1 Contaminated pulses with poor pulse height estimation 120

3.1.3.2 Data quality cuts 122

3.1.4 Template pulse construction 126

3.1.5 High-pass filter 130

3.1.6 Template pulse fit 131

3.1.7 Baseline energy resolution 135

3.1.8 Summary of phonon channel analysis 135

3.2 Light channel analysis . . . 136
3.2.1 $CaMoO_4$ data with "dead-time free" DAQ mode . . . 136
3.2.1.1 Photon grouping . . . 137
3.2.1.2 Baseline estimation . . . 137
3.2.1.3 Photon counting . . . 139
3.2.1.4 Scintillation decay . . . 145
3.2.1.5 Scintillation and dark pulse simulation . . . 146
3.2.2 $CaWO_4$ data with "fixed-length" DAQ mode . . . 153
3.2.2.1 Baseline estimation . . . 160
3.2.2.2 Photon counting . . . 161
3.2.2.3 Scintillation decay . . . 162
3.2.2.4 Statistical test . . . 162
3.3 Coincident signals . . . 162
3.3.1 Timestamp . . . 163
3.3.2 Synchronisation . . . 163
3.4 Light yield . . . 165
3.5 PMT characterisation . . . 169
3.5.1 Dark count rate . . . 170
3.5.2 Single electron response (SER) and gain . . . 172

4 Results and discussion 174

4.1 Phonon channel results . . . 174
4.2 Light channel results . . . 184
4.2.1 Light channel energy spectrum . . . 184
4.2.2 Scintillation Decay . . . 186
4.3 Result of coincident signals . . . 190
4.3.1 Scatter plots and energy spectrum plots of coincident signals 190
4.3.2 Anti-correlation between phonon and light channel . . . 194

4.4 Light yield plot 197
4.5 PMT characterisation results 200
4.5.1 Dark count rate result 200
4.5.2 Single electron response result and gain of the PMT 202
4.6 PMT intrinsic radioactive background 202
4.6.1 Radioactivity comparison 202
4.6.2 Monte Carlo simulation 205
4.6.2.1 Electron recoil backgrounds 208
4.6.2.2 Nuclear recoil backgrounds 210
4.6.3 Electron recoil leakage 213
4.6.4 Potential improvement of PMT radioactivity 214

5 Outlook and conclusions 217
5.1 Future improvement 217
5.1.1 Light detection 217
5.1.2 Powering multiple PMTs 218
5.2 Potential applications 219
5.2.1 CRESST upgrade 219
5.2.2 TeO_2 neutrinoless double-beta decay experiment 219
5.3 Conclusions 220

A R8520-06-Pt PMT room-temperature properties 223
A.1 Single electron response and dark count rate at room temperature 223

Bibliography 226

Chapter 1

Introduction

Dark matter is one of the most profound problems in modern physics. With ~26% of the mass-energy content of the Universe consistent with non-baryonic cold dark matter [1], the identification of the dark matter particle is likely to open a new chapter in physics. Also, neutrinoless double-beta decay, if observed, would establish the Majorana nature of the neutrino [2]. It would further provide information about the absolute neutrino mass scale and the neutrino mass hierarchy [3]. Even though this thesis focuses on the discussion of the dark matter, experiments aiming to detect dark matter directly and those aiming to search for neutrinoless double-beta decay share similar challenges in searching for rare events as the signal.

1.1 Evidence of dark matter in the Universe

So far, all the evidence for the existence of dark matter has come from astronomical observations (assisted by input from particle physics and nuclear physics) and the existence of dark matter is well established at this point. Its evidence spans from the galaxy scale (galaxy rotation curve), galaxy cluster scale (relative movements of galaxies in a cluster, colliding cluster and strong lensing), large scale

structure scale (structure formation), to the cosmic scale (Big Bang nucleosynthesis and cosmic microwave background). It is worth mentioning that these pieces of evidence are in different epochs of the Universe, making them more convincing. Some of these astronomical observations are discussed in this section.

Galactic rotation curves

The galaxy rotation curve is perhaps the most direct evidence for dark matter. A galaxy rotates around its centre. The luminosity of a galaxy declines gradually as the radius increases. If the mass follows the luminosity (i.e., assuming similar mass to light ratio), then beyond the radius with the majority of luminosity, the rotation speed should be Keplerian $v(r) = \sqrt{G \cdot M/r}$, where G is the gravitational constant, M is the mass inside the radius, and r is the distance to the centre (radius). Rubin and Ford, in the 1970s, used a device called DTM Image Tube Spectrograph [4], which can be mounted on large optical telescopes to measure the spectrum of the light in various positions of the nearby galaxies. Because of the Doppler effect, the measured spectrum of known emission lines tells the velocity of a particular position in the galaxy relative to the earth. The DTM Image Tube Spectrograph has signal amplification mechanisms that make it >10 times more efficient to detect light than previous instruments, thus shortening the observation time by a factor of >10, which is critical for completing the survey of rotation velocity versus radius in galaxies. The more sensitive spectrograph also enables them to measure emission lines with a larger radius and dimmer luminosity. First, they measured the rotation curve of the M31 Andromeda Galaxy [5], and they found that the rotation curve remained flat in the last 4 kpc to the 25 kpc radius (1 pc = 3.26156 light-years), the outermost region they measured. Afterward, others used the 21-cm line (radio frequency) emitted from the neutral hydrogen gas to measure the rotation speed, which enables them to measure the rotation curve

further away from the galactic centre than emission from optical light. Roberts and Whitehurst were able to extend the rotation curve of M31 to 30 kpc, and the rotation curve is found to be flat to the furthest data point [6].

For comparison, to characterize the optical radius of a galaxy, Holmberg radius is defined as the radius of the galaxy surface region where surface brightness has an apparent magnitude of 26.5 per square arcsecond in B filter [7], which is about 1% of the surface brightness of the darkest night sky. In other words, the Holmberg radius describes the radius of the galaxy where the surface luminosity becomes very low. The Holmberg radius of M31 is found to be 15.6 kpc. In other words, the rotation curve is flat ~ 2 times as far as its optical radius in the case of the M31 galaxy.

This flat galaxy rotation curve to radius much beyond the luminous region indicates a large amount of non-luminous matter distributed at a much larger radius than luminous matter in the M31 galaxy. From then on, many rotation curves of different galaxies have been measured (for example Galaxy NGC 6503 in Figure 1.1), and almost all of them show flat rotation curves to the outermost region, further supporting the existence of non-luminous matter in galaxies. One exception might be Galaxy NGC 4736, where some analysis claims this system lacks dark matter [8]. Galaxy is the smallest-scale astronomical system where evidence of dark matter exists.

Galaxy clusters

Zwicky, in 1933, noticed the velocity spread in the known velocities of 8 individual galaxies inside the Coma cluster of galaxies is close to 1000 km/s (standard deviation), measured from Doppler shift of spectral lines [10, 11, 12]. He then applied the viral theorem to deduce that there should be much more mass inside the Coma cluster than indicated by the luminous galaxies. It was observed that

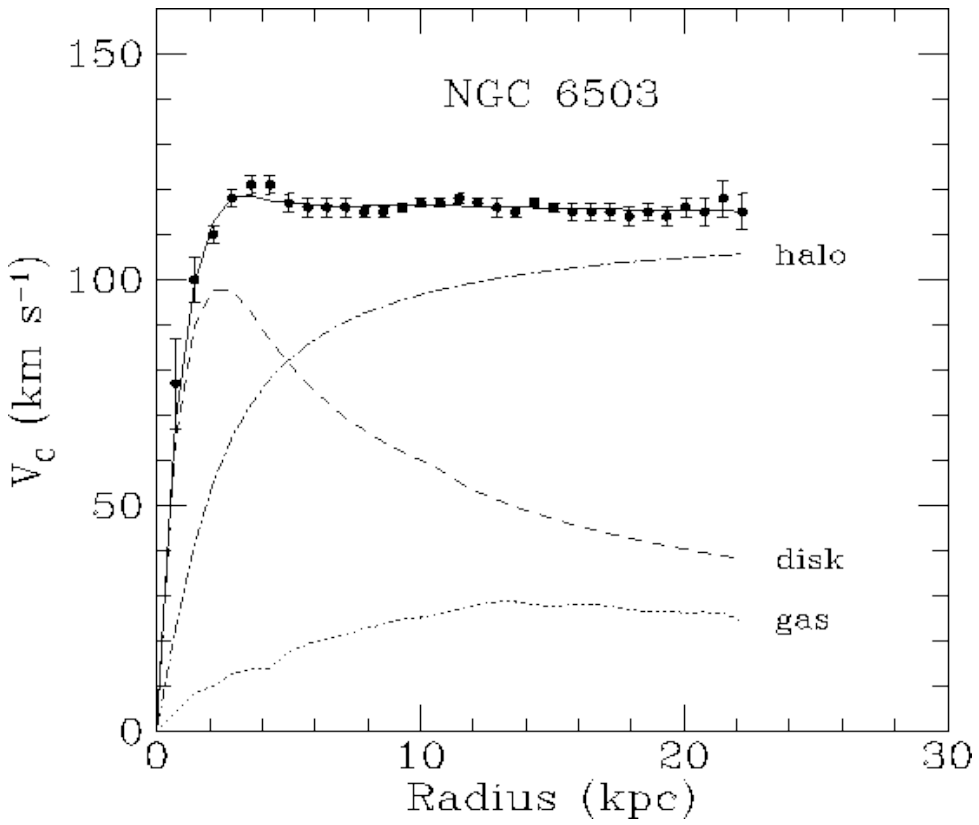

Figure 1.1: The galactic rotation curve of spiral galaxy NGC 6503. The points indicate the measured circular rotation velocities taken at different distances from the galactic centre. The contributions to the rotation curve due to the observed disk and gas are shown as dashed and dotted curves, respectively. The dot-dashed curve shows the contribution from the dark halo. The solid curve shows the combination of these three contributions. (From Figure 1 in Reference [9])

there were ~800 galaxies inside the Coma cluster at that time. Assuming each galaxy has 10^9 solar mas, he deduced that the total mass of the cluster system is $M \sim 800 \times 10^9 \times 2 \times 10^{33}\, g = 1.6 \times 10^{45}\, g$. Knowing the radius of the cluster R is ~ 1 million light-years, the mean potential energy $\langle E_p \rangle$ in the cluster system $\langle E_p \rangle = -3/5 \cdot G \cdot M^2/R$

The viral theorem indicates the average kinetic energy $\langle E_k \rangle$and the average potential energy has the following relationship

$$\langle E_k \rangle = -1/2 \cdot \langle E_p \rangle \tag{1.1}$$

The average velocity spread σ_v (standard deviation) of galaxies in the Coma cluster deduced from luminous mass is

$$\sigma_v = \sqrt{2 \cdot \langle E_k \rangle / M} = 80\, km/s\,. \tag{1.2}$$

This value deduced from the viral theorem is much smaller than the one measured from Doppler shift (1000 km/s). In other words, the mass inside the Coma cluster system should be 400 times more than that indicated by the luminous galaxies. Given the speed measured, the luminous matter inside the cluster is not enough to gravitationally bind the galaxies inside or to prevent them from flying apart. He then postulated that there must be a large amount of "dunkle Materie" (dark matter) in it. The modern understanding of dark matter is that it should be invisible instead of dark.

Colliding galaxy clusters

One empirical evidence of the existence of dark matter is seen in the colliding galaxy cluster systems (for example Bullet Cluster, 1E 0657--558), by observing the spatial offset of the total mass relative to the luminous mass in these systems

[13]. Figure 1.2 is a composite photo from different sources, showing the Bullet Cluster. The central features shown in pink are intergalactic hot gas in the plasma form, which emits the X-ray detected by the Chandra X-ray Observatory. The bright galaxies shown in yellow and white are observed by the Magellan Telescopes and the Hubble Space Telescope. The blue features shown are the locations of the respective majority of the mass in these two colliding clusters, and they are deduced from weak gravitational lensing.

From general relativity, we know that the gravity field bends light. In weak gravitational lensing, the detected shapes of background galaxies are slightly distorted by the gravity field of the foreground matter, but these distortions are very small, usually smaller than the dimensions of the background galaxies themselves. So the gravitation field of the foreground matter is not determined by a single distortion but by using statistics to count the shapes of many background galaxies in this weak gravitational lensing technique.

In this colliding cluster of galaxies system where the cores passed through each other ~100 million years ago, it appears that the galaxies in this colliding system just passed through each other without slowing down, but the hot gas got slowed down due to interactions and created a ram wave. This leads to the displacement of these two components. Because the hot gas makes up ~5% - 15% of the mass of the cluster of galaxies, and the stellar component in the galaxies only makes up 1% - 2 %, one would expect the mass centre as determined by the weak lensing would be the same as the hot gas if there was no missing mass. But surprisingly, weak lensing shows the majority of the mass in the cluster of galaxies follows the stellar component in the galaxies. The separation of the respective mass centre of the galaxy cluster and the hot gas mass centre is more than 8 sigma in statistical significance. It means an invisible non-baryonic component makes up the majority of the mass in these two clusters of galaxies. The Bullet Cluster also disfavours

models of Modified Newtonian Dynamics (MOND) as an alternative explanation without dark matter [13].

Since the discovery of dark matter in the Bullet Cluster system, many more colliding clusters with similar spatial separation of dark matter and hot gas components have been found. Reference [14] demonstrates that using 72 colliding clusters observed, an upper limit of non-gravitational self-interaction cross-section per unit mass in dark matter particles has been placed at $\sigma_{DM}/m < 0.47\ \mathrm{cm}^2\,\mathrm{g}^{-1}$, 95% CL. The dark matter component in all these 72 colliding clusters all appears to pass through each other without interacting or slowing down, just like the Bullet Cluster.

Strong gravitational lensing

Unlike weak gravitational lensing, which only slightly deforms images of the background sources, strong gravitational lensing produces multiple images, arclets, or even Einstein rings of the background sources (Figure 1.3). The foreground lensing object can be a galaxy (e.g. LRG 3-757 [16]) or a galaxy cluster (e.g. Abell 370 in Figure 1.3).

The amount of mass in the foreground lensing galaxy cluster can be deduced from the distorted image of the background source. The Einstein radius θ_E, which describes the radius of the Einstein ring in radians, can be expressed as [17]:

$$\theta_E = \sqrt{\frac{4GM}{c^2}\frac{d_{LS}}{d_L d_S}}\,, \tag{1.3}$$

where G is the gravitational constant, M is the mass of the foreground lensing cluster, c is the speed of light, d_{LS} is the distance between the foreground lensing cluster and the background source, d_L is the distance between Earth and the foreground lensing cluster, and d_S is the distance between Earth and the background source. d_{LS}, d_L and d_S are angular diameter distances. It is found that the mass

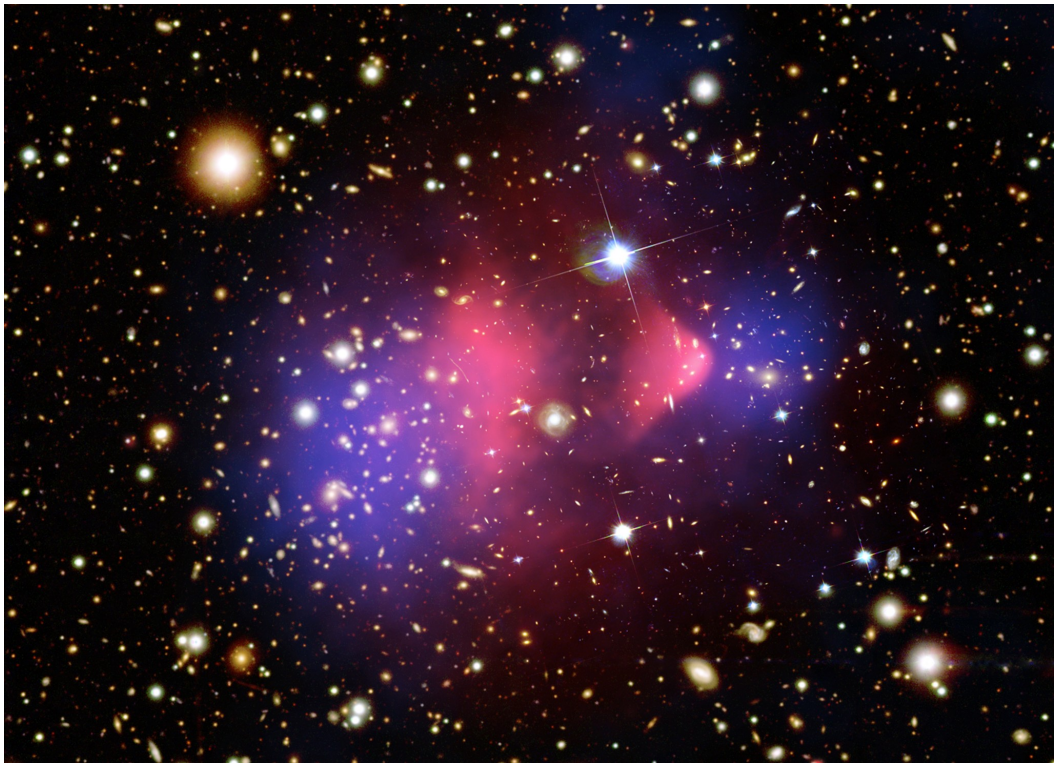

Figure 1.2: A composite image showing the Bullet Cluster (1E 0657-558) — a system of two colliding galaxy clusters. The X-ray image capturing mainly the intergalactic gas content of the clusters (which very substantially outweighs the mass of the galaxies) is shown in red. The total mass inferred from the weak gravitational lensing is shown in blue. (X-ray analysis from Reference [15] and gravitational lensing analysis from Reference [13]. Image Credit: X-ray: NASA/CXC/CfA/M.Markevitch et al.; Optical: NASA/STScI; Magellan/U.Arizona/D.Clowe et al.; Lensing Map: NASA/STScI; ESO WFI; Magellan/U.Arizona/D.Clowe et al.)

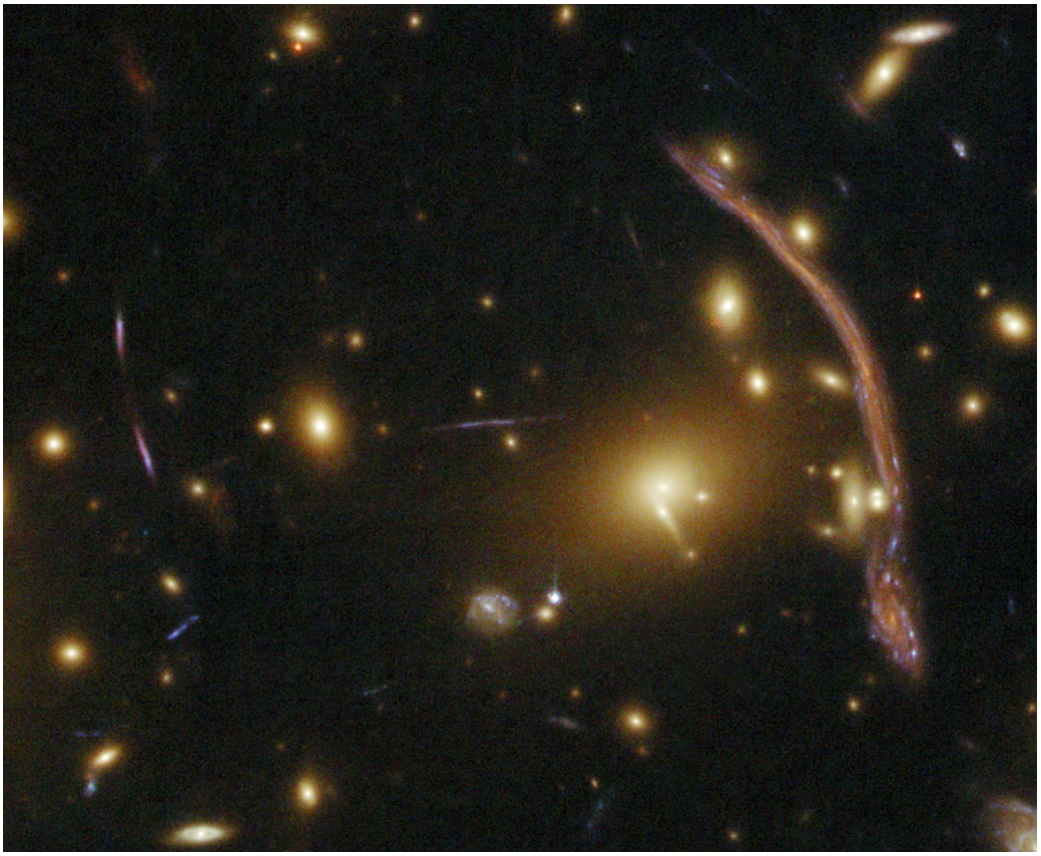

Figure 1.3: An image of arcs produced by strong lensing. The foreground galaxy cluster is Abell 370. Image credit: NASA, ESA, and the Hubble SM4 ERO Team & ST-ECF.

of the foreground lensing galaxy cluster deduced from Equation 1.3 is much larger than the mass inferred from the luminosity of the foreground galaxy cluster using the standard mass-to-light ratio. For example, a study of the strong gravitational lensing in the Abell 370 galaxy cluster (Figure 1.3) indicates the mass-to-light ratio of the cluster is around 10^2–10^3 solar units, as compared to the normal mass-to-light ratio of a few solar units. Consequently, strong gravitational lensing indicates that a large amount of dark matter exists in the Abell 370 galaxy cluster [18].

Large-scale structure

The Universe is homogeneous at scales larger than a few hundred Mpc, according to the cosmological principle. Below this scale, the planets, stars, galaxies, clusters of galaxies we observe today are the products of gravitational instability. The seeds of slight overdensity in the early universe grow by gravitationally attracting the matter nearby. The anisotropy in the cosmic microwave background was first detected by the COBE satellite at the level of $\Delta T/T = 10^{-5}$. But this temperature difference (thus density difference) is too small to explain the structure we observe today if the baryon is the dominant matter component in the Universe. There is simply not enough time for the structure to form from the observed CMB temperature difference because of the slow gravity instability process. Unlike baryons, non-baryonic dark matter is not subject to electromagnetic interaction; thus, the density of dark matter does not oscillate like the photo-baryon plasma before recombination. The structure of dark matter can grow once the Universe has transitioned from being radiation-dominated to matter-dominated. But the radiation pressure before recombination would prevent the growth of structure in the baryon sector before the recombination. In other words, the dark matter in the Universe jump-starts the structure formation process by forming gravitational potential wells before recombination and the ordinary matter later falls into thhose potential wells after the recombination.

Another evidence of dark matter from structure formation is from comparing N-body simulations to observation in large-scale structure. The three galactic redshift surveys by CfA2, SDSS, and 2dFGRS shows the cosmic web structure, with superclusters and connecting filaments, with voids separating them as shown in Figure 1.4. The same figure also shows the N-body simulation performed by Millennium Simulation to compare with observation. Without non-baryonic dark matter, the simulation could not recreate within the anticipated timescales the

features in the observation. More specifically, the type of dark matter cannot be hot dark matter (meaning its velocity at some point in the early universe is relativistic). For the hot dark matter (HDM) scenario, structures smaller than the typical length of the dark matter particle (speed times the age of the Universe) are washed out [19, 20], as the hot dark matter particles just fly past those smaller scales. In such scenarios, structures are formed top-down, meaning superclusters are formed first, and galaxies are formed later as the larger structure is fragmented into smaller structure. For cold dark matter (CDM) and warm dark matter (WDM) scenarios, small objects are formed first, and they merge and accrete into larger structures, and this process is called bottom-up. The observation indicates that the bottom-up process is correct, favoring CDM and WDM over HDM [21].

Big Bang nucleosynthesis (BBN)

According to the Big Bang theory, the Universe started hot and dense, and it subsequently expands and cools down. When the universe is cold enough, composite particles like protons and neutrons are formed from quarks. The Big Bang nucleosynthesis (BBN) started when the temperature of the universe was cold enough (a few seconds after Big Bang) so the photons did not break apart deuterium (binding energy 2.23 MeV) once deuterium is formed. The BBN stopped when the universe further expanded and cooled down, so the nuclear reaction could not continue because of the Coulomb barrier. In BBN, significant amounts of deuterium (through n + p $\rightarrow$ ^{2}H + γ reaction), tritium (^{2}H + ^{2}H $\rightarrow$ ^{3}H + p and ^{3}He + n $\rightarrow$ ^{3}H + p), He-3 (p + ^{2}H $\rightarrow$ ^{3}He + γ and ^{2}H + ^{2}H $\rightarrow$ ^{3}He + n), He-4 (^{3}H + ^{2}H $\rightarrow$ ^{4}He + n and ^{3}He + ^{2}H $\rightarrow$ ^{4}He + p), Li-7 (^{4}He + ^{3}H $\rightarrow$ ^{7}Li + γ and ^{7}Be + n $\rightarrow$ ^{7}Li + p), and Be-7 (^{4}He + ^{3}He $\rightarrow$ ^{7}Be + γ) were created. Be-7 was quickly decayed to Li-7 with 53s half-life via electron capture and tritium was decayed to

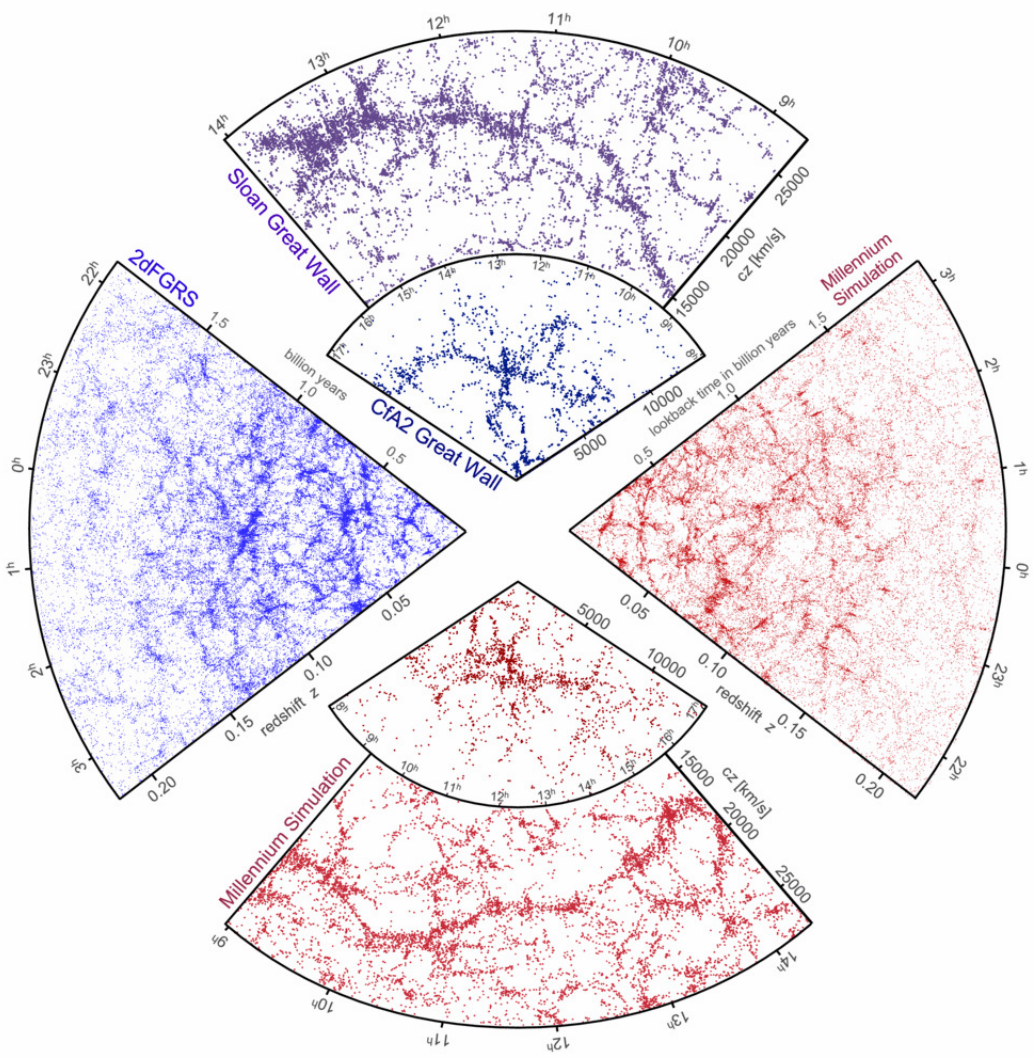

Figure 1.4: Distribution of galaxies observed from spectroscopic redshift surveys (left and top) and from cosmological N-body simulations (right and bottom) of the ΛCDM model (Λ stands for the cosmological constant as a form of dark energy and CDM stands for the cold dark matter). (From Reference [22])

He-3 with 12.3 years half-life via beta decay. Most of the heavier isotopes in the universe are later created in stellar nuclear reactions.

From our current understanding of the conditions during the BBN and nuclear physics process, numerical simulation code can calculate how much the primordial abundances of different isotopes are. As shown in Figure 1.5, the production of the primordial isotopes depends on the density of baryons (more precisely, nucleons) at that time. These calculations of primordial abundances are compared to the primordial abundance observation from regions with low metallic contents (any isotopes heavier than Li-7 are considered metal in this context as they are produced in stellar processes), avoiding abundance contamination from the later stellar processes. The observed abundance of deuterium is a lower limit of primordial abundance, as any deuterium produced in the stellar process is fused into He-4; thus, stellar processes only destroy deuterium. As shown in Figure 1.5, the calculated primordial abundance of He-4, deuterium, He-3, and Li-7 varies with the baryon density (shown in x-axis as baryon to photon ratio, and photon abundance is well constrained by the measured present CMB temperature of 2.7255K). The measurement of these primordial abundances thus provides a constraint on the density of baryons, which is expressed as a fraction relative to the critical density. The baryonic content deduced from BBN concordance range (mainly from the precise determination of primordial D/H ratio) is [23]:

$$0.021 \leq \Omega_b h^2 \leq 0.024 \ (95\% \text{ CL}) \ . \tag{1.4}$$

It is also worth noting that the baryonic density deduced from CMB is $\Omega_b h^2 = 0.0223 \pm 0.0002$, which is remarkably consistent with the value from BBN, despite these processes happened in different epochs of the universe. Using the Hubble constant H_0 inferred from the Planck 2015 results [1], $H_0 = (67.8 \pm 1.8)$ $\text{km}\,\text{sec}^{-1}\,\text{Mpc}^{-1}$ (95% CL), the baryon density Ω_b (normalised to the critical den-

sity ρ_c) determined by the BBN concordance range is:

$$0.048 \leq \Omega_b \leq 0.053 \ (95\% \text{ CL}) \ . \tag{1.5}$$

The total matter density deduced from the CMB is $\Omega_m \sim 0.3$, and it can be inferred that most of the mass in the Universe is in non-baryonic (more precisely, non-nucleonic) form. This determination of the baryon density from BBN is another crucial evidence for non-baryonic dark matter.

However, BBN has some issues. One issue is the so-called lithium problem. Figure 1.5 shows that the primordial ^{7}Li/H ratio observed is smaller than what is expected from the D/H ratio. It is unclear at this stage whether this deviation is due to the poor observation of the primordial lithium density or new physics [23]. Another issue is that, if primordial black holes formed before BBN, as a type of exotic baryonic matter, they would not be included in the Ω_b bound in Equation 1.5. The reason is that primordial black holes would not have a noticeable effect on the abundances of primordial light elements. Consequently, BBN does not rule out primordial black holes as a dark matter candidate [24]. Primordial black holes have been probed with other methods, such as gravitational microlensing [25]. Primordial black holes with a large range of mass scenarios ($1 - 10^4 \ M_\odot$) have been excluded as the dominant component of dark matter according to a recent study [26].

Cosmic microwave background (CMB)

Cosmic microwave background is the relic radiation of the Big Bang and it offers one of the most precise estimates of the dark matter content in the Universe.

After the Big Bang nucleosynthesis, the temperature of the Universe is still so hot that the photon energy is still higher than the binding energy of hydrogen atoms, so photons ionize hydrogen atoms. In this epoch, the photons, baryons

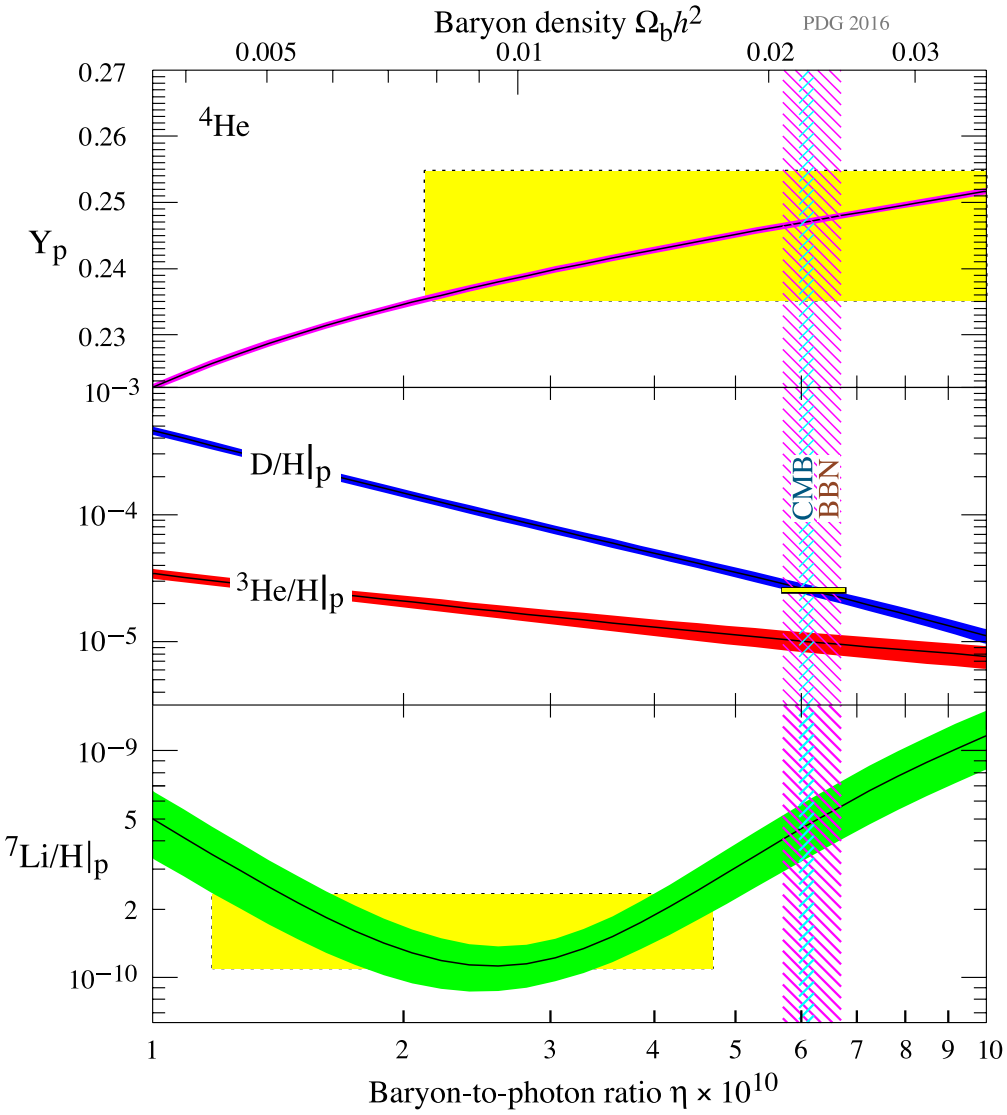

Figure 1.5: The abundances of primordial ^{4}He, D, ^{3}He, and ^{7}Li versus the baryon density, as predicted by the standard model of Big Bang nucleosynthesis. The bands show the 95% CL range. The observed light element abundances are indicated by boxes. The narrow vertical band indicates the cosmic baryon density measured from CMB, and the wider vertical band indicates the BBN concordance range (both at 95% CL). (From Reference [23])

(mainly protons and helium-4 nuclei), and electrons are tightly coupled by constant interactions, forming so-called photon-baryon plasma. As the Universe further expands and cools down, at T ~ 3000 K (corresponding to 380,000 years after the Big Bang), protons and electrons formed neutral hydrogen atoms, at an epoch called "recombination". Despite the name "recombination", this is actually the first time stable atoms were formed. After recombination, the Universe becomes transparent to the photons, and photons are free to propagate without constantly scattering off electrons. These photons become the first light we can observe from the infant universe. As the space-time expands, the photon wavelengths are stretched into microwave length (mm - cm), and they are called the cosmic microwave background (CMB).

COBE first measured that the CMB has a nearly perfect black body spectrum with a temperature of 2.73 K [27], indicating the Universe was in thermal equilibrium when the CMB was released. COBE also observed the anisotropy of the CMB across the sky in the level of 1 in 10^5 [28]. Later many earth-based experiments and subsequent space observatories WMAP and Planck further refined the observation of CMB anisotropy to higher angular and temperature precision, as shown in the anisotropy power spectrum in Figure 1.6. This precisely measured power spectrum of CMB anisotropy tells us a wealth of information about the energy distribution of different compositions and the history of the Universe, including the dark matter content. A good pedagogical material to understand the physics of CMB anisotropy can be found in Reference [29].

The photon-baryon plasma before recombination is like a gas, as it can be compressed and rarefied under different forces. The theory of inflation proposes the early universe rapidly expanded by a factor of $\sim 10^{26}$ from 10^{-36} to $\sim 10^{-32}$ s after singularity [30], and density fluctuations from the quantum fluctuation before the inflation expanded to overdensity and underdensity in the cosmic scale. The

gravity tries to pull photon-baryon plasma into denser regions, and the radiation pressure tries to fight this compression and rarefies the plasma, causing a process called acoustic oscillation. The compression first happened during the acoustic oscillation due to the gravitational pull. After reaching the compressional maxima, the radiation pressure causes the plasma to maximal rarefaction, and this cycle continues. Non-baryonic dark matter is not part of this plasma and it does not go through this density oscillation, as it does not interact with the ordinary matter or radiation through electromagnetism. The dark matter creates the gravitational well that the plasma can fall into. The acoustic oscillation happens at all the length scales. At recombination, the length scales with maximal compression or maximal rarefaction correspond to the peaks in the anisotropy power spectrum (Figure 1.6).

The first three peaks in the power spectrum tell us different information about the Universe. The first peak corresponds to the oscillation length scale with the first maximal compression at recombination. Knowing the sound speed and the recombination time, we know how much physical length the sound has traveled in this mode. The multipole (or the angle) of this first peak then tells us the spatial curvature of the Universe. If the Universe has negative curvature (open universe), the first peak we observe today would appear in the higher multipole (smaller angle). If the Universe has positive curvature (closed universe), the first peak would appear in the lower multipole (larger angle). From the observation of the location of the first peak in the power spectrum, it turns out that the Universe is consistent with being flat, indicating the total matter-energy density of the Universe is near the critical density ($\rho_c = 1.88h^2 \times 10^{-29} g \cdot cm^{-3}$).

The second peak tells us the amount of baryons in the universe. Because the content of baryon increases the magnitude of the compressional peaks (first, third, fifth ...) over the rarefactional peaks (second, fourth, sixth ...), due to an

effect called baryon loading. As an analogy to understand this effect, if we release a massive ball (corresponding to the baryonic mass) hanging vertically from a spring, the heavier the ball, the further the ball would fall into the gravitational well (corresponding to the compression of the photon-baryon plasma) before it returns to the initial start position (corresponding to the rarefaction maximal). The relative height of the first peak to the second peak tells us the extent of the baryonic loading, thus the baryon density.

The third peak tells us the photon to matter ratio, and thus the dark matter density at given baryon density. At the beginning of the universe, the photon energy density dominates over the matter density. But as the universe expands, the photon energy redshifts. At some point, the energy density of matter becomes larger than the photon energy density. In the scenario deficient of non-baryonic dark matter, the gravitational potential well is initially dominated by the photon energy. After photon-baryon plasma reaches the compressional maximal, the potential well for higher peaks (thus shorter physical length) dominated by the photon energy decays with the expansion of the universe. Without the potential well to fight against, the photon-baryon plasma could rebound to much larger amplitudes in the subsequent oscillations, and this effect is called radiation driving. This effect would drive up all the amplitudes in the higher peaks. Because the potential well is eliminated in this scenario with the absence of non-baryonic dark matter, the larger amplitude of odd-number peaks over even-number peaks from baryonic loading is also eliminated. Observing a third peak with comparable height to the second peak tells us the presence of a significant density of dark matter.

As shown in Figure 1.7, the change of dark matter density changes the power spectrum significantly.

The baryon content and the non-baryonic dark matter content inferred from

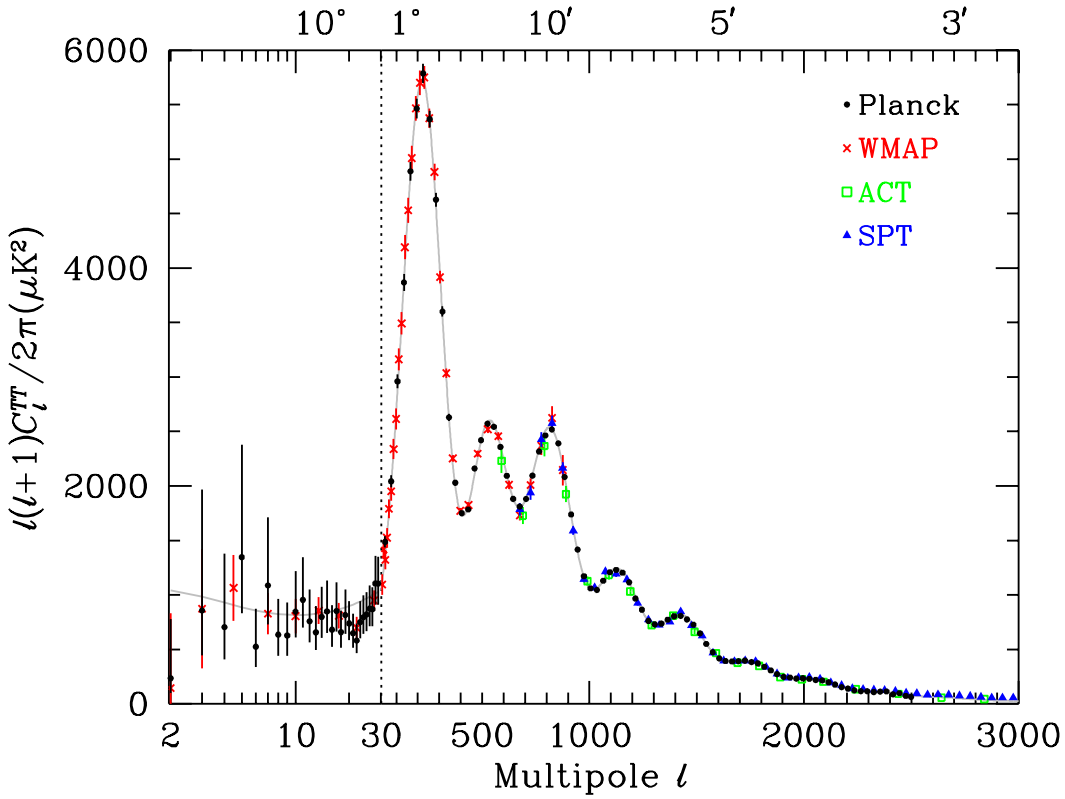

Figure 1.6: Cosmic microwave background anisotropy power spectrum from Planck, WMAP, ACT, and SPT experiment. The grey line is a fit by the ΛCDM model for the Planck data. The x-axis is logarithmic for the multipoles below 30 to show the Sachs-Wolfe plateau, and linear for the higher multipoles. The acoustic peaks are clearly observed from this anisotropy power spectrum. (From Reference [23])

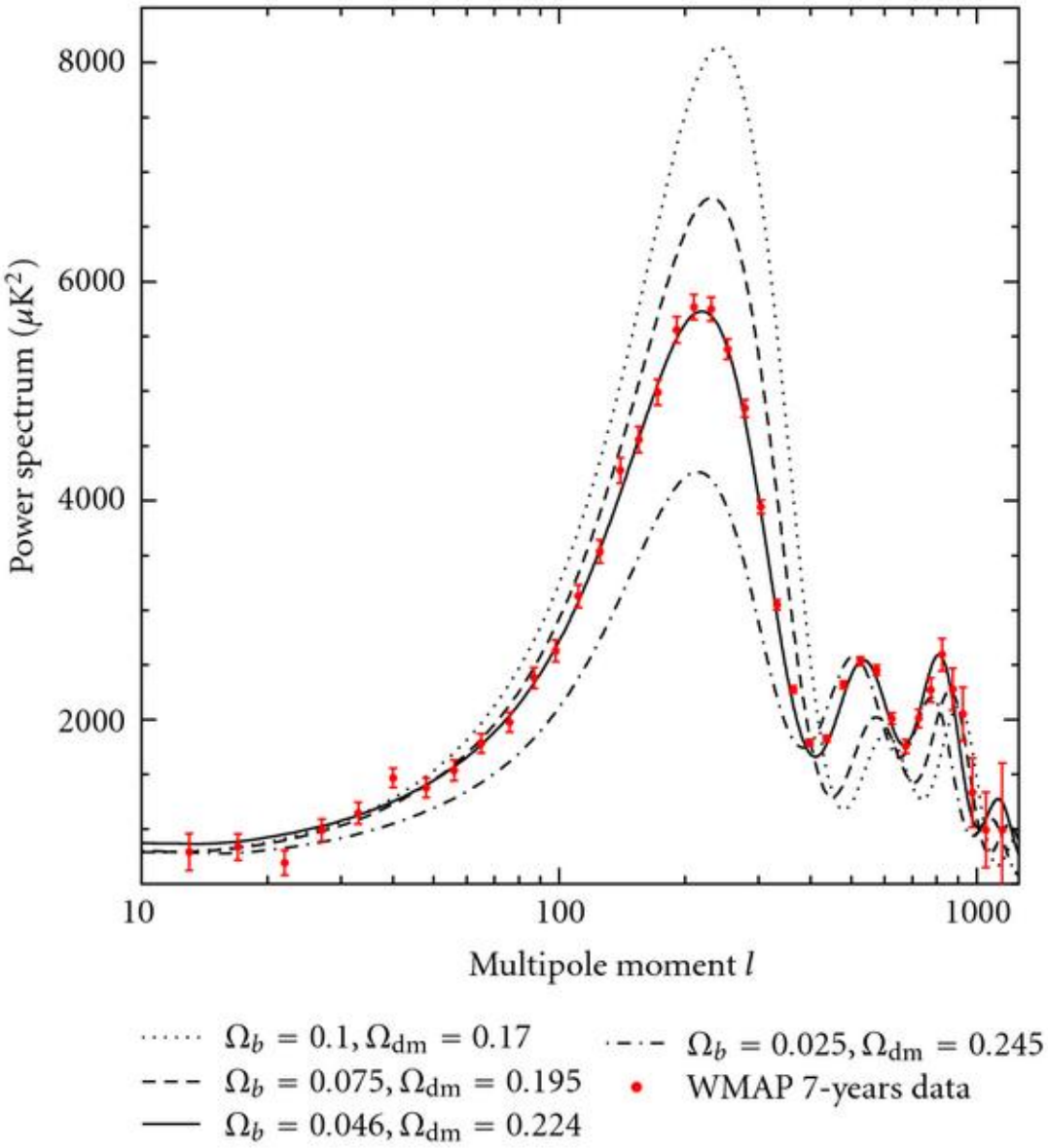

Figure 1.7: The CMB anisotropy power spectrum in different baryon density (Ω_b) and non-baryonic dark matter density ($\Omega_{\rm dm}$) scenarios (holding $\Omega_{\rm tot} = 1$) as shown in different curves, with the WMAP 7 years data (red points). (From Reference [31])

the Planck 2015 results [1] are:

$$\begin{aligned} \Omega_b h^2 &= 0.02226 \pm 0.00023 \,, \\ \Omega_{\rm dm} h^2 &= 0.1186 \pm 0.0020 \,, \end{aligned} \quad (68\%\ \text{CL}) \,, \tag{1.6}$$

where Ω_b and $\Omega_{\rm dm}$ are the baryon density and non-baryonic dark matter density, normalised to the critical density ρ_c, respectively. The reduced Hubble constant h is defined as $h \equiv H_0/100\,\mathrm{km\,sec^{-1}\,Mpc^{-1}}$. Using the Hubble constant H_0 inferred from the Planck 2015 results, $H_0 = (67.81 \pm 0.92)\ \mathrm{km\,sec^{-1}\,Mpc^{-1}}$ (68% CL), the Ω_b and $\Omega_{\rm dm}$ can be inferred as:

$$\begin{aligned} \Omega_b &= 0.0484 \pm 0.0014 \,, \\ \Omega_{\rm dm} &= 0.258 \pm 0.008 \,, \end{aligned} \quad (68\%\ \text{CL}) \,. \tag{1.7}$$

Equation 1.7 shows that the baryon content constitutes $4.84\% \pm 0.14\%$ of the total energy-mass density of the Universe, while non-baryonic dark matter constitutes $25.8\% \pm 0.8\%$ of the total energy-mass density. In other words, over 84% of the mass density of the Universe is in the form of non-baryonic dark matter.

With compelling evidence from different phenomena at scales spanning orders of magnitude and from different epochs of the Universe, the existence of non-baryonic cold dark matter in the Universe is well established.

1.2 Dark matter candidates

From the astronomical observations mentioned in Section 1.1, the requirements on non-baryonic dark matter candidates include: they should interact very weakly (if at all) with electromagnetic radiation (otherwise they would be visible); they should be non-relativistic (cold dark matter requirement); they should be stable on the cosmological scale (otherwise by now they would have decayed and would not be observed in nearby galaxies); they should have the right relic density

after being frozen out in the early Universe; and they should be gravitationally interacting (that is how we know about them in the first place).

There are many dark matter candidates, among which weakly interacting massive particles (WIMPs) and axions are especially well motivated and being most actively searched for by dark matter direct detection experiments. Axions were first proposed to tackle the strong CP problem of QCD [32]. As the experimental technique in this thesis focuses on the detection of WIMPs, WIMPs will be discussed in more detail below. More details of the experimental search for axions can be found in Reference [33].

WIMP

WIMPs correspond to a class of dark matter candidates, and one example is the lightest (thus stable) superparticle in supersymmetric models, such as the neutralino [34]. WIMPs are postulated to have a particle mass between around 10 $\mathrm{GeV\,c^{-2}}$ and a few $\mathrm{TeV\,c^{-2}}$, and the cross-sections of WIMPs are postulated to be roughly at the weak interaction scale. WIMPs are especially well-motivated dark matter candidates, because an annihilation cross-section at the weak interaction scale would produce a thermal relic density of the same order of magnitude as observed ($\Omega_{\mathrm{dm}} \approx 0.25$). This coincidence is the so-called "WIMP miracle" and it is discussed below.

In the standard cosmological model, the early Universe is initially hot and dense, and all the particles at that stage are in thermal and chemical equilibrium. As the Universe expands and cools down continuously, the temperature of the Universe T (in natural units) drops and becomes comparable to the mass of the WIMPs m_W. As the annihilation of WIMPs continues and there is not enough energy for lighter particles to produce WIMPs, the number of the WIMPs decreases exponentially as a function of temperature $e^{-m_W/T}$ (Boltzmann suppressed). As

the number of WIMPs continues to decrease and the Universe continues to expand, it gets to a stage where the Universe becomes so large and the WIMP gas becomes so dilute that the WIMPs cease to annihilate (the mean free path for annihilation is of the same order as the Hubble radius). Consequently, the number of WIMPs asymptotically approaches a constant value — the relic density. In other words, the WIMPs "freeze out" and chemically decouple from the particle "soup", so the co-moving density of WIMPs have remained roughly constant ever since. The WIMP relic density is determined by the thermally-averaged annihilation cross-section $\langle \sigma_A v \rangle$, as shown by numerical calculations in Figure 1.8.

Quantitatively, the present density of WIMPs (Ω_{W}) is approximately [34]:

$$\Omega_W h^2 \simeq \left(\frac{3 \times 10^{-27}\ \mathrm{cm^3\,s^{-1}}}{\langle \sigma_A v \rangle} \right) . \tag{1.8}$$

Equation 1.8 shows that a larger annihilation cross-section leads to a lower relic density. It is because a larger annihilation cross-section keeps the WIMPs in equilibrium for longer and decouples later, when the temperature of the Universe is lower, so the relic density is smaller.

The mass of the WIMP m_W affects Ω_{W} mainly through $\sigma_A v$, which can be written on dimensional grounds as [35]:

$$\sigma_A v = \begin{cases} k \frac{g_{weak}^4}{16\pi^2 m_W^2} , & \text{S-wave annihilation} \\ k \frac{g_{weak}^4}{16\pi^2 m_W^2} \cdot v^2 , & \text{P-wave annihilation} , \end{cases} \tag{1.9}$$

where the parameter $k = \mathcal{O}(1)$ accounts for deviations from this estimate and the weak interaction gauge coupling $g_{weak} \simeq 0.65$. Terms higher-order in v have been neglected in Equation 1.9. Considering both the S-wave and P-wave annihilation, and letting k vary from 0.5 to 2, it is found that a single WIMP with a mass from ~100 GeV c^{-2} to 1 TeV c^{-2} would reproduce the relic density of the same order of

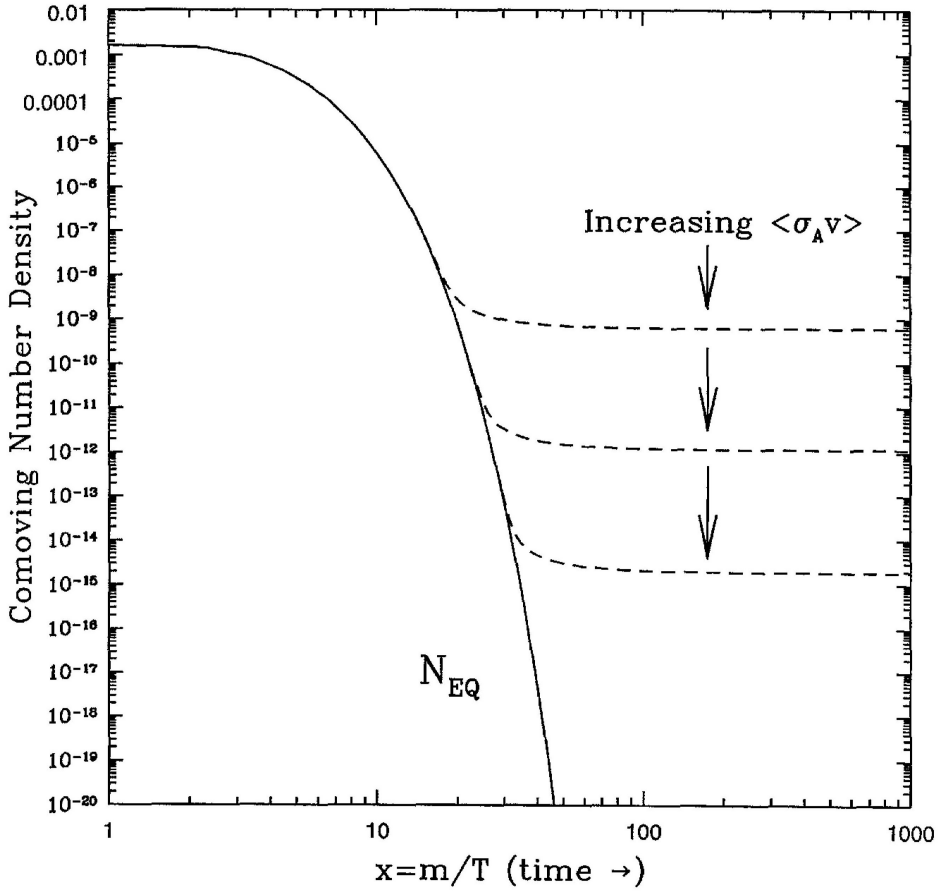

Figure 1.8: The co-moving WIMP number density and the resulting thermal relic density of WIMPs (dashed curves) versus temperature T (thus time) in the early universe. Higher annihilation cross-sections lead to lower relic densities by keeping the WIMPs in equilibrium to later times. The solid curve labled "N_{EQ}" shows the number density if a particle remains in equilibrium. (From Reference [34])

magnitude as observed [35]. Multiple WIMPs could also fit the roles of cold dark matter.

With motivations mentioned above, combined with the possibility of detecting them with current technology, most of the current experiments of dark matter direct detection are designed to search for WIMPs.

1.3 Direct detection of WIMPs - signal model

This section discusses how to calculate the differential event rate of WIMPs scattering off the detector's target. In the model described here, the Earth is moving relative to the galactic dark matter halo, with the Earth orbiting the Sun which in turn orbits the centre of the Milky Way galaxy. Thus, with this relative movement at a speed of $\mathcal{O}\left(100\,\mathrm{km\,s^{-1}}\right)$, WIMPs could deposit recoil energy in a detector on Earth by scattering off target nuclei in the detector.

In general, the differential WIMP-nucleus scattering rate $\mathrm{d}R$ per unit target mass can be expressed as [34]:

$$\mathrm{d}R = \frac{1}{m_N}\frac{\rho_0}{m_W} v f_t\left(v\right)\frac{\mathrm{d}\sigma}{\mathrm{d}\left|\vec{q}\right|^2}\mathrm{d}\left|\vec{q}\right|^2\mathrm{d}v\,, \tag{1.10}$$

where R is the event rate, m_N is the mass of the target nucleus, ρ_0 is the local WIMP density, m_W is the mass of the WIMP, v is the speed of the WIMP relative to the target nucleus, $f_t\left(v\right)$ is the speed distribution of the WIMP in the frame of the target nucleus, $\mathrm{d}\sigma/\mathrm{d}|\vec{q}|^2$ is the differential cross-section and $\vec{q}$ is the momentum transferred. Equation 1.10 shows that the differential scattering rate per unit target mass is proportional to the number density of target nuclei ($1/m_N$), to the number density of the WIMP (ρ_0/m_W), to the speed that the unit target mass sweeps through the WIMP halo (v), to the speed distribution $f_t\left(v\right)$ and to the differential cross-section $\mathrm{d}\sigma/\mathrm{d}|\vec{q}|^2$.

The differential cross-section can be written as [34]:

$$\frac{\mathrm{d}\sigma}{\mathrm{d}\left|\vec{q}\right|^2} = \frac{\sigma_0}{4\mu_N^2 v^2}F^2\left(|\vec{q}|\right)\,, \tag{1.11}$$

where σ_0 is the zero-momentum-transfer cross-section, the reduced mass of the WIMP-nucleus system is $\mu_N = m_N m_W/(m_N+m_W)$, and $F\left(|\vec{q}|\right)$ is the form factor. The interaction loses coherence due to the finite size of the target nucleus and

the form factor $F\left(|\vec{q}|\right)$ takes into account this effect. The form factor is defined separately for spin-independent and spin-dependent interactions.

The momentum transferred can be expressed as $|\vec{q}|^2 = 2\mu_N^2 v^2 (1 - \cos\theta^*)$, where θ^* is the scattering angle in the centre-of-momentum frame. The energy transferred to the target nucleus (the energy deposited in the detector) is [34]:

$$E_R = \frac{|\vec{q}|^2}{2m_N} = \frac{\mu_N^2 v^2}{m_N} (1 - \cos\theta^*) \ . \tag{1.12}$$

To calculate the total rate, $\mathrm{d}R$ is integrated over all possible speeds, and over deposited energies between the detector threshold energy E_T and $E_{max} = {}^{2\mu_N^2 v^2}/_{m_N}$. Combining Equations 1.10, 1.11 and 1.12, we have [34]:

$$\frac{\mathrm{d}R}{\mathrm{d}E_R} = F^2\left(E_R\right) \cdot \frac{\sigma_0}{2m_W \mu_N^2} \cdot \rho_0 \int\limits_{v \geq v_{min}} \frac{f_t\left(v\right)}{v} \mathrm{d}v \ , \tag{1.13}$$

where $v_{min} = \sqrt{{}^{m_N E_R}/_{2\mu_N^2}}$. Equation 1.13 shows that the WIMP-nucleus scattering spectrum depends on nuclear physics via $F^2\left(E_R\right)$, on particle physics via σ_0 and m_W, and on galactic astrophysics via ρ_0 and $f_t\left(v\right)$. These different factors are discussed separately below. For simplicity, only the spin-independent scenario is discussed. Details about the spin-dependent WIMP-nucleus scattering scenario are discussed in Reference [36].

Form factor

Data from electron-nucleus scattering is used to deduce the form factor $F_{SI}^2\left(E_R\right)$ for spin-independent scattering, and this form factor is parameterised as [37]:

$$F_{SI}^2\left(E_R\right) = \left(\frac{3j_1\left(qr_1\right)}{qr_1}\right)^2 \exp(-q^2 s^2) \ , \tag{1.14}$$

where $j_1(.)$ is the spherical Bessel function of the first kind, the momentum transferred is $q = \sqrt{2m_N E_R}$, and $r_1 = \sqrt{R^2 - 5s^2}$ with $R = 1.2A^{1/3}$ fm and $s \simeq 1$ fm. A is the mass number of the target nucleus.

Zero-momentum-transfer cross-section σ_0

For spin-independent scattering, assuming the WIMP effective scalar coupling to the proton and neutron are the same and the vector coupling is zero, the zero-momentum-transfer cross-section $\sigma_{0,SI}$ can be expressed as [38]:

$$\sigma_{0,SI} = A^2 \left(\frac{\mu_N}{\mu_n}\right)^2 \sigma_n \,, \tag{1.15}$$

where μ_n is the reduced mass of WIMP-nucleon system and σ_n is the scalar WIMP-nucleon elastic cross-section. σ_n is the quantity that is compared to theoretical models, and between experiments with different target nuclei.

Local dark matter density

By fitting the dynamic properties of the Milky Way galaxy, with some assumptions about the shape of the dark matter halo, the dark matter local density ρ_0 can be estimated. The estimated local dark matter density is in the range 0.2–0.4 GeV c^{-2} cm^{-3}, depending on the choice of the dark matter halo profile [39].

WIMP speed distribution

Canonically, the WIMP speed distribution in the rest frame of the galactic dark matter halo is assumed to be Maxwellian, with a truncation at the escape velocity v_{esc} of the Milky Way Galaxy [40]:

$$f_h\left(|\vec{v}|\right) = H\left(v_{esc} - |\vec{v}|\right) \frac{1}{N_{esc}} \left(\frac{3}{2\pi\sigma_v^2}\right)^{3/2} \exp\left(-\frac{3\,|\vec{v}|^2}{2\sigma_v^2}\right) \,, \tag{1.16}$$

where $H(.)$ is the Heaviside step function, N_{esc} is a normalisation factor and σ_v is the RMS speed dispersion. The speed dispersion σ_v is related to the local circular speed v_c by $\sigma_v = \sqrt{3/2}\, v_c$, and v_c is measured to be $220 \pm 20\,\mathrm{km\,s^{-1}}$ [41]. A recent study of the high-velocity halo stars from the RAVE survey sets v_{esc} to be 492–587 $\mathrm{km\,s^{-1}}$ (90% CL) [42].

The velocity of the detector in the dark matter halo frame, $\vec{v}_E(t)$, is the vector sum of the velocity of the Sun relative to the halo frame (~220 $\mathrm{km\,s^{-1}}$) and the velocity of the Earth relative to the Sun (~30 $\mathrm{km\,s^{-1}}$). Note that the relative direction of these two constituent velocities changes with a period of around one year, resulting in the annual modulation of the signal [43]. In principle, the velocity of the Earth's rotation (~0.5 $\mathrm{km\,s^{-1}}$ at the equator) is also a contributing factor, but it is much smaller than the other two factors. By taking account of the speed of the Earth relative to the dark matter halo, as described in Reference [40], the integration in Equation 1.13 becomes:

$$\int\limits_{v \geq v_{min}} \frac{f_t(v)}{v} \mathrm{d}v = \begin{cases} \frac{1}{v_c y}\,, & z < y,\ x < |y - z| \\ \frac{\left[\mathrm{erf}(x+y) - \mathrm{erf}(x-y) - \frac{4}{\sqrt{\pi}} y e^{-z^2}\right]}{2 N_{esc} v_c y}\,, & z > y,\ x < |y - z| \\ \frac{\left[\mathrm{erf}(z) - \mathrm{erf}(x-y) - \frac{2}{\sqrt{\pi}} (y+z-x) e^{-z^2}\right]}{2 N_{esc} v_c y}\,, & |y - z| < x < y + z \\ 0\,, & y + z < x\,, \end{cases} \tag{1.17}$$

where $x \equiv {v_{min}}/{v_c}$, $y \equiv {|\vec{v}_E(t)|}/{v_c}$, $z \equiv {v_{esc}}/{v_c}$ and $\mathrm{erf}(.)$ is the error function.

To calculate the differential event rate from WIMP-nucleus interaction, all the factors in Equation 1.13 need to be taken into account. The canonical assumptions are $v_{esc} = 544\,\mathrm{km\,s^{-1}}$, a standard Maxwellian velocity distribution with $v_c = 220\,\mathrm{km\,s^{-1}}$, and $\rho_0 = 0.3\,\mathrm{GeV\,c^{-2}\,cm^{-3}}$.

Figure 1.9 shows the differential event rates expected for three elements (Xe,

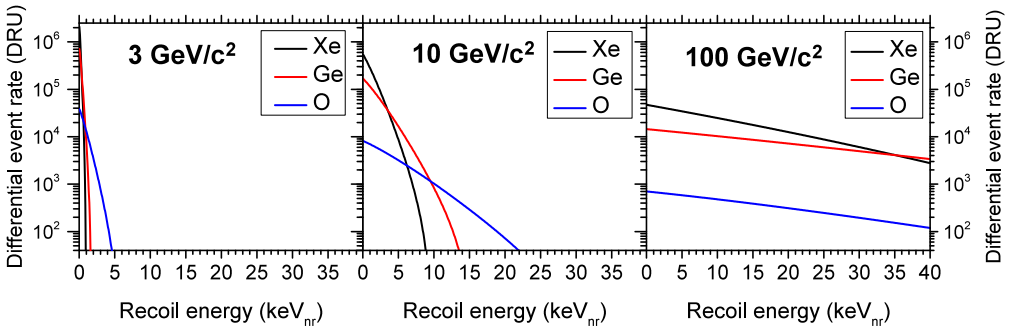

Figure 1.9: Differential event rate spectra with three different elements (Xe, Ge and O) in three WIMP mass scenarios (3, 10 and 100 GeV c^{-2}), for WIMP-nucleus elastic spin-independent scattering. The WIMP-nucleon elastic spin-independent cross-section is assumed to be 1 pb (10^{-36} cm^2). DRU stands for differential rate unit and 1 DRU = 1 count kg^{-1} keV^{-1} day^{-1}. The recoil energy is given in the unit keV_{nr}, which is the energy scale for nuclear recoil. These three elements and three WIMP masses are chosen as examples to show how different target elements could complement the searches for WIMPs in different mass regions.

Ge and O) as the detector target in three WIMP mass scenarios (3, 10 and 100 GeV c^{-2}), for WIMP-nucleon elastic spin-independent scattering. The WIMP-nucleon elastic spin-independent cross-section $\sigma_{n,\mathrm{SI}}$ is assumed to be 1 pb (10^{-36} cm^2) for the calculations in Figure 1.9. However, as $\frac{dR}{dE_R} \propto \sigma_{n,\mathrm{SI}}$, these calculations are applicable to smaller cross-sections as well.

Figure 1.9 shows that, in general, the differential event rates decrease exponentially with respect to the recoil energy. Consequently, detectors need low energy thresholds (< a few keV) to improve their sensitivity. For WIMPs with low masses, as the energy deposited in the detector is so small, the detector needs to have a correspondingly low energy threshold to probe it. Also, the complementary nature of different elements to probe different WIMP masses is discussed below. First, the kinematics of energy transfer dictates that the energy deposit is maximised when the target nucleus has a similar mass to the incoming WIMP particle. For low-mass WIMP (e.g. the 3 GeV c^{-2} scenario in Figure 1.9), low-mass target nuclei (e.g. oxygen) have more gradual slopes in their differential event rate spectra (more deposits with relatively high energy) compared to high-mass target nuclei

(e.g. Ge and Xe). Consequently, low-mass elements are good targets for probing low-mass WIMPs. Second, for high-mass WIMPs, the relatively flat event rate spectra and the factor of A^2 (Equation 1.15) in the coherent WIMP-nucleus scattering make high-mass target nuclei (e.g. Xe) optimal targets.

The above calculation provides an adequate model but it has known deficiencies. One of the deficiencies is that the calculation of the WIMP-nucleus differential event rate (thus the inverse operation of probing the WIMP-nucleon cross-section from experimental WIMP search exposure) is based on assumptions that are not very well verified (one example is whether the WIMP speed distribution is Maxwellian [44]). However, the WIMP-nucleon cross-section calculation from the WIMP search exposure tells us how much the direct detection field has progressed, at least for experiments with the same target material. Comparisons between direct detection experiments with different target elements need to bear in mind the assumptions made.

For WIMP searches, a region of interest in the energy spectrum needs to be defined. The lower end of the region of interest is usually the energy threshold of the detector. Considering the higher end of the region of interest, the differential event rate from WIMP scattering drops exponentially with increasing recoil energy (Figure 1.9), so it eventually comes to a point when including a larger energy range at the higher end does not make the search more sensitive to WIMPs. It is because the detrimental effects of including more radioactive backgrounds would outweigh the beneficial effects of having more WIMP events. The higher end of the region of interest in WIMP searches varies between different experiments due to the different differential event rate spectra and different radioactive background environments. As examples, it is set at 40 keV_{nr} for a $CaWO_4$ experiment [45], at 201 keV_{nr} for an Ar experiment [46], at 100 keV_{nr} for a Ge experiment [47], and at ~70 keV_{nr} for a Xe experiment [48].

The energy of the recoiled nucleus is measured through various channels depending on the detector technology. The most common channels include scintillation light, ionisation and phonons. More discussion of the detector technology is in Section 1.6.

1.4 Neutrinoless double-beta decay - signal model

If neutrinos are Majorana particles, the rare nuclear transition process of neutrinoless double-beta decay ($0\nu\beta\beta$) can occur [2]. In this process, a mother nucleus with Z protons decays to a daughter nucleus with Z+2 protons and the same mass number A, and two electrons are emitted at the same time: $(Z,\ A) \rightarrow (Z+2,\ A)+2e^{-}$. Neutrinoless double-beta decay is a lepton number violation process, which requires physics beyond the Standard Model. The sum of the kinetic energies of the two emitted electrons would be equal to the atomic mass difference of the mother isotope and the daughter isotope, and this value is called Q value for double-beta decay. This mono-energetic peak at the Q value, which is also at the end point of the total electron energy spectrum of two-neutrino double-beta decay ($2\nu\beta\beta$), is the signature of neutrinoless double-beta decay (shown in Figure 1.10). As an example, the double-beta decay Q value of ^{130}Te is found to be 2527.518(13) keV [49]. Because of the potential mono-energetic signal from neutrinoless double-beta decay at the Q value and the continuous energy spectrum from two-neutrino double-beta decay up to the Q value, the detector requires the best possible energy resolution and the lowest possible background near the Q value.

In neutrinoless double beta decay detectors, the energy of the two emitted electrons in neutrinoless double-beta decay is measured through various channels depending on the detector technology, similarly to that in dark matter direct detection but in a higher energy region (~2 MeV). The most common channels

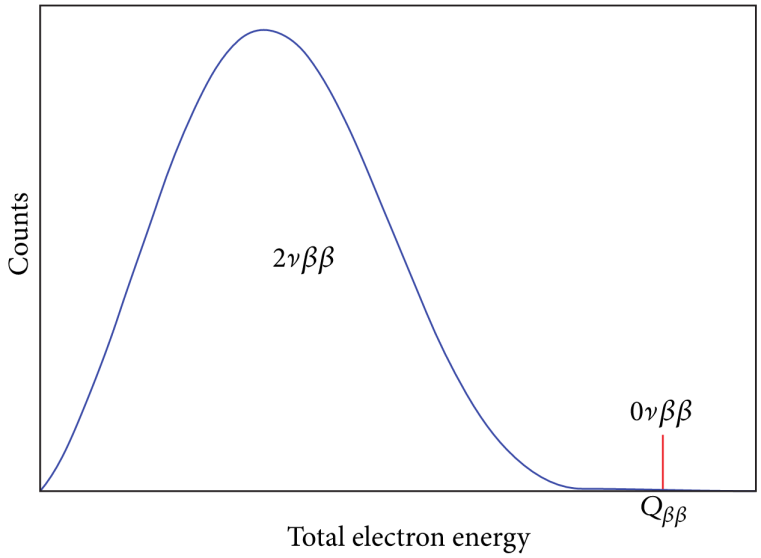

Figure 1.10: Schematic view of the total electron energy spectra of $2\nu\beta\beta$ and $0\nu\beta\beta$. The $0\nu\beta\beta$ spectrum has been exaggerated for clarity. (From Reference [50])

are scintillation light, ionisation and phonon channels. For example, in a cryogenic calorimeter experiment called CUORE [51], which uses TeO_2 as the absorber as well as the source of double-beta decay, the energy of the electron recoils first creates athermal phonons in the crystal. Those athermal phonons are thermalised in the detector, and the temperature rise from this thermalisation is read out by a thermistor (NTD in this case). In this way, the energy deposited by the two electrons can be accurately measured. A recent review of neutrinoless double beta decay experiments can be found in Reference [52].

With the assumption that the main mechanism responsible for lepton number violation in $0\nu\beta\beta$ is through the virtual exchange of light Majorana neutrinos ($m_{\nu_i} < 10\ \mathrm{MeV\,c^{-2}}$), the half-life of neutrinoless double beta decay (inversely proportional to the event rate) can be written as [53]:

$$\left(T^{0\nu}_{1/2}\right)^{-1} = G_{o\nu}\left(Q_{\beta\beta}, Z\right)\left|M_{0\nu}\right|^2 m^2_{\beta\beta}\,, \tag{1.18}$$

where $G_{o\nu}\left(Q_{\beta\beta}, Z\right)$ is a phase-space factor that is exactly calculable [54], $|M_{0\nu}|$

is a nuclear matrix element [55] and $m_{\beta\beta}$ is the effective Majorana mass of the electron neutrino. $m_{\beta\beta}$ can be written as:

$$m_{\beta\beta} = \left| \sum_i U_{ei}^2 m_i \right| , \tag{1.19}$$

where U_{ei} are elements of the PMNS matrix (also called neutrino mixing matrix) [56] and m_i are the neutrino mass eigenstates.

1.5 Radioactive backgrounds in rare event search experiments

Due to the small WIMP-nucleon interaction cross-section (current best limit smaller than 1 zeptobarn [48]), cosmic and radioactive backgrounds for an unshielded detector on the surface of the Earth are many orders of magnitude more frequent than the expected event rate from the WIMP interactions. Generally speaking, for a WIMP-nucleon cross-section of 1 zeptobarn and WIMP mass of 50 GeV c^{-2}, the event rate is on the scale of 10 μDRU (equal to ~0.1 count kg^{-1} keV^{-1} year^{-1}) at 25 keV$_{\rm nr}$ for Xe. Similarly, the long half-life of $0\nu\beta\beta$ (current best limits larger than 10^{25} years in some isotopes [57]) and the corresponding low event rate (on the scale of 1 decay kg^{-1} year^{-1} for a half-life of 10^{25} years) also require a quiet radioactive environment. Consequently, major experimental efforts are underway to minimise the radioactive backgrounds.

1.5.1 Background external to the detector

Compared to the radioactive background from the materials used to construct the detector, backgrounds external to the detector are usually easier to handle with passive shielding and active veto detectors (except neutrino background, Section

1.5.4). These external backgrounds usually only constitute a small part of the total backgrounds.

To shield against cosmic rays (especially muon-induced backgrounds), detectors are placed in deep (thousands of meter water equivalent) underground laboratories [58], and anti-coincidence muon veto devices are usually installed around the detector to tag the remaining few cosmic muons. Compared to the sea-level muon flux (~1 $\mathrm{cm^{-2}\,min^{-1}}$) [23], the muon flux is reduced to around 10^{-6}–10^{-10} $\mathrm{cm^{-2}\,s^{-1}}$ in deep underground laboratories [58], depending on the depth of the laboratories.

To shield against ambient radioactivity from the rock and the concrete in the underground laboratory, several layers of shielding surrounding the detector are needed, with steel or lead shielding often employed to attenuate the γ-rays, and water or other low-Z materials often used to attenuate neutrons. After the shielding, the external radiation from the laboratory is usually reduced to an insignificant level compared to the total radioactive background budget. For example, in the LUX experiment, the shielding reduces the external γ-ray flux from the laboratory by a factor of 2×10^{-10}, resulting in a low-energy electron recoil event rate of only 27 $\mathrm{nDRU_{ee}}$ in the active volume. Also, the neutrons from the rock are attenuated in LUX, and those neutrons contribute a single-scatter nuclear recoil rate of 60 $\mathrm{nDRU_{nr}}$ in the 3.4–25 $\mathrm{keV_{nr}}$ energy range, for a 100-kg fiducial mass [59].

1.5.2 Radioactive background from detector materials

With the muon-induced background and radiation from the laboratory environment reduced to low level, radioactive decays from the detector materials dominate the total radioactive background. Materials for detector construction are screened and only radiopure materials are chosen, and production processes are controlled

to avoid the introduction of additional radioactive backgrounds.

In general, four types of particles produced in radioactive decays are a concern for rare event search experiments: α-particles, electrons, γ-rays and neutrons. Neutrons and γ-rays are more penetrating than α-particles and electrons. These four types of particles could be classified according to different detector responses (usually manifest as the signal ratio of two readout channels): γ-rays and electrons cause electron recoil (ER) backgrounds; neutrons cause nuclear recoil (NR) backgrounds; α-particles cause their own band (e.g. this band is between the ER and NR bands in an experiment with $CaWO_4$ target [60]).

Below is a discussion about how these four types of particles can cause events within the region of interest (ROI) in WIMP searches. For WIMP direct detection experiments, as discussed in Section 1.3, the signal from WIMP interaction is single-scatter nuclear recoils with deposited energies usually below 100 keV.

Neutrons cannot be discriminated against on an event-by-event basis in WIMP searches, if they deposit energy in the ROI through single scattering in the active volume of the detector. Neutrons that have higher kinetic energy than the upper energy bound of the ROI may deposit only part of the full energy into the detector through elastic scattering and thus appear as events in the ROI.

Electrons and γ-rays cause ER backgrounds. Many of the modern dark matter detectors have a certain discrimination power (usually >99% for events with deposited energy more than a few keV) between ER and NR, so only a fraction of ER events are leaked to the NR band. The γ-rays that have higher energy than the maximum defined by the ROI could undergo Compton scattering and deposit only part of the total energy in the detector, thus in the energy range for WIMP searches but still within the ER band. Electrons usually stop within ~mm range [61], so electrons are only present not far from the source. High-energy electrons can produce bremsstrahlung X-rays which are more penetrating.

Alpha particles from radioactive decays usually have several MeV kinetic energy, and they deposit energy over a short distance (~tens of μm) before coming to a full stop. If α-particles are generated in the bulk volume, the deposited energies in the MeV range are far from the energy region for WIMP searches. If α-decays occur close to the surface of material surrounding the active volume, the α-particles could lose part of their energy in the material, before depositing the remaining energy in the active volume ("degraded alphas"). Consequently, they can appear in energy range for WIMP searches near the surface of the active volume. Similar to ER/NR discrimination, many dark matter detectors also have certain discrimination power between α-events and NR [62]. Also, α-particles can generate neutrons through (α,n) reactions in materials close to the detector (Section 1.5.3).

For $0\nu\beta\beta$ experiments, as discussed in Section 1.4, the signal is two electrons with total kinetic energy at the Q value of $0\nu\beta\beta$ (~2 MeV). Consequently, electrons and γ-rays with energy near or higher than the Q value are major sources of background. For a $0\nu\beta\beta$ experiment using a bolometric technique, α-particles from the surface of the detector and nearby copper structures are also a major source of background [51].

1.5.3 Common radioactive isotopes

Several radioactive isotopes in materials for detector construction are especially relevant in the radioactive background for dark matter experiments, and they are discussed below. Also, this section discusses how these radioactive decays generate the four types of particles discussed in Section 1.5.2.

1.5.3.1 U/Th chains

^{238}U, ^{235}U and ^{232}Th are long-lived primordial isotopes, with a half-life of 4.5×10^9 years, 7×10^8 years and 1.4×10^{10} years, respectively. Because of their long half-life, these three isotopes sustain decay chains (shown in Figure 1.11, 1.12 and 1.13), where secular equilibrium is usually assumed unless indicated otherwise. In secular equilibrium, the activity of each isotope in the same decay chain is generally equal to the activity of the head isotope of the decay chain, except when there is more than one decay mode. The effect from chain non-equilibrium of these three decay chains on Dark Matter search backgrounds is discussed in Reference [63]. ^{235}U has an abundance of 0.72% in natural uranium, compared to the abundance of 99.27% of ^{238}U.

As shown in Figure 1.11, 1.12 and 1.13, α-particles and electrons are generated in the decay processes in the chains. γ-rays can also be emitted in these processes. Note that the intensity of a γ-ray is defined as the probability of the emission of that γ-ray if the decay process happens, instead of the ratio of the number of that γ-ray to the sum of all γ-rays emitted in that decay process. Consequently, the sum of the intensities of the γ-rays in a decay process is usually not unity. In the U and Th decay chains, neutrons are generated through spontaneous fission and (α,n) reaction.

Spontaneous fission

For some high-Z nuclei, the electrostatic repulsive force between the protons is so large that the nuclear force can barely hold the nucleons together. As a result, spontaneous fission can happen and the nucleus is split. Spontaneous fission is a stochastic process, with different nuclei as fission products and emissions of different numbers of neutrons and other particles. Table 1.1 summarises the neutron yields in spontaneous fission processes for the relevant isotopes (^{232}Th,

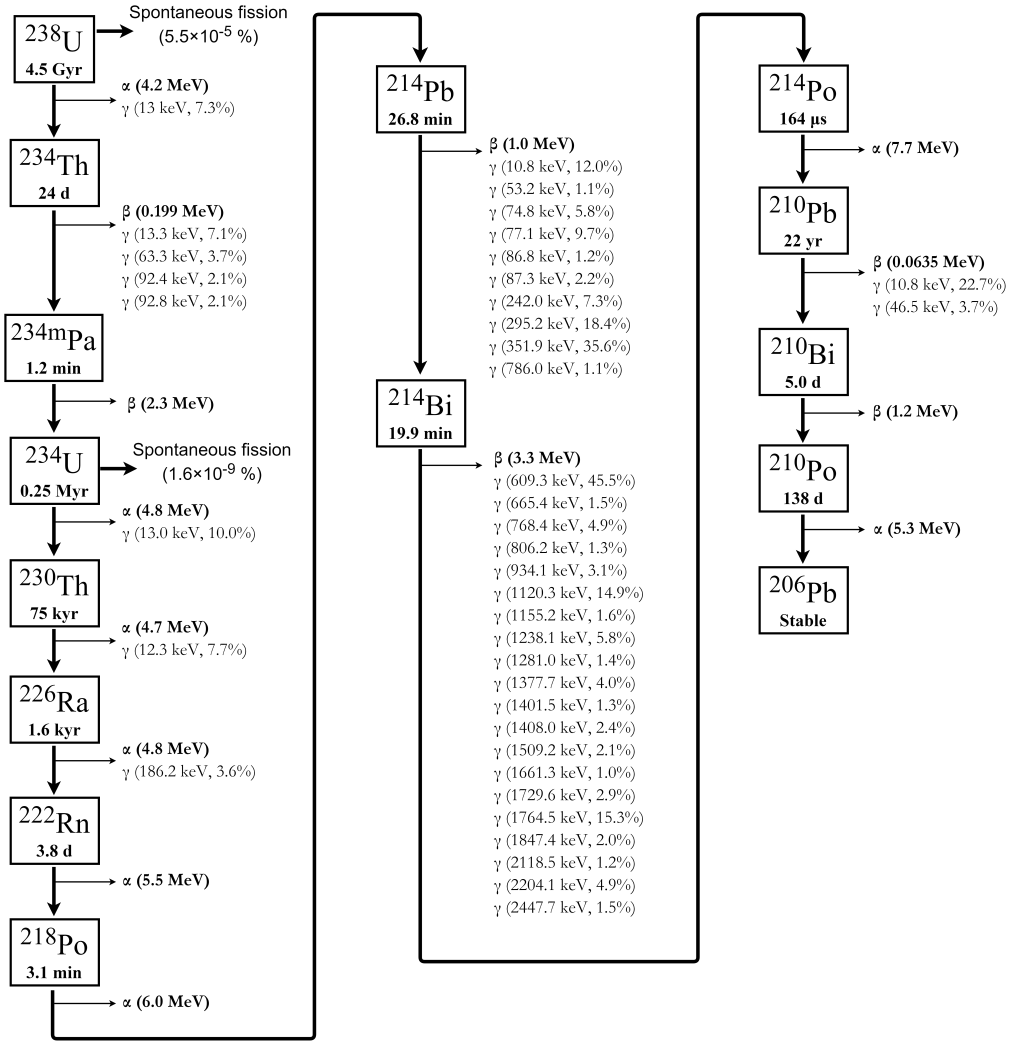

Figure 1.11: The ^{238}U decay chain. The half-life is given for each isotope. Branching ratio of the decays is more than 99% if no branching ratio number is given. Decays with less than 1% branching ratio are omitted for clarity. For α-decays, the energy given is the mean α energy. For β-decays, the energy given is the electron end point energy. γ emissions with intensity more than 1% are listed with energies and intensities. Data from [64].

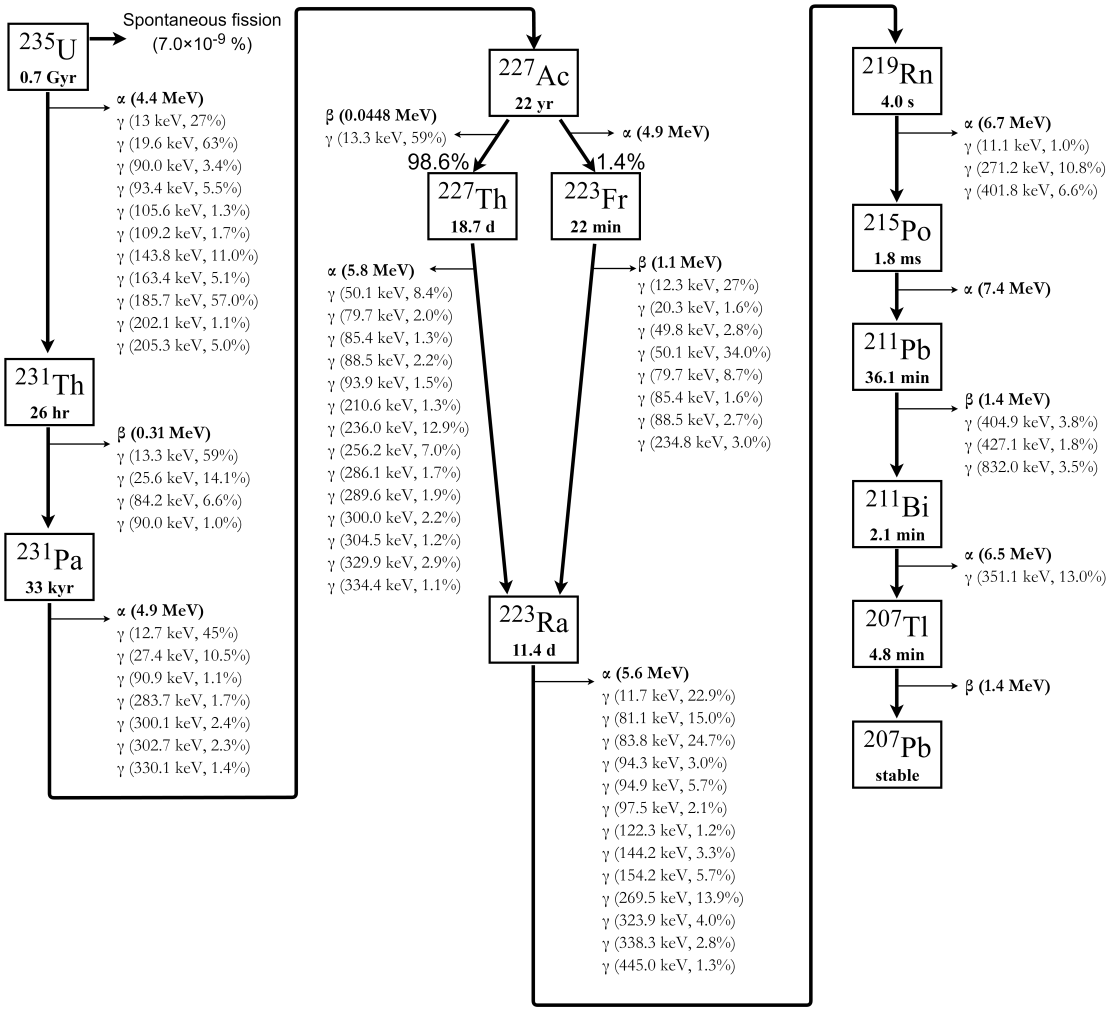

Figure 1.12: The ^{235}U decay chain. The half-life is given for each isotope. Branching ratio of the decays is more than 99% if no branching ratio number is given. Decays with less than 1% branching ratio are omitted for clarity. For α-decays, the energy given is the mean α energy. For β-decays, the energy given is the electron end point energy. γ emissions with intensity more than 1% are listed with energies and intensities. Data from [64].

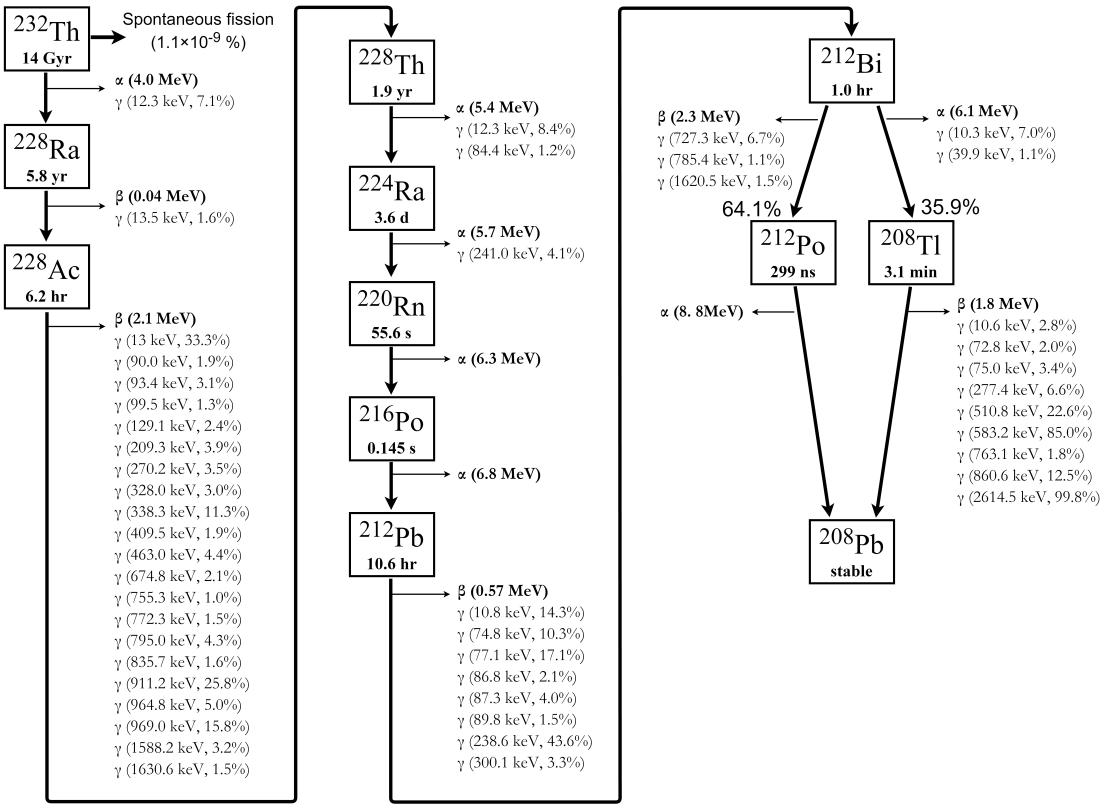

Figure 1.13: The ^{232}Th decay chain. The half-life is given for each isotope. Branching ratio of the decays is more than 99% if no branching ratio number is given. Decays with less than 1% branching ratio are omitted for clarity. For α-decays, the energy given is the mean α energy. For β-decays, the energy given is the electron end point energy. γ emissions with intensity more than 1% are listed with energies and intensities. Data from [64].

Isotope	Isotope half-life (From Ref. [64])	Spontaneous fission probability per decay (From Ref. [64])	Average neutrons per spontaneous fission (From Ref. [65])
^{232}Th	1.4×10^{10} years	1.1×10^{-11}	2.14
^{234}U	2.5×10^{5} years	1.6×10^{-11}	1.81
^{235}U	7.0×10^{8} years	7.0×10^{-11}	1.86
^{238}U	4.5×10^{9} years	5.5×10^{-7}	2.01

Table 1.1: Spontaneous fission neutron yields.

^{234}U, ^{235}U and ^{238}U) in the U/Th decay chains. Note that ^{238}U has spontaneous fission probability per decay four orders of magnitude larger than the other three isotopes.

(α,n) reaction

Alpha particles emitted in the U/Th decay chains can generate neutrons through (α,n) reactions with certain elements, with one neutron produced per (α,n) reaction. The presence of low-Z elements such as fluorine near the α-emitters allows the α-particles to participate the (α,n) reaction before losing their kinetic energy totally, as the MeV α-particles can only travel through around tens of μm in matter.

When an α-particle reaches a nucleus, the probability for (α,n) reaction is a function of the threshold energy (related to the Q value), the height of the Coulomb barrier and the kinetic energy of the α-particle [65]. Here the Q value is defined as the difference between the binding energies of the two initial nuclei (target nucleus and the α-particle in this case) and the two reaction products (product nucleus and the neutron in this case). Positive Q value means the (α,n) reaction releases energy, so there is no minimum energy required for the α-particle. Negative Q value means the α-particle needs to have at least this minimum energy in the centre-of-mass frame for the reaction to happen. The threshold energy is this minimum energy requirement transformed into the laboratory frame [65]:

$$\text{Threshold Energy} = \begin{cases} -Q\left(1 + {}^{4}/_{A}\right) , & Q < 0 \\ 0 , & Q > 0 , \end{cases} \tag{1.20}$$

where A is the mass number of the target nucleus.

The Coulomb barrier is the energy potential of the repulsive electrostatic force between the α-particle and the target nucleus, and the α-particle must penetrate or overcome this barrier to enter the target nucleus for the nuclear reaction to happen [65].

$$\text{Coulomb barrier} = \frac{Z_1 Z_2 e^2}{r_0 \left(A_1^{1/3} + A_2^{1/3}\right)} , \tag{1.21}$$

where $Z_1 = 2$, Z_2 is the atomic number of the target nucleus, $e^2 = 1.44$ MeV fm, $r_0 = 1.2$ fm, $A_1 = 4$ and A_2 is the atomic number of the target nucleus. Consequently, (α,n) reaction is allowed energetically only if the α-particle has the kinetic energy to: i) exceed the threshold energy; ii) overcome or penetrate the Coulomb barrier (these two requirements are not additive). Because of the Coulomb barrier, the (α,n) reaction tends to have lower cross-sections for high-Z elements than for low-Z elements. As an example, Figure 1.14 shows the neutron yields in (α,n) reaction for several elements that are commonly found in detector construction materials.

The ^{238}U, ^{235}U and ^{232}Th decay chains generate eight, seven, and six α-particles per parent decay, respectively.

Radon

Among the isotopes in the decay chains, ^{222}Rn in the ^{238}U chain and ^{220}Rn in the ^{232}Th chain are gaseous. The half-life of 3.8 days and low chemical reactivity of ^{222}Rn leads to its widespread presence. Airborne radon could diffuse into mate-

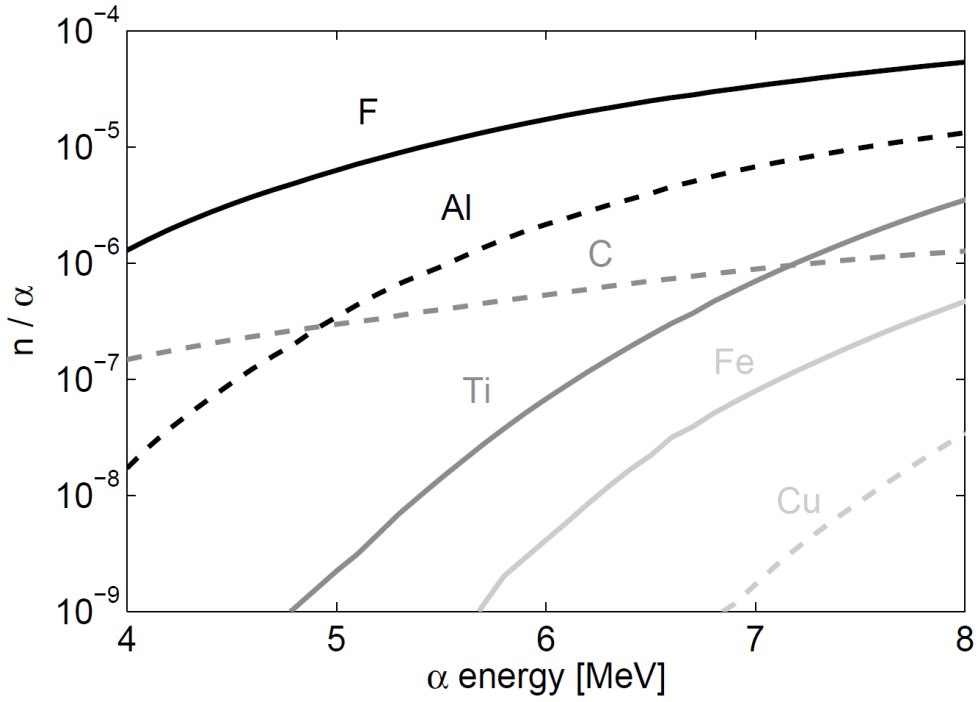

Figure 1.14: Number of neutrons produced per incident α-particle versus the α-particle energy, for various elements that are commonly found in detector construction materials. These elements include F (dark solid line), Al (dark dashed line), Ti (medium solid line), C (medium dashed line), Fe (light solid line), and Cu (light dashed line). (From Reference [63]).

rials and radon progeny could settle on surfaces. Below ^{222}Rn, the only isotope with a long half-life is ^{210}Pb (22.3 years). ^{220}Rn (half-life 55.6 s) has no long-lived daughters. Consequently, among radon progeny, ^{210}Pb and its daughters (^{210}Bi and ^{210}Po) are special concerns for dark matter experiments. To mitigate the radon contamination, de-radonized gas can be used and the components for detector construction should limit their exposure to air.

1.5.3.2 Other radioactive isotopes

^{40}K [64]

^{40}K has a half-life of 1.25×10^9 years and it is a primordial radionuclide. ^{40}K has two decay modes. One decay mode is β-decay to ^{40}Ca (branching ratio 89.3%) with a Q value of 1.31 MeV. The other mode is electron capture to ^{40}Ar (branching ratio 10.7%) with an emission of 1.46-MeV γ-ray (10.7%).

^{60}Co [64]

^{60}Co has a half-life of 5.27 years, and it can be generated by cosmic ray neutron interactions [66]. The decay mode of ^{60}Co is β-decay to ^{60}Ni (branching ratio 100%) with a Q value of 317 keV. The decay also emits two γ-rays at 1.17 MeV (99.85%) and 1.33 MeV (99.98%) in close interval (~1 ps).

^{137}Cs [64]

^{137}Cs has a half-life of 30.1 years, and it is an anthropogenic radionuclide generated in nuclear fission. ^{137}Cs decays to ^{137}Ba through β-decay (branching ratio 100%). The decay of ^{137}Cs emits electrons with a mean energy of 187.1 keV, and γ-rays with 31.8 keV (2.0%), 32.2 keV (3.6%) and 661.7 keV (85.1%).

1.5.4 Neutrino background

For future tonne-scale dark matter experiments such as LUX-ZEPLIN, the background from solar neutrinos becomes significant [67]. Neutrinos are not possible to shield against because of their small interaction cross-sections. Neutrino signals themselves are interesting, especially for the coherent elastic neutrino-nucleus scattering which is a standard model process not yet observed [68]. However, the presence of solar and atmospheric neutrino backgrounds leads to the so-called "neutrino floor" for WIMP direct detection, where the neutrino background poses challenges in probing lower WIMP-nucleon interaction cross-sections [69].

To translate the radioactivity in different detector components into the number of recoil events in the active volume of the detector, Geant4 [70] is widely used. The radioactivity of the PMT in this thesis and its contributions to the total radioactive background of a cryogenic detector module are discussed in Section 4.6.

1.6 Direct detection of WIMPs - a survey to experiments

Below is a survey of the mainstream experiments using liquid noble gas detectors and cryogenic detectors, as the dual-phase xenon experiments and cryogenic detector experiments set the best limits on the WIMP-nucleon elastic spin-independent cross-section, for the high-mass and low-mass WIMP, respectively. More information about the different experiments in the direct detection field can be found in Reference [71]. As shown in Figure 1.15, the WIMP-nucleon interaction cross-section versus WIMP mass plot shows the sensitivity of different experiments, under the canonical assumptions similar to those described in Section 1.3.

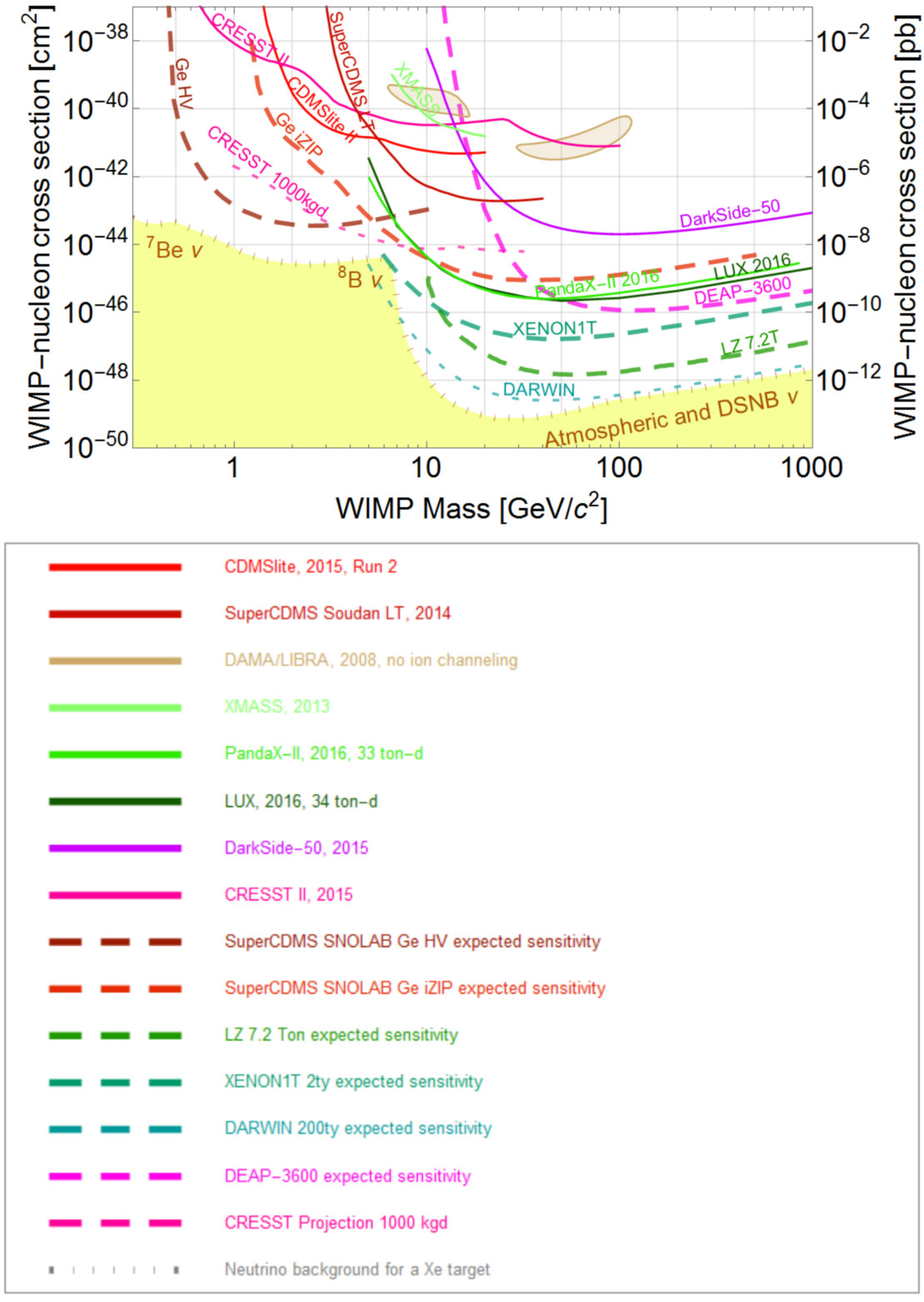

Figure 1.15: Parameter space of the spin-independent elastic dark matter-nucleon cross-section (vertical axis) versus the dark matter particle mass (horizontal axis). Figure produced with the Dark Matter Limit Plotter maintained by SuperCDMS collaboration.

1.6.1 Liquid noble gas detector experiments

1.6.1.1 Detector medium

Xenon

Liquid xenon has many merits as a detector medium for the direct detection of WIMPs. It has a relatively high density of 3 $\mathrm{g\,cm^{-3}}$, thus a detector with a tonne-scale or more xenon target could be constructed relatively compactly. It is a high-Z material, allowing self-shielding against some background radiation. It has a high absolute light yield of more than 60 $\mathrm{ph\,keV^{-1}}$ at zero electric field in respond to electron recoil [72], and the scintillation light has a wavelength of 178 nm [73], which can be detected by a PMT directly without a wavelength shifter. Liquid xenon has relatively high electron drift speed (low-field mobility 2.2×10^3 $\mathrm{cm^2\,s^{-1}\,V^{-1}}$ [74]). Xenon is a noble gas, so it is relatively easy to use a commercial getter to remove electronegative impurities and achieve a long electron lifetime (usually hundreds of μs). The high electron drift speed and long electron lifetime facilitate the readout of the ionisation channel. Xenon has no long-lived radioactive isotopes (except ^{136}Xe with a 2.16×10^{21} year half-life for double-beta decay), and the ^{85}Kr and ^{222}Rn contamination in xenon can be removed by purification.

Argon

Liquid argon (LAr) emits scintillation light with a wavelength of around 130 nm [73], which is difficult to be directly detected with PMTs, thus a wavelength shifter (e.g. TPB) is usually needed. The scintillation light decay constants of LAr have two well-separated components, with the fast scintillation decay time constant measured to be 7 ns and the slow one measured to be 1600 ns [75]. Nuclear recoils and electron recoils have a different ratio of the fast and slow scintillation decay

components, thus the pulse shape of the scintillation can be used more effectively for discrimination between nuclear recoils and electron recoils, compared to xenon.

Atmospheric argon contains the radioactive isotope ^{39}Ar, a product of cosmogenic activation, with a specific activity of ~1 $\mathrm{Bq\,kg^{-1}}$. ^{39}Ar has a half-life of 269 years and it decays 100% through β-decay with 565 keV end-point energy [64]. Using argon extracted from certain underground sites with low ^{39}Ar content (<5% relative to the atmospheric argon) can alleviate this background [76].

Details of the liquid noble gas technology applied to the direct detection of dark matter can be found in Refs. [77, 78].

1.6.1.2 Dual-phase noble gas detector experiments

Dual-phase noble gas detectors operate as time projection chambers (TPCs, shown in Figure 1.16). A particle hitting the detector medium generates scintillation photons as well as ionisation. A prompt signal (S1) is generated by the PMT arrays detecting the scintillation photons, while the electrons from ionisation are drifted towards the liquid surface under the electric field of the TPC. At the liquid surface, the electrons are extracted from the liquid phase to the gas phase. Subsequently, electroluminescence from the extracted electrons happens in the xenon gas under the high electric field. The electroluminescence generates an S2 signal, delayed relative to S1. In this way, the z position of a particle interaction vertex can be inferred from the time difference between S1 and S2, as this duration multiplied by the electron drift speed gives the electron drift length. The x-y position can be inferred from the hit pattern of the top PMT arrays. Thus, the three-dimensional position of the particle interaction vertex can be reconstructed, and a fiducial volume at the centre of the TPC with low radioactive background can be defined for WIMP searches, making use of the self-shielding of the noble liquid. The monolithic nature of the detector means smaller surface to volume

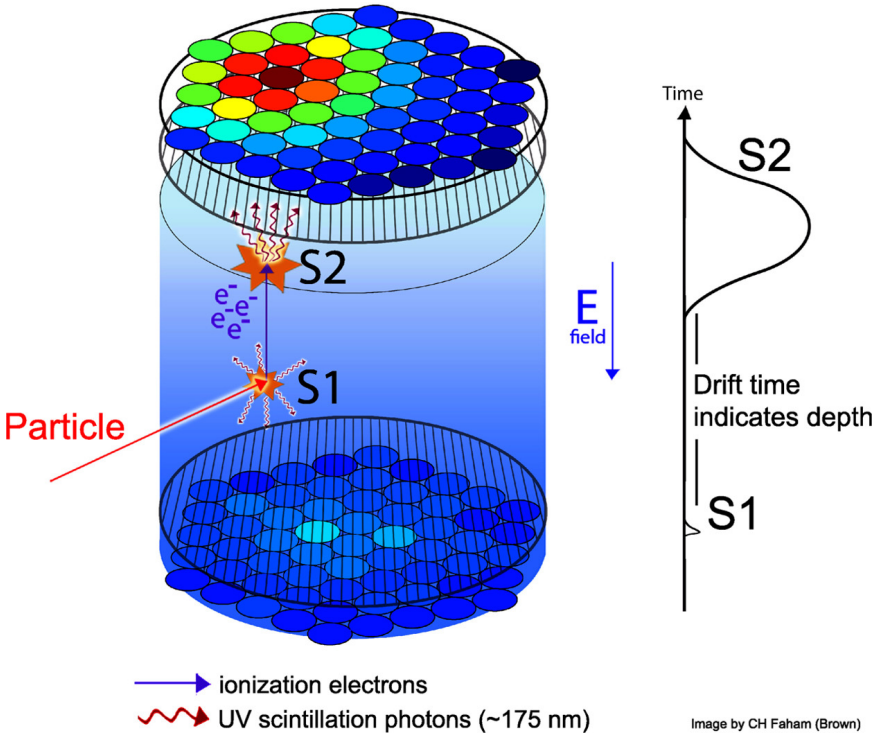

Figure 1.16: Illustration of an example event in a dual-phase xenon experiment (e.g. the LUX experiment). A particle interaction generates electrons and scintillation photons. The scintillation photons are detected by the PMT arrays as a prompt signal (S1). The electrons are drifted to the liquid surface, then extracted into the gas under high electric field. Afterwards, electroluminescence from the extracted electrons happens under high electric field, measured by the PMT arrays as a delayed signal (S2). (From Reference [79])

ratio when the experiments scale up, which increases the dark matter signal to radioactive background ratio. It is because the dark matter signal is proportional to the mass (thus the volume) of the detector, while the radioactive background from the detector construction materials is positively correlated with the surface area of the detector. Also, nuclear recoil and electron recoil give different ratios of S1 to S2, and this ratio can be used for particle discrimination. For an argon detector, the pulse shape of S1 can be used more effectively for particle discrimination in addition to the S1/S2 ratio, facilitating a higher rejection efficiency.

Xenon

The dual-phase xenon experiments have produced the tightest limits on the spin-independent (SI) WIMP-nucleon cross-section in recent years. With the coming tonne-scale dual-phase xenon experiments, this technology will be even more competitive.

The Large Underground Xenon (LUX) detector is a 370-kg dual-phase xenon time projection chamber with 250 kg active mass, and ~118 kg fiducial mass (fiducial mass is analysis-dependent) [80, 81]. A relatively high light detection efficiency (0.117 photons detected per photon emitted), combined with lowering the analysis threshold to require only two-PMT coincidence in S1 pulses, contributes to the low energy threshold (1.1 $\mathrm{keV_{nr}}$) and, subsequently, the sensitivity to low-mass WIMPs in LUX. LUX also employed various techniques for the energy calibration of a large xenon TPC to very low energies, including using tritium for electron recoil (ER) calibration [82], and using Deuterium-Deuterium neutrons for nuclear recoil (NR) calibration down to 0.7 $\mathrm{keV_{nr}}$ [83]. LUX recently announced the result of a WIMP search with 332 live days of data, and the result is compatible with the background, with a four-fold sensitivity improvement over the previous result to cross-section 2.2×10^{-46} $\mathrm{cm^2}$ at 50 $\mathrm{GeV\,c^{-2}}$ for SI WIMP-nucleon elastic

interaction [48]. The recent LUX WIMP result from 332 live days sets the world-leading sensitivity for SI WIMP-nucleon cross-section for WIMP masses larger than 7 GeV c^{-2} (Figure 1.15).

The next-generation LUX-ZEPLIN (LZ) detector will be a 10-tonne xenon detector with 7 tonne active mass and 5.6 tonne fiducial mass [84], located in the same water tank used by LUX after LUX is removed. To maximise the fiducial mass, the skin region of the TPC will be monitored by PMTs, and a detector with liquid scintillator will be installed outside the ultra-pure titanium vessels, along with the water tank for shielding and veto purposes. LZ is expected to start running at 2020.

The XENON1T detector has a total mass of 3.2 tonnes of xenon, of which 2 tonnes are active and ~1 tonne is fiducial mass [85]. It is currently undergoing commissioning, and the science run is expected to start in autumn 2016 [86]. Its design includes features to facilitate upgrading to a larger detector (called XENONnT) quickly in the future.

The PandaX-II detector has 500 kg of xenon, with 329 kg fiducial mass. Recently it published WIMP search results from 98.7 days of data [87], and the result is compatible with the background, which leads to a limit on the SI WIMP-nucleon cross-section similar to that from LUX's 332 live days (Figure 1.15).

DARWIN is a proposed project after LZ and XENONnT, which would have about 45.4 tonnes (50 tons) of xenon in total, of which 36.3 tonnes (40 tons) is active [88]. It is going to probe the parameter space down to the "neutrino floor" for relatively high-mass WIMPs for spin-independent WIMP-nucleon interactions.

Argon

The DarkSide-50 detector has an active mass 46.4 kg of argon, and the fiducial mass is 36.9 kg. Recently it reported a WIMP search result using underground

argon with a low ^{39}Ar content (0.73 mBq kg^{-1}) with data of 70.9 live days (Figure 1.15) [46]. The experiment demonstrated powerful pulse shape discrimination by using the fraction of S1 light detected in the first 90 ns of the pulse to discriminate against ER events.

The ArDM-1t detector has a total mass of around two tonnes of LAr. Although it is operating with atmospheric argon and is thus dominated by the ^{39}Ar background, its recent result indicates that pulse shape discrimination against ER events can be efficiently achieved with tonne-scale LAr detectors [89].

Both the DarkSide and ArDM collaborations are actively developing SiPMs to replace PMTs as the light detector, with the aim to improve light yield [89, 90].

1.6.1.3 Single-phase noble gas detector experiments

For single-phase noble gas detectors, only the scintillation light from particle interactions is read out, thus this type of detector could not use the signal ratio of ionisation to scintillation for particle discrimination. However, argon detectors could still effectively use pulse shape discrimination in the scintillation signal to discriminate against the radioactive background. The hit pattern and time difference between signals in different PMTs are used to reconstruct the vertex of the particle interaction, but with a much lower accuracy compared to dual-phase detectors, limiting the definition of a fiducial volume to make use of the self-shielding of the noble gas. Because there is no need to provide any high voltage, light detectors (e.g. PMTs) can be placed evenly on the surface of a spherical volume. Hence larger photocathode coverage and subsequently higher light yields can usually be achieved compared to dual-phase noble gas detectors.

Xenon

The XMASS-I detector has a total mass 835 kg of liquid xenon, instrumented by 642 PMTs. It has reported a large photocathode coverage (>62%) and a high light yield of 14.7 ± 1.2 photoelectron $\cdot$ keV^{-1} [91]. Recently it reported results on searching for inelastic WIMP-nucleus scattering on ^{129}Xe [92] and Bosonic super-WIMPs [93]. However, the difficulty of constructing event vertex with information of hit pattern of PMTs prevents XMASS-I from defining a large fiducial region [94]. This, combined with the difficulty of using pulse shape discrimination to discriminate against the electron recoil background [95], makes the XMASS-I detector not as competitive as its dual-phase counterparts.

Argon

The DEAP-3600 detector has a total mass of 3600 kg of liquid argon, of which ~1000 kg is fiducial mass [96]. Atmospheric argon with a high content of ^{39}Ar is used, thus good pulse shape discrimination against the ER is critical for a WIMP search. The experiment is being commissioned, and a physics run is expected later in 2016.

1.6.2 Cryogenic detector experiments

Cryogenic detectors are usually solid state detectors operated at milli-Kelvin temperatures in a ^{3}He/^{4}He dilution refrigerator, equipped with sensitive phonon sensors, e.g. superconducting transition-edge-sensors (TES) or neutron transmutation doped Ge (NTD-Ge) sensors. As a first order approximation, because the heat capacity is minimised at such low temperatures, the tiny energy deposit from a particle interaction in the absorber crystal will cause a measurable temperature change that will be picked up by a TES or NTD-Ge sensor. Besides the phonon channel, the signal from another channel (either the ionisation channel or the

scintillation light channel) is usually read out simultaneously, and the signal ratio of the two channels can be used for event type discrimination. Compared to noble gas detectors, cryogenic detectors are relatively difficult to scale up due to practical difficulties (e.g. consistency in detector performance between different detectors). Also, the cryogenic experiments currently consist of individual detector modules with smaller than 1 kg detector mass each, thus the surface to volume ratio is roughly unchanged even when the experiments scale up. As mentioned before, the external radioactive background is positively correlated with the surface area of the detector, and the WIMP signal is proportional to the mass (thus the volume) of the detector. A relatively high surface to volume ratio, compared to the monolithic detectors in noble gas experiments, makes it difficult for the experiments with cryogenic detectors to minimise the backgrounds from detector construction materials. However, cryogenic detectors usually feature better electron/nuclear recoil discrimination power (e.g. >99.99% in CDMS II [97]) than liquid noble gas detectors (e.g. 99.6% in LUX [98]). Consequently, cryogenic detectors could tolerate more electron recoil events in the fiducial region. Moreover, cryogenic detectors have been demonstrated to achieve very low energy thresholds (< 1 keV) [99, 45]. The low energy threshold, coupled with the availability of low atomic mass target, makes cryogenic detectors very suitable for probing low-mass WIMPs, given that liquid noble gas experiments are more competitive in the high mass range. Details of cryogenic detector technology are described extensively in Refs. [100, 101, 102].

1.6.2.1 Cryogenic germanium detector experiments

Cryogenic germanium detectors measure the signals from particle interactions in the phonon channel and ionisation channel simultaneously, and use the ratio of signals (ER has a higher ionisation yield than NR) in these two channels to

discriminate NR from ER. The particle interaction generates ionisation that is collected and read out by electrodes on the surface of the Ge crystal. One issue with such detectors is that ERs which happen near the surface ("surface events") have lower ionisation yields than those in the bulk volume of the detector. Hence those surface ER events could be mistaken as NR. To reject the surface events and thus define a fiducial volume, the upgraded germanium detectors feature interleaved electrodes on the surface of the crystal (Figure 1.17), so that ionisation from surface events is collected at the electrodes nearby, and the ionisation from bulk events is collected at the electrodes further away. The detectors with interleaved electrodes are called FID (Full InterDigit) detectors by the EDELWEISS experiment [103] and iZIP (interleaved Z-sensitive Ionization Phonon) detectors by the CDMS experiment [104].

The EDELWEISS-III experiment has 40 germanium FID detectors, each with 800 g total mass of which 600 g is fiducial, and it uses NTD-Ge as the phonon sensor (Figure 1.17). Thus, the experiment has a total fiducial mass of 24 kg [107]. It recently reported a low-mass WIMP search with 582 kg days fiducial exposure from 8 FID detectors [105], with a null result (not shown in Figure 1.15).

The SuperCDMS detectors have two operation modes — normal iZIP and high voltage; both use TES as the phonon sensor. The CDMS low ionisation threshold experiment (CDMSlite) biases the iZIP detector in relatively high voltage, and uses the resulting Neganov-Luke effect to amplify the signals, to lower down the energy threshold. Recently, it published a low-mass WIMP search result from one detector module that has an electron recoil energy threshold as low as 56 eV, with a 70 kg days exposure [99]. It sets the world's best limit on the SI WIMP-nucleon cross-section for WIMP masses between 1.5 $\mathrm{GeV\,c^{-2}}$ and 3.5 $\mathrm{GeV\,c^{-2}}$ (Figure 1.15). SuperCDMS Soudan has 15 detectors, each with 0.6 kg detector mass. It reported on the low-mass WIMP search result, from 577 kg days exposure [108].

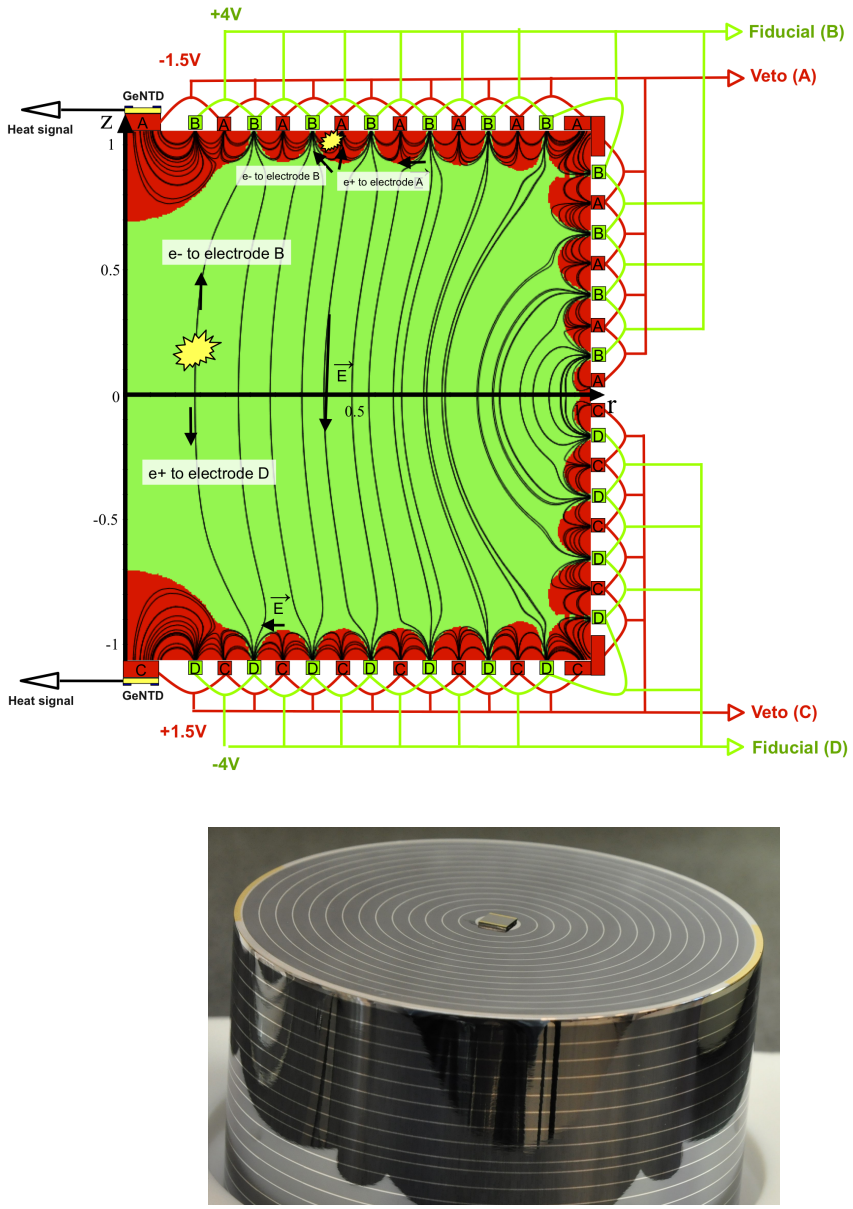

Figure 1.17: Schematic view (top) and photo (bottom) of the FID detector in the EDELWEISS experiment. As shown in the schematic view, ionisations generated by a particle recoil in the skin region (red) of the detector are collected at the electrodes nearby; ionisations generated by a particle recoil in the bulk region (green) of the detector are collected at the electrodes further away. The photo shows an NTD-Ge sensor at the middle of the detector top surface and the circular electrodes. (Figures from [105, 106])

SuperCDMS SNOLAB is the next phase development for the CDMS program. It will feature a cryostat that could accommodate 400 kg detector modules and the initial deployment will include ~30 kg of Ge and ~5 kg of Si detectors, and both iZIP and high voltage detectors will be used [109]. Also, EDELWEISS will install some detectors in the SuperCDMS cryostat [110], which has extra capacity intended for future deployments.

Both EDELWEISS and CDMS are actively working on using the Neganov-Luke effect to amplify the signals, to lower the energy threshold by improving the signal-to-noise ratio [111, 112]. The mechanism is that under a relatively high electric field (tens of volts across the crystal), the electron-hole pairs released in ionisation are accelerated and more phonons are generated in the electron-hole drifting process. Thus, the signal originally in the ionisation channel gets amplified in the phonon channel. However, because the amplified signal in the phonon channel is proportional to the signal in the ionisation channel, and the amplified signal is one order of magnitude larger than the original phonon signal, the discrimination power against ER is lost as the discrimination relies on the signal ratio of the two channels.

1.6.2.2 Cryogenic phonon-scintillation detector experiments

Cryogenic phonon-scintillation detectors (CPSD) measure the phonons and the scintillation photons from particle interactions simultaneously to discriminate NR against ER. CPSD will be discussed more in detail in Section 1.7.

The CRESST-II experiment features 18 detector modules with a total mass of 5 kg, using $CaWO_4$ as the absorber (schematic shown in Figure 1.18). As shown in Figure 1.15, recently it reported on a low-mass WIMP search using 52 kg days exposure from a single detector module with an energy threshold for nuclear recoils of 307 eV, and it sets the world best limit on SI WIMP-nucleon cross-section for

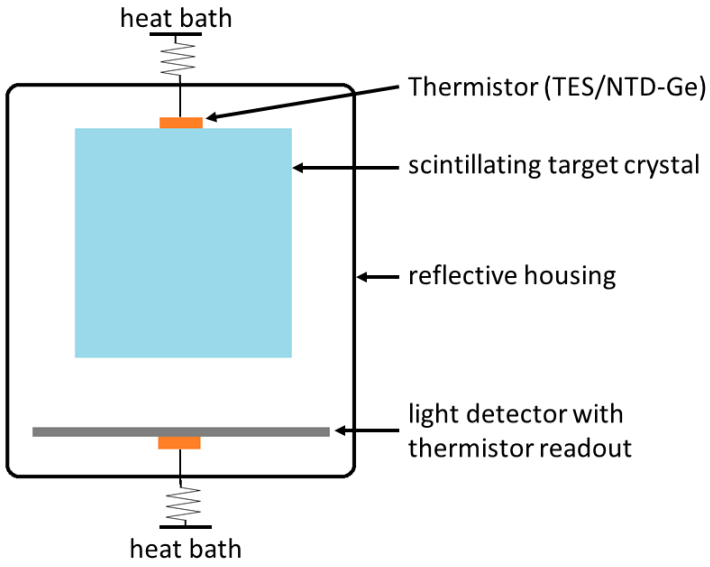

Figure 1.18: Schematic view of the cryogenic phonon-scintillation detectors (CPSD). A particle interaction in the target crystal generates phonons and scintillation photons. The phonons are read out by a thermistor (transition-edge-sensor or TES in the case of CRESST experiment), while the scintillation photons are detected by a nearby calorimeter-based light detector with thermistor readout (TES for CRESST experiment).

WIMP masses below ~1.5 GeV c^{-2} [45].

The CRESST-III experiment plans to significantly decrease the mass of the individual absorbers (potentially to ~24 g) to lower the heat capacity and, subsequently, further decrease the energy threshold of the detector to 100 eV [113]. With a 1000 kg days exposure (from 100 modules of the 24-g detectors) and a factor of 100 reduction in ER background compared to the current level, the sensitivity of the experiment will be close to the "neutrino floor" for WIMP masses from 1 GeV c^{-2} to 6 GeV c^{-2}.

1.7 Overview of cryogenic phonon-scintillation detectors

Cryogenic phonon detectors can determine the energy deposits by ionising radiation very precisely when operating at temperatures below 100 mK. Much better than any of the mainstream ionisation detectors, an energy resolution of better than 2 eV at 5.9 keV has been demonstrated by cryogenic phonon detectors [100]. In addition, by simultaneously recording the energy deposited through the phonon channel and the scintillation photon channel, cryogenic detectors can have powerful particle type discrimination [114, 115]. In cryogenic phonon scintillation detectors (CPSD), the phonon channel is usually read out by a phonon sensor (e.g. TES or NTD-Ge) attached to the scintillating absorber, and the scintillation photons are usually measured by a light detector in the vicinity of the absorber, being not in direct contact. The potential of this technique has been demonstrated by results searching for WIMPs from the CRESST experiment [116, 45], as mentioned in Section 1.6.2.2.

Due to fundamental losses, the majority of the deposited energy in a scintillator is converted to phonons and, in general, less than 10% of the energy is converted

to scintillation [117]. Thus, the phonon channel is used for precisely measuring the energy deposited in the interaction and scintillation light channel senstivity is critical for the the discrimination power of the CPSD [118]. Even though it is always a priority for a scintillation light detector to have high photon detection efficiency, it is very challenging to achieve this goal at milli-Kelvin temperature. Installing the light detector close to the scintillator crystal can maximise the light collection efficiency, thus improving the photon detection efficiency. As the operation of the cryogenic calorimeter rerquires the crystal itself to be cooled down to milli-Kelvin temperature, so far the only solution devised was to use another phonon detector specially configured for detecting visible photons.

Cryogenic calorimeter-based light detector

Calorimeters equiped with superconducting transition edge sensors (TES) can achieve a sensitivity to a few scintillation photons in principle [119]. To achieve the optimal sensitivity of the TES, it is necessary to stabilise their operating temperature precisely within the phase transition edge between the superconducting state and the normal state. A superconducting quantum interference device (SQUID) is used to read out the signal from a TES. An example of light detectors using TES for the CRESST experiment achieve an energy threshold of 3 keV (energy deposited in the $CaWO_4$ crystal) [120] and demonstrate an energy resolution of 180 eV at 5.89 keV, which corresponds to the K_α-line of ^{55}Mn [121]. However, it is very challenging to produce TES sensors reliably with the same properties of phase transitions. As a result, despite the excellent performance individual detectors can reach, their wider-spread adaption remains limited due to the lack of reproducibility and consistency in performance, and the specialist knowledge needed for production.

The development of other types of cryogenic calorimeter-based light detectors

can be found in the following references: NTD-Ge detector [122, 123, 124], NTD or TES detectors with Neganov-Luke amplification [125, 126], magnetic metal calorimeter [127], phonon-mediated kinetic inductance detectors [128].

Sensitivity to the tiny temperature changes caused by the interaction of particles or photons is the primary advantage of cryogenic phonon detectors. But the detector is also very responsive to other kinds of energy deposition as an integrating device. Mechanical vibrations around the cryogenic detector can cause excessive background noise [124]. The background noise determines the detector threshold in the cryogenic calorimeter-based light detector and, consequently, affects the experiment sensitivity reach. Another disadvantage is the poor timing resolution of the CPSD caused by the relatively large time constant ($\sim 1-10\,\mathrm{ms}$) of such a calorimeter-based light detector [124, 120, 121].

PMT as scintillation photon detector

Given the practical difficulty in the cryogenic calorimeter-based light detectors, photomultiplier tubes (PMTs) can potentially provide the most scalable solution to detect visible photons at milli-Kelvin temperatures. PMTs have many merits: they are mature and commercially available, thus the performance could be guaranteed by the manufacturer; they are relatively easy to use and handle, thus scalable, and one particle physics experiment has used more than ten thousand PMTs [129]; they are becoming increasingly better regarding to radiopurity, due to the campaigns in the liquid noble gas experiments to lower their radioactivity [130, 131]. PMTs are currently the preferred option for detecting scintillation photons for these following reasons: i) high quantum efficiency for photon detection (20%–40%), ii) fast (~10 ns) responsivity, iii) large photon sensitive area (from 1 inch to as large as 12 inches), iv) ruggedness, and v) reliability and reproducibility of operation. Consequently, major research efforts in the last decade have directed

to improve the performance of PMTs (e.g. quantum efficiency) and widen their operational temperature range. Numerous studies have demonstrated the operation of low-temperature PMTs at liquid noble gas temperatures [132, 133, 134] and they are currently widely deployed in the relevant experiments (see [135] and reference therein). Recently, it has been demonstrated that low-temperature PMTs can detect single photons reliably when cooled close to the liquid helium temperature [136, 137, 138].

Operating a detector in the photon counting mode has one main advantage compared to an integrating light detector, which is the much better signal-to-noise ratio, especially in low frequency. The dark pulse from the PMT caused by the spontaneous emission of electrons from the photocathode and dynodes [139], which are noise in the photon counting mode, usually become mush less severe. In addition, if tagging for true events can be performed by another independent detector instantly (e.g. the phonon detector of the CPSD), the impact of the dark pulse can be alleviated significantly. PMT readout has another advantage regarding the timing resolution for the scintillation measurement, as the timing characteristics of the signal detected by the PMT is almost totally decided by the scintillation decay time characteristics (typically $<$1 ms). Consequently, the pile-up between events, a potential problem for the relatively slow cryogenic detectors, can be alleviated by the improvement in time resolution of the detector.

Overall, this provides strong motivation for testing PMT as a cryogenic light detector for CPSD. In this thesis, two CPSD modules were successfully tested (Figure 2.1). First module used a $CaMoO_4$ scintillator crystal as the absorber, the other module later switched the absorber to $CaWO_4$. Both calorimeters were read out by the same NTD-Ge sensor in the phonon channel and the scintillation channel was read out by the same cryogenic PMT from Hamamatsu (R8520-06-PT). At milli-Kelvin temperatures, the scintillation decay of the $CaMoO_4$ and

$CaWO_4$ crystals were measured in this experiment, as will be discussed in Section 4.2.2.

The cold-temperature PMT working at milli-Kelvin temperatures in this thesis could replace a whole detector component in CPSD experiments for rare event searches (e.g. CRESST), the scintillation light readout with a much more reliable system which is consistent in performance and scalable. While the scintillation detector in CRESST can be very good, judging from published material, there is widespread in detector performance, usually linked to the light detector. Consequently, replacing it with the cold PMT could potentially improve the science reach of the CRESST experiment significantly. The phonon channel in CRESST experiment in principle could also be replaced by the successfully demonstrated NTD-Ge technology used in EDELWEISS. This thesis demonstrates a complete cryogenic phonon-scintillation detector system, to demonstrate that a cold-temperature PMT as an integrated component in the CPSD works well.

This thesis contains material from two papers published by the author [140, 141].

Chapter 2

Experimental apparatus

2.1 Overview of the experiment setup

The CPSD module consisted of two separate detectors close to each other (Figure 2.1): a cryogenic calorimeter with a scintillating crystal as the absorber (Section 2.2) and a low-temperature PMT (Section 2.3). The calorimeter and the PMT respectively measure the phonon and scintillation signals, simultaneously from the energy deposit caused by a particle. The module was installed inside an Oxford Instruments Kelvinox400 ^{3}He/^{4}He dilution refrigerator (Figure 2.3 and Figure 2.2), which cooled the detectors to mK temperatures for operation. The PMT was powered by a Cockcroft-Walton generator (CWG), and the CWG was installed in the still stage of the dilution refrigerator (reasons discussed below). The CPSD module was read out by custom-made electronics (Section 2.5).

The CPSD module in this experiment uses an NTD-Germanium sensor as the readout for calorimeter channel, and a PMT as the readout for scintillation/light channel. The following requirements are needed for the design of the experiment setup: i) dimensionally, the coldest space available in the Oxford Instruments Kelvinox400 ^{3}He/^{4}He dilution refrigerator in use (below the mixing

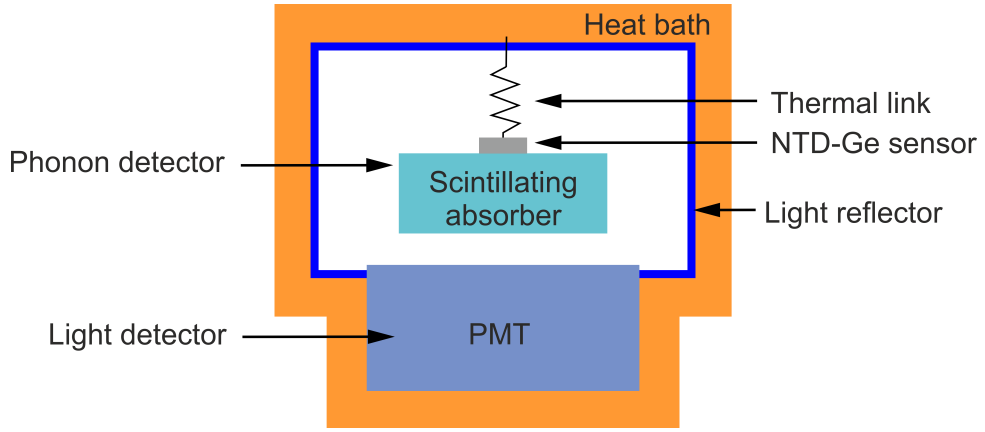

Figure 2.1: Schematic view of the CPSD module with a low-temperature PMT as light detector

chamber stage) has cylinder shape with a diameter of around 90 mm and height of around 250 mm. The calorimeter and PMT need to be installed in the coldest stage for operation; ii) electrically, the operation of PMT requires high voltage biasing. Manufacturer recommendation for the PMT biased voltage at room temperature is ~900 V between cathode and anode, but the PMT might need higher than the recommended voltage at milli-Kelvin temperatures. The danger of high voltage discharge should be mitigated; iii) thermally, the heat conducted and generated by the detector module should not prevent the dilution refrigerator from cooling close to the base temperature (around 10–15 mK), for the optimal operation of the calorimeter. Also, a stable heat bath is needed for the calorimeter; iv) in consideration of signal integrity, the biasing, excitation and signal readout should have as little interference/crosstalk to each other as possible; v) the phonon collection and light collection needs be optimised to increase signal size; vi) price is also an important factor.

The experiment setup is shown in Figure 2.2. Below is a brief review in general how the experiment setup addresses the requirements above, while the detailed discussion of the calorimeter is in Section 2.2 and the light detector in Section 2.3.

To address requirements (i) and (vi), small crystals (dimensions smaller than

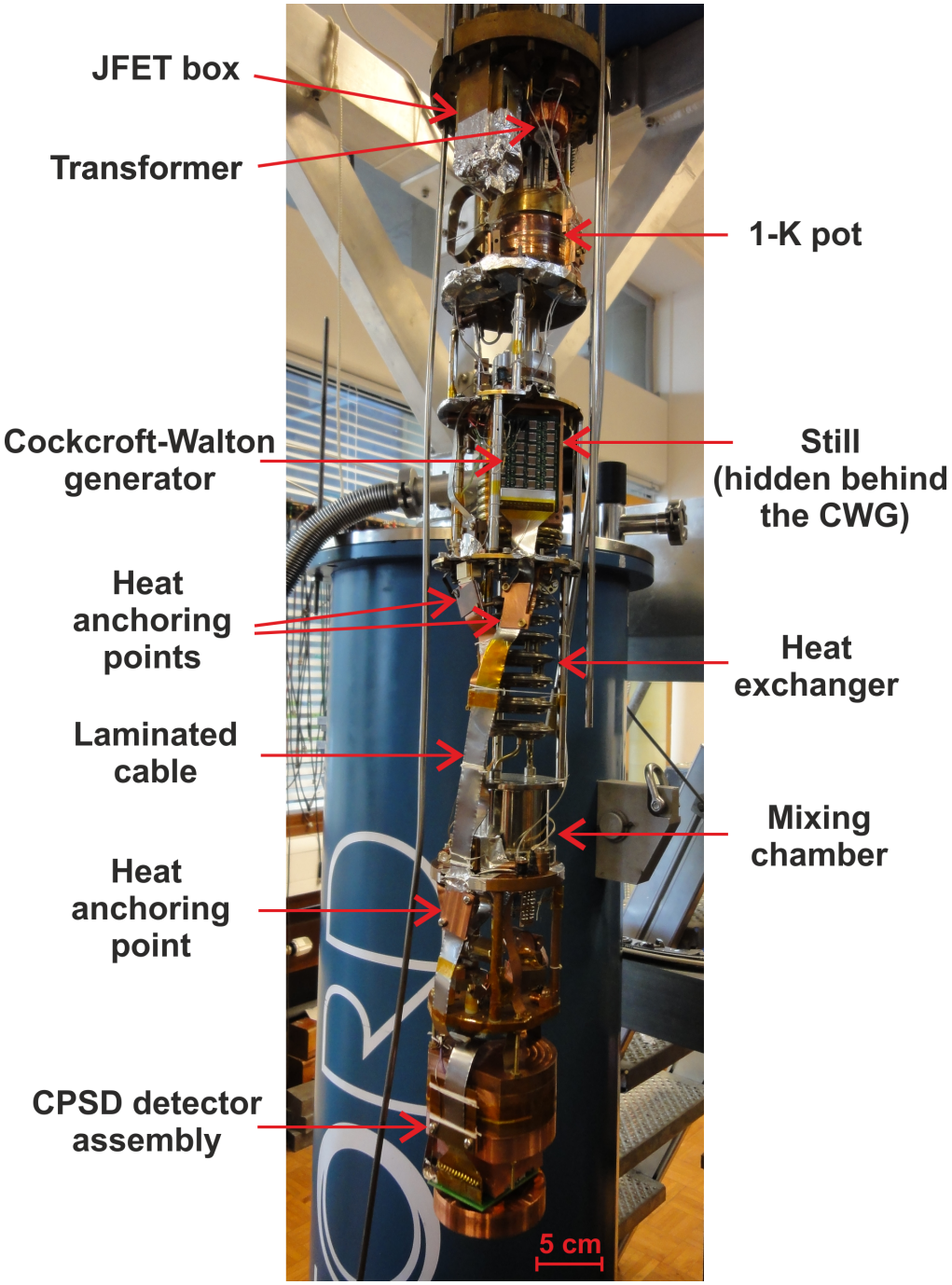

Figure 2.2: The experimental setup in the Oxford Instrument Kelvinox400 ^{3}He/^{4}He dilution refrigerator. The main components of the dilution refrigerator are annotated on the right side, while the main components specific to this experiment are annotated on the left side.

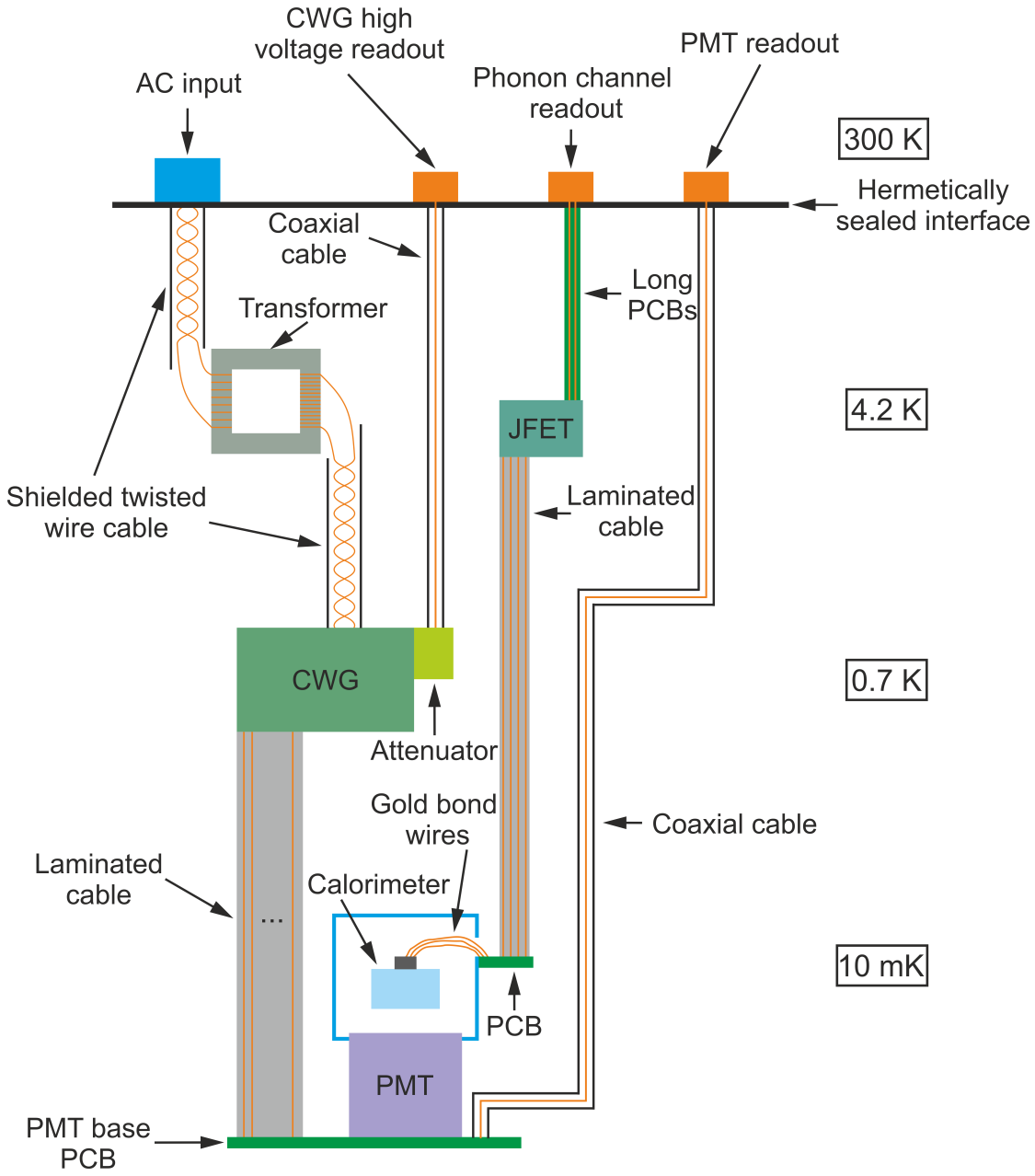

Figure 2.3: Schematic view of the high-voltage delivery and monitoring system, and the readout systems of the PMT and phonon detector. The temperatures on the right side show the temperatures that the different components were heat-sunk to. These are nominal values, not actual measurements. The JFETs were weakly heat-linked to 4.2 K but they were heated to about 120 K with a heater for optimal performance.

10 mm) and one-inch PMT are chosen for this study, which is suitable for this stage of feasibility study.

For requirement (ii), with the constraint from requirement (iii), it is easy to calculate that a voltage divider at the mixing chamber stage generates too much heat, because cooling power provided by the dilution refrigerator at around 20 mK is around 15 μW. Consequently, the option of using voltage divider at the PMT base is ruled out. Alternatively, it is possible to provide the individual voltages required by the PMT from a power supply on the air side. However, the required high-voltage vacuum feedthrough and the long high-voltage cable from the air side all the way to the coldest stage is not desirable, especially the required biased voltage at milli-Kelvin temperatures is potentially higher (later confirmed) than that recommended by the manufacturer. A high-voltage delivery system based on Cockcroft-Walton generator is chosen for this experiment. The Cockcroft-Walton generator was installed in the still stage of the dilution refrigerator, generating the different voltage required by the PMT, and the different voltages were delivered to the PMT through laminated cable with individual tracks. In this way, the high voltage was confined in the area between the still stage and the PMT, and no high voltage feedthrough was needed. A small AC voltage (a few volts) from a function generator is all needed to be provided on the air side.

For requirement (ii) (iii) and (iv), laminated cable is used for the delivery of high voltage and readout of heat channel (Figure 2.3). Laminated cable is flat, thus it is easier to be heat anchored compared to coaxial cable. Also, it is proven to be enough to prevent the high voltage discharge and to prevent crosstalk between challenge. These laminated cables are also being extensively used in EDELWEISS-III experiment.

For requirement (iii), a large detector housing made from copper was used, and the detector module was heat sunk to this copper housing. The copper housing

provides mechanical support, works as a heat bath as well as shield the ambient radioactivity.

For requirement (v), the PMT was located close to the scintillation crystal (as the absorber of the calorimeter) but not touching, to maximise the phonon collection and light collection. Also, to increase light collection efficiency, the inner surface of the cavity where the CPSD module locates were lined with reflective foil, and the detector geometry and the surface conditions of the crystal were optimised with the help of optical simulation.

2.2 Calorimeter setup

The calorimeter setup is shown in Figure 2.4. The scintillating absorber was either a $CaMoO_4$ crystal ($5.0\times9.5\times9.5$ mm^3) or $CaWO_4$ crystal ($3.3\times8.4\times9.7$ mm^3). A thin layer (250 nm thickness) of gold film (area 6.2×2.2 mm^2 for $CaMoO_4$ and 3.0×3.0 mm^2 for $CaWO_4$) was evaporated on the crystal top to thermalise the phonons in the absorber created by an energy deposit from a particle and help collect those phonons. A neutron transmutation doped germanium (NTD-Ge) thermistor ($1.5\times1.5\times0.5$ mm^3) was glued on the gold film with a thin layer (25 μm thickness) of Araldite adhesive. A string of thin Teflon fibres was placed on top of the adhesive before it was cured to prevent physical touching between the the gold film and the NTD-Ge, which could create a short across the electrodes in the NTD-Ge thermistor.

The energy deposit from a particle creates athermal phonons and they get collected and thermalised in the thin gold film, causing a heat up in the crystal, the gold film and, eventually, the NTD-Ge. The temperature rise of the NTD-Ge is measured by the change of its resistance according to:

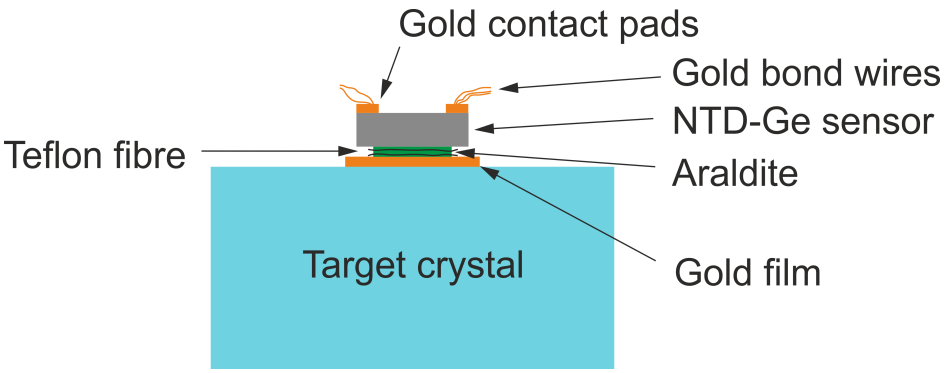

Figure 2.4: Schematic view of the calorimeter with an NTD-Ge sensor as the phonon sensor.

$$R(T) = R_0 \exp\left(\frac{T_0}{T}\right)^{1/2}, \tag{2.1}$$

where R is the resistance of the NTD-Ge, T is temperature, and R_0 as well as T_0 are constants which are specific to individual NTD-Ge sensors. For the NTD-Ge in this experiment, a generic calibration gives $R_0 = 5.52\ \Omega$ and $T_0 = 2.99$ K. Several strings of thin gold wires (25 μm diameter) were bonded to the two gold electrodes on two strips on the top surface of the NTD-Ge. The other end of the gold wires was connected to landing pads on a printed circuit board (PCB) with silver paint. The PCB was bolted to the copper housing. The gold wires provided electric connections for readout as well as thermal connections for the operation of the calorimeter, as the heat generated by the energy deposit could be transferred to the heat bath. Solder at very low temperature becomes a superconductor and, in the superconducting state, it has very low thermal conduction, which is undesirable for the thermal connection between the calorimeter and heat bath. As silver paint remains non-superconducting even at the lowest temperatures, silver paint is used instead of solder. As shown in Figure 2.5, the PCB with landing pads was mounted in an NOSV copper (a type of copper with low hydrogen content, reasons discussed later) housing structure in a horizontal orientation. The horizontal PCB was connected to another PCB on the vertical side, which

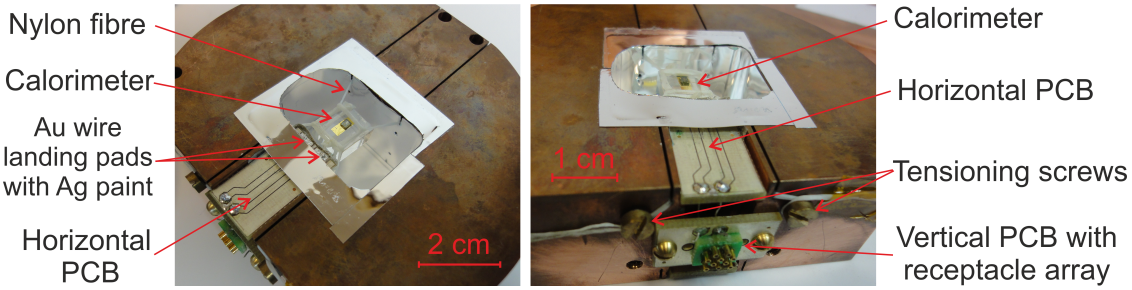

Figure 2.5: Calorimeter setup in NOSV copper housing. The inner surface of the copper housing was lined with reflective foil for light collection purpose. The calorimeter was suspended in the copper housing structure with nylon fibres, and the tension of the nylon fibres could be adjusted with tensioning screws. Thin gold wires (25 μm diameter, too thin to be visible in photos) connected the calorimeter to the landing pads of the horizontal PCB with silver paint. The horizontal PCB is connected to the vertical PCB, which had a receptacle array for the laminated cable.

was mounted in the same copper structure. The vertical PCB featured a receptacle array to provide connectivity for the custom-made semi-flexible laminated cable, which connected the NTD-Ge sensor to the cold JFETs. A cable made from several long PCBs connected the cold JFETs to room temperature readout electronics. The cabling scheme for the phonon channel is shown in Figure 2.3. The JFETs were weakly heat-linked to the 4.2-K stage but they were heated up to 120 K for optimal performance [142] and the box containing JFETs was covered with aluminium tapes to mitigate the thermal radiation from this warm part (Figure 2.2). The cables were well heat sunk at different temperature points in the dilution refrigerator. All the surfaces of the rectangular $CaMoO_4$ crystal were polished, while five faces of the rectangular $CaWO_4$ crystals were roughened to improve the light collection efficiency (details in Section 2.6). The calorimeter was suspended in the copper housing structure with nylon fibres and the tension of the nylon fibres could be adjusted with tensioning screws.

2.2.1 Heat capacity

As a first-order approximation, the temperature rise ΔT of the calorimeter resulting from the energy deposit E of a particle follows:

$$\Delta T = \frac{E}{C}\,, \tag{2.2}$$

where C is the heat capacity of the calorimeter. Thus, the heat capacity of the calorimeter is important for the signal size resulting from the energy deposit of a particle and, consequently, the performance of the calorimeter such as its energy resolution and energy threshold. The heat capacities of the major components in the two calorimeter modules with a $CaMoO_4$ crystal and a $CaWO_4$ crystal, respectively, are listed in Table 2.1. The NTD-Ge sensor dominates the heat capacity of the calorimeter at <20 mK temperature, and its heat capacity is at least 20 times as large as the absorber crystal. In other words, the absorber crystal can be enlarged to ~20 times bigger before its heat capacitance starts to have significant effects on the heat capacitance of the calorimeter.

2.3 Light detector setup

The PMT used in this experiment was a Hamamatsu R8520-06-PT 10-stage Bialkali PMT with platinum underlay. The photocathode of a normal Bialkali PMT becomes too resistive when it is cooled down to low temperature, leading to positive charge accumulation in the cathode and, thus, a decrease of the PMT quantum efficiency. The Pt underlay of the cathode remains conductive at the lowest temperature, solving the charge accumulation issue. However, the presence of the Pt underlay also decreases the room-temperature quantum efficiency of the PMT to ~15%, compared to ~ 30% of a similar PMT model with Al strips designed for liquid xenon temperature in a dark matter experiment [143]. The Pt underlay in

$CaMoO_4$ module			
Components	Dimensions (mm^3)	Heat capacity (pJ/K)	
		At 20 mK	At 15 mK
NTD-Ge sensor	$1.5 \times 1.5 \times 0.5$	45.0	33.8
Araldite	$\pi \times 0.66^2 \times 0.025 \times 2$	7.6	5.7
Gold film on crystal	$6.2 \times 2.2 \times 0.00025$	4.6	3.5
$CaMoO_4$ crystal	$9.5 \times 9.5 \times 5.0$	1.8	0.7
NTD-Ge gold pads	Negligible		
Total heat capacity of calorimeter (pJ/K)		59.0	43.7
$CaWO_4$ module			
Components	Dimensions (mm^3)	Heat capacity (pJ/K)	
		At 20 mK	At 15 mK
NTD-Ge sensor	$1.5 \times 1.5 \times 0.5$	45.0	33.8
Araldite	$\pi \times 0.66^2 \times 0.025 \times 2$	7.6	5.7
Gold film on crystal	$3.0 \times 3.0 \times 0.00025$	3.0	2.3
$CaWO_4$ crystal	$8.4 \times 9.7 \times 3.3$	2.1	0.9
NTD-Ge gold pads	Negligible		
Total heat capacity of calorimeter (pJ/K)		57.7	42.7

Table 2.1: Heat capacity of the major components in the calorimeters with $CaMoO_4$ and $CaWO_4$ as the absorber, respectively.

this PMT is not visible through inspection by eye, while Al strips in PMTs for liquid xenon temperature are in the form of thin strips in a cross shape, which indicates the Pt underlay covers the whole photocathode area. The PMT faced the scintillating crystal with a gap, which is required for the optimal operation of the calorimeter, as thermalization should only be through the gold wires bonded to the NTD-Ge for the best performance.

With the PMT located close to the sensitive calorimeter at the lowest temperature stage of the cryostat, the high voltage delivery system of the PMT should not introduce too much heat and prevent the calorimeter from reaching its optimal performance at low temperature, or create excessive noise in the calorimeter signal channel. To achieve this, the PMT was powered by a high voltage delivery system with a 25-stage Cockcroft-Walton generator (CWG) (Figure 2.6) [144]. As shown in Figure 2.3, a hermetic seal feedthrough connected a small air-side AC signal through a twisted wire pair to a transformer with a winding ratio of

25:600, which ramped up the AC voltage initially. The transformer was installed at the 4.2-K stage, inside the inner vacuum chamber (IVC). Inside electrically grounded shielding, another twisted wire pair connected the AC voltage from the transformer to a 25-stage Cockcroft-Walton generator, which transformed the AC low voltage to different DC high voltages at different stages of the generator. The CWG was made from a printed circuit board with capacitors (470 nF) and diodes (low leakage) soldered on, as shown in Figure 2.6 and Figure 2.7. The Cockcroft-Walton generator was mounted at the still level of the dilution refrigerator, which was about 700 mK. The still level was chosen as it provides enough cooling power to heat dissipated by the diodes and the attenuator resistors. The high voltage generated by the CWG was monitored from outside the cryostat after be attenuated by a resistive voltage divider, with room-temperature resistance values of 1 MΩ and 1 GΩ, which are soldered on the same PCB of the CWG. The CWG generated the different suitable DC high voltages in its stages, and these high voltages were then passed through a custom-made semi-flexible laminated cable with individual tracks for different voltages and connected to an array of pins soldered on the side of a PCB below the PMT. As a PMT base, that PCB had an array of receptacles connecting to the PMT pins, and it delivered the different DC high voltages individually to the PMT pins. As mentioned, only a small AC voltage (few volts) from a function generator was needed from the air side and any high voltage feedthrough was avoided (around 2–3 kV voltage is needed to power the PMT, as discussed later in this session). Also, the presence of high voltage was confined in a small space below the still stage between the CWG and PMT, avoiding long cryogenic high voltage cables from room temperature to the still stage. There was no need for voltage dividers at the mixing chamber level of the dilution refrigerator near the PMT because the CWG generated various voltages for the cathode, grid, dynodes and anode of the PMT. As mentioned before, the

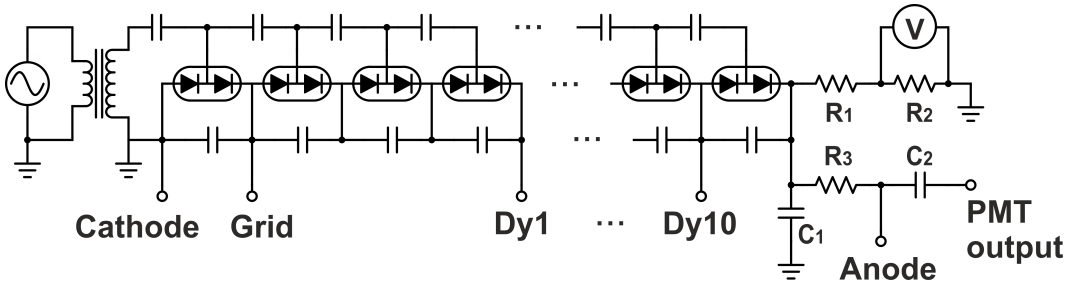

Figure 2.6: Schematic of the 25-stage Cockcroft-Walton generator (CWG) based high-voltage power supply. The connections of the power supply to the various stage of the PMT are also shown. For clarity, only the first few and last few stages of the CWG are shown. The power supply to the PMT follows the voltage distribution ratio recommended by the PMT manufacturer [145]. Top right corner shows an attenuator consisting of two resistors as a voltage divider, R_1 and R_2 ($R_1 = 1$ GΩ and $R_2 = 1$ MΩ at room temperature), for high-voltage monitoring purpose. As shown at bottom right corner, a high-pass filter consisting of a resistor R_3 (0.67 MΩ) and a capacitor C_2 (1 nF) enables powering the anode of the PMT with DC voltage, while the high-frequency signal (single photoelectron pulse) from the PMT anode could be readout.

heat dissipated by voltage dividers (>1 mW) is calculated to be excessive for the mixing chamber level of the dilution refrigerator (cooling power ~400 μW at 100 mK and ~15 μW at 20 mK) and the calorimeter. Consequently, the absence of the voltage dividers at the mixing chamber stage is essential for the cryostat to reach the required milli-Kelvin temperatures and for the operation of the calorimeter. The signal of the PMT was carried by a coaxial cable from the PMT base PCB, all the way to the readout electronics located outside the cryostat at room temperature. The PMT itself is thought to generate only an insignificant amount of heat from electron multiplication and no heat generated by the PMT itself has been observed at mK temperatures.

No detrimental effect on detector operation has been found while running the CWG, especially on the signal of the low-temperature calorimeter, which was sensitive and co-located. The use of a semi-flexible laminated cable for the calorimeter readout and for the delivery of high voltages to the PMT was demonstrated to be enough to shield any detrimental effects from the operation of CWG and enough

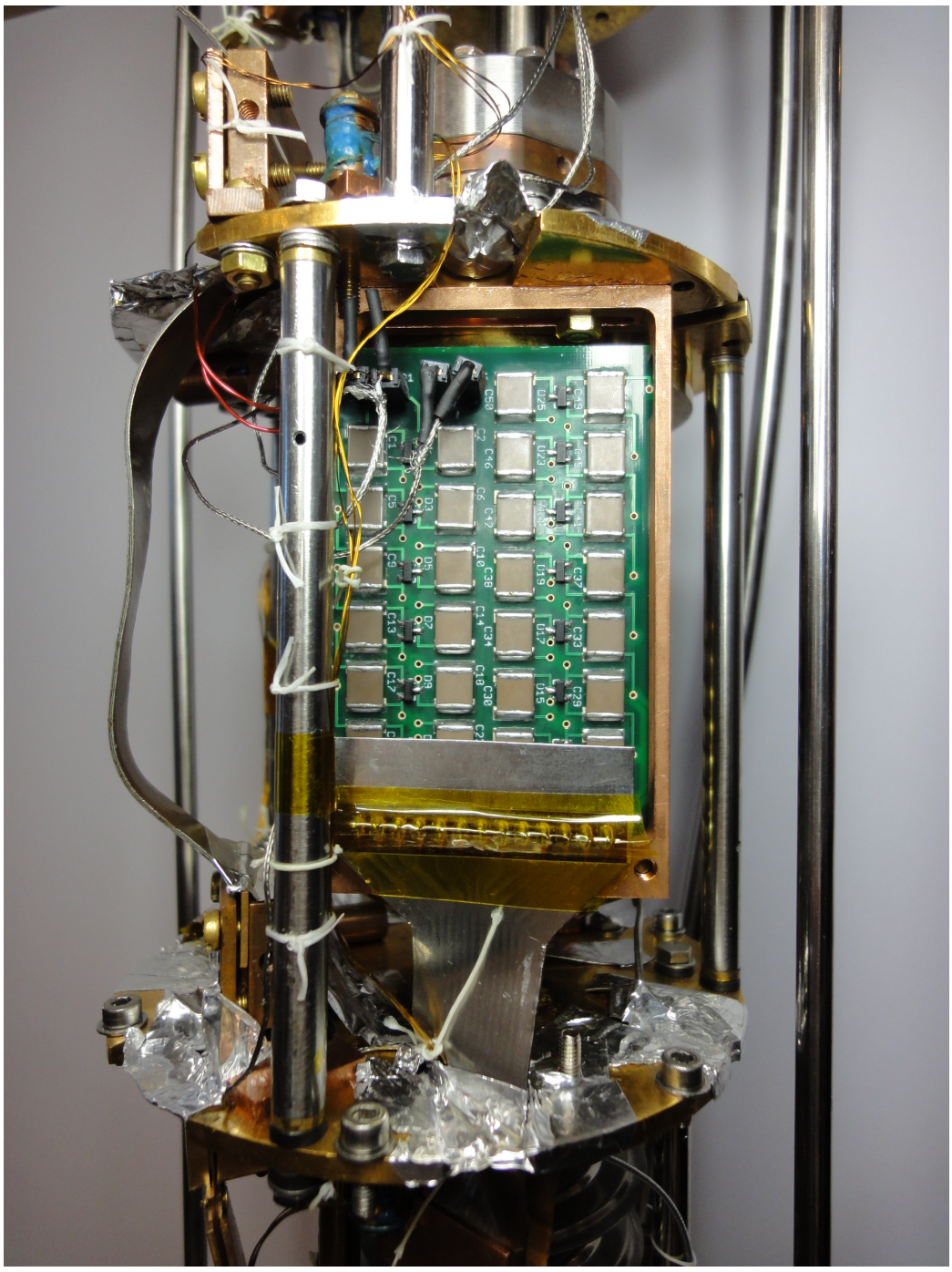

Figure 2.7: The 25-stage Cockcroft-Walton generator board (PCB dimensions: 72×48 mm^2) heat-sunk to the still stage of the dilution refrigerator. A semi-flexible laminated cable carried the voltages from different stages of the CWG with individual tracks, to deliver them to the different stages of the PMT.

to prevent high voltage discharge, even though the delivery of the high voltages for the cathode/dynode/anode stages of the PMT was adjacent to the readout cables of the calorimeter. The CWG was driven at 23 kHz frequency, well above the NTD-Ge modulation frequency in the calorimeter (500 Hz or 1 kHz), also above the typical bandwidth of the readout system based on SQUID for transition-edge sensors (TES) in the CRESST experiment [146]. Also, no temperature rise was observed on the calorimeter from the introduction of the PMT readout system into the cryostat or the operation of the PMT and the calorimeter was able to cool down to as low as 13 mK when the PMT was on.

The PMT in this experiment is recommended by the manufacturer to be biased up to 950 V between cathode and anode at room temperature. However, it was observed that, at milli-Kelvin temperatures, this recommended bias potential is not enough to multiply the photoelectrons to be well separated from the noise of the readout electronics. The PMT was thus biased to 2–3 kV to have a good single photoelectron response at milli-Kelvin temperatures (Section 4.5). The reason for the need of this much higher voltage is unknown. It could be due to the secondary electron emission efficiency of PMT dynodes dropping significantly at milli-Kelvin temperatures compared to room temperature, or it could be due to the decrease of electron collection efficiency resulting from dynode shape deformation at low temperature. However, even at such high voltage, no electric breakdown was observed during the PMT operation at milli-Kelvin temperatures.

2.4 Detector assembly

Compared to the well-shielded environment against comics rays and the stable environment found in an underground laboratory, there are additional challenges when operating cryogenic detectors in an above-ground laboratory, including am-

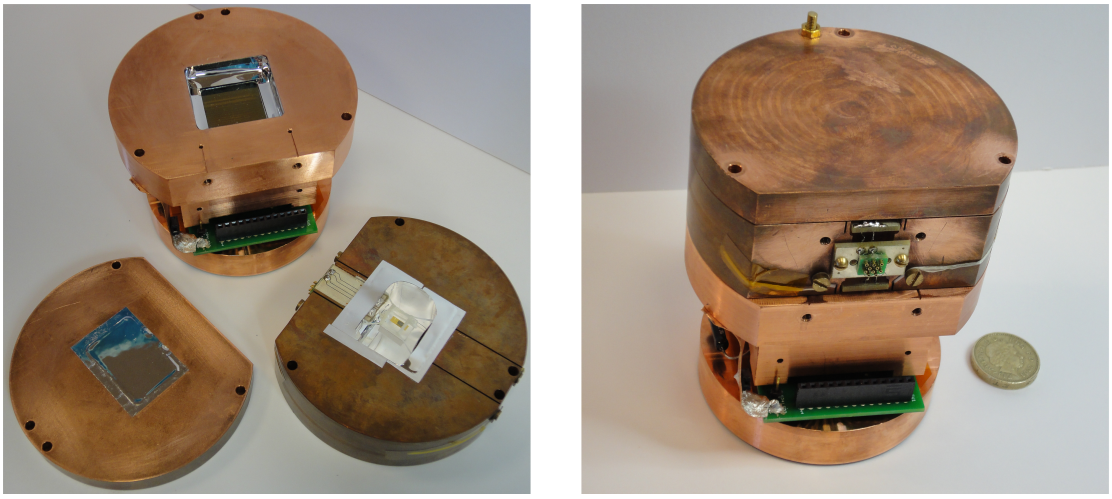

Figure 2.8: Detectors in copper housing. The image on the left shows different components separated, with the back reflector shown in bottom left corner, the PMT inside the copper housing with a PCB as mounting base shown in the upper middle corner, and the calorimeter with the scintillating absorber shown in the bottom right corner. The image on the right shows the detectors after assembly, which shows (from the top to the bottom) the back reflector, calorimeter component and the PMT with PCB mounting component.

bient radiation and vibration. These issues were addressed by providing copper housing structures with a relatively large mass around the detectors. As shown in Figure 2.1 and Figure 2.8, the two detectors mentioned above were housed inside copper structures which provided mechanical support, shielded the detector from ambient radiation and provided cooling power as a heat bath. The copper housing structures were heat-sunk to the mixing chamber stage in a dilution refrigerator, which is the lowest temperature stage in the cryostat. NOSV copper with low hydrogen content was used for constructing the housing structures, as below 20 mK the slow heat leak by ortho-para conversion of hydrogen in copper prevents the cryostat from further cooling down to base temperature [147]. The inner surface of the copper housing is covered with VM2000 highly reflective foil (manufactured by 3M) to improve light collection efficiency [148].

2.5 Data acquisition

Two separate custom-made DAQ systems were deployed to read out the phonon channel and the light channel, respectively.

2.5.1 Phonon channel DAQ

The aim of the phonon channel DAQ was to measure the resistance between the two electrodes of the NTD-Ge thermistor over time, as the resistance change corresponded to energy deposit. The excitation was a square-wave current of fixed amplitude with a modulation frequency of 500 Hz or 1 kHz. To capture the whole square-wave modulation waveform, the data were digitised at a rate of 100 kHz. With a constant-amplitude excitation current, the readout voltage amplitude was proportional to the resistance of the NTD-Ge sensor. A modulated excitation signal instead of a DC signal was used to mitigate the voltage offset effects in the low-frequency region of the readout system. Different from the EDELWEISS experiment, which also uses NTD-Ge as the thermistor and has a similar readout scheme in the phonon channel, there was no firmware triggering in the phonon channel in this experiment and the DAQ in this experiment recorded continuously during data taking. The data rate was around 670 Mbyte/hour. The only pulse identification of the phonon channel signal was during offline data analysis, which will be described in Section 3.1.

2.5.2 Light channel DAQ

The light channel data were collected by another custom-made data acquisition system. To resolve individual photons, the data from the PMT were digitised with 5 ns intervals at the ADC, which corresponds to a clock frequency of 200 MHz. However, with such short times, it was quite challenging for the Spartan-6 FPGA

in the electronics to manipulate the data. To circumvent this, 8 consecutive data points were always grouped and the subsequent manipulation was performed on groups of 8 data points instead of on individual data points. The grouping lowered the required frequency to 25 MHz, which was more readily achievable given the limitations of the FPGA chosen. The groups of 8 data points kept updating the pre-trigger region, which was a ring buffer with enough capacity to accommodate data in the pre-trigger region length required. Besides updating the pre-trigger region, the average of the group of 8 data points was compared to the threshold level, which was set by the user. Once the average value was larger than the pre-set threshold, the triggering condition was met and an output FIFO (a type of data buffer) started to transfer the pre-trigger region data and the post-trigger data to a computer and, finally, the data was stored on disk. Because the average value of the group of 8 data point was used, there were maximum 40 ns between the triggering point and the natural rising edge of the analogue signal.

In this experiment, two different modes of data taking were used for $CaWO_4$ data and $CaMoO_4$ data respectively, mainly because $CaMoO_4$ has a too long scintillation decay time constant (~3.41 ms) for continous recording in the PMT channel. For $CaWO_4$ data taking, a fixed length of pre-trigger and post-trigger data were recorded. With this method, a continuous record was produced, capturing a scintillation event, including the baseline as well as the photoelectron spikes. An example of these records is shown in Figure 2.9. However, because a large amount of data needed to be transferred from the memory of the digitizer, this had the disadvantage of creating dead time in the data acquisition. For $CaMoO_4$ data, instead of recording a fixed length of data once triggered, the triggering condition was configured so that the trigger would send a reset signal when the 8-point average dropped below the threshold for at least two consecutive 8-point groups, and this marked the end of the post-trigger region. In this way,

only the photoelectron spikes and a small fraction of the baseline data in the pre-trigger region were recorded, as shown in Figure 2.9. With this method, so-called "dead-time free" data acquisition was achieved by a decrease in data rate and this applies to scintillators with longer decay time constants than that allowed by the capacity of data buffer on board. In a short time, usually more than dozens of photons are emitted by a typical scintillation event, but that depends on the energy deposit of the incoming particle and the time constants of the scintillation of the crystal used.

The data taking parameters in firmware, including digitized time interval, record length, length of pre-trigger region, cutoff frequencies of the low-pass filters on the data used in triggering and on the data recorded on disk, the trigger mode and the threshold level could be set by the user through the interface of the control software, Oxrop. Oxrop has developed by the Oxford research group over many years.

2.6 Light detection optimisation

The number of photons detected by the PMT is critical for the performance of the CPSD, including threshold, energy resolution and discrimination power. Consequently, the number of photons detected $N_{detected}$ is a quantity that needs to be maximised and it is the product of three factors: the absolute scintillating yield, the light collection efficiency, and the quantum efficiency of the PMT.

$$N_{detected} = N_{scintillated} \cdot \eta_{collection} \cdot Q.E. . \tag{2.3}$$

The absolute scintillating yield is a property of the scintillation crystal, affected by the production process of the crystal (~28 ph $\mathrm{keV_{ee}^{-1}}$ for $CaWO_4$ at 9 K [117]). The quantum efficiency of the PMT, currently estimated at ~15% at 420 nm

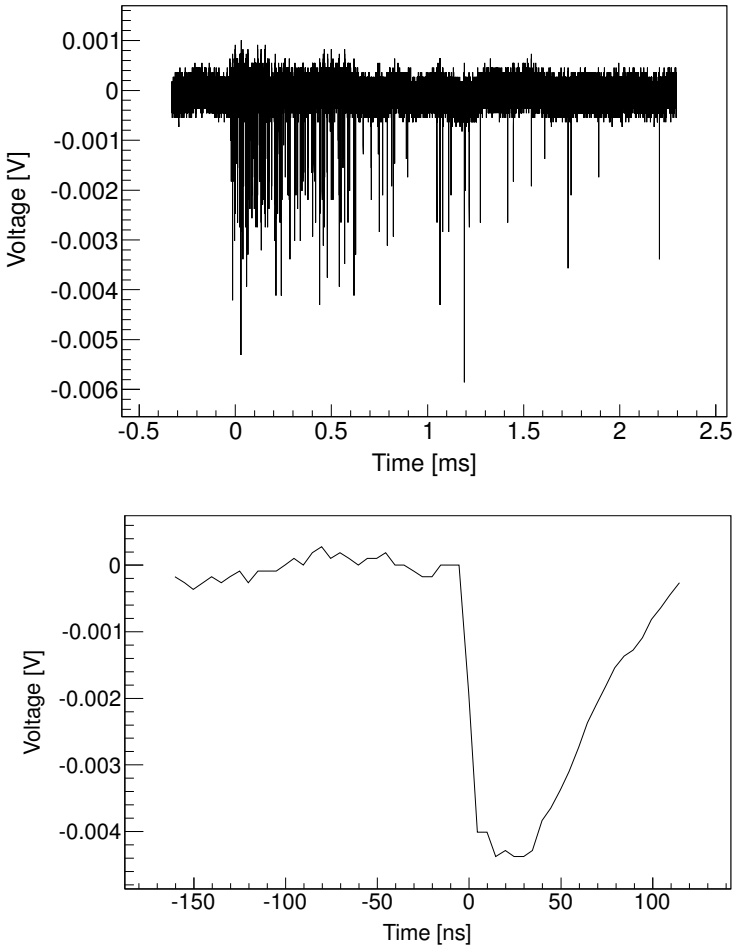

Figure 2.9: Top, a typical event of a 122-keV γ quantum measured by the light detector in the CPSD module with $CaWO_4$ as the absorber, in the "fixed-length" DAQ mode. Bottom, a typical record of an individual photon pulse measured by the light detector after subject to a low-pass filter with 50 ns time constant in the CPSD module with $CaMoO_4$ as the absorber, in the "dead-time free" DAQ mode.

wavelength, has the largest potential to improve significantly, as it is much lower than the quantum efficiency of current mainstream PMTs at 25%–30%. However, the improvement of PMT quantum efficiency requires efforts and resources that are beyond the scope of this thesis. Compared to the two factors above, it is relatively easy to carry out optimisation for the light collection efficiency by adjusting the geometry of the detector, the reflector on detector housing surface and surface conditions (e.g. surface roughness) of the scintillation crystal.

An acceptable energy resolution of the light channel was obtained by the first detector module which used a $CaMoO_4$ crystal with polished surfaces as the scintillating absorber. Afterwards, as a second detector module, we changed the absorber to a $CaWO_4$ crystal with five faces roughened to get a better light channel response. The improvement was three-fold. Firstly, according to the manufacturer, the spectral sensitivy of the Hamamatsu R8520-06-PT Bialkali PMT overlaps better with the emission spectrum by the $CaWO_4$ crystal (peak at 420 nm) than that of the $CaMoO_4$ crystal (peak at 540 nm), as shown in Figure 2.10. However, the VM2000 reflective foil has lower reflection efficiency for the low wavelength component of the $CaWO_4$ emission, as shown in Figure 2.11. Because the scintillation photons were reflected multiple times on average before they were captured by the PMT photocathode, the light collection efficiency of photons with a specific wavelength had a power law dependence of the reflection efficiency. For example, with a reflection efficiency X for photons with a specific wavelength, and N as the average number of times a photon gets reflected before reaching the light detector, the light collection efficiency of photons of that wavelength is X^N. Secondly, the roughened surface is known increased the light collection efficiency [149], as fewer photons were trapped inside the crystal by total internal reflection, especially in the configurations of no optical coupling between the scintillation crystal and the light detector as in this experiment. As the light attenuation coef-

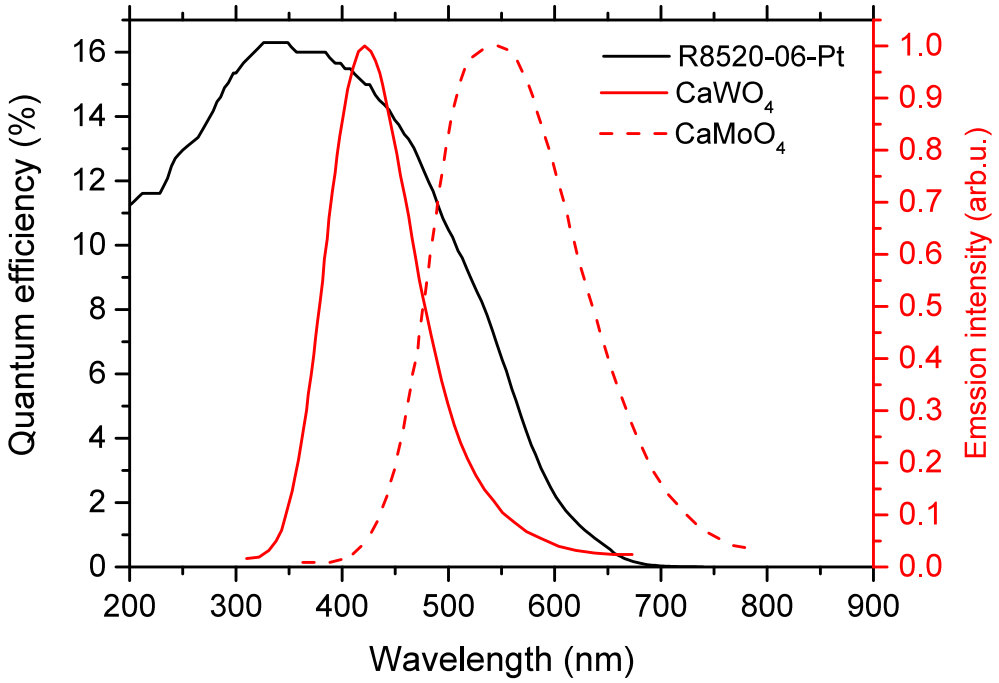

Figure 2.10: Luminescence spectra of $CaWO_4$ and $CaMoO_4$ measured at $T = 8\,\mathrm{K}$ for excitation with 31 eV VUV photons (red, from [117]), and the typical spectral response of an R8520-06-Pt PMT (black).

ficient of $CaWO_4$ in the range of 0.03–0.3 cm^{-1}, depending on the crystal growth process and the treatment later on, a significant fraction of scintillation photons are self-absorbed by the crystal if they remain trapped inside the crystal due to total internal reflection. In the $CaWO_4$ crystal, the side facing the PMT was polished. On the opposite side, the area with the gold film evaporated on was also polished while the rest of that face was roughened. Thirdly, the detector geometry in the $CaWO_4$ module was carefully optimised with optical modelling and experimental validation at room temperature (described below). Overall, there were around 2.8 times as many photons detected in the $CaWO_4$ detector module (~170 photons for 122 keV) as in $CaMoO_4$ detector module (~60 photons for 122 keV), even though the absolute scintillating yields (27–28 $\mathrm{ph\,keV_{ee}^{-1}}$) are similar for these two crystals at milli-Kelvin temperatures [117].

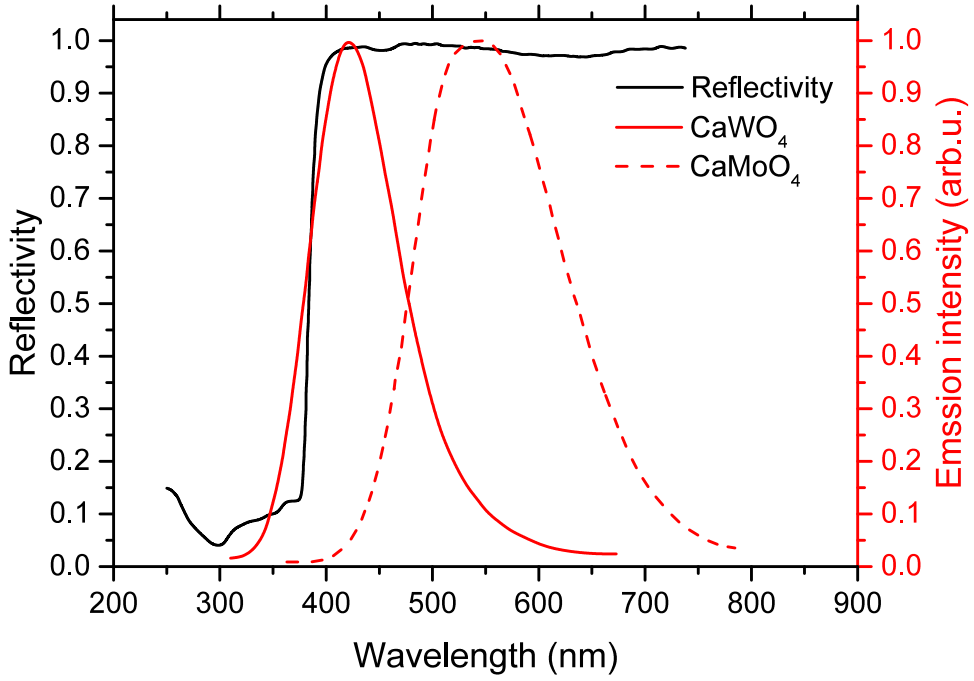

Figure 2.11: Luminescence spectra of $CaWO_4$ and $CaMoO_4$ measured at $T = 8\,K$ for excitation with 31 eV VUV photons (red, from [117]), and the measured reflectivity spectra of VM2000 foil (black, from [150])

Optical Modelling

A simulation of the light collection efficiency in the $CaWO_4$ setup was carried out with the aim of improving the light collection efficiency. The simulation output was confirmed with experimental data at room temperature. The level of modelling was only meant to reveal general trends in the light collection, but not give a perfect prediction of light collection. The modelling method is similar to that in Reference [151].

ZEMAX ray-tracing software was employed to model the light transport in the detector module. The non-sequential mode in the software was chosen for the simulation, which means light rays being traced do not have predefined sequence of surfaces that they must impinge upon. In this mode, the rays may hit any part of any objects in the simulation, and they can hit the same object multiple times. Physical positions and properties of the objects, as well as the directions of the rays determine the ray trajectories. In this way, the total internal reflections, polarisation effects and ray splitting at the interfaces are all taken into account in the simulation, along with the standard reflection, refraction and absorption of light.

Figure 2.12 shows an example of the optical model, which corresponds to geometry Scenario C discussed below. As shown, the geometry model is a $CaWO_4$ crystal floating inside a cuboid cavity without any suspension. Mirrors are on five sides of the cavity, and the remaining side is modelled as the PMT window and the photocathode. To eliminate uncertainty at the surface, the scintillation source was simulated as a volume with the shape of the $CaWO_4$ crystal, but with dimensions 0.001 mm less than the actual geometrical sizes of the scintillation crystal ($3.3 \times 8.4 \times 9.7$ mm^3). The scintillation photons were set to be not polarised and they were distributed isotropically. In each simulation run, 100,000 photons with fixed wavelength 420 nm (emission peak of $CaWO_4$) were traced, as they were

randomly distributed in the volume of the crystal. The number of photons leads to a statistical error ±0.3% in the simulation. The isotropic approximation with an average dispersion curve and $CaWO_4$ refractive index $n = 1.96$ at 420 nm were adopted for the simulation, because of the negligible effects from the small anisotropy of calcium tungstate ($n_e - n_o = 0.02$) on the final results. The absorption coefficient α of the $CaWO_4$ crystal was taken as 0.11 cm^{-1}, and this value was obtained from the measured transmission spectra after correcting it for multiple reflections, as discussed in Reference [152]. The bulk scattering coefficient σ of the $CaWO_4$ crystal was taken as 0.06 cm^{-1}, determined by previous studies of the crystal [153]. The PMT window was modelled as 1 mm thick, made of synthetic silica with refractive index $n = 1.47$. The inner surface of the PMT window was modelled to be an ideal absorber, for the calculation of the light collection efficiency. The diffused surfaces of the crystal were modelled as Lambertian diffuser. The mirrors in the model take the reflectivity of the VM2000 reflective foil (0.986) and the mirrors were modelled as specular reflectors. The result of the simulation was the fraction of the number of photons generated in the scintillation source that reaches the inner surface of the PMT window.

Three geometry scenarios were modelled and the modellings were confirmed with real scintillation data at room temperature: A) control geometry, where the PMT-scintillator distance is 26 mm, and the gap between the scintillator and the back reflector is 2 mm; B) PMT-scintillator distance is shortened to 9 mm, and the gap between the scintillator and the back reflector is 19 mm; C) PMT-scintillator distance is 9 mm, and the gap between the scintillator and the back reflector is shortened to 3 mm. It is expected that the shortening of the gap between the PMT and the scintillator and that between the scintillator and the back reflector would improve the light collection efficiency, as photons would be reflected fewer times on average before entering the PMT window. The results of the simulations

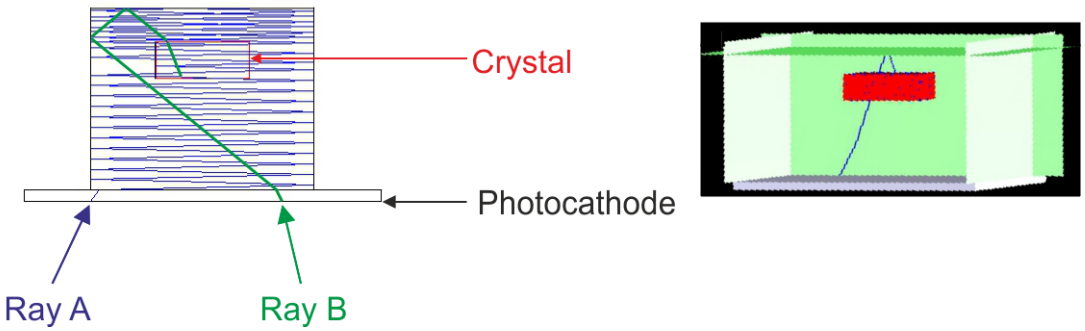

Figure 2.12: 2D (left) and 3D (right) illustration of the three-dimensional optical model used in simulations. In the left image, the scintillation crystal is represented by the red rectangle. The light rays shown are absorbed in the photocathode behind the PMT quartz window. For illustration and clarity only two light rays in the left image are shown, Ray A (blue) and Ray B (green). Ray A is an example of light propagation that involves a large number of reflections in the cavity before getting absorbed in the photocathode. Ray B has simpler tracks before getting absorbed in the photocathode. In the right image, the crystal is shown in red, and the PMT window is shown in grey, below which is the photocathode. The reflective foils are as modelled as mirrors and in the right image they are shown in green. The ray in the right image is Ray C, and its tracks are shown in three-dimensional space.

agree with this expectation (Figure 2.13). These simulation results were confirmed experimentally with the scintillation response of the detector at room temperature with a ^{57}Co source as excitation.

More discussion about other potential methods to improve light detection is in Section 5.1.1.

2.7 Helium permeation and cryostat cooldown procedure

Helium is known to be able to permeate into PMTs through their glass bulb, especially through the synthetic silica glass window of the PMT in this study [154]. The synthetic silica glass window transmits photons down to a wavelength of 160 nm. The presence of residual helium gas inside the PMT causes the degradation

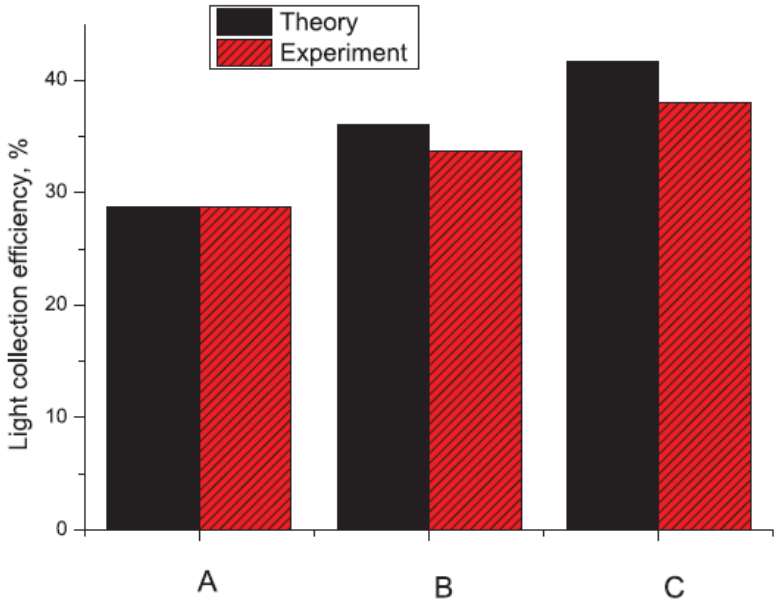

Figure 2.13: Black bar: light collection efficiency simulated. Red bar: the light collection efficiency measured at room temperature, by excitation of the detector module with a ^{57}Co source. Normalisation are applied to the experimental results relative to the simulated result in the control geometry A for comparison. See discussion for the geometry of different scenarios. Figure published in [140].

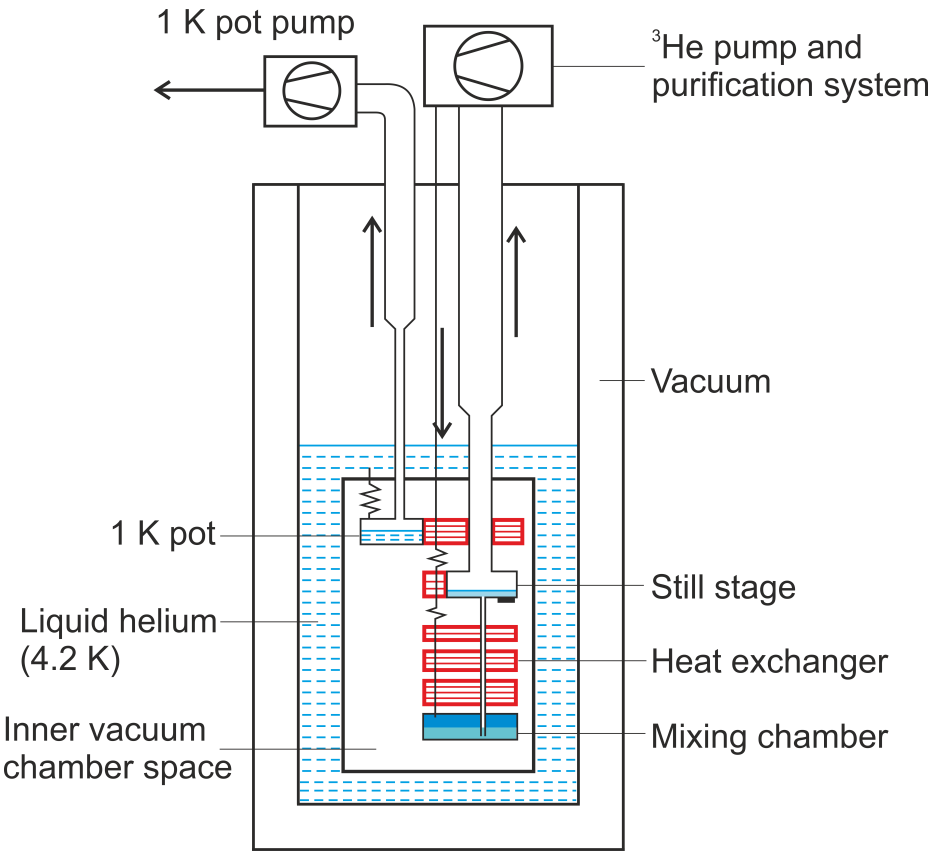

Figure 2.14: Schematic view of the wet ^{3}He/^{4}He dilution refrigerator.

of PMT performance, including an increase of dark current, an increase of after pulse and causing voltage breakdown. Hence caution is needed when helium is present around PMTs. In order to cool down the dilution refrigerator to milli-Kelvin temperatures, an important step is the introduction of helium gas as a heat exchange gas into the inner vacuum chamber (IVC) space (Figure 2.14) where the PMT is located because of the low boiling point of helium at 4.2 K. Unlike other gases which liquefy at much higher temperatures and lose the capability of heat conduction when the dilution refrigerator cools down, helium remains effective as a heat exchange gas from room temperature down to 4.2 K.

The solution to this issue lies in the fact that the permeation coefficient of the helium through glass (including synthetic silica) depends exponentially on the

temperature [155]:

$$k(T) = k_0 \exp(-\frac{Q_0}{RT}) \ , \tag{2.4}$$

where k is the permeation coefficient, T is temperature, k_0 is a constant, Q_0 is the activation energy of permeation, and R is the gas constant. The exponential dependence was confirmed experimentally down to 175 K [156]. An estimation using the permeation coefficient measured at 175 K already indicates the helium permeation rate drops to an acceptable level when the temperature is around 175 K.

Instead of using the usual cool down procedure in which helium is introduced at room temperature, we devised a way to introduce helium exchange gas only after the cryostat was cooled down to around 77 K, but still successfully cooled down the cryostat to milli-Kelvin temperature. From room temperature to the boiling point of nitrogen (77 K), nitrogen heat exchange gas instead of the usual helium heat exchange gas was introduced to the IVC. Only after the cryostat reached a temperature of about 77 K was nitrogen gas pumped out and replaced by the helium heat exchange gas in the IVC. Then the normal procedure of cooling a dilution refrigerator was resumed, which include filling the main bath with cold helium gas first, and then with liquid helium, to cool it down to 4.2 K. Subsequently, the helium exchange gas was pumped out, and then the 1-K pot (a device which pumps the helium vapour to cool down using helium evaporation) started to operate. Later the ^{3}He/^{4}He mixture was condensed in the still and the mixing chamber and circulation of the inner ^{3}He/^{4}He circuit started, cooling down the cryostat to the base temperature. In the condensing step, so-called "reverse condensing" through the still line was adopted, because the lack of a helium cold-trap in this cryostat increases the possibility of blockage in the capillary. Condensing through the wide still line gets the contamination in the mixture frozen out on the wall of the still line wall first, before the mixture enters the

capillary, and thus decreases the chance of blockage in the capillary. No effects from residual helium gas in the energy spectrum of the PMT were observed when it was operated at milli-Kelvin temperatures and later at room temperature. In this way, with only a small change in the sequence of exchange gas introduction, the dilution refrigerator could be cooled down successfully without affecting the PMT and without costing significantly more regarding helium, efforts or time than a normal cool down.

Alternative cooldown procedure without introducing the helium exchange gas after the cryostat is cooled down to 77 K was tried out but without success. Instead of introducing helium exchange gas into IVC, circulation of inner ^{3}He/^{4}He circuit was carried out with the intention to cool down the various components in the inner circuit, but it was found that this cooldown method is not efficient enough to cool down the cryostat in a reasonable time.

Because the PMT was mainly operated at milli-Kelvin temperatures in this study, at such low temperature even helium freezes out if there is any residual gas in the PMT. Consequently, the residual helium gas might not have significant effects on the PMT operation at milli-Kelvin temperatures within reason. However, the residual helium gas would cause performance degradation of the PMT at room temperature later, limiting the possibility of diagnostic operation of the PMT at room temperature.

2.8 ^{57}Co source

In this experiment, a ^{57}Co source was placed externally to the cryostat to characterise the detector module. Considering the decay time constants of the calorimeter was in the range of tens milliseconds to a few hundreds of milliseconds, the distance of the radioactive source to the detector was decided so that the event

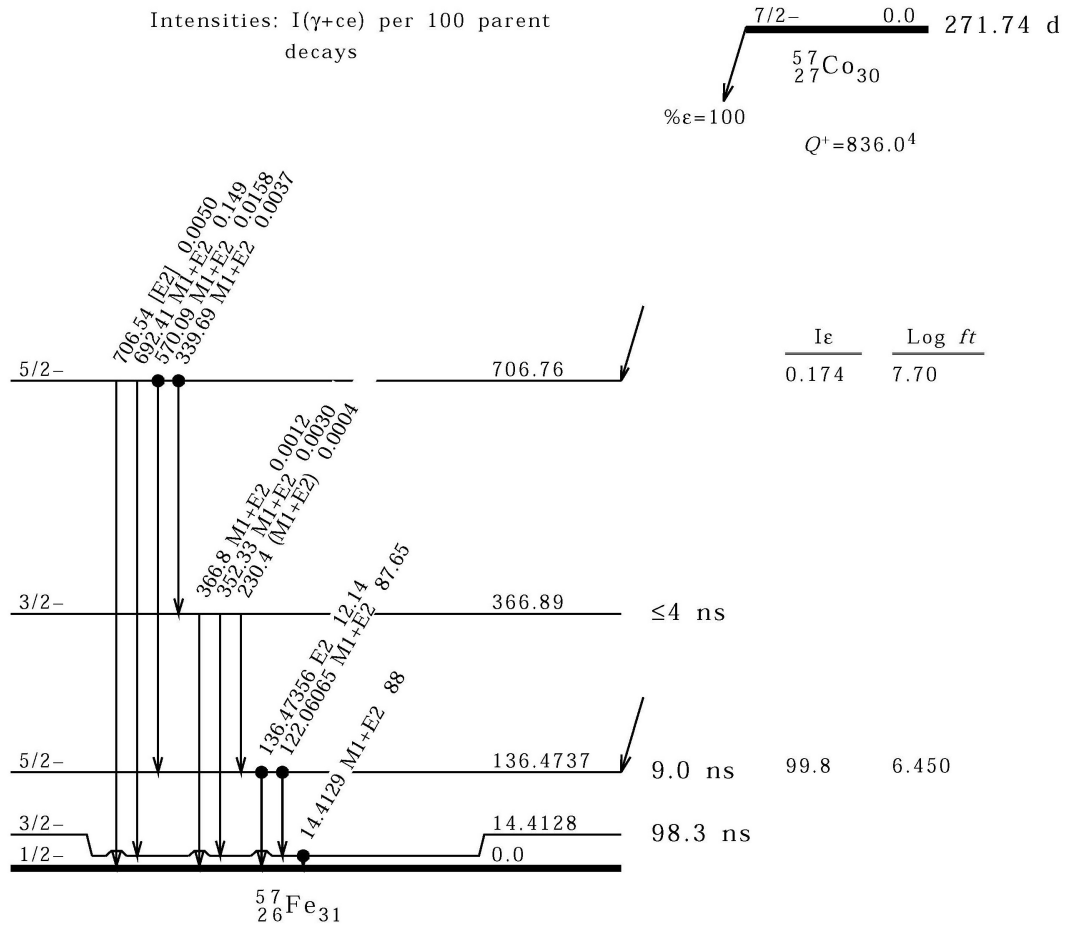

Figure 2.15: Decay scheme of ^{57}Co. Besides the three prominent γ lines of 136.5 keV, 122.1 keV and 14.4 keV, there are γ lines at higher energy with intensities at sub-percent levels. (From Reference [157])

rate is ~1 Hz, in order to avoid pulse pile-up. ^{57}Co has a half-life of 271.8 days, and its decay scheme is shown in Figure 2.15.

Chapter 3

Data analysis

In this chapter, the offline data analysis for the cryogenic phonon-scintillation detectors (CPSD) is discussed. The analyses of phonon channel and light channel data are discussed in Section 3.1 and Section 3.2, respectively. In Section 3.3, the analysis of coincident signals from the two channels is discussed. The light yield analysis (for discrimination) is discussed in Section 3.4. Finally, the characterisation of the PMT including its dark count rate and single electron response is explained in Section 3.5. Unless specified otherwise, these data were taken using γ-rays from a ^{57}Co source placed next to the cryostat. The decay scheme of ^{57}Co (Figure 2.15) leads to the emission of γ-rays of several energies, with 122 keV and then 136 keV having the highest intensities. Figure 3.1 shows a typical event of energy deposit in the absorber by a 122-keV γ quantum, measured by the light detector and the phonon detector in the CPSD module with $CaMoO_4$ as the absorber. Figure 3.2 shows a typical event for the energy deposit by a 122-keV γ quantum in the CPSD module with $CaWO_4$ as the absorber.

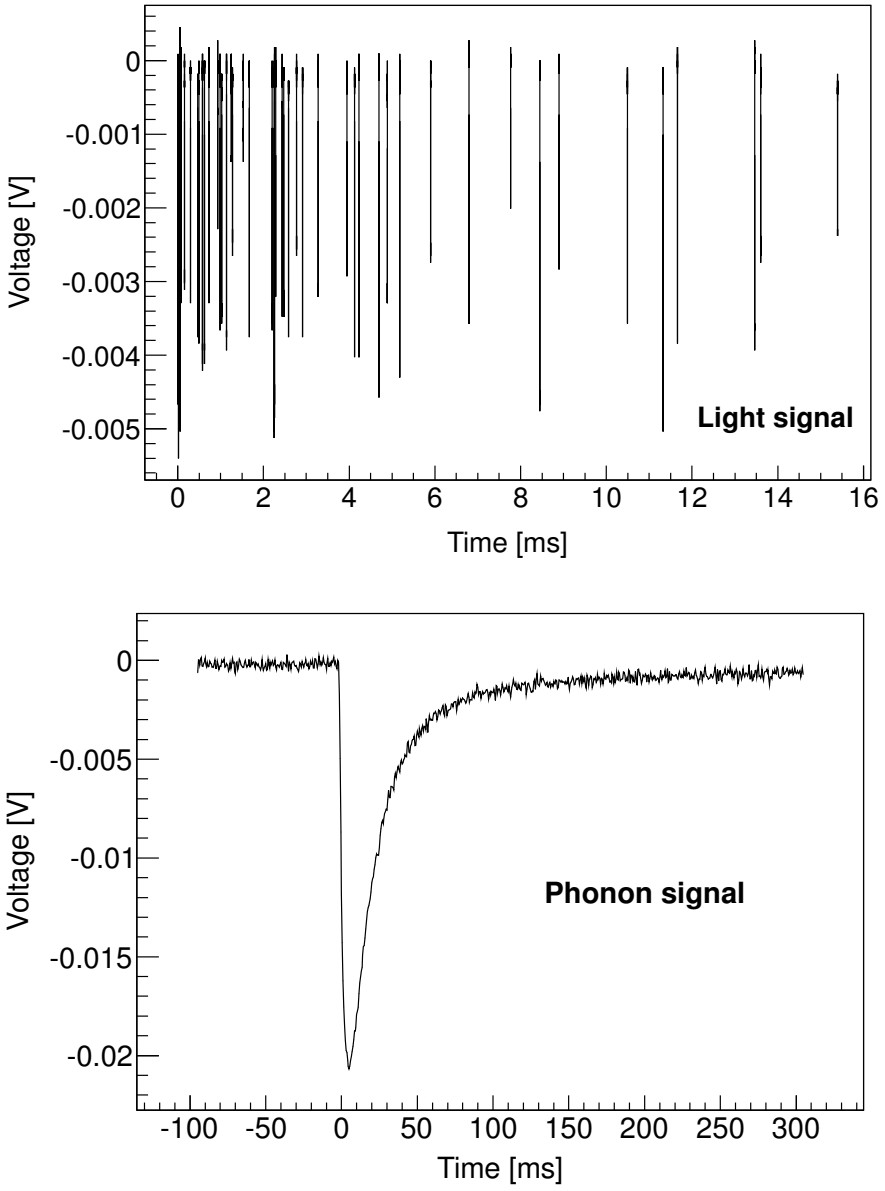

Figure 3.1: A typical event of energy deposit in the absorber by a 122-keV γ quantum, measured by the light detector (top) and the phonon detector (bottom) in the CPSD module with $CaMoO_4$ as the scintillating absorber. The signal of the light detector shown in this figure contains a group of individual photons shown in Figure 2.9 after the grouping procedure (Section 3.2.1.1), as each spike represents a photoelectron pulse. The signal of the phonon detector has been demodulated (Section 3.1.1).

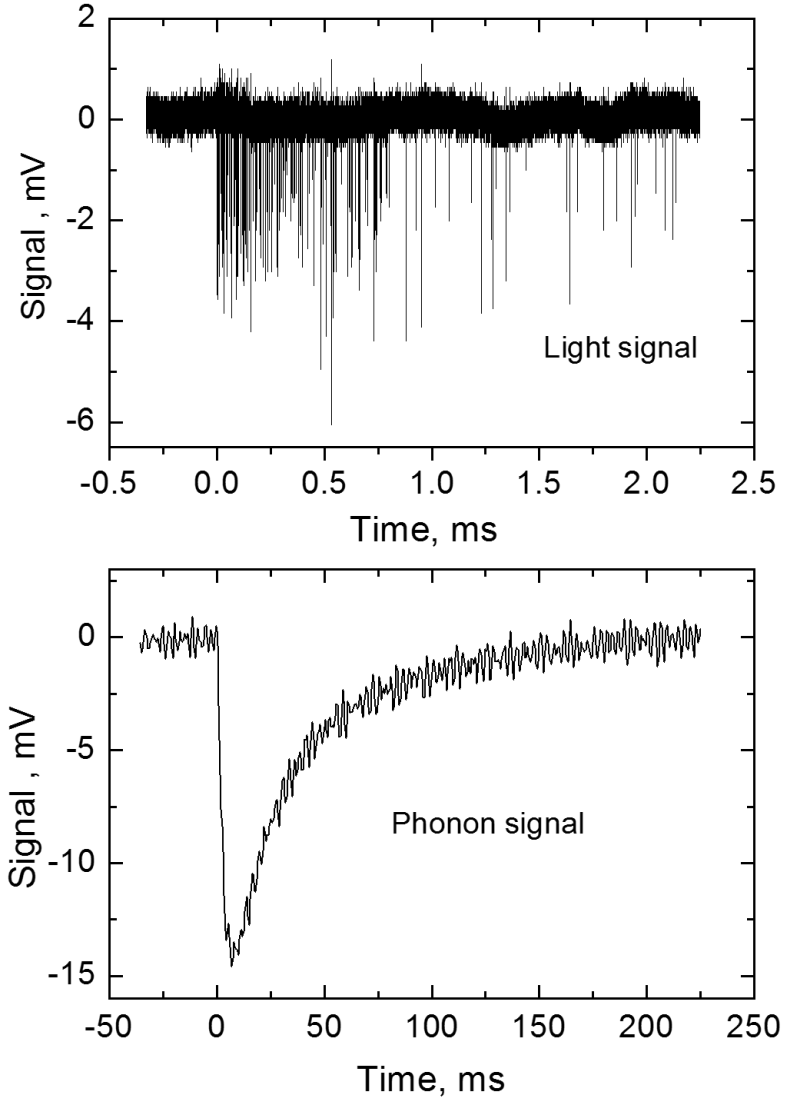

Figure 3.2: A typical event of energy deposit in the absorber by a 122-keV γ quantum, measured by the light detector (top) and phonon detector (bottom) in the CPSD module with $CaWO_4$ as the scintillating absorber. The data of the light detector captured the photon signal spikes as well as the baseline noise. The data of the phonon detector has been demodulated (Section 3.1.1). Note the 100 times difference in scale of the time axis. Figure published in [140].

3.1 Phonon channel analysis

Unlike the light channel, in which two different DAQ modes were used for the $CaMoO_4$ and $CaWO_4$ data, respectively, the phonon channel DAQ mode was the same for both the $CaMoO_4$ and $CaWO_4$ data. Consequently, the analysis of phonon channel data is the same for $CaMoO_4$ and $CaWO_4$ absorbers. As mentioned in Section 2.5.1, to eliminate the effects of the voltage offset introduced by the electronic readout system, a readout scheme with modulated signal was employed. The modulated signal is the starting point for offline analysis of phonon channel data (Figure 3.3). The aim of the phonon channel analysis is to extract the amplitude of signal pulses caused by energy deposits. Because the amplitude of a signal pulse at the output of the analogue electronics is in the millivolt range (Figure 3.1 and Figure 3.2), while the modulated amplitude is in the few volt range (Figure 3.3), precision is critical to improving the energy resolution of the phonon detector.

The data analysis for the phonon channel starts with demodulation of the signal (Section 3.1.1), after which a pulse finding algorithm (Section 3.1.2) is applied. Data quality cuts (Section 3.1.3) are then applied to select pulses to construct a template pulse (Section 3.1.4). A high-pass filter (Section 3.1.5) is then applied to both the candidate pulses and the template pulse. Finally, the filtered template pulse is fitted to the filtered candidate pulses (Section 3.1.6) and filtered baseline (Section 3.1.7), resulting in the final energy spectrum and the baseline energy resolution of the phonon detector, respectively.

3.1.1 Demodulation

The first step of the phonon channel analysis is the demodulation of the raw signal (Figure 3.3). The general idea of demodulation is to calculate the area of

signal traces, relative to the voltage offset. The aim of the demodulation is to extract the amplitude of the modulated signal over time precisely, as the change of amplitude of the modulated signal is proportional to the change of temperature, thus proportional to the energy deposit according to Equation 2.2. Due to the resistance of the NTD-Ge (~MΩ typically) and the parasitic capacitance of the detector/cabling/readout system (~hundreds of pF typically), a resistor-capacitor low-pass was formed and, consequently, the square-wave excitation transformed into a series of exponential rises and falls with an RC time constant. The area of the signal trace, rather than the extreme values (maxima and minima) of the signal trace, is chosen to estimate the amplitude of the modulated signal. This is because the changing RC time constant could exceed the modulation period, preventing the modulated signal trace from reaching the plateau region. Thus, the area is a more stable estimation of the modulation amplitude than the extreme values.

As shown in Figure 3.4, a record in the phonon channel is defined as a dataset with ~327 periods of modulated signal (in the same way as a record was written to disk by the DAQ), with the number of periods depending on the record length and modulation frequency chosen in data taking. A data file incorporates all the records during a session of data taking. As a specific case, with a modulation period of 1 ms, a record contains ~327 ms of data, and the data file contains ~ 1 hour of data. As mentioned in Section 2.5.1, the data acquisition for the phonon channel was continuous during data taking.

To calculate the area of the signal trace relative to the voltage offset, first an estimation of the voltage offset of the modulated signal in a record is required. The time-varying voltage offset was inevitably introduced by the readout electronics due to the changing environment and the voltage offset is what the readout scheme using modulated signal was designed to mitigate. In this step, the data points $D[i]$

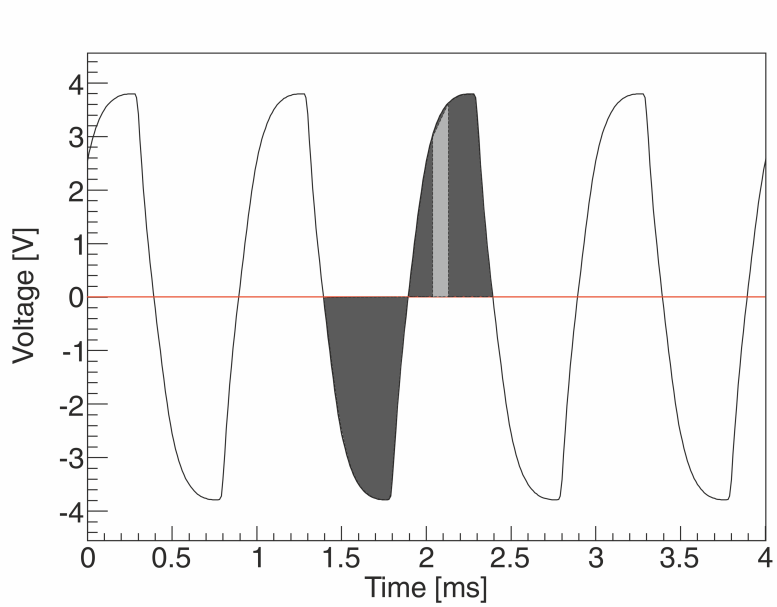

Figure 3.3: A section of the modulated signal in the phonon channel of a CPSD module, with a modulation frequency of 1 kHz. The horizontal red line shows the voltage offset level calculated from the whole signal trace in a record (including the region from 4 ms to 327 ms, which is not shown). The dark grey area between the data points and the offset level in one period is calculated by summing the successive slices like the light grey trapezium between two consecutive data points.

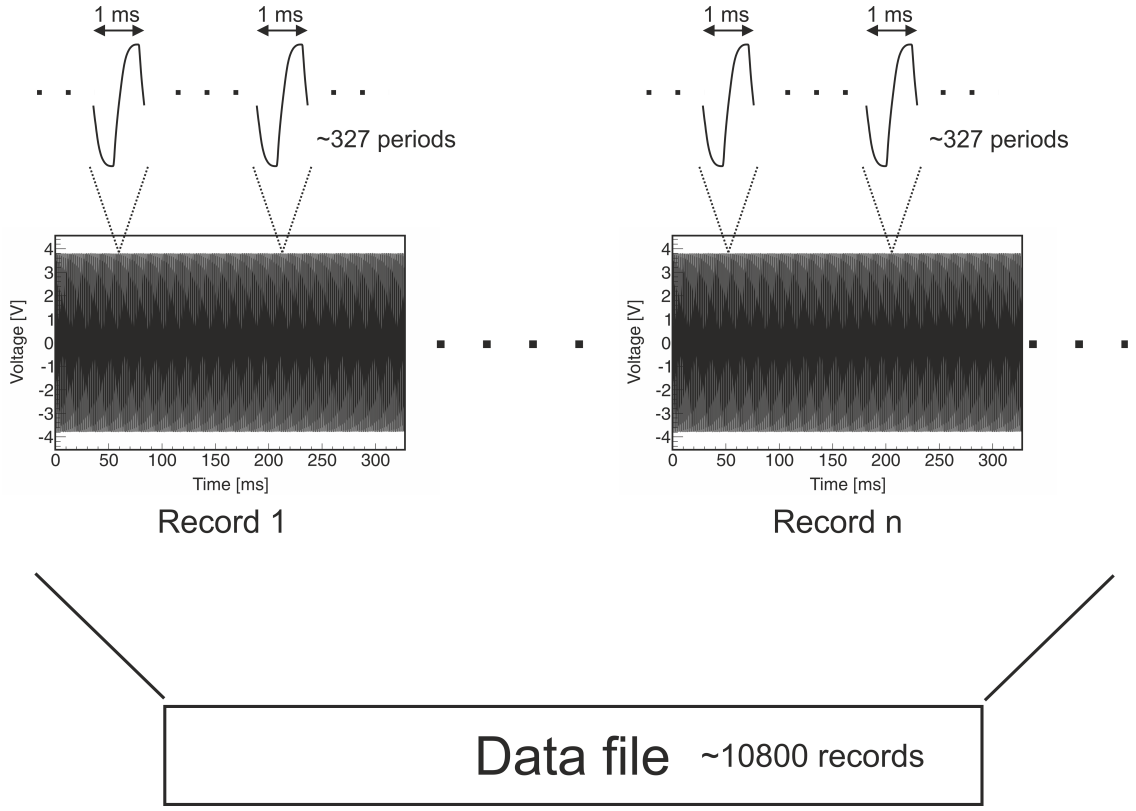

Figure 3.4: Data structure of the phonon channel. As an example, a record contains ~ 327 periods of signal trace, and a data file contains ~10800 records.

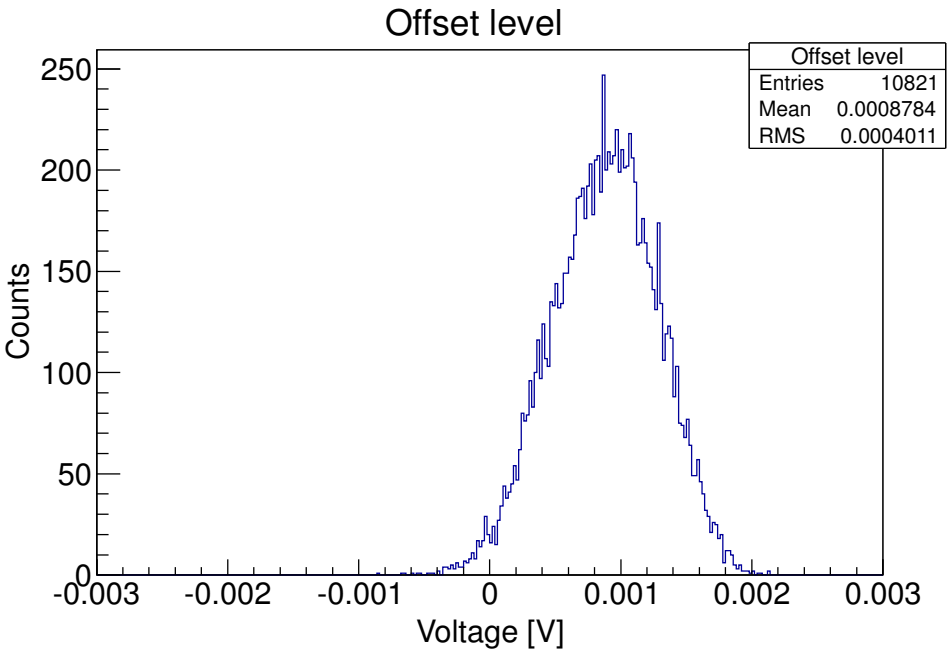

Figure 3.5: Histogram of the offset level estimated from records.

between the signal trace crossing the zero value twice are regarded as one period. These points are averaged to get an estimation of the voltage offset of that period, $A[j]$. However, the potential existence of an energy deposit signal in a record could distort this estimation of the offset by a sudden decrease of the modulation amplitude in a half period at the start of the pulse. Thus, an algorithm is used to select out among one record 10 consecutive $A[j]$ with the smallest variance, and the average of these 10 values of $A[j]$ is taken as the estimate of offset of the record. Because the variance of $A[j]$ in a pulse is bigger than those outside a pulse, choosing the 10 periods with the smallest variance mitigates the concern from the presence of a pulse. As shown in Figure 3.5, the offset estimated is very small (~1 mV), but this step is still important because of the small pulse height (~ mV) from an energy deposit and the precision required.

Since the time interval of two consecutive raw data points in the modulated signal was chosen to be 10 μs, this known quantity is used to estimate the modulation period. The indices of the points when the signal trace crosses the voltage

offset each time are marked. The period T could be estimated from the time difference of these crossing points. $T = 2 \cdot 10 \cdot (i_n - i_1)/(n-1)\,\mu$s , where i_n is the index of the n^{th} switching data point, i_1 is the index of the first switching point. The factor of 2 originates from the fact that two crossings complete one cycle of modulation. The modulation period was a constant in a specific data file.

The amplitude of the modulation signal is calculated by the definite integration of signal trace minus the voltage offset over the modulation period. As shown in Figure 3.3, a trapezoidal rule is employed for the integration of the body of data points in a half period. As shown in Figure 3.6, for the beginning and the end of a half period, because the signal trace crosses the offset level, the trapezoidal rule is not applicable and the triangle area is used in the integration instead. For each half period of modulation, it could form a complete cycle of modulation with the half period before and the half period after it, respectively (Figure 3.7). Thus, in each modulation period, two demodulated data points instead of only one could be extracted, except for the first period and last period of the data file. Because the rising edge of a pulse, resulting from an energy deposit, was fast (from a few ms to about 10 ms), getting twice as many demodulated data points leads to greater detail in the reconstruction of a pulse.

The last section of a record usually cannot form a half period, as the exact duration of a record is 327.67 ms, which is not an integer number of modulation periods. Thus, the data points in the last section of a record are chained to the beginning of the subsequent record and used in the demodulation process in the next record. In this way, the data are bridged between different records and the continuity of the demodulation process is ensured.

A section of the signal after the demodulation process is shown in Figure 3.8, and each data point in it corresponds to the amplitude of modulated signal at that time. All the subsequent analysis is applied to the demodulated data as it

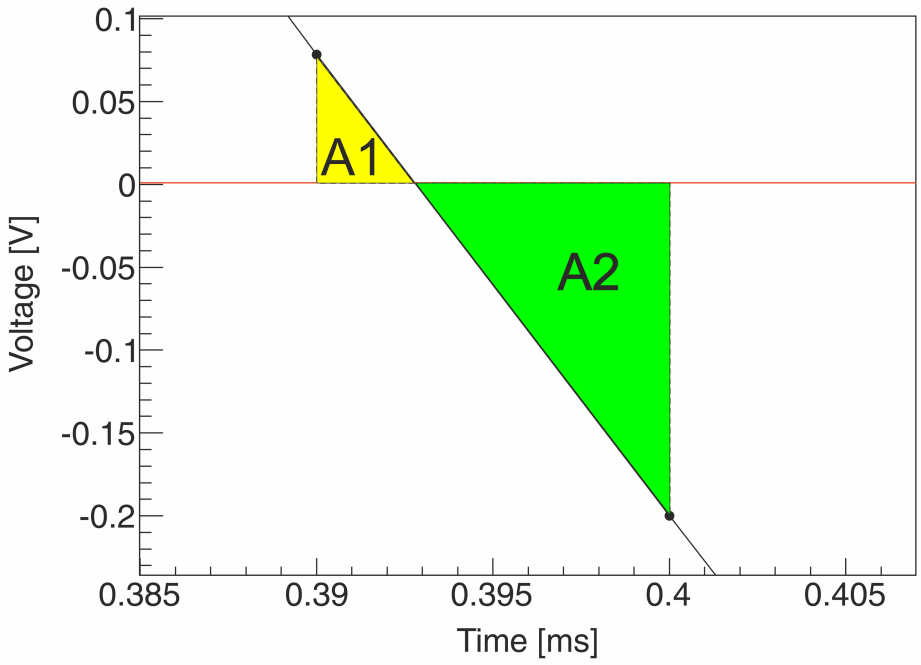

Figure 3.6: A section of the modulated signal in the phonon detector, in which the offset voltage (horizontal red line) is between the voltages of two consecutive points ($x = 0.39$ ms and $x = 0.4$ ms). The usual trapezoidal rule for integration is not applicable in this section, and the triangle area is used for the integration instead. The area A1 (yellow) is assigned to the earlier half period, and the area A2 (green) is assigned to the latter half period.

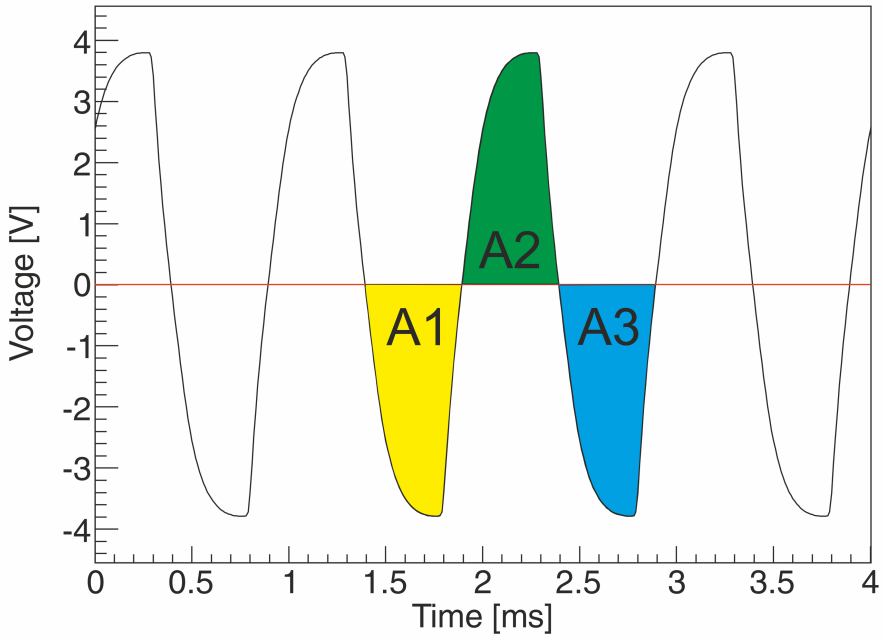

Figure 3.7: A section of the modulated signal in the phonon detector. The areas A1 (yellow) and A2 (green) form a complete period thus a demodulated data point could be calculated from the combination of A1 and A2. Also, A2 (green) and A3 (blue) form another complete period thus another demodulated data point could be calculated from them. In this way, instead of typically only one, two demodulated data points could be calculated from every period of modulation.

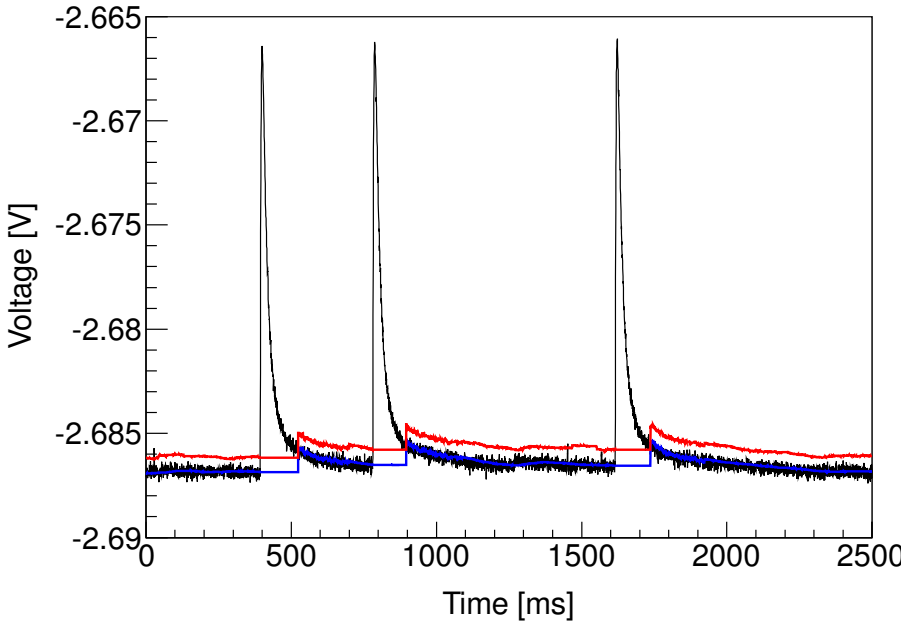

Figure 3.8: The demodulated signal trace after its signal polarity is inverted (dark). The trace in blue shows the estimated baseline. The trace in red shows the threshold for the pulse finding algorithm, which corresponds to baseline plus 4 times standard deviation in the baseline region. It is shown that the baseline and the threshold of the pulse finding algorithm correctly adjust for the change in the signal trace.

contains the information of the resistance of NTD-Ge versus time, which is all needed for event reconstruction in the phonon channel. For ease of discussion, the demodulated signal is inverted so that an energy deposit leads to a pulse with positive amplitude.

3.1.2 Pulse finding

After the demodulation process, a pulse finding algorithm is employed to identify pulses. As discussed in Section 2.5.1, there was no triggering in the firmware level of the phonon channel, thus the pulse finding is the only process to identify energy deposits.

Pulse finding algorithm

The pulse finding algorithm evaluates the demodulated data points one by one in sequence. The time of the current data point under evaluation is $t = 0$ for ease of discussion. The algorithm first calculates the average and the standard deviation of the data values from $t = -100$ ms to $t = -15$ ms, which is designated as the pre-trigger baseline region, as shown in Figure 3.9. The reason for not using the signal trace between $t = -15$ ms and $t = 0$ for baseline calculation, is to avoid the rising edge of a pulse affecting the calculation of the average and the standard deviation of voltage in the pre-trigger baseline region. The average of the pre-trigger baseline region represents the baseline level and the standard deviation of the voltage represents the noise level in the pre-trigger baseline region. The reason for using time instead of the number of data points to define pre-trigger baseline region is that modulation frequency could be changed by the user, but the pulse shape is decided by the physics of the calorimeter. Thus, the modulation frequency (and, consequently, the number of data points) could be changed from data file to data file by the user, but the pulse shape over time remained the same in the same data run.

The criterion of pulse finding is that each of four consecutive data points from $t = 0$ has a larger value than the average plus 4 times the standard deviation of the voltage in the pre-trigger baseline region. 4 times the standard deviation of the voltage above baseline level as the threshold is chosen in order to stay above the noise and further optimisation to lower the threshold may be possible by applying a low-pass filter first. Using 4 times the standard deviation of the voltage above baseline level instead of a fixed value as threshold level is to adjust for the changing noise environment usually present when operating a calorimeter. Both the baseline level and the noise level slowly changed during data taking, due to the slowly changing environment, such as the liquid helium level in the main bath of the

cryostat, the operation of pumps and the changing room temperature. Requiring the values of four consecutive data points instead of one data point larger than the threshold is because the pulse from a real energy deposit in the calorimeter usually has a plateau region (see Figure 3.16) and it decays much more slowly than a noise spike. Consequently, requiring four consecutive data points instead of one data point could select true pulses while avoiding noise spikes. If the triggering condition is not met, the algorithm moves to the next data point and calculates the average and the standard deviation of voltage in the relevant pre-trigger baseline region (now moving one point forward) with the same rules and it evaluates the trigger condition again. If the criterion is met, the algorithm finds a pulse. The algorithm then searches for the maximum point in the pulse by evaluating the values of the data points in sequence from $t = 0$ and it records the timestamp of the maximum point as the timestamp of the pulse. The algorithm searches for the maximum point until a data point in the signal trace returns to below the average plus 3.5 times the standard deviation of voltage in the pre-trigger baseline region, or there has been no update of the timestamp of the maximum location for 300 ms, whichever comes first. The end of maximum point search also marks the start of the searching for the next pulse. The interval between 100 ms before the maximum point and 300 ms after the maximum point is defined as the range of the pulse for further investigations and operations. The timestamp of the maximum point instead of the natural onset of the pulse is adopted as the timestamp of the pulse because the presence of the noise makes it difficult to determine the onset point precisely. However, in contrast, the maximum point is very well defined. The time difference between the maximum point and the natural onset of the pulse is similar between different pulses because it is determined by the physics of the calorimeter, thus the timestamp of the maximum point is a good representation of the timestamp of the pulse.

If the signal amplitude returns to below the baseline level plus 3.5 times the standard deviation of voltage in the baseline region, before 300 ms following the maximum point of a pulse, the signal trace is still at the decaying baseline of the earlier pulse (Figure 3.9) when the search for a new pulse begins. For the data point under consideration (the first point that drops below the average plus 3.5 times the standard deviation of voltages in the pre-trigger baseline region of the old pulse), which is now the new $t = 0$, the originally defined $t = -100$ ms to $t = -15$ ms interval would incorporate a region of decaying baseline from the old pulse. Incorporating decaying baseline would incorrectly elevate the estimated baseline level and the standard deviation of voltages in the pre-trigger baseline region of the new pulse. To address this issue, if the point under evaluation for pulse searching is in the region of 300 ms following the maximum point of an old pulse, the pre-trigger baseline region for the new pulse is shortened to $t = -25$ ms to $t = -15$ ms for the estimation of baseline level. The standard deviation of voltage in the pre-trigger baseline region is replaced by that of the old pulse (noise level does not change in hundreds of ms scale). As a result, the baseline level and the threshold level follows the decaying baseline closely (shown as the blue line and the red line in Figure 3.9).

Pulse finding efficiency

To investigate the pulse finding efficiency, the pulse finding algorithm is applied to a group of simulated pulses. The simulated pulses are generated by scaling the template pulse of 122 keV (Section 3.1.4) to different pulse energies, with the baseline noise added. The simulated pulses are generated separately for the $CaMoO_4$ and $CaWO_4$ modules, as these two modules have different pulse heights and noise levels. Figure 3.10 shows the pulse finding efficiency with respect to the pulse energy. Because of the lower noise level and higher pulse heights, the phonon

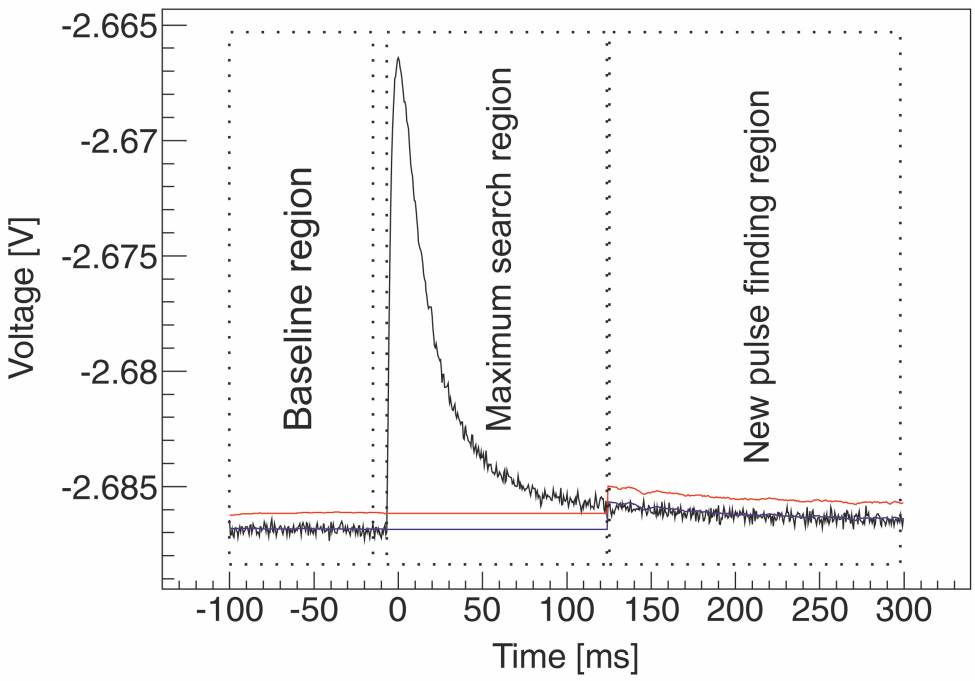

Figure 3.9: An example pulse from a 122-keV γ quantum measured in the phonon channel of the CPSD module with $CaMoO_4$ as the absorber. The signal trace is the solid black line. The estimated baseline level is the blue line. The calculated threshold for the pulse finding algorithm is the red line. The signal trace in the $t = -100$ ms to $t = -15$ ms region is the designated pre-trigger baseline region, and signal in this region is used for the estimation of baseline level and the noise level. The region between the signal trace surpassing the baseline level plus 4 times the standard deviation of voltage in the pre-trigger baseline region and the signal trace subsiding to below the baseline plus 3.5 times the standard deviation, is the designated maximum search region. The period after the maximum search region is the start of the searching for the new pulses.

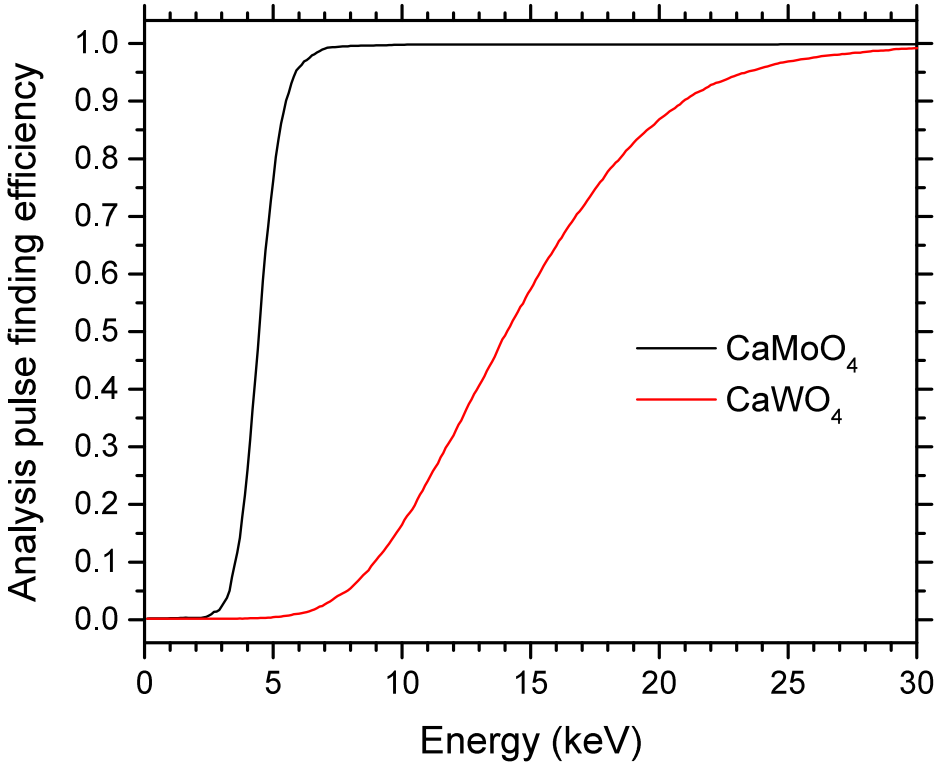

Figure 3.10: The analysis pulse finding efficiencies versus the pulse energy, for the phonon channel of the CPSD with $CaMoO_4$ and $CaWO_4$ as the absorber, respectively. The pulse finding efficiency is obtained by applying the pulse finding algorithm to simulated pulses with baseline noise. The statistical errors are ~2%.

channel of the $CaMoO_4$ module has higher pulse finding efficiency than that of the $CaWO_4$ module. The pulse finding efficiency can potentially be improved further, especially in the low-energy region, which is important for low-mass WIMP searches. However, given the main goal of this experiment is to characterise the detector modules with a ^{57}Co source, the pulse finding algorithm is sufficient for the goal of this stage.

After the pulse finding process, the maximum point minus the baseline level of a pulse gives the first estimation of the pulse height and a preliminary pulse height spectrum is constructed (Figure 3.11). This estimation is preliminary mainly

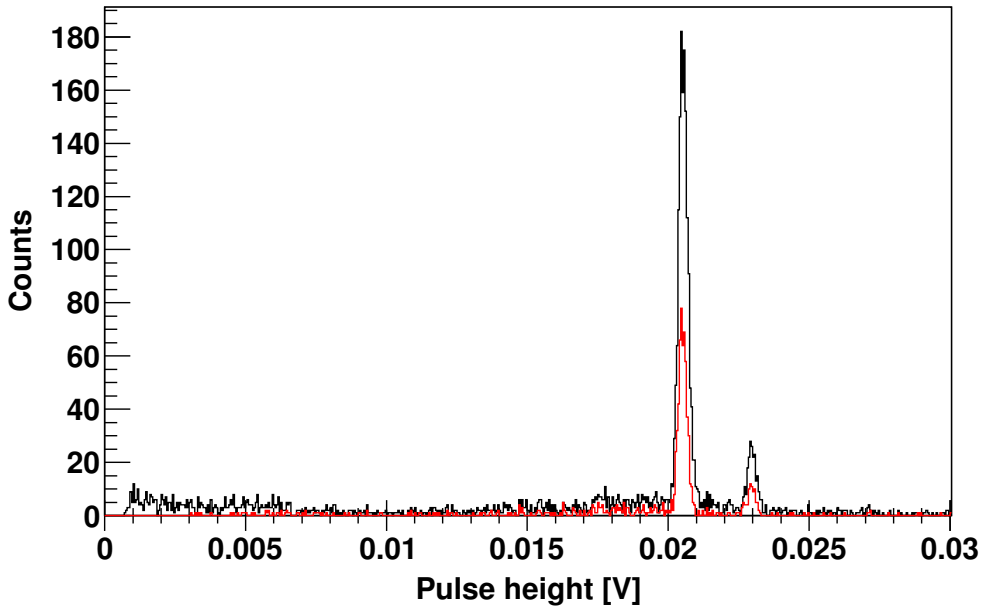

Figure 3.11: Preliminary pulse height spectra in the phonon channel of the CPSD module with $CaMoO_4$ as the absorber, before (dark) and after (red) the data quality cuts. The pulse height is estimated by subtracting the pre-trigger baseline level from the maximum value of the pulse. The pulses with pulse height around 0.0205 V correspond to 122-keV energy deposits, and the pulses with pulse height around 0.023 V correspond to 136-keV energy deposits.

because the maximum point value is plagued by the electronic noise in a single data point.

3.1.3 Data quality cuts

3.1.3.1 Contaminated pulses with poor pulse height estimation

Several effects could make the pulse height estimation incorrect, which means that the estimated pulse height calculated by using the maximum minus the baseline level would be unusually far from the true pulse height. Also, if the contaminated pulses are selected to construct the template pulse, they could distort the template pulse.

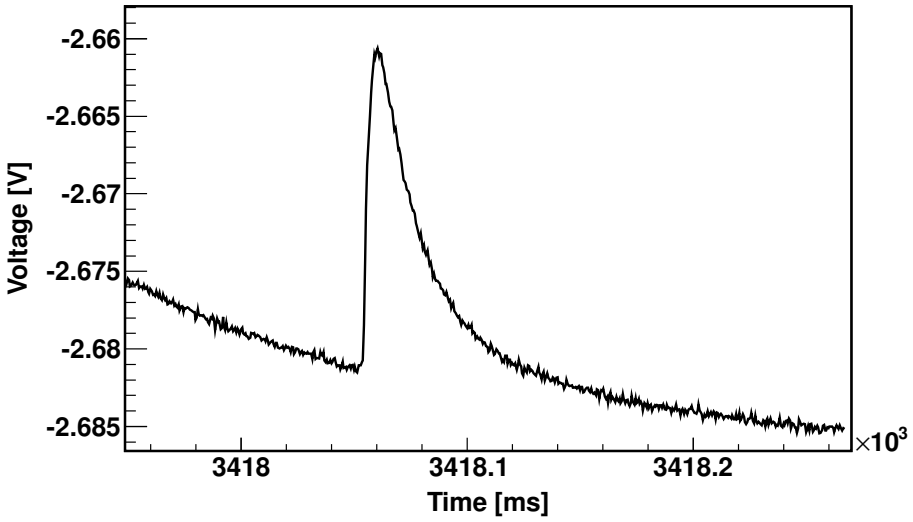

Figure 3.12: An example of a pulse with a decaying baseline measured in the phonon channel of the CPSD module.

Decaying baseline

As shown in Figure 3.12, if another pulse happened on the tail of the previous pulse, the baseline of the new pulse would decay and it is then difficult to estimate the new pulse height correctly. The decaying baseline is a more serious problem after a high energy (MeV) energy deposit, e.g. a cosmic muon, as it takes longer for the calorimeter to return to the base temperature.

Pile-up

Sometimes overlapping with the decaying baseline effect, the pile-up effect is two or more energy deposits happen very close to each other in time (Figure 3.13). In this case, the pulse height estimation of at least one pulse involved is incorrect, or the second pulse is not identified by the pulse finding algorithm. Due to shielding by the thick copper walls of the detector holder, the pile up rate was relatively small. Deterioration of the energy resolution was still observed, especially with a relatively high rate of γ-rays from the ^{57}Co source (~1 Hz) and the slow decay time of the calorimeter (~25 ms). The pile-up effect would be negligible in dark

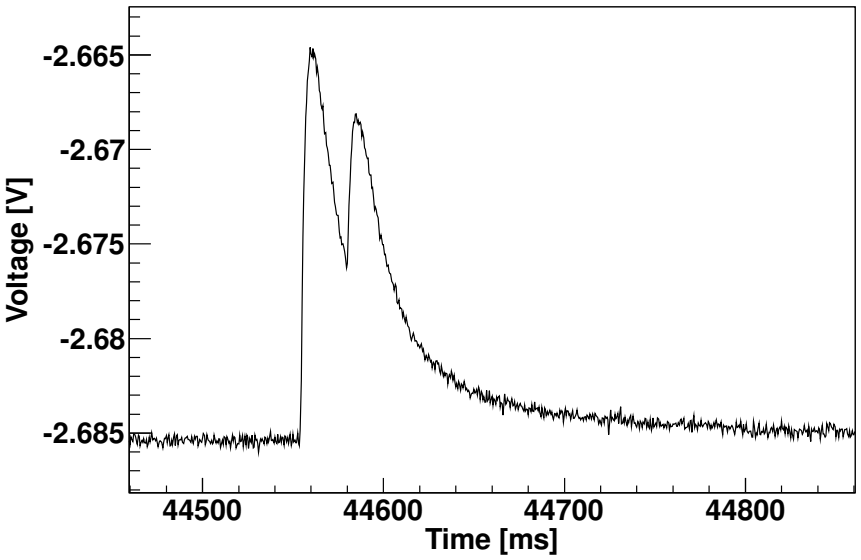

Figure 3.13: An example of pile-up pulses measured in the phonon channel of the CPSD module.

matter experiments but significant in the calibration with a radioactive source.

3.1.3.2 Data quality cuts

After the pulse finding process, an array of candidate pulses are found and, subsequently, various data quality cuts are employed with the aim of constructing a good template pulse. Because a single event with pile-up pulses or decaying baseline could already distort the template pulse constructed significantly, data quality cuts are necessary to ensure that the template pulse constructed is free from those distortions and that the template pulse is a true representation of the standard response of the phonon detector to energy deposits.

The data quality cuts discussed in this section are used for selecting pulses for the construction of the template pulse. However, they are not used for constructing the final energy spectrum due to their low efficiency (~30%). It is found that the goodness of fit for the template pulse against candidate pulses from the data is an effective way of identifying and discarding non-standard (contaminated)

calorimeter events with a higher efficiency (~50%).

The procedure of data quality cuts is as follows: First, find a parameter that indicates the difference between good pulses and contaminated pulses; Second, find the distribution of that parameter for uncontaminated pulses (usually Gaussian). Third, set a critical value for the parameter above or below which pulses will be flagged as the contaminant type. The critical value can be some factor times the standard deviation around the mean in the Gaussian distribution.

Parameters of data quality cuts investigated in this section are as follows and the order in which these parameters are presented is the same as data quality cuts are performed.

Baseline gradient (BG)

The pre-trigger baseline region is defined from 100 ms before the pulse maximum to 15 ms before the pulse maximum. The decaying baseline has a much larger value in baseline gradient than the one resulting from noise. The baseline gradient also identifies potential periods over which the baseline was rising or falling due to the short-term temperature fluctuation, which is undesirable if present.

Voltage ratio parameter (R_D) [158]

The maximum of a pulse is defined as the principal maximum. The voltage difference parameter, D_{max}, is defined as the largest voltage difference other than the pulse in the principal maximum, as shown in Figure 3.14. The voltage ratio parameter $R_D \equiv D_{max}/\sigma_{baseline}$, where $\sigma_{baseline}$ is the standard deviation of voltage in the pre-trigger baseline region. The algorithm is detailed in Reference [158]. In the presence of pile-up, D_{max} becomes very large relative to the standard deviation of voltage in the pre-trigger baseline region. D_{max} is comparable to the noise level without pile-up, as in this case D_{max} is only the maximum point in noise minus

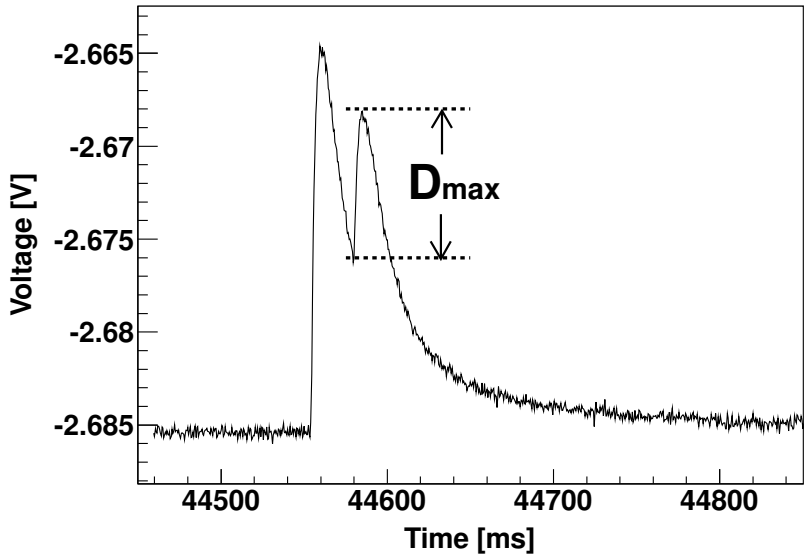

Figure 3.14: Illustration of the voltage ratio parameter D_{max} calculated from an event with two pile-up pulses. The principal maximum is at around 44560 ms in the record.

the minimum point in noise. So R_D could be used to flag pile-up pulses or any large temperature fluctuation in a short time.

Rise time (RT)

The rise time is defined as the time during which a pulse rises from 1/e of the pulse height to the maximum. Contaminated pulses which escape the initial cuts can be identified by an abnormally short or long rise time.

Right baseline minus left baseline (RML)

In an uncontaminated pulse, the signal will exponentially decay back to the baseline level after a particle interaction. Hence, in the region to the right of the pulse after the signal decay, the signal value should be similar in the region before the start of the pulse in an uncontaminated pulse. The RML should be close to zero or slightly above zero, taking into account noise and the signal pulse might not decay to baseline level but close to it. However, in a decaying baseline or other

contaminated pulse types, the RML may be far from zero. Here the left baseline is the same as the pre-trigger baseline and the right baseline is defined as the region between 215 ms after the maximum point to 300 ms after the maximum point.

Standard deviation of voltage in baseline region ($\sigma_{\mathbf{baseline}}$)

The standard deviation of voltage in the pre-trigger baseline region is used to identify especially noisy baselines around which the pulse shape or the baseline level measurement becomes unreliable because of the abnormally high noise level.

Integral over pulse height (IOPH)

Integral is defined as the signal trace minus the pre-trigger baseline level integrated over time between 15 ms before the maximum point and 300 ms after the maximum point. As the calorimeter is a linear system in the energy region of interest, the integral over pulse height gives information about the pulse shape. For example, particles hitting the NTD-Ge directly instead of the absorber give different pulse shapes compared to the majority of pulses originating from particles hitting the absorber due to different thermalisation processes involved [103].

Decay time (DT)

The decay time is defined as the time during which the pulse decays from maximum to 1/e of pulse height. Contaminated pulses may be identified by an abnormally short or long decay time.

Results of data quality cuts

As mentioned, the aim of the data quality cuts is to produce a good template pulse. The effects on the template pulse from choosing different critical values are investigated. Figure 3.15 shows that if there are no data quality cuts, the

constructed template pulse has some deviations from a signal pulse with an exponential decay back to the baseline, as would be expected from the thermal model of the calorimeter. Data quality cuts improve the shape of the template pulse, by removing these deviations. In Figure 3.15, 2 Sigma means the critical values chosen in this scenario of the data quality cuts are $\mu_P \pm 2\sigma_P$, where μ_P and σ_P are the mean value and the standard deviation of the Gaussian distribution of the parameter under investigation, respectively. In general, any pulses with a value of the parameter outside the range $[\mu_P - 2\sigma_P, \mu_P + 2\sigma_P]$ are flagged as the contaminant type. The definition for 1 Sigma scenario is similar. Figure 3.15 shows that the difference in the resulting template pulse between 2 Sigma and 1 Sigma scenarios is negligible, which indicates the resulting template pulse is not sensitive to the critical values chosen in this range. As a result, critical values corresponding to the scenario of 2 Sigma cuts are chosen for data quality cuts finally used.

As shown in Table 3.1, the reduction of the pulses by the data quality cuts is decreasing in general. For example, in the $CaMoO_4$ module, the first cut reduces ~29% of the original pulses, while the second cut reduces ~22% of the original pulses, which is ~28% of the pulses left after the first cut. The later cuts reduce far less. It indicates that the data quality is improved by the cuts.

3.1.4 Template pulse construction

After the various data quality cuts in Section 3.1.3, a preliminary pulse height spectrum in the phonon channel could be constructed from the pulses remaining, as shown in Figure 3.11. The pulse height is estimated simply by the difference between the maximum and the pre-trigger baseline level of the pulse. From this preliminary energy spectrum after various data quality cuts, pulses for the construction of the template pulse are selected from the bin with the maximum bin

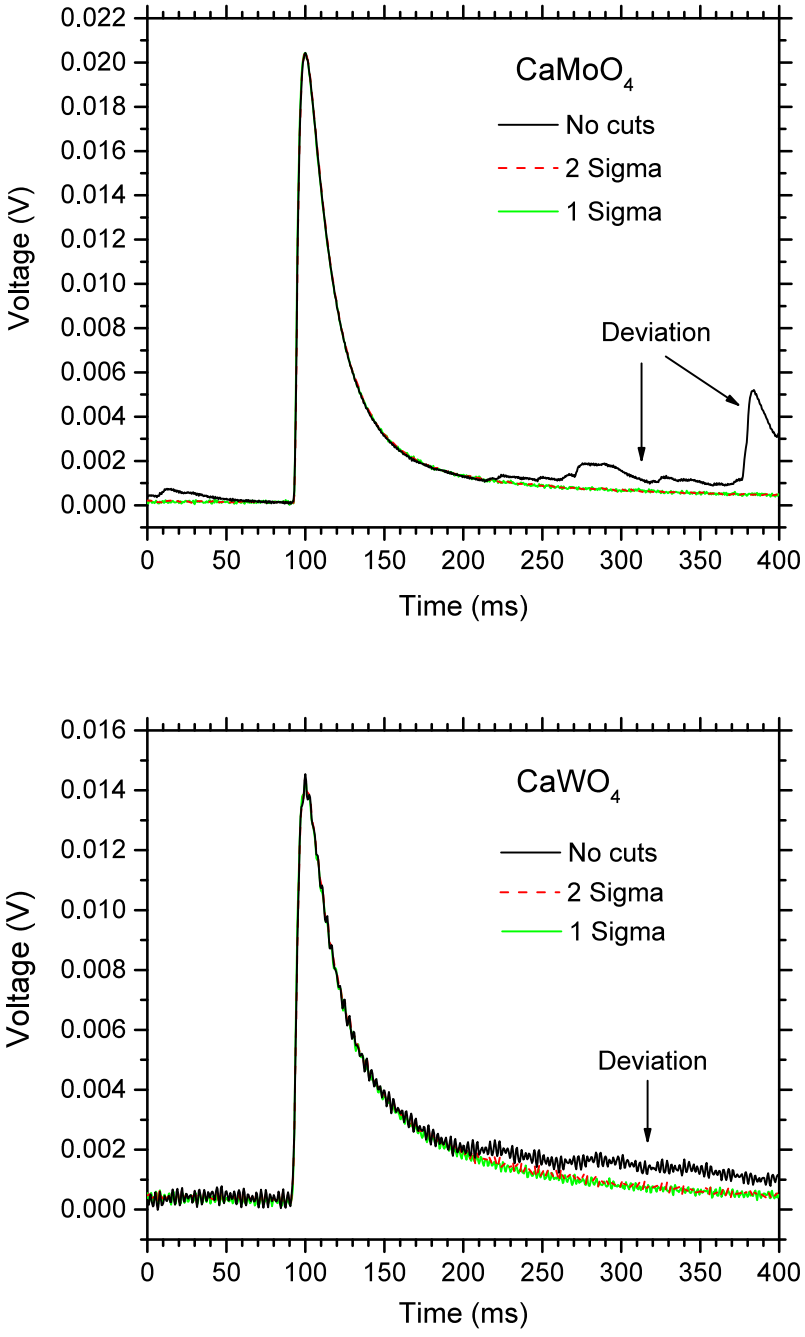

Figure 3.15: The template pulses constructed from three data quality cut scenarios (no cuts, 2 Sigma cuts and 1 Sigma cuts) for the phonon channel of the CPSD with $CaMoO_4$ (top) and $CaWO_4$ (bottom) as the absorber, respectively. 2 Sigma means the critical values chosen for the cuts are $\mu_P \pm 2\sigma_P$, where μ_P and σ_P are the mean value and the standard deviation of the Gaussian distribution of the parameter under investigation, respectively. The definition for the scenario of 1 Sigma cuts is similar.

Cut parameter	Percentage of the original pulses (100%) left after the cut	
	$CaMoO_4$	$CaWO_4$
BG	71%	77%
R_D	49%	54%
RT	45%	51%
RML	39%	45%
$\sigma_{baseline}$	37%	43%
IOPH	33%	40%
DT	31%	32%

Table 3.1: Percentage of the original pulses (as 100%) from pulse finding process left after different cuts for the phonon channel of the CPSD with $CaMoO_4$ and $CaWO_4$ as the absorber, respectively. The sequence of cut parameters in the table is the same as that of the cuts performed in the analysis.

contents. Because the calibration source ^{57}Co predominantly emits 122-keV γ photons, those selected pulses correspond to the 122-keV energy deposits. After removing the baseline from those pulses by subtracting the average voltage in the pre-trigger baseline region from the voltage of the signal trace, the template pulse is then constructed by the average of those pulses. The template pulse corresponds to the standard response of the phonon detector to a 122-keV γ photon.

Because the alignment of the pulses in the averaging process is by referring to their respective maximum point, the maximum point of the template pulse is biased up as shown in Figure 3.16. The reason for this bias is as follows. For a specific data point in a pulse not near the maximum, the chances for that point to fluctuate up or down due to electronic noise are equal, thus the averaging process in template pulse construction is unbiased. However, for those points near the peak of the pulse in the plateau region, because their values are close to each other, only those that fluctuate up become the maximum points in the pulses. The averaging process for template pulse construction only picks up the fluctuated-up point for the maximum point in the template pulse, because the different pulses that are used to construct the template pulse are aligned by the

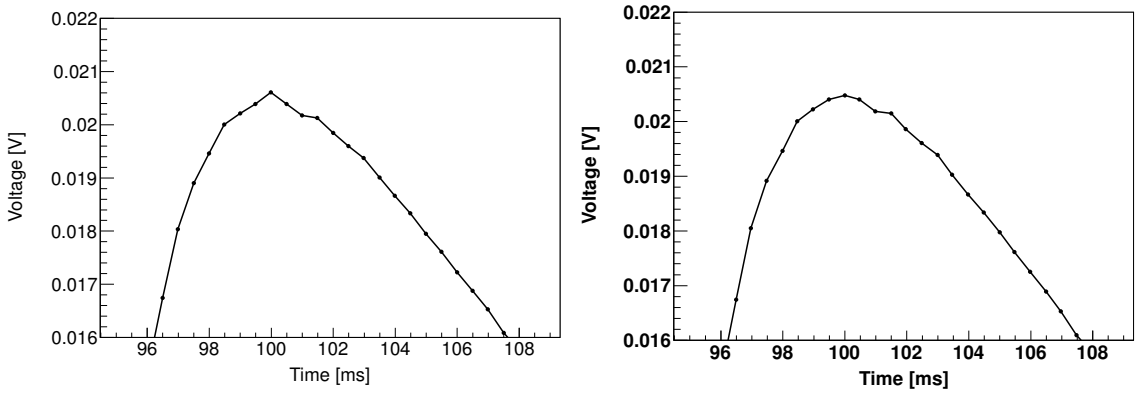

Figure 3.16: The plateau region of the constructed template pulse. Left, uncorrected for the positive bias at $t = 100$ ms point (maximum point). Right, after manually corrected for the positive bias at the $t = 100$ ms point (maximum point). There are a few points next to the maximum point with similar voltage values, which support the choice of 4 consecutive points above threshold level as the trigger condition in the pulse finding process (Section 3.1.2).

maximum point. That is why the template pulse has such a positive bias. This positive bias artefact is manually corrected with the result of a smoothed pulse shape as shown in Figure 3.17.

After the template pulse is constructed, a function described by Equation 3.1 is fitted to the template pulse to get an analytical description of the template pulse for later steps.

$$V(t) = \begin{cases} a + bt + ct^2, & t < t_1 \\ a + bt + ct^2 + A_1 \exp\left(\frac{t}{\tau_1}\right) + A_2 \exp\left(\frac{t}{\tau_2}\right) + A_3 \exp\left(\frac{t}{\tau_3}\right), & t > t_1, \end{cases} \tag{3.1}$$

where $V(t)$ is the voltage of the signal trace with respect to time t, a is the baseline level, b is the baseline gradient, and c is the baseline quadratic factor, A_1, A_2 and A_3 are the amplitudes of the exponential with τ_1, τ_2 and τ_3 as time constants, respectively, and t_1 is the timestamp of the pulse start. Since the construction of the template pulse is from those pulses with baseline removed, the baseline value

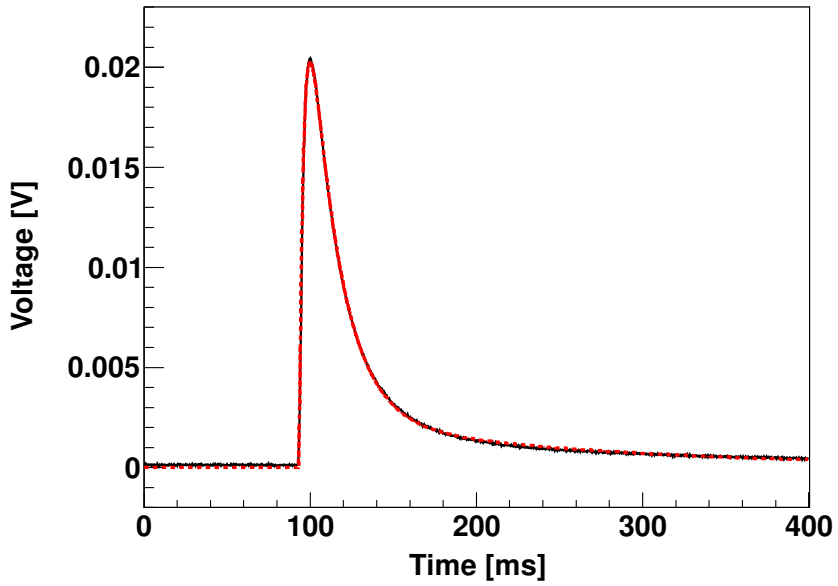

Figure 3.17: The template pulse (in black solid line) constructed from 122-keV energy deposits measured by the phonon detector in the CPSD module with $CaMoO_4$ as the absorber. A function described in Equation 3.1 is fitted to the template pulse trace and the fitted function is in dotted red line.

should be zero. There might still be a gradient term and a quadratic term for the baseline, so setting the baseline as $a + bt + ct^2$ is a preemptive measure and those three factors are found to be very close to zero.

3.1.5 High-pass filter

A high-pass filter is employed in this step to improve the signal-to-noise ratio of the data. In the view of frequency analysis, the signal of the pulse has a specific frequency distribution and the noise has a different frequency distribution. A digital filter could be used to exploit this difference to improve the signal-to-noise ratio, which is critical to improving the energy resolution of the detector. The digital filter is used to attenuate the data in a specific frequency range, purposely in the frequency range where the noise dominates in the data. A two-pole Butterworth high-pass filter with variable cutoff frequency is applied to both the

candidate pulses and the template pulse. In implementing the high-pass filter, an infinite impulse response (IIR) digital filter is chosen. The algorithm first generates the feed-forward coefficients $A[0]$, $A[1]$, $A[2]$ and feed-backward coefficients $B[1]$, $B[2]$ of the two-pole Butterworth high-pass filter, according to the cutoff frequency selected. The filtered data point $y[i]$ is generated according to:

$$y[i] = A[0] \cdot x[i] + A[1] \cdot x[i-1] + A[2] \cdot x[i-2] + B[1] \cdot y[i-1] + B[2] \cdot y[i-2], \tag{3.2}$$

where $x[i]$ is the original data point before the filter is applied.

The template pulse in the analytical form is sampled at the same frequency as the raw data because digital filters are only applicable to the discrete points. Then the points in the template pulse go through the IIR filtering process. The resulting template pulse after the high-pass filtering is shown in Figure 3.18.

The IIR filtering process is then applied to the raw signal trace. Because the pulse finding process in Section 3.1.2 records the timestamps of the pulses, and the high-pass filter does not change the time locations of the pulses, candidate pulses after being filtered could be located by the original pulse timestamp. The candidate pulse after filtering is shown in Figure 3.18.

The optimal cutoff frequency is determined by comparing how the cutoff frequency affects the energy resolution and it is found that cutoff frequencies of 7 Hz for the $CaWO_4$ module and 6 Hz for the $CaMoO_4$ module produce the best energy resolutions (Figure 3.19).

3.1.6 Template pulse fit

At this point, filtered candidate pulses as well as a filtered template pulse have been constructed (Figure 3.18). The next step is to use the filtered template

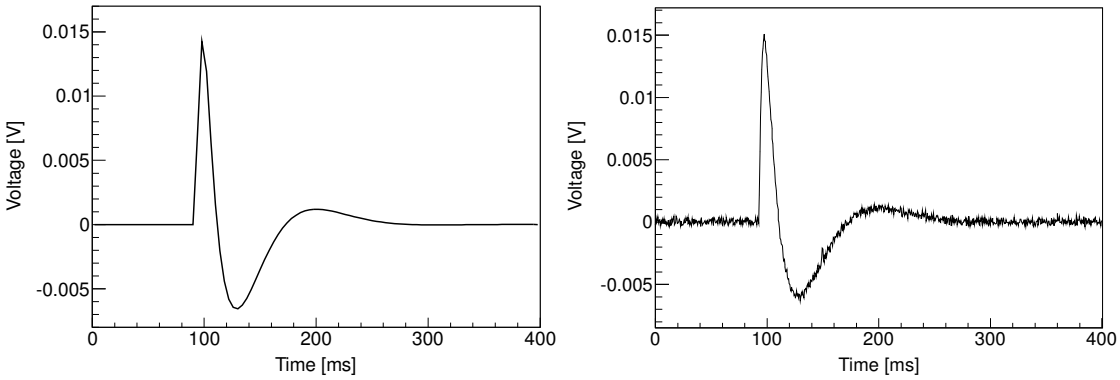

Figure 3.18: The template pulse (left) and a candidate pulse (right) with 122 keV energy deposit measured in the phonon channel of the CPSD module with $CaMoO_4$ as the absorber, after a two-pole Butterworth high-pass filter with the cutoff frequency of 6 Hz is applied to them.

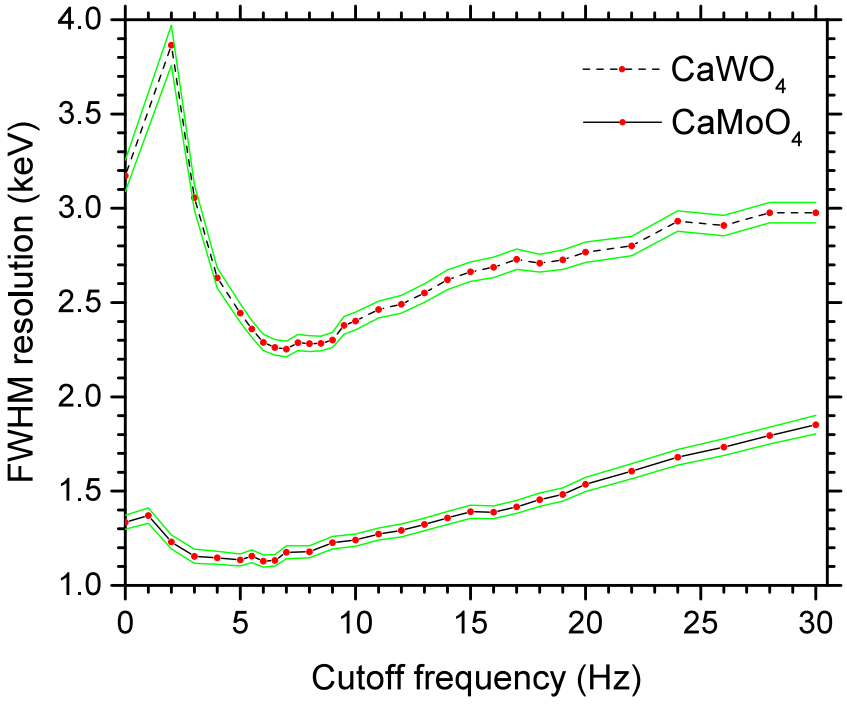

Figure 3.19: The FWHM energy resolutions versus the cutoff frequency of the two-pole Butterworth high-pass filter, for the phonon channel of the CPSD with $CaMoO_4$ and $CaWO_4$ as the absorber, respectively. The red dots represent the sampling points, and the black lines between the red dots are just for guidance. The green lines on the upper and lower sides of the black lines represent the statistical error of the FWHM energy resolution.

pulse to fit the filtered candidate pulses. At this step, all the pulses identified by the pulse finding algorithm (Section 3.1.2) before the data quality cuts (Section 3.1.3) are used. After the high-pass filter process in Section 3.1.5, the template pulse consists of discreet points, due to the requirement of digital filters. To be used as a fitting function, the values between the discrete points in the template pulse are generated using a linear interpolation. Template pulse fitting means the pulse shape is fixed, and the only two fit parameters are the amplitude factor and the time offset. Two variables in the fitting result have been examined and compared to find the best representation of the amplitude. One is the amplitude factor resulting from the fitting and the other one is the maximum point value of the fitted pulse. It is found that the amplitude factor is more precise than the maximum point value, but only by an insignificant margin. Following the template fit, the Chi-squared of the fit is used for a goodness of fit cut. This is the only cut used in selecting the pulses for the final energy spectrum, as all the previous data quality cuts were only used for improving the construction of the template pulse. Compared to the previous data quality cuts (~30% pulses retained) in Section 3.1.3, the goodness of fit (Chi-squared) cut has higher efficiencies (~53% pulses retained for $CaMoO_4$ and ~50% for $CaWO_4$) while producing better energy resolution (FWHM resolution <1 keV at 122 keV energy for $CaMoO_4$). As the bin with the largest count in the pulse height spectrum corresponds to 122 keV and the calorimeter system is found to be a good linear system, the pulse height is then translated to the recoil energy measured in the detector. The translation of pulse height to recoil energy is the final step of extracting the energy spectrum for the phonon channel.

The final energy spectra for the phonon detectors are shown in Figure 4.1 for $CaMoO_4$ and Figure 4.3 for $CaWO_4$ in Section 4.1.

The ~50% reduction in the number of pulses by the goodness of fit (Chi-

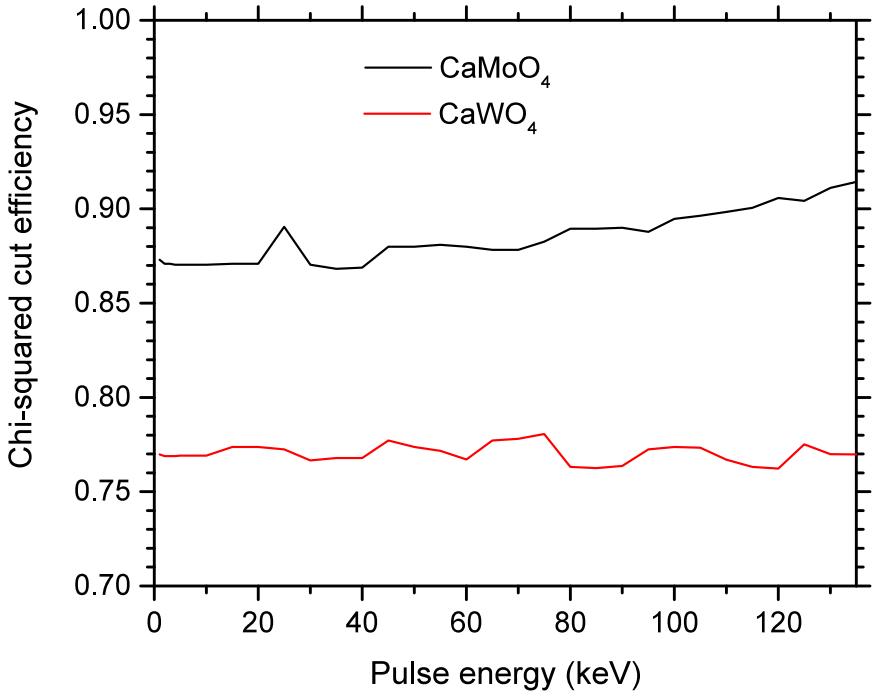

Figure 3.20: The efficiencies of Chi-squared (goodness of fit) cut in the phonon channel of the CPSD with $CaMoO_4$ and $CaWO_4$ as the absorber, respectively. This efficiency is obtained by applying the high-pass filter and the template pulse fitting algorithm to simulated pulses. The statistical errors are ~2%.

squared) cut is a superposition of the presence of contaminated events and the intrinsic efficiency of the goodness of fit cut. The intrinsic efficiency of the cut is defined as the ratio of the number of uncontaminated pulses remained after the cut to the original number of uncontaminated pulses. To estimate the intrinsic efficiency of the cut, the analysis algorithm is applied to simulated pulses. The generation of simulated pulses is discussed in Section 3.1.2. As shown in Figure 3.20, Chi-squared cut efficiency is around 87%–90% for $CaMoO_4$, and it is ~77% for $CaWO_4$. The Chi-squared cut efficiency shows only a very weak (in the $CaMoO_4$ case) or no (in the $CaWO_4$ case) dependence on the pulse energy. The reason for the weak dependence on the pulse energy is that the Chi-squared of the fit is mainly decided by the noise level but not the pulse height.

3.1.7 Baseline energy resolution

After the template fit, the baseline energy resolution is estimated from the template pulse fitted to the data. The baseline energy resolution is defined as the energy resolution of the detector when the deposited energy is zero. Baseline energy resolution is an important parameter to characterise the detector, as it describes what the detector energy resolution is for low energy deposit.

The baseline resolution of the heat detector is estimated by using the same procedure of extracting the pulse heights in recoil events, but the procedure is applied to the periods of the signal trace that are not triggered by the pulse finding algorithm in Section 3.1.2, corresponding to a baseline period without recoil events. The procedure of the estimation for baseline energy resolution includes a high-pass filter to the signal trace as well as to the template pulse (Section 3.1.5), and afterwards a template pulse is fitted to all the periods which are at least 400 ms away from any triggered pulses. The fitted energy spectrum of the baseline region is a Gaussian distributed with the mean around zero and the full-width-half-maximum of the Gaussian is then the baseline energy resolution.

The baseline energy spectrum is shown in Figure 4.2 for $CaMoO_4$ data and Figure 4.4 for $CaWO_4$ data in Section 4.1.

3.1.8 Summary of phonon channel analysis

In summary, as shown in the Figure 3.21, the phonon channel analysis goes through the following steps: First, the raw data gets demodulated and then a pulse finding algorithm identifies and locates all the pulses. Afterwards, an array of data quality cuts are applied to the candidate pulses identified in the pulse finding process, and the pulses that remain after the data quality cuts are averaged to construct a template pulse. All the candidate pulses identified in the pulse finding process and the template pulse both go through the same high-pass filter

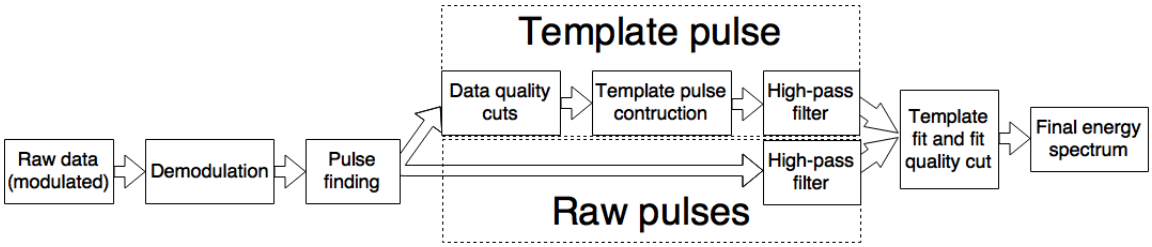

Figure 3.21: A flow diagram showing the different steps in the phonon channel analysis, which is from the modulated raw data to the final energy spectrum.

and then the filtered template pulse is fitted to the filtered pulses. After a single cut based on the fit quality, the final energy spectrum of the phonon detector is produced.

3.2 Light channel analysis

The main goal of the analysis of data from the light channel is to count the number of photons in a scintillation event precisely and accurately, as the difference in light yield (number of photons per unit deposited energy) is used for event type discrimination (ER versus NR). As described in Section 2.5.2, two modes of data taking were employed for the light channel: a fixed-length mode for the $CaWO_4$ data and a "dead-time free" mode for the $CaMoO_4$ data. Unlike the phonon channel, the difference in the DAQ modes in the light channel means the analysis is significantly different between the $CaWO_4$ data and $CaMoO_4$ data.

3.2.1 $CaMoO_4$ data with "dead-time free" DAQ mode

For the "dead-time free" mode for the $CaMoO_4$ data, because of the trigger rules described in Section 2.5.2, each record usually contains one or two photoelectron pulses and a very short (~150 ns) pre-trigger region (Figure 2.9). The general strategy of the analysis is to group the records into scintillation events according to their timestamps first, then estimate the baseline voltage in each scintillation

event from all the records in that group. With the baseline voltage established, the photon counting algorithm estimates the number of photons in each record. Thus, the number of photons detected in a scintillation event is the sum of the number of photons from all the records in that scintillation event. Details of each analysis step are described below.

3.2.1.1 Photon grouping

As the first step, the algorithm groups the records into scintillation events according to the timestamps of the records. The algorithm evaluates the records one by one in sequence and the grouping rule is as follows: if the difference of timestamps in two consecutive records is no larger than 7 ms, these records are assigned to the same scintillation event; if their time difference is larger than 7 ms, the earlier record marks the last photon in the earlier scintillation event and the later record is considered to be the first photon in a new scintillation event. This grouping rule also takes care of dark counts, as they appear isolated in time and are usually separated by more than the time constants (like the 7 ms here) chosen for grouping scintillation events. The grouping criterion of 7 ms was chosen because the $CaMoO_4$ scintillation slow decay time constant is 3.41 ms (Table 4.2). It has been checked that this choice is suitable using simulations of scintillation events and dark pulses (Section 3.2.1.5) and the study of the energy resolution of the scintillation events. The timestamp of the first record in a scintillation event is taken as the timestamp of that scintillation event.

3.2.1.2 Baseline estimation

The algorithm then estimates the pre-trigger baseline voltage of individual records. The pre-trigger baseline voltage of a record is estimated as the average voltage value of N consecutive data points with the least variance (the value N is chosen

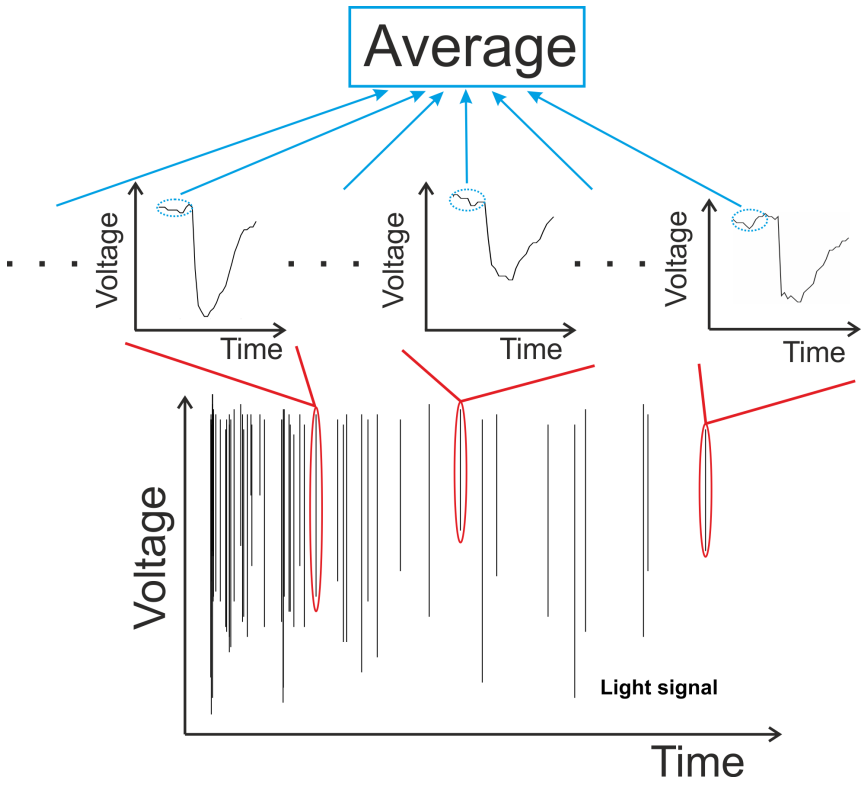

Figure 3.22: Illustration of the process of averaging the pre-trigger baseline voltages from the records in the same scintillation event. In this way, even though each event only gets a short pre-trigger baseline region, the averaging process establishes a baseline with enough statistics. Also, the standard deviation of the voltage in the baseline regions is calculated from all the data points used for the baseline estimation process from multiple records instead from an individual record.

with respect to the pre-trigger length set by the user in the DAQ). Because of the small number of data points (small statistics) in the pre-trigger baseline region in each record, it is difficult to construct the baseline for each record reliably. To alleviate this issue, the pre-trigger baseline voltages estimated from the individual records in the same scintillation event are averaged (Figure 3.22) and this average value replaces the pre-trigger baseline voltage calculated for the individual records as the estimated pre-trigger baseline voltage. In this way, even though the majority of the baseline data points are not recorded on the disk, we still have a good estimation of the pre-trigger baseline voltage for the records, as shown in Figure 3.23. Also, as a representation of the noise level, the standard deviation of the voltage in the pre-trigger baseline regions within a scintillation event is estimated from the multiple records in a scintillation event instead of from individual records. To do this, the standard deviation of all the data points used for the baseline estimation is calculated with respect to the averaged pre-trigger baseline voltage calculated above.

3.2.1.3 Photon counting

After obtaining a good estimation of the pre-trigger baseline voltage level, the next step is to count the number of photoelectron pulses in the signal. Precision in taking account of every single photoelectron pulse is important as for N photons detected on average for a specific energy, an averaged error of one photon in counting the photons means the energy resolution (σ) deteriorates approximately by $1/N$. In this study, for 122-keV energy deposits from γ quanta, the light detector detects an average of ~60 photons in $CaMoO_4$, and ~170 photons in $CaWO_4$. An error of one photon corresponds to a deterioration of the energy resolution (σ) by approximately $^1/_{60}$ (~1.6%) for $CaMoO_4$ data and approximately $^1/_{170}$ (~0.6%) for $CaWO_4$ data. In general, a pulse finding algorithm based on the

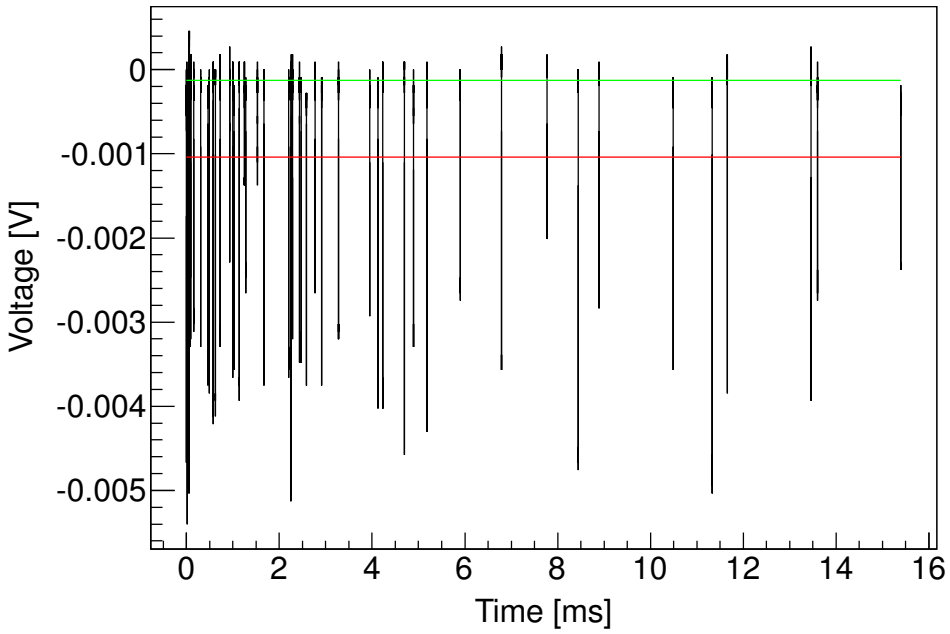

Figure 3.23: A typical event of a 122-keV γ quantum measured by the light detector of the CPSD module with $CaMoO_4$ as the absorber. The black vertical lines are individual photoelectron pulses. The green horizontal line represents the estimated baseline level (Section 3.2.1.2). The red horizontal line represents the calculated offline analysis threshold for initial pulse finding. (Section 3.2.1.3).

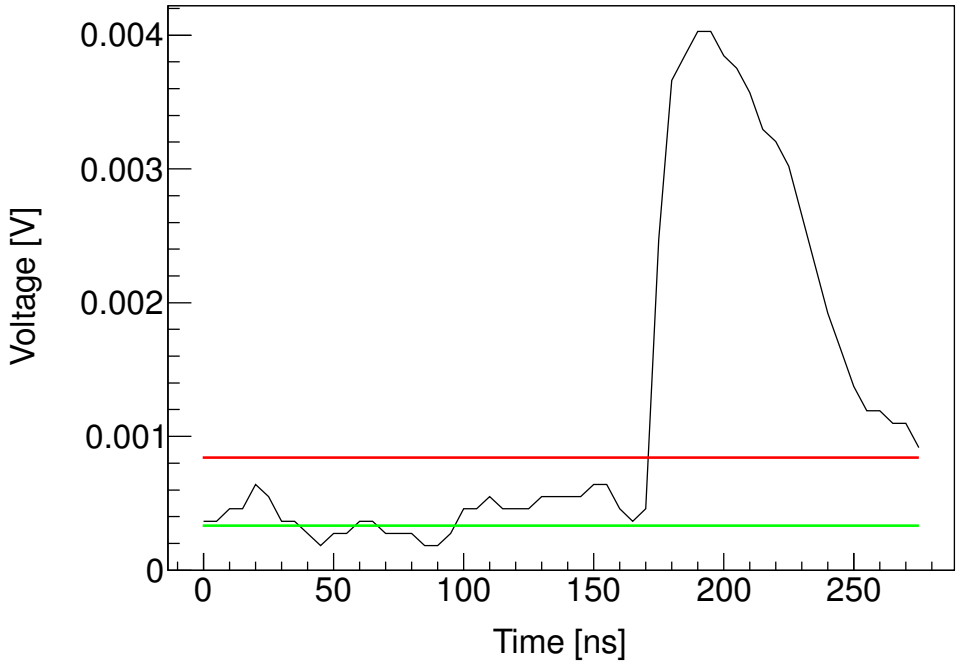

Figure 3.24: Example of a photoelectron pulse after the inversion of polarity, for ease and clarity of discussion in the photon counting section. The green horizontal line represents the estimated baseline level (Section 3.2.1.2). The red horizontal line represents the calculated offline analysis threshold for initial pulse finding (Section 3.2.1.3).

peak and trough method is used to search for the individual photoelectron pulses.

For ease and clarity of discussion, the polarity of the signal of the light channel is inverted in this section (as shown in Figure 3.24), so a photoelectron pulse corresponds to a pulse with positive amplitude.

Initial pulse finding

The pulse finding threshold is set as the pre-trigger baseline voltage plus five times the standard deviation of the voltage in the pre-trigger baseline regions calculated for the scintillation event, as described in Section 3.2.1.2. This pulse finding threshold is set so that as few noise spikes as possible are mistaken for photoelectron pulses, while the algorithm still finds the majority of the photoelectron pulses. From the start of the record, the algorithm evaluates the data points

in the signal trace one by one in sequence, and it marks the pulse if the data point under consideration $D[i]$ meets the following three criteria simultaneously: (i) $D[i]$ is larger than the pulse finding threshold; (ii) $D[i]$ is larger than $D[i-1]$ plus the standard deviation of the voltage in the pre-trigger baseline regions; (iii) $D[i]$ is larger than $D[i-2]$. If the signal trace meets those three criteria simultaneously, a pulse is found and the array index $i-1$ is marked as the start of the photoelectron pulse. The end of the photoelectron pulse is marked as the signal trace returns to be a value smaller than the pulse finding threshold. After the end of a photoelectron pulse, the algorithm moves on to the next data point in the signal trace and compares its value to the analysis triggering conditions to see if it is the start of the next photoelectron pulse, and so on. The time position of the maximum point between the start and the end of the photoelectron pulse is marked as the timestamp of the photoelectron pulse and the pulse height is taken as the voltage difference between the voltage of the data point representing the maximum and the pre-trigger baseline voltage.

Separating overlapping pulses

For photons arriving in quick succession (pile-up), the algorithm also tries to resolve two overlapping photoelectron pulses. Due to the very different time scales and different signal topologies between the light and the phonon channels, it is not possible to apply the method involving the voltage ratio parameter (Section 3.1.3) that was successful in the phonon channel to the light channel. Due to the scintillation decay characteristics of the $CaMoO_4$ crystal (Equation 4.2, which also applies to $CaWO_4$), at the start of a scintillation event there is a significant probability that two photons arrive so close to each other in time that the signal trace does not return to below the threshold level between the signals of these two photoelectron pulses. The initial pulse finding procedure above would mistakenly

regard these two photons as one, so the algorithm tries to correct it as follows. For the photoelectron pulses longer than three data points, the algorithm searches for all the extreme values between the start and the end of the photoelectron pulse. As shown in Figure 3.25, the algorithm evaluates the local minima one by one, as comparing each to a threshold (called "split threshold") set by the baseline voltage and the two local maxima adjacent to the local minimum. The split threshold is set as the smaller of two values calculated by $0.65M_i + 0.35B,\ i = -1, +1$, where B is the pre-trigger baseline voltage, M_{-1} is the voltage of the adjacent local maximum before the local minimum and M_{+1} is the voltage of the adjacent local maximum after the local minimum. If the following two conditions are met simultaneously, the local minimum point is regarded as the split point of two photoelectron pulses and a pile-up event is flagged: i) the value of the local minimum point is lower than the split threshold, which means the signal trace returns closer to the baseline than the split threshold; ii) the two adjacent local maximum points are at least 3 data points apart. This split point marks the end of the first photoelectron pulse and the start of a second photoelectron pulse. If the conditions are not met, there is no pile-up discovered for the local minimum under consideration, and the algorithm moves on to evaluate the next local minimum inside the pulse region.

Overshoot

Overshoot height and overshoot integral are also calculated after each single photoelectron pulse. They correspond to the points below the pre-trigger baseline voltage at the end of the pulse (for a positive polarity pulse), if there are any. The start of the overshoot region is the point where the signal trace is below the baseline after the end of the photoelectron pulse and the end is the point where the signal trace returns to above the baseline. Also, peak height and the integral

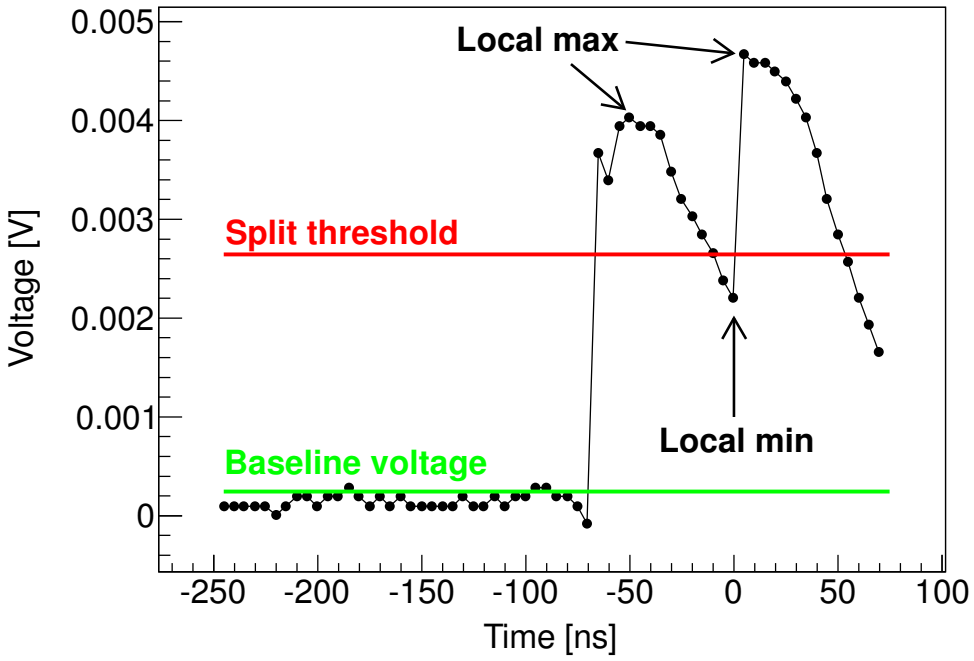

Figure 3.25: A diagram showing how the process of separating overlapping pulses works. The split threshold level for a local minimum ($t = 0$) is deduced from the voltages of the two adjacent local maxima and the baseline voltage. If the voltage of a local minimum is smaller than the split threshold and the two adjacent local maxima are at least 3 data points apart, the local minimum is taken as the split point and the pulses are separated.

of data points below the baseline voltage before the photoelectron signal are also calculated, if they are present, to further characterise the photoelectron signal.

Remove ringing

Ringing at the end of a photoelectron pulse, if it is present, might be mistakenly regarded as new photoelectron pulses by the algorithm. Consequently, the following measures are taken to alleviate this issue. If the peak position (maximum point for positive polarity pulse) of a photoelectron pulse is no more than four data points away from the peak position of the adjacent photoelectron pulse, the latter photoelectron pulse is taken as a false photoelectron pulse.

Peak integral

After removing the falsely assigned photoelectron pulses, the list of photoelectron pulses is regarded as containing the true photoelectron pulses. The voltages of data points with the baseline removed between the start and the end of a photoelectron pulse are then summed for each photoelectron pulse, and this gives the peak integral of the photoelectron pulse. The distribution of this peak integral could be used as a cross-check for the baseline estimation.

The number of photons in a scintillation event is the sum of the number of photoelectron pulses in the individual records grouped in that scintillation event.

3.2.1.4 Scintillation decay

In this experiment, a study has been performed to measure the scintillation decay time constants of a $CaMoO_4$ crystal at milli-Kelvin temperatures for the first time [141]. The study of scintillation properties of slow scintillator crystals is discussed in detail in [117]. Because of its capability of resolving individual photons, the low-temperature PMT in this experiment is very suitable for studying the scintillation

properties of crystals from milli-Kelvin temperatures to temperatures of a few Kelvin. With the "dead-time free" data acquisition mode, there is in principle no upper limit on the scintillation decay time constant under study. After the photon grouping, the timestamp of the first record in the group is taken as the start time of the scintillation event. The difference between the timestamp of a record with a single photoelectron pulse and the start time of the scintillation event is then the arrival time of that specific photon relative to the start of the scintillation event. In this way, we can study how the scintillation intensity evolves over time.

3.2.1.5 Scintillation and dark pulse simulation

To investigate the effects of the photon grouping algorithm discussed in Section 3.2.1.1, a simulation of the scintillation and dark pulse is employed. Because, in the simulation, the number of energy deposits and the number of scintillation photons generated by each of those energy deposits are known quantities, it is easy to compare the results from the analysis algorithm to the "simulated truth" to investigate the performance of the photon grouping algorithm. Two sources of signals from the PMT are simulated: scintillation photons and dark pulses from the PMT. The general approximations of this simulation include: i) the PMT has perfect gain and zero electronic noise, i.e. it detects every photoelectron generated in the cathode and every dark pulse, and there are no spurious events from electronics noise; ii) the PMT readout system has zero time resolution, i.e. it could distinguish two photons (or dark pulses) arriving infinitely closely in time. With these two approximations, the only relevant quantity is the arrival times of the scintillation photons and dark pulses, so the arrival timestamps are the only data generated by the simulation.

The algorithm of the simulation is shown in Figure 3.26, and it is detailed as follows.

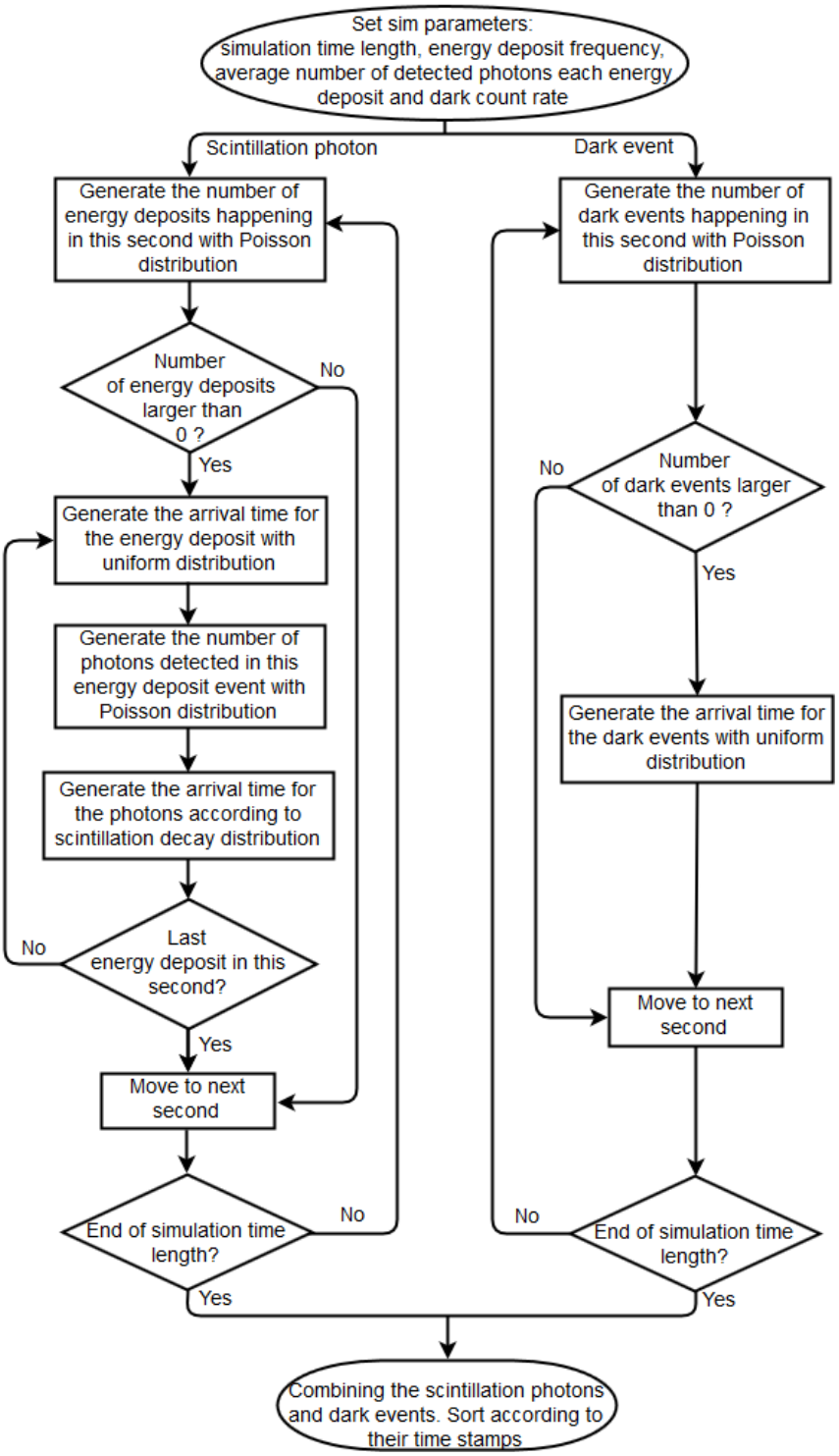

Figure 3.26: A flow diagram showing the simulation algorithm for the scintillation photons and the dark pulses.

Scintillation photon simulation

The simulation algorithm generates the scintillation photons for one second, before moving to the next second. With a frequency of energy deposits of R_r Hz, there are, on average a number of R_r energy deposits in one second. The actual number of energy deposits k_r that happen in a specific second follows the Poisson distribution, $P(k_r, R_r) = \frac{R_r^{k_r} e^{-R_r}}{k_r!}$. The simulation algorithm first generates the number of energy deposits in a specific second by generating a random integer with probability following the Poisson distribution. If the result is $k_r = 0$, i.e. there are no energy deposits in a specific second, the simulation algorithm then moves to next second and restarts the process of generating the number of energy deposits. If $k_r > 0$, the simulation then generates the arrival times for each of the energy deposits according to a uniform distribution between 0 and 1. As the absorber under evaluation is $CaMoO_4$ and the excitation is γ-rays from ^{57}Co, around 90% of all energy deposits are 122-keV γ quanta; the other 10% are from 136-keV γ quanta. With around 60 photons detected for each 122-keV γ quantum, there would be a difference of around only seven photons between the average number of scintillation photons detected for 122-keV and 136-keV γ quanta. Hence, it is reasonable to simplify the simulation to assume that the energy deposits are all with the same energy, i.e. 122 keV. The average number of scintillation photons detected in each energy deposit is D. For each energy deposit, the simulation algorithm generates a random integer number of photons detected N, according to the Poisson distribution $P(N, D) = \frac{D^N e^{-D}}{N!}$. The algorithm then generates a random arrival time for each of the N photons relative to the arrival time of corresponding energy deposit according to a probability distribution described by the sum of two exponential functions fitted to the scintillation decay curve, as described by Equation 4.2. The simulated photons are sorted by their arrival times in ascending order, in the same way the real photons were recorded with

the DAQ. The absolute arrival time of a simulated scintillation photon is the sum of the start time of the second under consideration, the arrival time of the radiation energy deposit relative to the start of the second and the arrival time of the scintillation photon relative to the energy deposit. Because the scintillation process could last for many milliseconds, it is possible that the scintillation photons from the tail of an earlier radiation energy deposit could arrive later than the scintillation photons at the beginning of the radiation energy deposit. Thus, all the simulated photons from different radiation energy deposits are sorted again in ascending order according to their absolute arrival times.

Dark pulse simulation

The simulation of dark pulses is also on a second-by-second basis, i.e. the simulation generates the dark pulses for one second, before moving on to the next second to generate more dark pulses. With a dark count rate of R_d Hz, the actual number of dark pulses k_d that happen in a specific second follows the Poisson distribution $P(k_d, R_d) = \frac{R_d^{k_d} e^{-R_d}}{k_d!}$. If the random number generated is $k_d = 0$, the simulation algorithm then moves to next second and restarts the process of generating the number of dark pulses in the new second. If $k_d > 0$, the simulation then generates the arrival time for each of the dark pulses relative to the start of the second, according to a uniform distribution between 0 and 1. The arrival times of the dark pulses are then sorted into ascending order. The absolute arrival time of a simulated dark pulse is the sum of the start time of the second under consideration and the arrival time of dark pulse relative to the start of the second.

Combination of the simulated scintillation photons and dark pulses

To combine the simulated scintillation photons and dark pulses, the combination of these two groups are sorted in ascending order according to their absolute

Simulation input parameters	Energy deposit rate (Hz)	Average number of photons per event	Dark count rate (Hz)	Simulation length (s)
Quantity	1.1	60	5	3600
Simulation output variables	Number of energy deposits	Number of scintillation photons	Number of dark pulses	
Expectation	3960	237,600	18,000	
Result	3983	239,096	17,859	

Table 3.2: The input parameters and output variables of the simulation in this study. The input parameters are taken from the estimation of the $CaMoO_4$ data.

arrival times. In a real PMT readout system, it is impossible to differentiate a real photon signal from a dark pulse on a pulse-by-pulse basis. In the simulation, signals from the scintillation photons and dark pulses are combined and their difference is invisible to the photon grouping algorithm under test.

Validation of the simulation

To validate the simulation, the total number of scintillation photons and dark pulses generated in the simulation is checked, as shown in Table 3.2. The input parameters are taken from the estimation of the $CaMoO_4$ data, and these input parameters are used throughout this section. Also, the scintillation decay curve generated by the simulation is compared to the measurement, as shown in Figure 3.27. The time intervals between consecutive dark pulses generated by the simulation are shown in Figure 3.28.

Time criterion for the photon grouping algorithm

The scintillation photon and dark pulse simulations are employed to study the time criterion for the photon grouping algorithm. As discussed in Section 3.2.1.1, the records with single photoelectron pulses in the light channel are grouped into

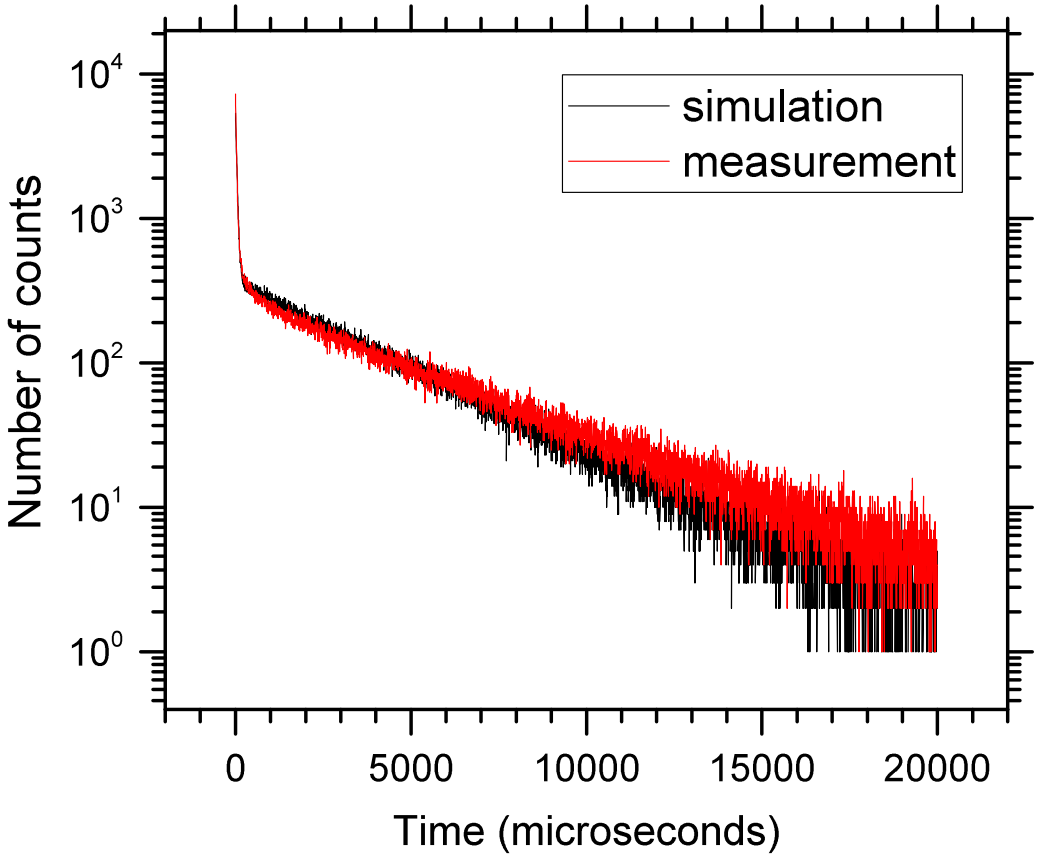

Figure 3.27: The scintillation decay curves of $CaMoO_4$ at a temperature of 18 mK. The simulation is shown in black and the measurement is shown in red. The simulation includes the scintillation photons and the dark pulses.

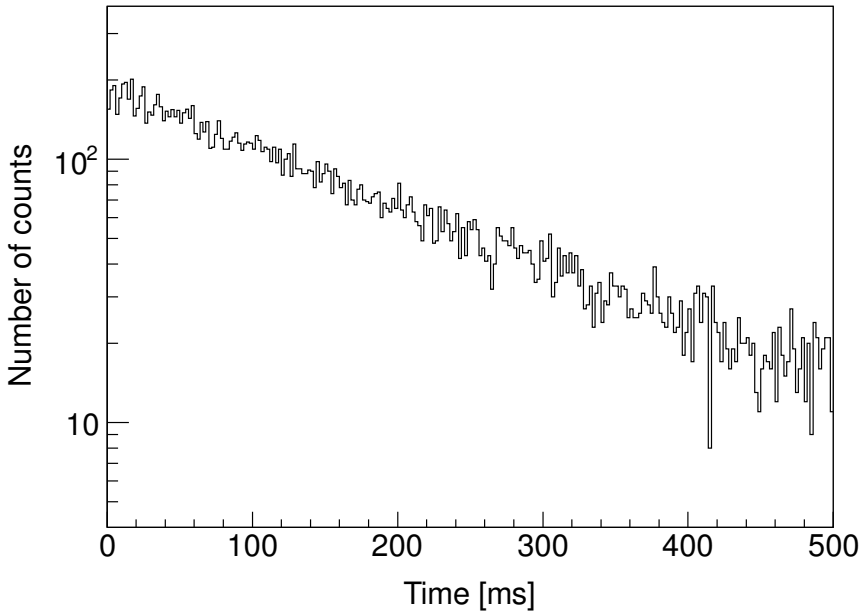

Figure 3.28: The time interval between consecutive dark pulses in the simulation. The dark count rate is set at 5Hz. The exponential decay is expected for a uniform distribution of dark pulses in time [159].

the same scintillation event if the interval between two consecutive photons is not larger than a pre-set criterion, t_c. The value of t_c is not trivial, because if t_c is too small, the scintillation photons happening at the end of the scintillation event could be mistakenly omitted, as illustrated in Figure 3.29. As the slow scintillation decay time constant of $CaMoO_4$ is ~3.4 ms at 18 mK [141], the time interval between consecutive photons at the end of the scintillation event becomes very long. Figure 3.32 shows that with $t_c = 2$ ms, for scintillation only simulation data (no dark pulse simulated) and an average of 60 detected photons for each energy deposit, the photon grouping algorithm falsely detects a significant number of scintillation events in the pedestal region (number of photons less than 20). Because the simulated data is scintillation only, practically there should not be any scintillation events with such a small number of photons, as the number of photons in each scintillation event follows a Poisson distribution with an average number of 60. If t_c is too large, the photons from two or more scintillation events could

be mistakenly taken as from the same scintillation event (Figure 3.30), especially when random dark pulses could function as a "bridge" to connect photons from two scintillation events. Also, a photon from an earlier scintillation or a dark pulse could be grouped with the photons from a scintillation event (Figure 3.31), leading to errors in estimating the number of photons and errors in the scintillation timestamp (timestamp of the first photon in the group taken as the timestamp of the group) and later difficulty in the study of coincident signals between the phonon channel and the light channel. Eventually, t_c is chosen to be 7 ms. With $t_c = 7$ ms, only less than around 0.25% of the photons are eventually assigned to the pedestal region (Table 3.3). Moreover, the grouping criterion of 7 ms gives the best energy resolution after the grouping process. Figure 3.32 ~ 3.35 and Table 3.3 show how the grouping criterion affects the number of photons in the grouping result.

3.2.2 $CaWO_4$ data with "fixed-length" DAQ mode

For the fixed-length mode in $CaWO_4$ data, because the data are recorded in a fixed-length time window for each triggered event, most of the photons in the scintillation event are recorded within that time window. The number of photons in that fixed-length record is used to estimate the number of photons in the detected scintillation event. This DAQ mode has the advantage of eliminating the possibility of the firmware mistakenly failing to trigger on a real photon, as is possible in the "dead-time free" mode. However, it creates a dead time after each triggered event, as the data rate generated in this DAQ mode is more than the maximal data transfer rate allowed between the front-end electronics and the computer. Consequently, the data fill up the FIFO in the front-end electronics. Only after the FIFO becomes empty as the data stored in it are transferred to the computer, the data taking of a new event can be started. The fixed-length mode

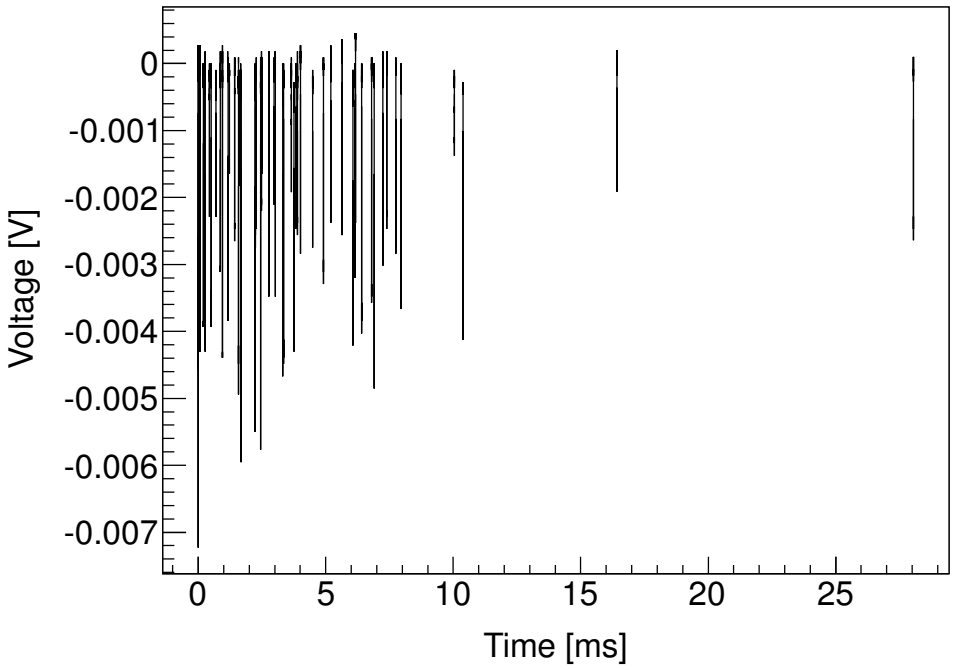

Figure 3.29: A scintillation event measured in the light channel of the CPSD with $CaMoO_4$ as the absorber at 18 mK, excited by a ^{57}Co source. As the slow scintillation decay time constant of $CaMoO_4$ is ~3.4 ms at 18 mK, the time interval between consecutive photons at the end of the scintillation event becomes very long. If the grouping time criterion is too short, the photons at the end of the scintillation event would be mistakenly omitted.

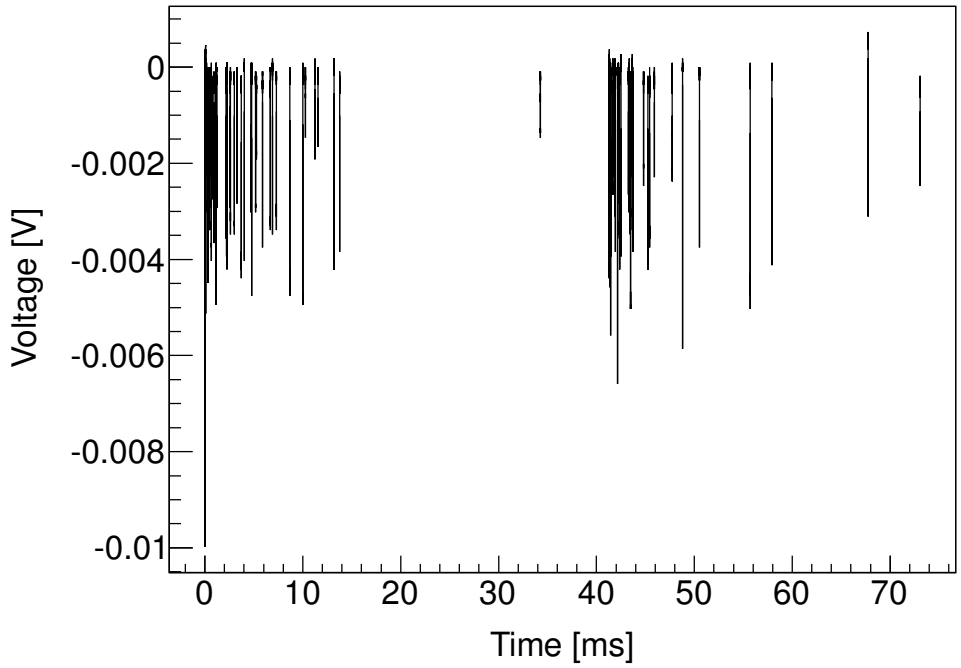

Figure 3.30: Example of two scintillation events (start at $t = 0$ and $t \approx 40$ ms) mistaken as one due to a long grouping criterion in the photon grouping algorithm. The photons are measured in the light channel of the CPSD with $CaMoO_4$ as the absorber at 18 mK, excited by a ^{57}Co source.

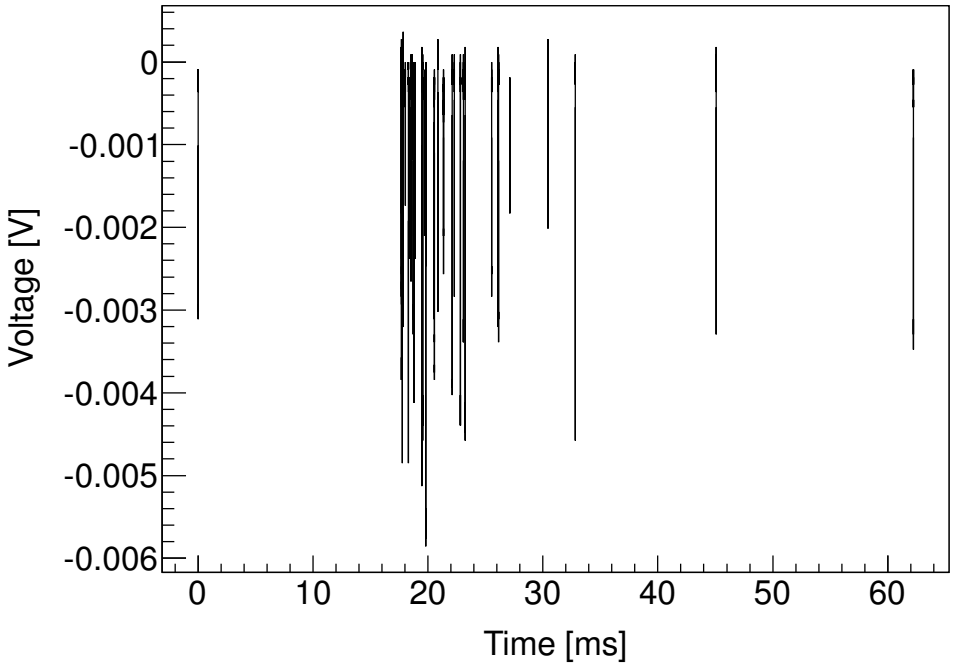

Figure 3.31: Example of a photon from an earlier scintillation event or a dark pulse (shown in $t = 0$) mistakenly grouped with photons from a later scintillation event ($t \approx 17$ ms). Because the timestamp of the first photon in the group is taken as the timestamp of the scintillation event, the mistake of grouping a photon from an earlier scintillation event or a dark pulse causes errors in the timestamp estimation of the later scintillation event. They are measured in the light channel of the CPSD with $CaMoO_4$ as the absorber at 18 mK, excited by a ^{57}Co source.

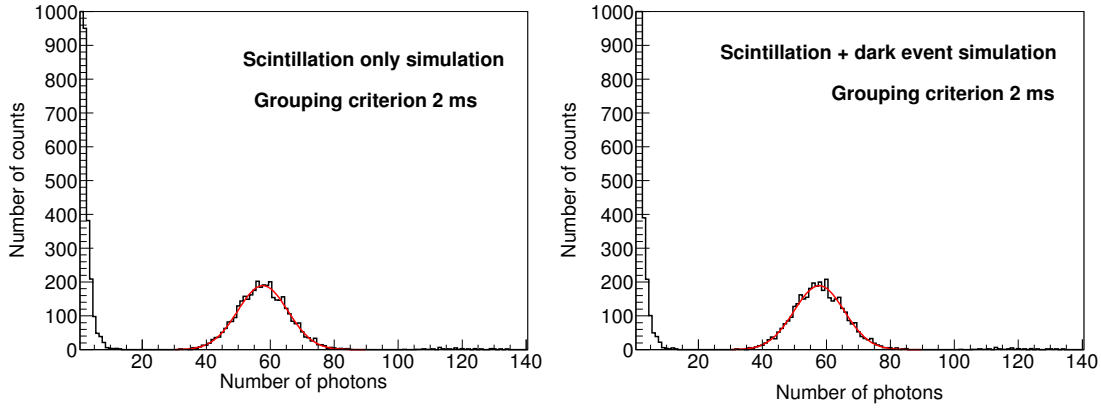

Figure 3.32: Histograms of the number of photons per grouping calculated by the photon grouping algorithm, from scintillation only simulation data (left) and scintillation plus dark pulse simulation data (right). The red lines show the Gaussian functions fitted to the data. The grouping criterion is a 2-ms time interval. There is a significant population in the pedestal region in the scintillation only simulation data, which is due to the photon grouping algorithm with a too short grouping window.

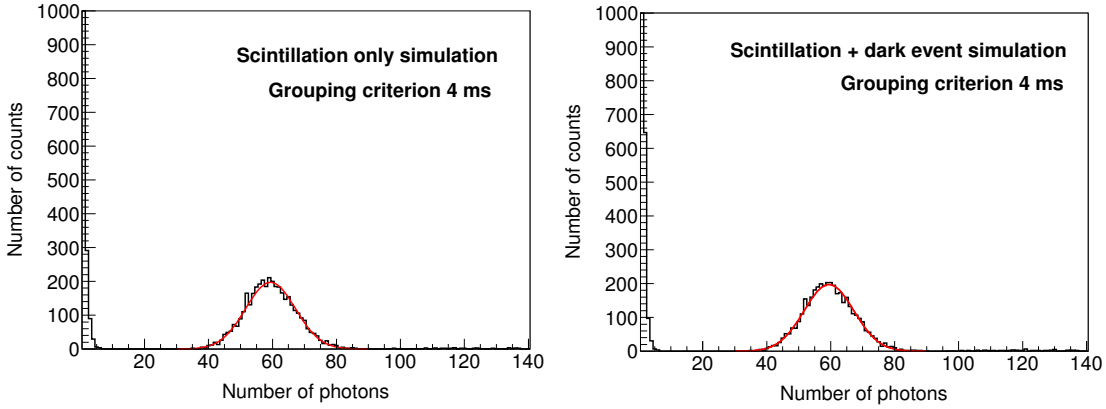

Figure 3.33: Histograms of the number of photons per grouping calculated by the photon grouping algorithm, from scintillation only simulation data (left) and scintillation plus dark pulse simulation data (right). The red lines show the Gaussian functions fitted to the data. The grouping criterion is a 4-ms time interval.

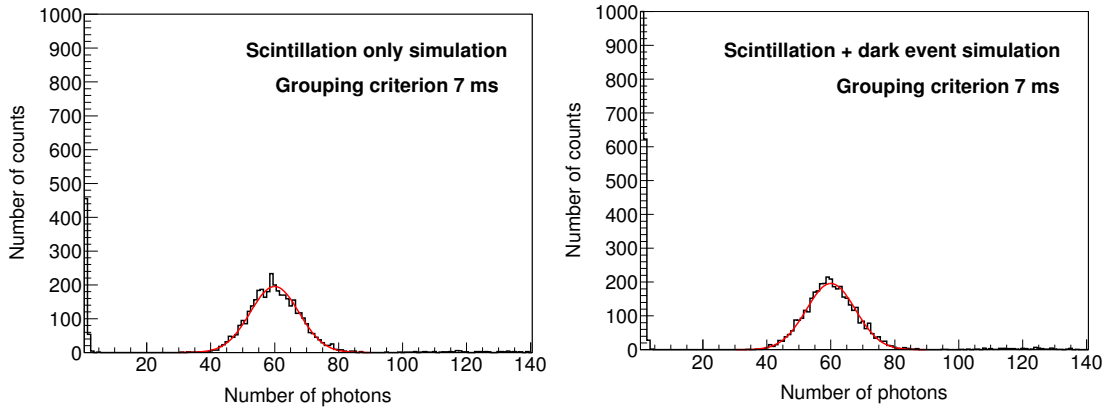

Figure 3.34: Histograms of the number of photons per grouping calculated by the photon grouping algorithm, from scintillation only simulation data (left) and scintillation plus dark pulse simulation data (right). The red lines show the Gaussian functions fitted to the data. The grouping criterion is a 7-ms time interval.

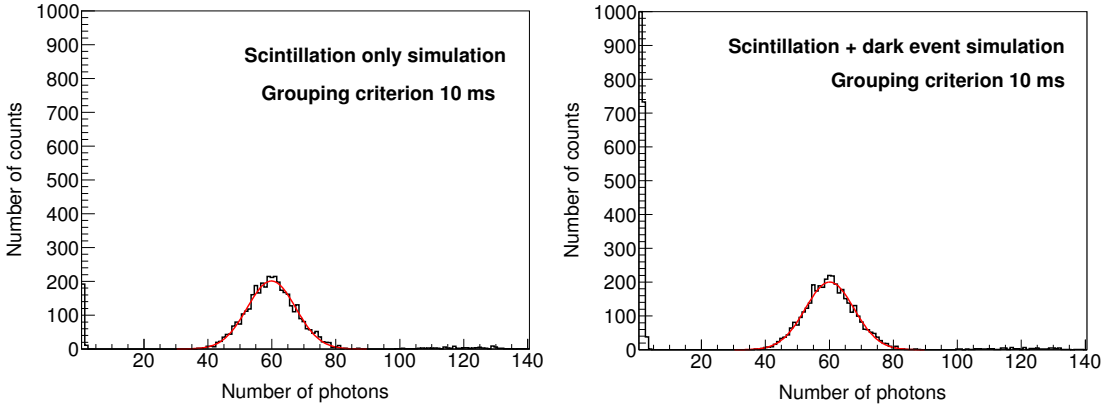

Figure 3.35: Histograms of the number of photons per grouping calculated by the photon grouping algorithm, from scintillation only simulation data (left) and scintillation plus dark pulse simulation data (right). The red lines show the Gaussian functions fitted to the data. The grouping criterion is a 10-ms time interval. In the scintillation only simulation data, there is only a very small population of photons in the pedestal region.

Grouping criterion	Simulation type	Gaussian mean	FWHM resolution	Percentage of photons in pedestal region	Percentage of double events
2 ms	Scintillation only	57.8	31.8%	3.5%	1.0%
	Scintillation + dark pulse	57.9	31.7%	3.5%	1.0%
4 ms	Scintillation only	59.4	30.4%	0.97%	2.0%
	Scintillation + dark pulse	59.5	30.4%	0.95%	2.0%
7 ms	Scintillation only	60.0	29.8%	0.25%	2.3%
	Scintillation + dark pulse	60.1	29.9%	0.25%	2.3%
10 ms	Scintillation only	59.9	28.7%	0.08%	2.6%
	Scintillation + dark pulse	60.0	28.2%	0.08%	2.6%

Table 3.3: The results of the photon grouping analysis with different grouping criterion (2 ms, 4 ms, 7 ms or 10 ms), applied to the scintillation only simulation data as well as the scintillation plus dark pulse simulation data. The input parameters to the simulation are taken from Table 3.2. The FWHM resolutions are that in the Gaussian peaks. Percentage of photons in pedestal region is relative to the total number of scintillation photons generated. The percentage of double events is relative to the total number of energy deposits generated.

would not be suitable for crystals with a longer scintillation decay time constant (e.g. $CaMoO_4$) than the record length allowed by the data storage capacity of the FIFO in the front-end electronics.

3.2.2.1 Baseline estimation

The actual method of baseline estimation is different between data analysis for the $CaMoO_4$ data and that for the $CaWO_4$ data. Due to the fixed-length DAQ mode deployed for taking data with a $CaWO_4$ scintillator, each record already captures the majority of the signal traces in a scintillation event. As a result, there is no need to group the records. Also in the $CaWO_4$ data, the majority of the data points in a record are baseline data points between photoelectron pulses, and there is a long pre-trigger baseline region. Three different methods are tested for the estimation of the baseline level:

90% baseline

First the algorithm ranks the data points according to their values, then the average of the largest 90% (negative polarity for pulses) of the data points is taken as an estimation of the baseline level and the standard deviation of these data points is taken as the standard deviation of the baseline region.

First 1/16 baseline

In the fixed-length DAQ mode, the pre-trigger baseline region could be chosen to be long, unlike the short pre-trigger baseline required by the "dead-time free" DAQ mode in the $CaMoO_4$ data. The first 1/16 section of the record is taken as the pre-trigger baseline region. The average and the standard deviation of the data points in this first 1/16 section are calculated as estimations for the baseline level and the standard deviation of voltages in the baseline region, respectively.

Baseline without pulses

The algorithm could also search preliminarily for any pulses. If a data point exhibits a value smaller than both of the two data points before it and both of the two data points after it, it is marked preliminarily as a pulse minimum point (negative polarity pulse). The region between three data points before and eight data points after this minimum point is defined as the pulse region. The pulse height is provisionally estimated as the value of the pulse minimum point minus the 90% baseline calculated above. This process detects more pulses than there actually are, but it is appropriate as, in this process, we try to find the baseline region without pulses for more accurate baseline estimation. After the pulses are found, a new baseline is estimated from the data points where there are no pulses. The standard deviation of data points in the baseline region is also calculated from these points.

Eventually, the 90% baseline value is adopted as the baseline level for the subsequent analysis and the standard deviation among the data points selected in the baseline without pulses process is adopted as the standard deviation of the baseline. This combination is proven to provide good estimations of the baseline level and the noise level, as confirmed by the precision achieved in the photon counting in the later stage.

3.2.2.2 Photon counting

The photon counting for the $CaWO_4$ data is similar to that for the $CaMoO_4$ data, as described in Section 3.2.1.3. The only difference is how the pulse finding threshold is calculated. It is chosen as the smallest value among these three values (negative polarity pulses): (i) baseline level minus one bit ADC value; (ii) baseline minus 5% the average from pulse heights calculated in Section 3.2.2.1; (iii) baseline level minus five times the standard deviation of voltages in the baseline region.

3.2.2.3 Scintillation decay

For the $CaWO_4$ data, because a record captures most of the photoelectron pulses in a scintillation event, the first photoelectron pulse marks the start of the scintillation event. The arrival times of the other photons are calculated relative to the first photoelectron pulse. The distribution of the arrival times could be fitted with Equation 4.2. Because of the limit on the maximum number of data points in a record, imposed by the finite capacity of the FIFO (data buffer) in the front-end electronics, there is a limit to the maximum arrival time of the photons that could be captured by the DAQ.

3.2.2.4 Statistical test

Two scintillation events could accidentally happen very close in time and create a record with the photon signal from these two scintillation events. This type of event could be discriminated by statistics, as discussed in [160].

3.3 Coincident signals

As discussed in Section 1.7, one of the main features in CPSD technology is the ability to measure the phonon and the light signal simultaneously and, subsequently, the ability to perform particle discrimination through the signal ratio of the two. To demonstrate this feature, a study of coincident signals from these two channels is performed. The phonon channel and light channel have separate data acquisition systems as discussed in Section 2.5 and this gives rise to the necessity for data synchronisation.

3.3.1 Timestamp

For the phonon channel data, because the modulation frequency is constant and the data taking by the phonon channel DAQ is continuous, the number of demodulated data points since the beginning of data taking corresponds to the duration since the start of data taking. As the modulation frequency is constant, the interval between two consecutive demodulated data points corresponds to a period that is the inverse of the modulation frequency times two, where the factor of two is from the demodulation process described in Section 3.1.1. As mentioned in Section 3.1.2, because of the difficulty in determining the onset of a pulse, the time position of the pulse maximum point is taken as the timestamp of a pulse. There is an approximately constant time offset between the maximum point position and the real onset of the pulse.

For the light channel, the timestamps of records made by the DAQ are used for both the $CaWO_4$ data and the $CaMoO_4$ data. For the $CaWO_4$ data taken with fixed-length trigger mode, the photons from a scintillation event are contained in the same record, so the timestamp of the record is taken as the timestamp of the scintillation event. For the $CaMoO_4$ data taken with "dead-time free" trigger mode, the timestamp of the first photon in the group after photon grouping is used as the timestamp of the scintillation event, as discussed in Section 3.2.1.1.

3.3.2 Synchronisation

Because of the modulation scheme used (Section 2.5.1), the phonon channel has a time resolution of ~0.5 ms after demodulation, with the highest modulation frequency deployed (1 kHz). The phonon channel and the light channel of the CPSD should detect the signals from the same energy deposit simultaneously better than 0.5 ms in the physics level [103, 161, 117]. Thus, all the discrepancy between the timestamps of the two channels about the same energy deposit is

from errors introduced at the later stages of the signal chain. This understanding is used to synchronise the two channels.

After the timestamps of the phonon channel events and the light channel events are obtained, the timestamps from the two channels are plotted side by side for visual inspection. Due to the time pattern of when energy deposits happen, it is easy to notice how the timestamps of the two channel should be aligned. As an example, it is easy to notice the time offset of the stamps for the two channels, from the beginning section of the plot (Figure 3.36), which is introduced by the DAQ systems and the time difference between the pulse maximum and the real onset of pulses in the phonon channel. This offset is manually compensated by adding a time offset to the timestamp of every event in one of the channels (phonon channel chosen). After aligning the timestamps at the beginning of the data taking period, it is found that the relative difference of the timestamps between the two channels drifts over time. This drifting is understood to be introduced by the data acquisition systems. The exact frequencies of modulation in the phonon channel and the data sampling in both channels are controlled by crystal oscillators in the electronics and the oscillation frequency of the crystals are affected by temperature. Two methods are investigated to overcome this time-drifting effect. As the first method, a linear time drifting factor is calculated by the ratio of how much the timestamps have been drifted at the end of the data taking, relative to the duration of the whole data taking. Then, every timestamp in one of the channels (phonon channel chosen) is corrected by the calculated linear time drifting factor. After this correction, the timestamps between the two channels are found to be well aligned throughout the data taking. The second method is to align a small section (chosen to be 30 seconds) of timestamps at a time. As the time drifting effect is only significant in the longer term (around 6 microseconds drifted per second on average), by adding another time offset to

every timestamp in one of the channels (phonon channel chosen) in a small time window, the timestamps in the two channels could be aligned. The value of the offset is decided through a search algorithm, which searches the time offset value from -50 ms to 50 ms with a 0.03-ms step size, so a maximum number of phonon channel timestamps are aligned with the timestamps in the light channel. If there are two or more time offset values with the same number of aligned phonon channel timestamps, then the one which minimises the sum of the difference between the aligned timestamps of the two channels is chosen. The first method was found to work better for the $CaMoO_4$ data and was applied to this data. The second method is found to work better for the $CaWO_4$ data, and the second method is applied to $CaWO_4$ data.

After all the corrections in the timestamps of the two channels are performed, the coincidence window for the two channels is set as 2 ms (i.e. if the timestamps of the events in the two channels are closer than 2 ms), they are taken as being in coincidence. The results of the study of coincident signals are presented in Figure 4.12 and Figure 4.13 in Section 4.3.

3.4 Light yield

The light yield is defined as the number of photons detected by the light channel divided by the energy measured in the phonon channel of the CPSD, normalised to electron recoil events. Because nuclear recoil events produce only a small proportion of light (described by the quenching factors for different nuclei) compared to electron recoils, the light yield can be used to discriminate between nuclear recoil events and electron recoil events. No neutron source has been applied in this experiment, so only electron recoil events are investigated. The quenching factors for different nuclei of $CaWO_4$ have been well measured [162]. For the CPSD

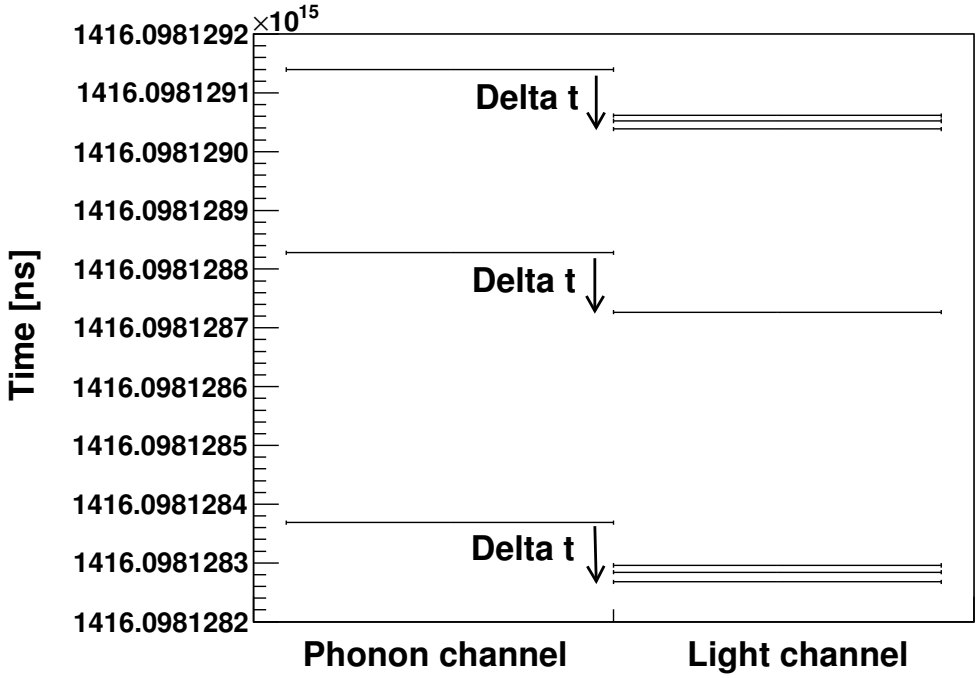

Figure 3.36: A section of the timestamps (horizontal lines) of events detected by the phonon channel (left) and the light channel (right) of the CPSD module with $CaMoO_4$ as the absorber, at the beginning of data taking. The timestamps are in the Unix time format, i.e. the time since 1 January 1970, but they are in the unit of nanoseconds. It is easy to notice that a time offset exists between the timestamps of the two channels, as notated by "Delta t" in the figure.

module, the efficiency to discriminate electron recoils against nuclear recoils is illustrated by the 90% upper and lower boundaries of electron recoil band in the light yield plot.

Because the light channel in the CPSD with $CaWO_4$ as the absorber has a much better energy resolution than that of the $CaMoO_4$, only the $CaWO_4$ data is used in the study of discrimination power with light yield in this work.

The procedure to obtain the 90% upper and lower boundaries of the electron recoil band is discussed as follows.

The energy resolution of the phonon channel (σ_P) of the CPSD is parameterised by:

$$\sigma_P(E) = \sqrt{a + b \cdot E + c \cdot E^2}\,, \tag{3.3}$$

where E is the energy measured by the phonon detector in the unit of keV, a, b, and c are coefficients. The fitting of the data points in energy resolutions with Equation 3.3 is shown in Figure 3.37.

The energy resolution of the light channel (σ_L) of the CPSD is described by the Poisson distribution as follows:

$$\begin{aligned} \sigma_L(E) &= \sqrt{\tfrac{N(E)}{N(122\,\mathrm{keV})}} \cdot \sigma_L(122\,\mathrm{keV}), \\ \sigma_L(E) &= \sqrt{\tfrac{1}{N(122\,\mathrm{keV})} \cdot \tfrac{N(122\,\mathrm{keV})}{122\,\mathrm{keV}} \cdot E} \cdot \sigma_L(122\,\mathrm{keV}), \\ \sigma_L(E) &= \sqrt{\tfrac{E}{122\,\mathrm{keV}}} \cdot \sigma_L(122\,\mathrm{keV}), \end{aligned} \tag{3.4}$$

where $\sigma_L(122\,\mathrm{keV})$ is the energy resolution of the light channel for the energy deposits by 122-keV γ quanta, $N(E)$ is the number of photons detected by the light detector for electron recoil events with energy E. The assumption in this equation is that the number of scintillation photons detected is proportional to the deposited energy. As not enough low-energy deposits happenedin the experiment, it is not possible to explore the non-proportionality effect of the $CaWO_4$

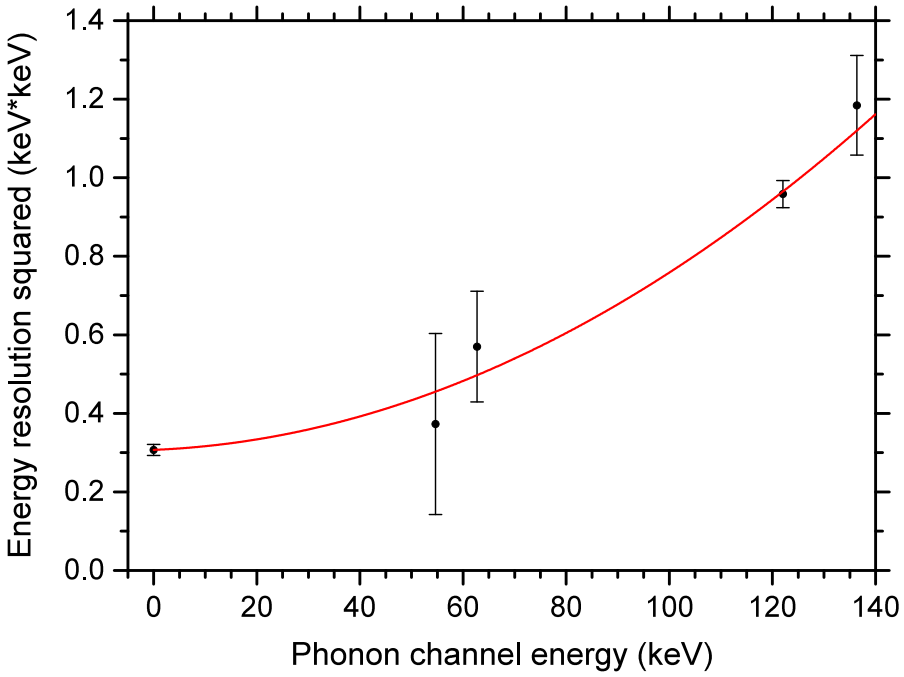

Figure 3.37: The energy resolution (σ) squared versus the energy measured by the phonon channel of the CPSD module with $CaWO_4$ as the absorber. The curve is described by Equation 3.3 fitted to the data, while the energy resolution is measured at the various energy points of the phonon channel with $CaWO_4$ as the absorber under the excitation of ^{57}Co γ-source. The χ^2 of the fit is 0.70, the degree of freedom is 2, and the corresponding p-value is 0.71.

scintillation [163]. The normalised light yield LY is described as:

$$LY(E) = \frac{E_L}{E_P}, \tag{3.5}$$

where E_L is the energy measured in the light channel and E_P is the energy measured in the phonon channel by the CPSD with $CaWO_4$ as the absorber for electron recoil events.

The error of the light yield is described by:

$$\sigma_{LY}(E) = \frac{E_L}{E_P}\sqrt{(\frac{\sigma_L(E)}{E_L})^2 + (\frac{\sigma_P(E)}{E_P})^2 - 2 \cdot \frac{cov_{L,P}(E)}{E_L \cdot E_P}}\,. \tag{3.6}$$

The covariance of the signals between the phonon and the light channels $cov_{L,P}(E)$ is calculated as follows:

$$cov_{L,P}(E) = \sigma_L(E) \cdot \sigma_P(E) \cdot \frac{cov_{L,P}(122\,\mathrm{keV})}{\sigma_L(122\,\mathrm{keV}) \cdot \sigma_P(122\,\mathrm{keV})}\,, \tag{3.7}$$

where the covariance at 122 keV, $cov_{L,P}(122\,\mathrm{keV})$, is estimated by events with 122 keV energy deposit, as shown in the scatter plot of coincident signals between the light channel and the phonon channel of the CPSD (Figure 4.17 in Section 4.3.2).

Finally, $\sigma_{LY}(E)$ multiplied by 1.645 is the value for 90% confidence level. Thus $1 \pm (1.645 \cdot \sigma_{LY}(E))$ marks the 90% boundary values for the electron recoil band in the light yield plot. The result of the light yield plot is shown in Figure 4.19.

3.5 PMT characterisation

The characteristics (dark count rate, single electron response and gain) of the PMT at milli-Kelvin temperatures are important to the application of the PMT as a light detector at this temperature and are discussed in the following.

3.5.1 Dark count rate

Dark count rate is one important characteristic of the PMT and its value at milli-Kelvin temperature for application in rare-event searches, especially when a small number of photons are expected from a signal. A dark current event in the PMT is defined as a signal pulse at the output of the PMT when there are no photons hitting the PMT cathode. In this study, there was no "dark run" when there was no light source shining on the PMT cathode. The scintillation photons from the $CaMoO_4$ or $CaWO_4$ crystal were shining on the PMT cathode under the excitation of external radiation during the experiment. Even without calibration source, the scintillation photons were still present, as there were ambient radioactivity and cosmic muons in the above-ground laboratory as the excitation for scintillation. However, the phonon detector can be used as a veto to search for the intermittent periods without scintillation photons, so a study of dark count rate is still possible. The $CaMoO_4$ data rather than the $CaWO_4$ data are used for the study of dark count rate for several reasons: i) compared to the $CaWO_4$ data, there were fewer scintillation photons in the $CaMoO_4$ data on average for each energy deposit, as discussed in Section 2.6, which means fewer scintillation photons could be mistakenly identified as dark pulses; ii) lower number of scintillation photons per energy deposit detected in the $CaMoO_4$ data means that for a specific number of photons detected, the corresponding phonon signal is larger, leading to higher veto efficiency. Also, the phonon channel in the $CaMoO_4$ setup had a lower noise level, leading to a higher veto efficiency as well; iii) the DAQ in the $CaMoO_4$ data was in the "dead-time free" mode as discussed in Section 2.5.2, which means the dark count estimation is more straightforward, without the need to take into account the significant dead period, as in the $CaWO_4$ data.

There is a report about spontaneous electron emission from a cold metal surface [159]. The electron emission from a cold metal surface is reported as a group

of electrons ("electron burst") emitted from the cold surface from time to time. Consequently, the grouping of pulses in the light channel is avoided in the dark count rate estimation, as it is difficult to know whether the group of pulses is from a scintillation event or an "electron burst".

To estimate the dark count rate, a relatively long period before (set as 20 ms) and after (set as 80 ms) every individual pulse detected by the phonon channel is taken as a "scintillation period". The timestamps of events in the phonon channel are adopted from those after the synchronisation process in the study of coincident signals (Section 3.3). The "scintillation period" (80 ms) may contain a longer period than the actual period within which scintillation happens (the slow scintillation decay time constant for $CaMoO_4$ is ~3.4 ms at 18 mK), but it decreases the possibility of scintillation photons at the tail of a scintillation event contaminating the samples used for dark count rate estimation. Also, an overly long period does not bias the estimation of dark count rate as the dark pulses are distributed randomly in time. The setting of 20 ms before the pulse in the phonon channel is a pre-empting measure to ensure the photons at the start of the scintillation is captured in the "scintillation period". The region outside the "scintillation period" is taken as the "dark period", which is used for dark count rate estimation. All the individual pulses of the photon channel in the "dark period" are taken as dark pulses. The dark count rate is estimated as the number of pulses in the "dark period" divided by the duration of the "dark period". Because the detection efficiency of the phonon channel is not 100%, there might still be "scintillation periods" mistakenly taken as "dark periods" by failing to identify a pulse in the phonon channel. Consequently, this estimation gives only an upper limit of the dark count rate of the PMT. The result of the dark count rate estimation is presented in Section 4.5.1.

3.5.2 Single electron response (SER) and gain

Because of the various processes involved, mainly the secondary electron emission in the various dynode stages, the response of the PMT readout system to a single photoelectron is a random process. The gain of the PMT is related to the DC bias voltage applied to the PMT, as is its dark count rate. Typically, the higher the bias voltage, a PMT gets higher gain and higher dark count rate. Thus, for the study of single electron response, the same set of the $CaMoO_4$ data in the dark count rate study is chosen.

For the $CaMoO_4$ data, to increase the signal-to-noise ratio for triggering purpose, in the firmware level the signal went through a low-pass filter with a 50-ns time constant. The low-pass filter integrated the signal, thus the noise (bipolar) was significantly attenuated while the signal pulse (monopolar) was only modestly attenuated. The integral of the pulse is unchanged by the low-pass filter, as confirmed by a simulation. The tail of the pulse might not be recorded on the disk (Figure 3.38) because, in the "dead-time free" mode, the DAQ stopped writing the data to disk after the 8-sample average dropped below the threshold for at least two 8-sample groups to decrease the data rate (Section 2.5.2). To overcome the tail truncation issue, the analysis algorithm selects those photoelectron pulses with a signal trace of 30 ns before and 100 ns after the peak recorded on the disk. The signal trace is integrated over this period, which corresponds to the charge collected on the PMT anode. The integration of the pulse region over time forms the "SER" region at $x \approx 0.2\,\mathrm{V\,ns}$ in Figure 4.20. After confirming the signal trace also has enough length in pre-trigger baseline region in the record, the algorithm also integrates the same length of the signal trace in the pre-trigger baseline region to characterise the electronic noise level. The integration of pre-trigger baseline region forms the "pedestal" region in Figure 4.20.

From the single electron response, the gain of the PMT can also be extracted.

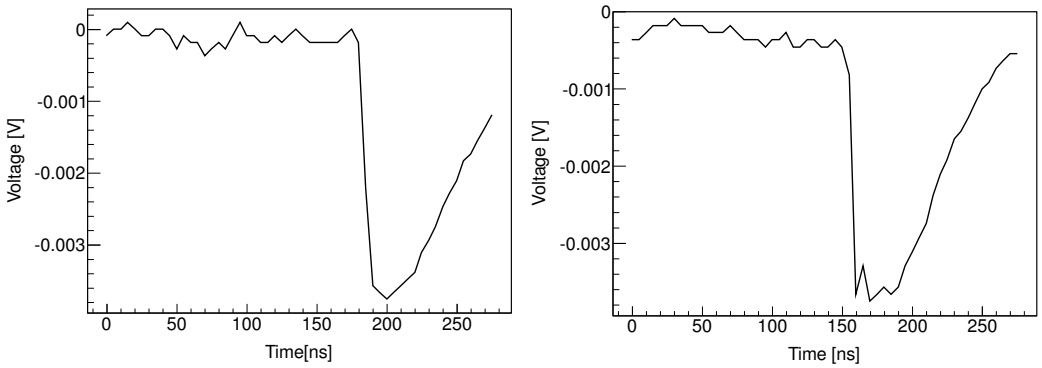

Figure 3.38: Examples of the signal trace recorded on disk for the light channel of the CPSD with $CaMoO_4$ as the absorber. Due to the "dead-time free" DAQ mode, some of the signal traces have been truncated at the tail (left), which is not applicable for the study of the single electron response (SER). The algorithm selects those with a complete signal trace without truncation (right) for the study of SER.

The readout electronics has a gain $G_{electronics} \approx 11$ and it has an input impedance $R = 33.3\,\Omega$. The charge (Q) collected from the anode of the PMT is calculated as $Q = \int V(T) \cdot dT/(R \cdot G_{electronics})$. Because only a single photoelectron starts from the photocathode, the PMT gain is the ratio of Q to the charge of a single electron.

Chapter 4

Results and discussion

This chapter discusses the results obtained with the cryogenic phonon-scintillation detectors (CPSD) equipped with PMT readout. The γ quanta emitted by a ^{57}Co source were used for calibration and characterisation of the detectors. The detailed analyses behind these results were discussed in Chapter 3.

4.1 Phonon channel results

$CaMoO_4$

Figure 4.1 shows the energy spectrum of the phonon channel of the CPSD with $CaMoO_4$ as the absorber excited by a ^{57}Co γ-source. The peaks at 122.1 keV and 136.5 keV are most prominent, as they correspond to the detection of the γ quanta from a ^{57}Co source with the full energy deposited in the absorber. The few events with higher than 136.5 keV energy measured may be explained by ambient radioactivity and cosmic rays. To the left of the 122.1-keV and 136.5-keV peaks, there is a population of events continuously extending to lower energy due to Compton scattering, as some of the γ quanta lose part of their energy by Compton scattering on the components surrounding the CPSD, including the

cryostat and the detector copper housing, before depositing the remaining energy in the absorber crystal. Also, Compton scattering may happen inside the absorber crystal, as the γ-ray deposits only part of the energy in the absorber crystal. The peak at $x = 104.6\,\text{keV}$ is explained by X-ray escape. The mechanism is that the incoming γ-ray ionises an inner-shell electron and then the hole left behind is filled by an outer-shell electron which has higher energy potential. The difference of energy potentials between these two electrons is released as an X-ray, which is characteristic for the electron shell of the atom. With some probability, the X-ray does not interact with the absorber crystal before leaving it. Thus, the energy of the X-ray is not measured by the phonon channel. The horizontal axis value of the escape peak in the energy spectrum (Figure 4.1) is the energy difference between the incoming γ-rays and the corresponding outgoing X-rays. As an example, the escape peak at $x = 104.6\,\text{keV}$ is the result of 122.1 keV of the γ-rays from ^{57}Co minus the 17.5 keV of the X-rays from the K_α line of molybdenum. The same mechanism applies to the 136.5-keV γ-rays from ^{57}Co as well, but the intensity of 136.5-keV γ-quanta is lower than that of 122.1-keV quanta, thus the escape peak corresponding to 136.5 keV minus the K_α line of molybdenum is not prominent above the continuous background. The intensity of the X-ray escape peak depends on the intensity of the incoming γ-rays, the geometry of the absorber crystal as well as the energy of the characteristic X-rays. If the characteristic X-ray deposits its energy in the absorber, the phonon channel still measures the full energy of the incoming γ-ray. The energy resolution (full-width-at-half-maximum, FWHM) for the phonon channel is found to be (0.97 ± 0.03) keV (statistical) at 122.1 keV for the $CaMoO_4$ data, corresponding to a relative resolution (FWHM) of $(0.80 \pm 0.02)\,\%$ (statistical). The overall cut efficiency for the goodness of fit in the template fit is 53.0% for $CaMoO_4$ data.

The baseline energy spectrum of the phonon channel of the CPSD with $CaMoO_4$

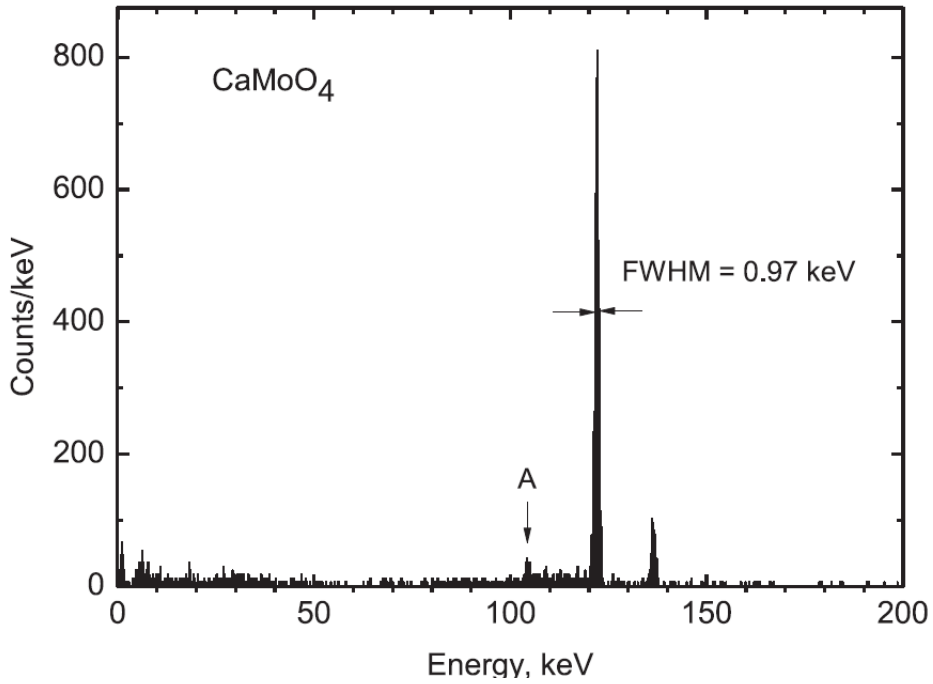

Figure 4.1: Energy spectrum of the phonon channel of the CPSD with $CaMoO_4$ absorber, excited by a ^{57}Co γ-source. The FWHM energy resolution at 122.1 keV is found to be (0.97 ± 0.03) keV (statistical), corresponding to a $(0.80 \pm 0.02)\,\%$ (statistical) relative resolution (FWHM). The escape peak A corresponding to the 122.1 keV minus K_α of molybdenum is less prominent than the escape peaks in $CaWO_4$, as the K line of molybdenum is less energetic, thus this characteristic X-ray is less likely to escape from the absorber crystal. Other escape peaks are too weak to identify. Figure published in [140].

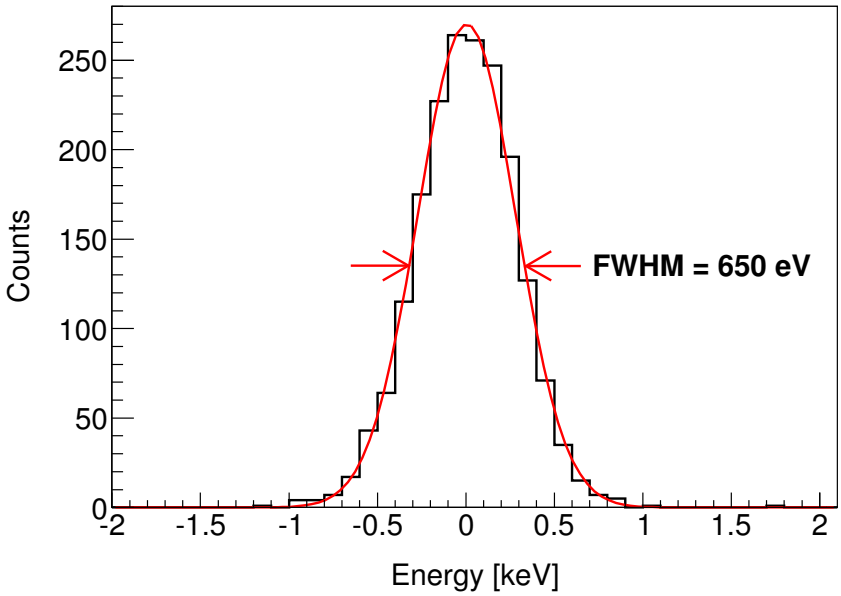

Figure 4.2: The energy spectrum of the baseline region, detected by the phonon channel of the CPSD with a $CaMoO_4$ absorber. The red line represents a fit of a Gaussian function to the data. The FWHM baseline energy resolution is found to be (0.65 ± 0.01) keV (statistical). The χ^2 of the Gaussian fit is 11.82, the degree of freedom is 19, and the corresponding p-value is 0.89.

as the absorber is shown in Figure 4.2 and the baseline energy resolution (FWHM) is determined to be (0.65 ± 0.01) keV (statistical).

$CaWO_4$

Figure 4.3 shows the energy spectrum of the phonon channel of the CPSD with $CaWO_4$ as the absorber excited by a ^{57}Co γ-source. Except for the peaks at 122.1 keV and 136.5 keV and the continuous Compton scatter population, there are more features in the lower energy range. The escape peaks at 62.7 keV and 54.7 keV correspond to 122.1 keV minus the energy taken away by the K_α and K_β characteristic X-rays of tungsten, respectively. An indication of energy loss caused by K_α of tungsten from 136.5 keV, resulting in an escape peak at around 77.2 keV, is also visible. Due to the continuous background (Compton scattering, etc.), further features are difficult to identify. The energy resolution (FWHM) for

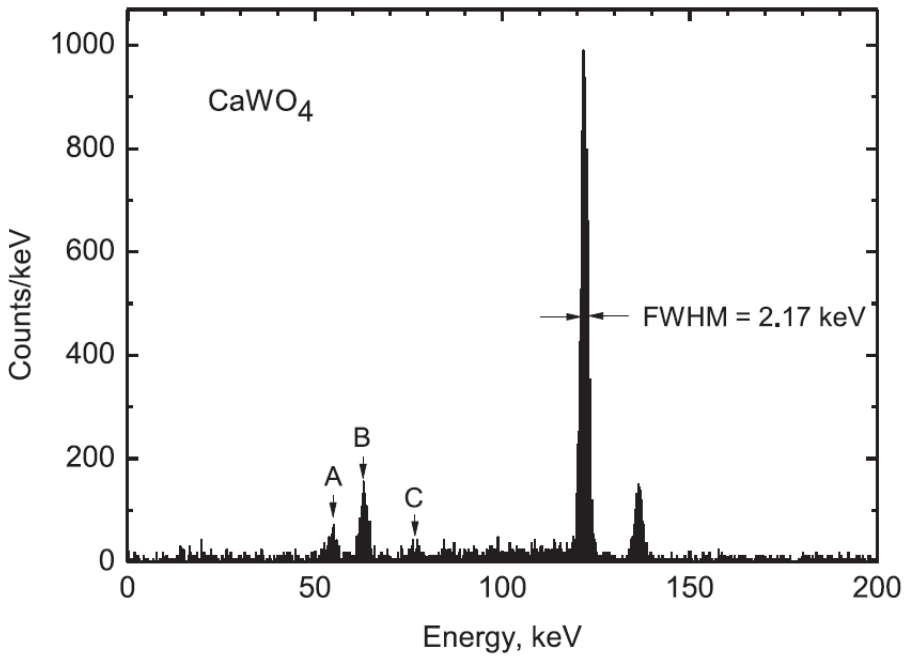

Figure 4.3: Energy spectrum of the phonon channel of the CPSD with $CaWO_4$ absorber, excited by a ^{57}Co γ-source. The FWHM energy resolution at 122.1 keV is found to be (2.17 ± 0.04) keV (statistical), corresponding to a (1.78 ± 0.03)% (statistical) relative resolution (FWHM). The escape peaks A (122.1 keV minus K_β line of the tungsten), B (122.1 keV minus K_α line of the tungsten), and C (136.5 keV minus K_α line of the tungsten) are more prominent than those in the $CaMoO_4$. The reason is that tungsten K_α and K_β characteristic X-rays have higher probabilities of escaping without depositing energy in the absorber crystal, due to the relatively high energy of these two characteristic X-rays. Figure published in [140].

the phonon channel with the $CaWO_4$ absorber is (2.17 ± 0.04) keV (statistical) at 122.1 keV, corresponding to a 1.8% relative resolution (FWHM). The overall cut efficiency by the goodness of fit in the template fit is 50.0% for $CaWO_4$ data.

The baseline energy spectrum of the phonon channel with $CaWO_4$ absorber is shown in Figure 4.4. Even though a single Gaussian function is found to not fully describe the baseline energy spectrum, such effect is negligible for the subsequent analysis, as discussed below. Two scenarios of fitting are evaluated for this spectrum: fitting with one Gaussian function and fitting with the sum of two Gaussian functions. Table 4.1 summarises the results of these two fit scenarios.

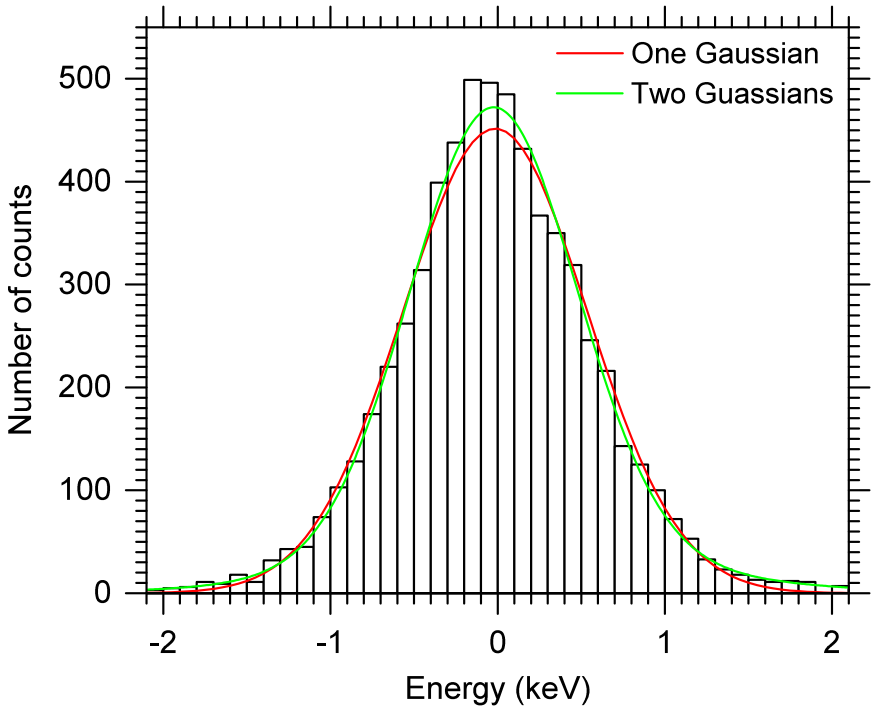

Figure 4.4: The energy spectrum of the baseline regions, detected by the phonon channel of the CPSD with a $CaWO_4$ absorber. The width of this energy spectrum is the baseline energy resolution. Two scenarios of fitting are assessed: fitting with single Gaussian function (shown in red line) and fitting with the sum of two Gaussian functions (shown in red line). Table 4.1 shows the parameters and the results of the fits.

The scenario of fitting with one Gaussian function leads to a large $\chi^2/_{ndf}$ value ($^{90.35}/_{38}$) and a small p-value (3.8×10^{-6}), which indicates the single Gaussian function poorly describes the spectrum. The scenario of fitting the spectrum with the sum of two Gaussian functions results in a smaller $\chi^2/_{ndf}$ value ($^{33.79}/_{35}$) and a larger p-value (0.53), which indicates it better describes the spectrum.

The cause of this feature in the baseline energy spectrum is discussed as follows. As shown in Figure 4.4 and Table 4.1, the baseline energy spectrum is better fitted by a sum of two Gaussian functions than by a single Gaussian function. When fitted by the sum of two Gaussian functions ($G_1(E)$ and $G_2(E)$), $G_1(E)$ has a scale factor of 439.6 ± 22.7 and a Sigma of (0.50 ± 0.02) keV, while $G_2(E)$

Fit scenario	Results of the fit					
	Scale factor	Mean (keV)	Sigma (keV)	χ^2	Degree of freedom (ndf)	p-value
One Gaussian function	451.4 $\pm$7.5	-0.015 $\pm$0.007	0.551 $\pm$0.006	90.35	38	3.8×10^{-6}
Sum of two Gaussian functions	439.6 $\pm$22.7	-0.026 $\pm$0.009	0.50 $\pm$0.02	33.79	35	0.53
	33 $\pm$25	0.12 $\pm$0.12	1.04 $\pm$0.27			

Table 4.1: The results of two fit scenarios: using a single Gaussian function or using the sum of two Gaussian functions to fit the baseline energy spectrum of the phonon channel of the $CaWO_4$ module (Figure 4.4). Only statistical errors are included.

has a scale factor of 33 ± 25 and a Sigma of (1.04 ± 0.27) keV. It means $G_2(E)$ represents relatively short periods of baseline regions with a larger noise level, than the baseline regions represented by $G_1(E)$. Baseline regions with $|E| > 1.7$ keV in Figure 4.4 are almost exclusively distributed within the $G_2(E)$, as $G_1(E) < 1$ for $|E| > 1.7$ keV. Those baseline regions with $|E| > 1.7$ keV are selected and plotted along with the standard deviation of the baseline energy distribution versus time, as shown in Figure 4.5. The standard deviation of the baseline energy distribution represents the baseline noise level which is found to vary over time. Figure 4.5 shows baseline regions with $|E| > 1.7$ keV (exclusively distributed in $G_2(E)$) coincide with local maximums in baseline standard deviation curve, indicating $G_2(E)$ represents the baseline regions with elevated noise level.

The effect of fitting with a non-single Gaussian function for subsequent analysis is discussed as follows. From the fit with one Gaussian function, the standard deviation is (0.551 ± 0.006) keV. From the fit with the sum of two Gaussian functions, the variance is defined as the second central moment. Thus, the variance of the mixture (sum) of two Gaussian functions can be deduced as:

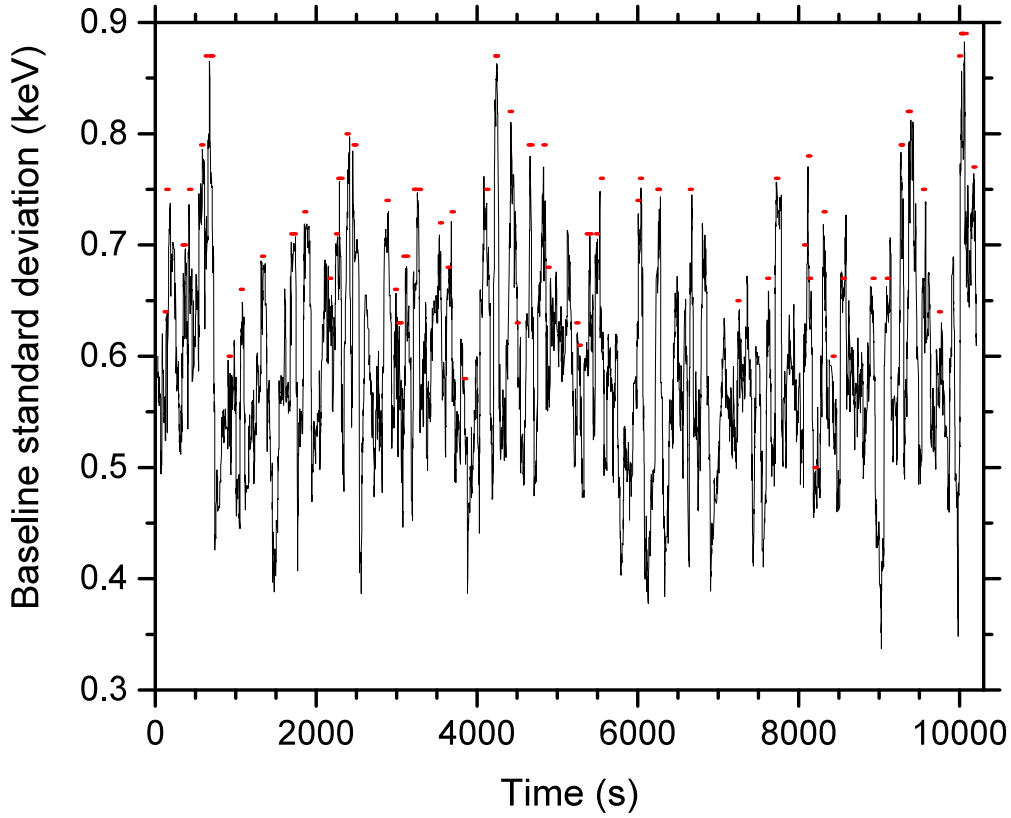

Figure 4.5: Standard deviation of the baseline energy distribution versus time (shown in black line) and baseline regions with $|E| > 1.7$ keV (exclusively from $G_2(E)$, shown in red dots). The vertical coordinates of the red dots are adjusted individually for clarity.

$$\sigma^2_{two\,Gaussian} = \frac{a_1}{a_1+a_2}\sigma_1^2 + \frac{a_2}{a_1+a_2}\sigma_2^2 + \frac{a_1}{a_1+a_2}\frac{a_2}{a_1+a_2}\left(\mu_1-\mu_2\right)^2 \ , \qquad (4.1)$$

where a_1 and a_2 are respectively the scale factor of $G_1(E)$ and $G_2(E)$, σ_1 and σ_2 are respectively the standard deviation of $G_1(E)$ and $G_2(E)$, and μ_1 and μ_2 are respectively the mean of $G_1(E)$ and $G_2(E)$. Using results in Table 4.1, it is found that $\sigma^2_{two\,Gaussian} = 0.307\ \mathrm{keV}^2$. From the covariance matrix of numerical fitting and the error propagation deduced from Equation 4.1, the error on the $\sigma^2_{two\,Gaussian}$ is $0.014\ \mathrm{keV}^2$. In comparison, the variance from the fitting with a single Gaussian function is $(0.304 \pm 0.007)\ \mathrm{keV}^2$. The difference on baseline energy resolution resulted from these two scenarios of fitting is small (~0.5%). Besides representing the energy resolution of the phonon channel of the detector when it approaches zero energy deposit, the baseline energy resolution is also used in the parameterisation of the phonon-channel energy resolution as a function of energy (Section 3.4). Figure 4.6 shows the difference of the parameterisation due to the different baseline energy resolutions resulted from the two fitting scenarios. It is shown that the difference of the parameterisation is negligible. As a result, the deviation of the baseline energy spectrum to a single Gaussian distribution does not have significant impacts on the characterisation of the detector module.

Comparison

Compared with 1.4 keV (FWHM) at 122.1 keV reported for a phonon detector that uses $CaWO_4$ as the absorber for the CRESST experiment [164], the energy resolution of the phonon channel of the CPSD with $CaWO_4$ absorber achieved in this study (2.17 keV FWHM) is inferior. However, the energy resolution measured in the phonon channel of the CPSD with $CaMoO_4$ absorber in this study is better than the resolution of a calorimeter with magnetic metal phonon sensors for the

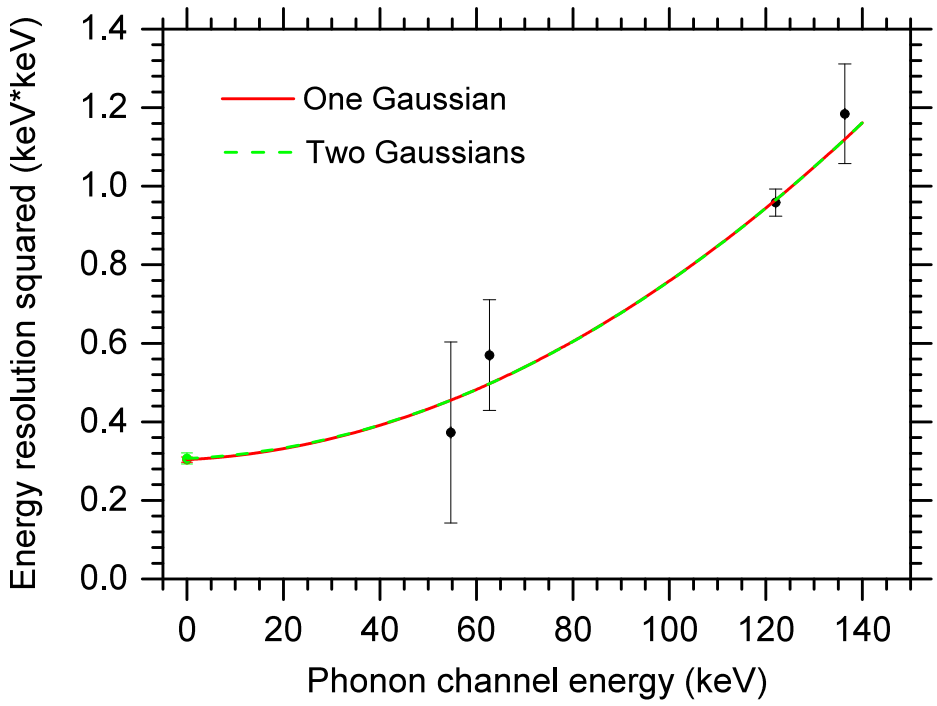

Figure 4.6: The energy resolution (σ) squared versus the energy measured by the phonon channel of the CPSD with $CaWO_4$ as the absorber. The energy resolution data points are measured at the various energy points of the phonon channel, with $CaWO_4$ as the absorber under the excitation of a ^{57}Co γ-source. The red data point at zero of the horizontal axis (hidden behind the green data point) represents the baseline energy resolution obtained from a single Gaussian function fit scenario, and the red curve is the corresponding fitted curve using this baseline energy resolution. The green data point at zero of the horizontal axis represents the baseline energy resolution obtained from the sum of two Gaussian functions fit scenario, and the green curve is the corresponding fitted curve using this baseline energy resolution. Both red and green curves are described by Equation 3.3 fitted to the data.

neutrinoless double-beta decay experiment [165]. The combination of all CPSD parameters at this proof-of-principle stage is far from optimal, as this was not the priority. However, optimising the phonon channel should be achievable, given the excellent energy resolution demonstrated in the phonon channel in many examples of cryogenic detectors (see Reference [100] and references therein).

The cause of the higher noise level and thus inferior energy resolution of the phonon channel of $CaWO_4$ data compared to the $CaMoO_4$ data is not clear. They use the same NTD-Ge sensor as the NTD-Ge sensor was installed on the $CaMoO_4$ crystal, dismantled after the $CaMoO_4$ run finished and later installed on the $CaWO_4$ crystal for the $CaWO_4$ run. The main suspect is the nylon fibres which suspend the calorimeter in the detector holder were not tightened enough in the $CaWO_4$ setup, thus it introduced extra noise in the phonon channel of the $CaWO_4$ data.

4.2 Light channel results

4.2.1 Light channel energy spectrum

The light channel of the CPSD typically has an energy resolution an order of magnitude worse than that of the phonon channel because, for the initial excitation energy, only a few percent are emitted as scintillation photons and contribute as a useful signal to the light channel. It is particularly interesting to evaluate the quality of the scintillation response measured by the PMT at milli-Kelvin temperatures, as this is directly related to the discrimination power of the CPSD. After the data analysis process discussed in Section 3.2, a histogram of the number of photons detected by the PMT channel with the $CaMoO_4$ absorber (Figure 4.7) shows a broad peak at number of photons $N \approx 60$, corresponding to energy deposited in the absorber by 122.1-keV or 136.5-keV γ-rays from ^{57}Co, as the energy

resolution of the light channel is not good enough to resolve these two closely spaced lines. Because the 122.1-keV and 136.5-keV lines are too closely spaced for the light channel to resolve, the resulting energy peak is broader than it would be if there were only one energy, thus the width of the broadened peak is an inaccurate representation of the light channel energy resolution. To investigate the energy resolution of light channel, the study of the coincident signals between the phonon channel and the light channel is used to select the scintillation events corresponding to 122.1keV energy measured by the phonon channel. The resulting histogram of the number of photons, corresponding to 122.1-keV energy deposits is shown in Figure 4.8. The relative energy resolution for the light channel of the CPSD with the $CaMoO_4$ absorber is determined to be $(29.7 \pm 0.3)\%$ (statistical) with 122.1-keV γ excitations.

In Figure 4.9, the histogram of the number of photons in $CaWO_4$ data shows a major peak at the number of photon $N \approx 170$, due to the full energy deposits of 122.1-keV and 136.5-keV γ quanta in the absorber. As with $CaMoO_4$, the energy resolution of the photon channel is not good enough to resolve the two lines. Also, there is a peak at the number of photons $N \approx 80$, corresponding to the escape lines of tungsten and the energy resolution is not good enough to resolve the individual lines. Again, the coincident signals between the phonon and the light channel are used to select the scintillation events corresponding to the full energy deposit by 122.1-keV γ quanta in the absorber. The FWHM energy resolution of the light channel with a $CaWO_4$ absorber is $(19.9 \pm 0.2)\%$ (statistical) at 122.1 keV with γ excitation (Figure 4.10). Comparing this result to other experiments, the best energy resolution at 122.1 keV for $CaWO_4$ has been measured to be 14.6% at room temperature, for a PMT in optical contact with the scintillator [166]. When $CaWO_4$ was used in CPSD applications, a cryogenic light detector has achieved an energy resolution equal to 17% [120]. Nonetheless, typical energy resolutions

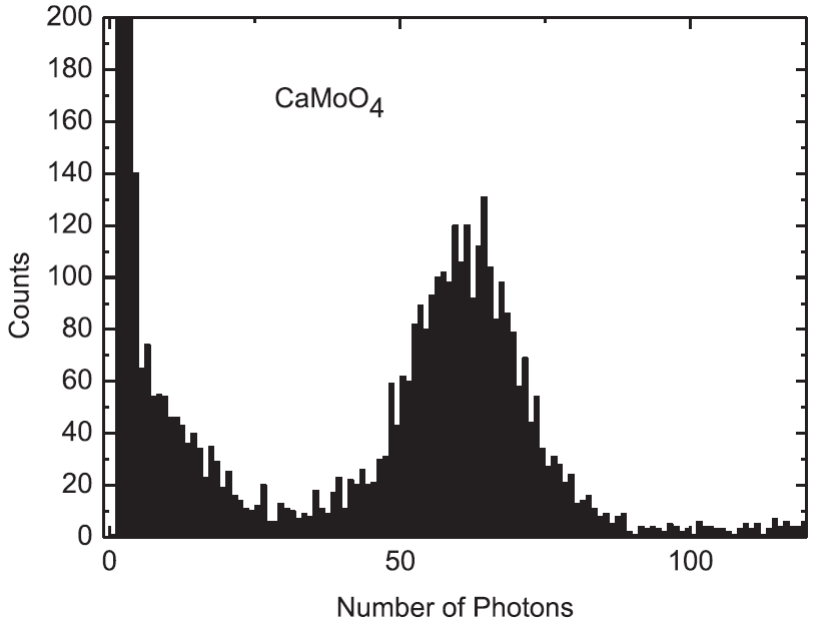

Figure 4.7: Histogram of the number of photons detected in the light channel of the CPSD with a $CaMoO_4$ absorber, excited by a ^{57}Co γ-source. The peak at $x \approx 60$ is due to the 122.1-keV and 136.5-keV γ quanta from ^{57}Co, and the two lines are not resolved by the light channel. Figure published in [140].

in Dark Matter search experiments are 20% [167]. When compared with light detectors based on cryogenic calorimeter, the light channel with PMT readout of the CPSD with a $CaWO_4$ absorber in this work shows a competitive energy resolution.

The $CaWO_4$ data shows a larger number of photons detected by the PMT, thus a better energy resolution than that of the $CaMoO_4$. As discussed in Section 2.6, although the two crystals have quite similar absolute light yields of scintillation at cryogenic temperatures, $CaWO_4$ has a better spectral overlap of its emission spectrum and the PMT spectral sensitivity than that of $CaMoO_4$ [117].

4.2.2 Scintillation Decay

The scintillation decay curves of $CaWO_4$ and $CaMoO_4$ scintillators at ~18 mK, measured by the PMT channel of the CPSD (2.10), can be characterised by the

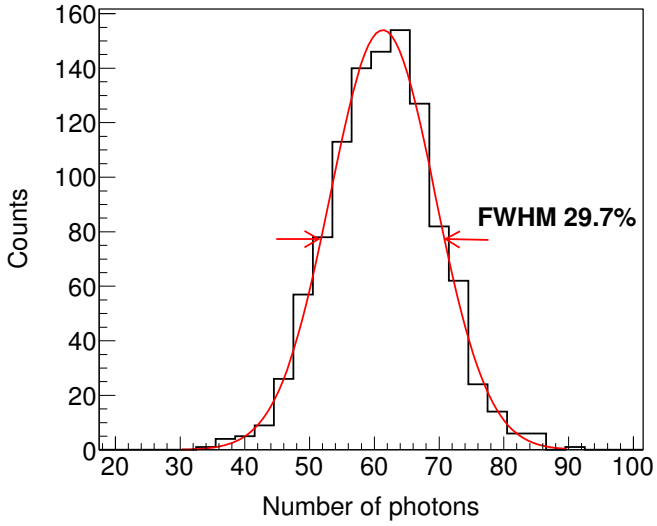

Figure 4.8: Histogram of the number of photons detected in the light channel of the CPSD with a $CaMoO_4$ absorber, excited by 122.1-keV γ quanta. The 122.1-keV γ quanta are selected by the energy measured at the phonon channel, with the study of the coincident signals between the light channel and the phonon channel of the CPSD. The FWHM relative energy resolution is found to be $(29.7 \pm 0.3)\%$ (statistical). The χ^2 of the Gaussian fit is 10.1, the degree of freedom is 15, and the corresponding p-value is 0.81.

sum of two exponential functions as follows:

$$y(t) = A_f \exp(-\tau_f^{-1} t) + A_s \exp(-\tau_s^{-1} t) + y_0 \,, \tag{4.2}$$

where y is the intensity of the scintillation light (number of scintillation photons emitted per unit time), t is time since the start of the scintillation, A_f is the amplitude of the fast scintillation decay component, τ_f is the fast scintillation decay time constant, A_s is the amplitude of the slow scintillation decay component, τ_s is the slow scintillation decay time constant, and y_0 is a constant (accounting for the random dark pulses). The two exponential functions represent the fast and slow decay modes, corresponding to the relaxation of excited states in the scintillator. Table 4.2 shows the values of the parameters, after fitting Equation 4.2 to the scintillation decay curves in Figure 4.11

The two scintillation decay curves show significant differences. First, the slow

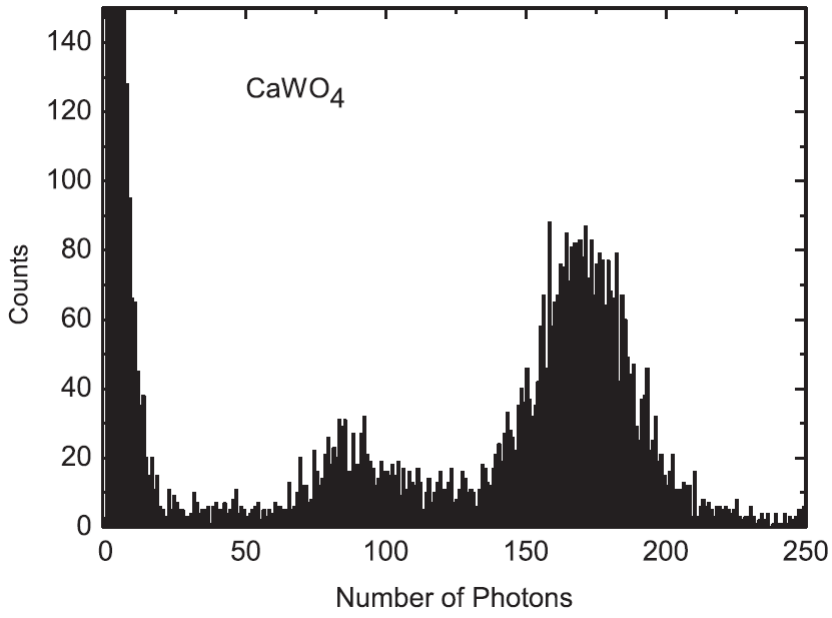

Figure 4.9: Histogram of the number of photons detected in the light channel of the CPSD with a $CaWO_4$ absorber, excited by a ^{57}Co γ-source. The peak at $x \approx 170$ corresponds to the absorber detecting the full 122.1-keV and 136.5-keV γ quanta from ^{57}Co, and the two lines are not resolved by the light channel. The peak at $x \approx 80$ corresponds to the escape lines of tungstate. Figure published in [140].

Table 4.2: Parameters of scintillation decay kinetics in $CaWO_4$ and $CaMoO_4$ crystals at ~18 mK obtained from fitting the decay curves in Figure 4.11 by Equation 4.2.

Crystal	A_f	τ_f (μs)	A_s	τ_s (μs)	y_0
$CaWO_4$	460	12.8(6)	2600	382(2)	58
$CaMoO_4$	2500	40.6(8)	158	3410(30)	0

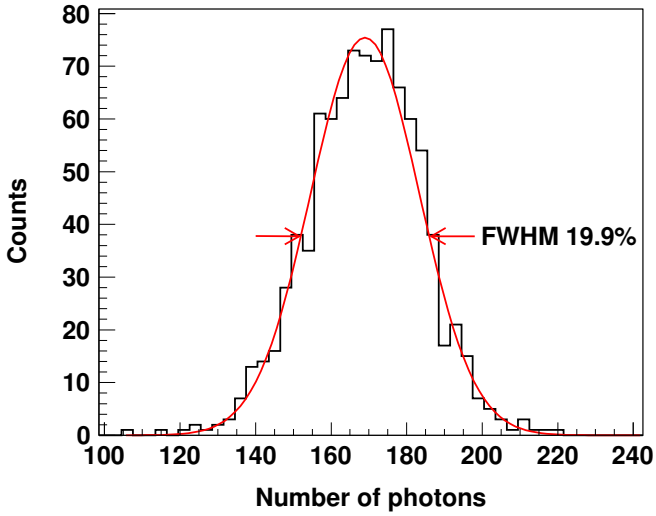

Figure 4.10: Histogram of the number of photons detected in the light channel of the CPSD with a $CaWO_4$ absorber, excited by 122.1-keV γ quanta. The 122.1-keV γ quanta are selected by the energy measured at the phonon channel, with the study of the coincident signals between the light channel and the phonon channel of the CPSD. The relative energy resolution (FWHM) is found to be $(19.9 \pm 0.2)\%$ (statistical). The χ^2 of the Gaussian fit is 21.2, the degree of freedom is 31, and the corresponding p-value is 0.67.

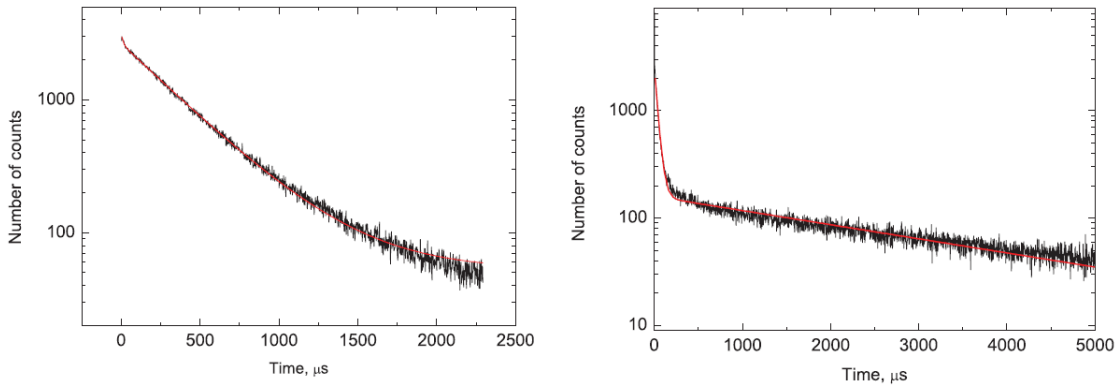

Figure 4.11: $CaWO_4$ (left) and $CaMoO_4$(right) scintillation decay curves, both measured at ~18 mK by the light channel of the CPSD with excitation from a ^{57}Co source. The red lines are described in Equation 4.2, fitted to the data. Figure published in [140].

decay component dominates in $CaWO_4$, while the fast decay component is quite small, as shown by the amplitudes of the two components. In contrast, the fast decay component dominates at the begin the $CaMoO_4$ scintillation decay curve, and slow decay component emerges only later when the fast decay component vanishes. Second, the slow decay component of the $CaWO_4$ is about one order of magnitude shorter than that of $CaMoO_4$. The model of emission centres [168, 141], which is developed for tungstate and molybdate crystals, could explain both of these features.

4.3 Result of coincident signals

4.3.1 Scatter plots and energy spectrum plots of coincident signals

Figure 4.12 shows the scatter plot with energy measured in the phonon channel (horizontal axis) versus the number of photons measured in the light channel (vertical axis) in the CPSD module with the $CaMoO_4$ absorber, with the excitation from a ^{57}Co γ-source. Electron recoil events induced by γ interactions form the diagonal band. Nuclear recoils induced by neutron and massive particles have much less light yield and these events will subsequently create a separate band with much smaller gradients in the scatter plot (not visible here as only a ^{57}Co γ-source was deployed near the detectors). Most of the points are in the diagonal band, which indicates good coincidence between the two channels. The population of 122.1-keV and 136.5-keV energy deposits are visible.

Figure 4.13 shows a similar scatter plot for the $CaWO_4$ data. Most of the points lie near the diagonal band. In addition to the 122.1-keV and 136.5-keV energy deposits, the population from 55-keV and 63-keV escape lines of tungstate are also visible.

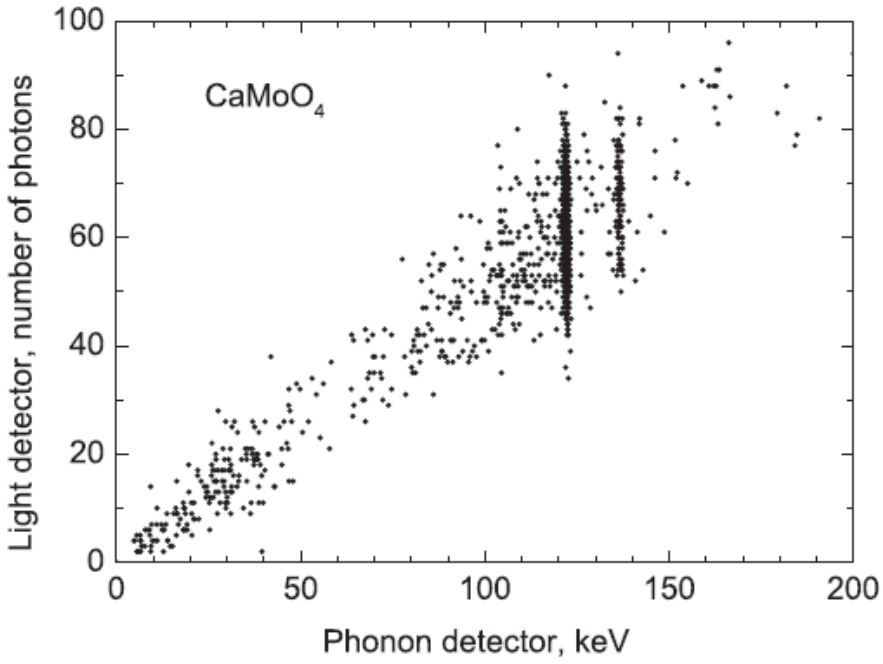

Figure 4.12: Scatter plot of energy measured by the phonon channel (horizontal axis) versus the number of photons measured by the light channel (vertical axis) in the CPSD with a $CaMoO_4$ absorber, exposed to a ^{57}Co γ-source. The diagonal band corresponds to electron recoil events induced by γ quanta from the ^{57}Co source, and the 122-keV and 136-keV lines are visible. Figure published in [140].

Figure 4.14 shows the energy spectrum measured in the phonon channel overlapping with the histogram of the number of photons measured in the light channel of the CPSD with $CaMoO_4$ absorber as another way to plot the same events in the scatter plot. Compared to Figure 4.7, there are very few events with a low number (<20) of photons detected in the light channel in Figure 4.14, indicating the majority of events with a low number of photons shown in Figure 4.7 are not caused by energy deposits from γ quanta. They are probably caused by dark counts in the PMT and artefacts in the photon grouping algorithm.

Figure 4.15 shows similar histograms for coincident signals of the CPSD using the $CaWO_4$ absorber. It also shows very few events with a low number (<20) of photons compared to Figure 4.9.

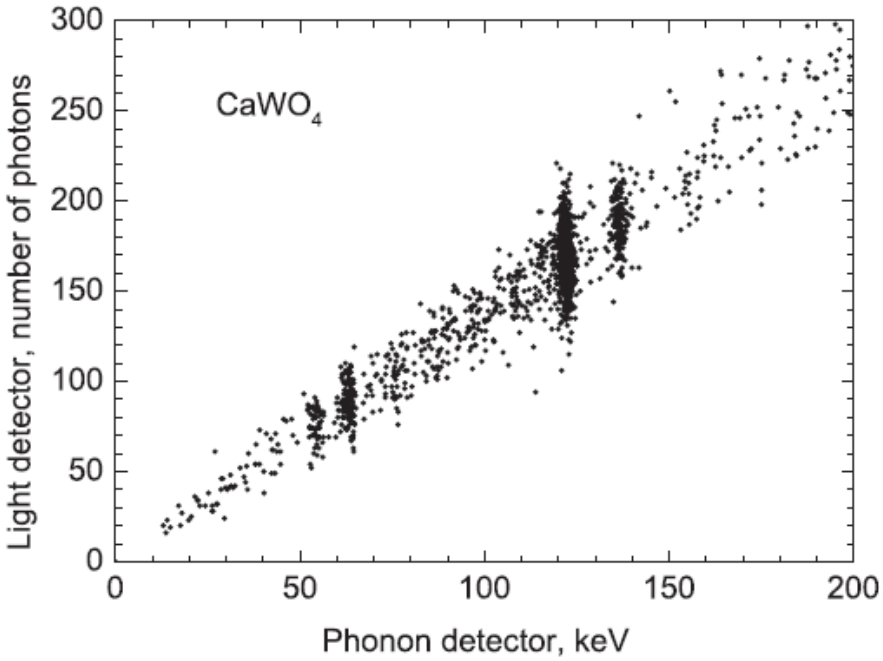

Figure 4.13: Scatter plot of energy measured by the phonon channel (horizontal axis) versus the number of photons measured by the light channel (vertical axis) in the CPSD with a $CaWO_4$ absorber, exposed to a ^{57}Co γ-source. The diagonal band corresponds to electron recoil events induced by γ quanta from the ^{57}Co source. Prominent lines at 122 keV and 136 keV, corresponding to full energy deposits of the γ quanta from the ^{57}Co source are visible. Also, the population corresponding to escapes lines of the tungstate is visible at $x = 55$ keV and $x = 63$ keV. Figure published in [140].

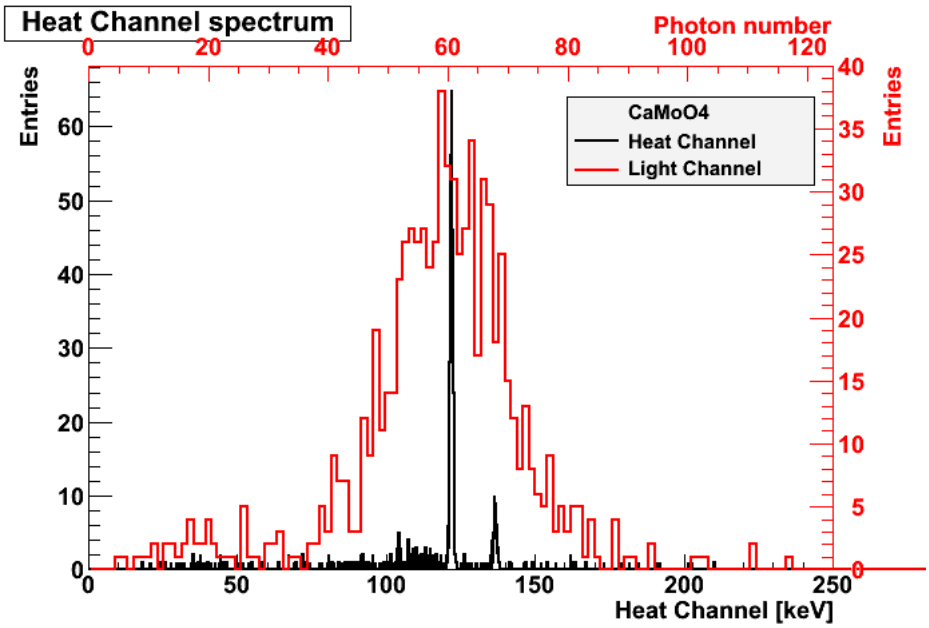

Figure 4.14: The energy spectrum measured by the phonon channel (black) and the histogram of the number of photons measured by the light channel (red), in the CPSD with $CaMoO_4$ absorber. The events represented are those with corresponding signals in both channels in the coincidence window.

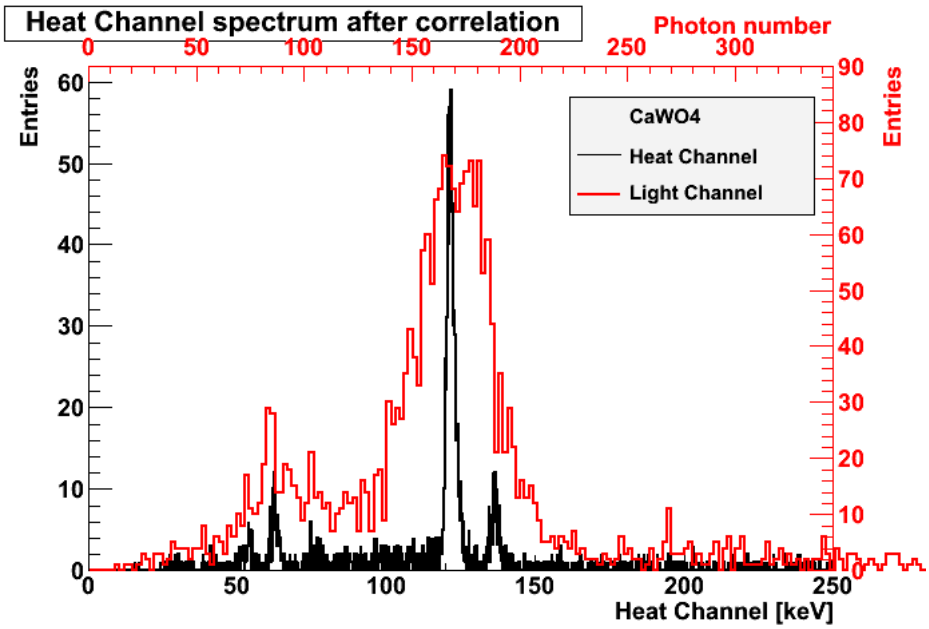

Figure 4.15: The energy spectrum measured by the phonon channel (black) and the histogram of the number of photons measured by the light channel (red), in the CPSD with $CaWO_4$ absorber. The events represented are those with corresponding signals in both channels in the coincidence window.

4.3.2 Anti-correlation between phonon and light channel

As discussed in detail in Reference [118], anti-correlation between the energy measured by phonon and light channel can be used to improve the energy resolution of the detector module. The procedure discussed in Reference [118] is applied to this experiment as discussed below. Assuming there are no blind channels (channels in which the energy deposited to the crystal do not contribute to the readout signal, such as photons escaped from the detector module if there are any), or a fixed fraction of the total energy is lost in blind channels, the cause of the anti-correlation is described as when the energy detected by light channel fluctuates up (more photons detected by light detector), the phonon channel tends to fluctuate down accordingly (fewer photons get absorbed in the crystal and contribute to phonon channel signal), and vice versa. In other words, the fluctuations between the two channels are anti-correlated. Consequently, by combing the signal from the two channel in an appropriate way, the energy resolution can be improved compared to that from a single channel, because the effect of the energy fluctuations between the two channels is significantly mitigated.

As shown in Figure 4.16, the energy correction by combing the signal between the two channels is performed through rotation of the coordinate in the scatter plot. Assuming a rotation angle ϑ, the projections of the events on the rotated phonon coordinate and rotated light coordinate can be described as:

$$\text{Phonon}_\theta = \text{Phonon} \cdot \cos\theta + \text{Light} \cdot \sin\theta \,, \tag{4.3}$$

$$\text{Light}_\theta = -\text{Phonon} \cdot \sin\theta + \text{Light} \cdot \cos\theta \,. \tag{4.4}$$

One cause for anti-correlation in CPSD module is position-dependent light collection efficiency. The anti-correlation is prominent when the amplitude of

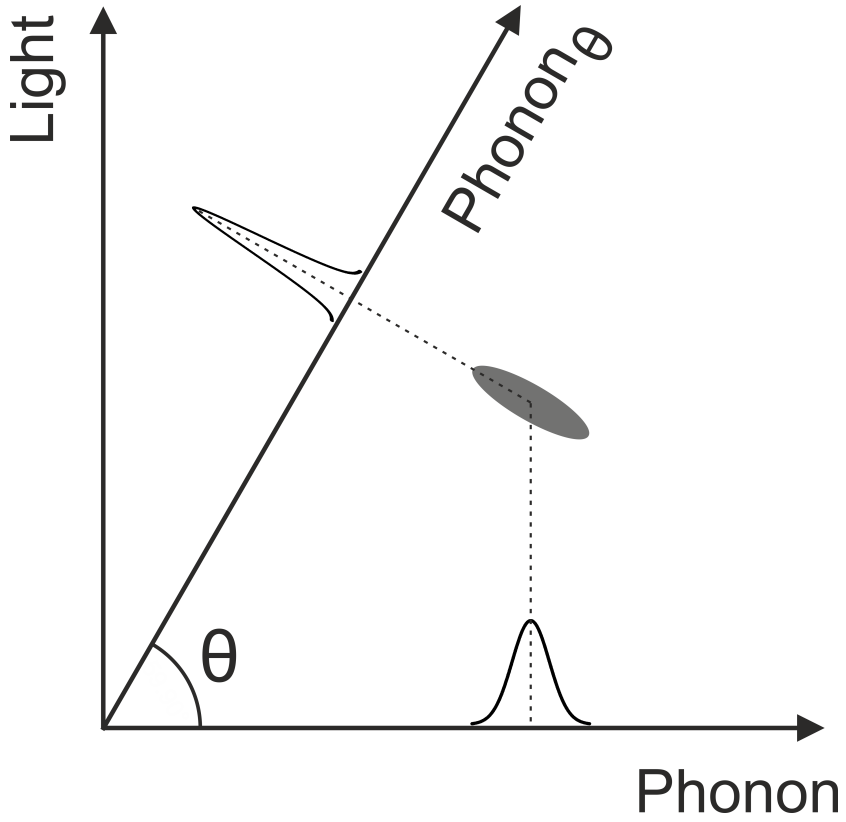

Figure 4.16: A schematic view of using the anti-correlation between phonon channel and light channel for energy correction, to improve the energy resolution. The ellipse represents the monochromatic events (e.g. events from 122-keV γ-rays from ^{57}Co source) in the scatter plot. By a rotation of coordinate in the scatter plot, in which the value in the rotated phonon channel Phonon$_\vartheta$ coordinate is derived from the combination of the values in the original phonon channel coordinate and original light channel coordinate, the energy resolution from the phonon channel can be improved.

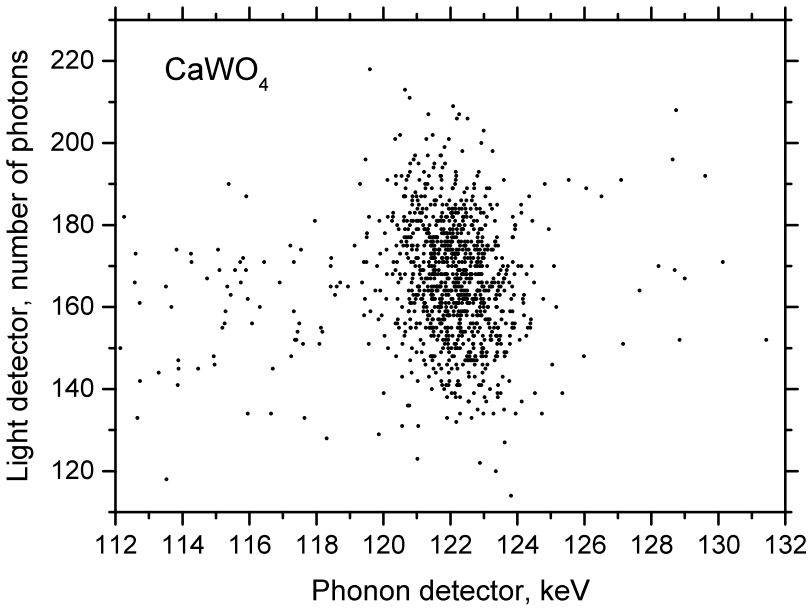

Figure 4.17: Zoom-in view of the scatter plot about the population of 122-keV events from ^{57}Co in the $CaWO_4$ module. A very weak anti-correlation between the phonon channel and light channel is visible and the Pearson product-moment correlation coefficient is -0.20, deduced from the events between 119.5 keV and 124.5 keV in the phonon detector coordinate.

fluctuations between the two channels is much larger than the intrinsic energy resolution of the detectors. However, as shown in Figure 4.17, the events from 122-keV γ-rays show a relatively weak anti-correlation trend (correlation coefficient -0.20) in the scatter plot. It indicates that the amplitude of fluctuations between the two channels is comparable or smaller than the intrinsic energy resolution of the detectors. One can also see from Figure 4.17 that the rotation angle ϑ (meaning shown in Figure 4.16) is quite small, and the exact value is discussed below.

Nonetheless, energy correction using the anti-correlation between the phonon channel and the light channel is still possible. To search for the correct rotation angle θ, the energy resolution in the projected Phonon$_\theta$ axis is evaluated. The rotation angle θ which results in the best energy resolution in Phonon$_\theta$ axis is

adopted as the correct rotation angle. To implement this method, the value of rotation angle θ varies between 0° to 9°, and an energy spectrum in the Phonon$_\theta$ axis for each rotation angle is produced by using Equation 4.3 to project the data points to the Phonon$_\theta$ axis. By using a Gaussian function to fit the 122-keV peak in each energy spectrum, the FWHM energy resolutions are evaluated, as shown in Figure 4.18. The optimal rotation angle θ for $CaWO_4$ module is determined to be 1.15°, leading to an FWHM energy resolution of (2.09 ± 0.05) keV (statistical) at 122.1 keV, a 3.7% improvement compared to the energy resolution obtained by phonon detector only (2.17 keV).

An alternative method to evaluate the rotation angle by fitting a negative slope line to the monochromatic event populations [118] (e.g. 122-keV events from ^{57}Co) has been tried out. However, due to the large spread in the monochromatic populations in the scatter plot, this method does not work very well in this experiment.

It is difficult to evaluate quantitatively how the anti-correlation would improve the energy resolution in the scenario with an improved light collection (thus improved light channel energy resolution). The extent of anti-correlation between on several factors, such as the position-dependent light collection in the crystal and the process of energy escaped to insensitive channels (such as light escape from the module or get absorbed on the reflector).

4.4 Light yield plot

Figure 4.19 shows the scatter plot with energy measured in the phonon channel (horizontal axis) versus the light yield (ratio of the number of photons to the phonon signal) for the $CaWO_4$ data. Because the light yield is normalised relative to those in the electron recoils, the light yield for the energy deposits from

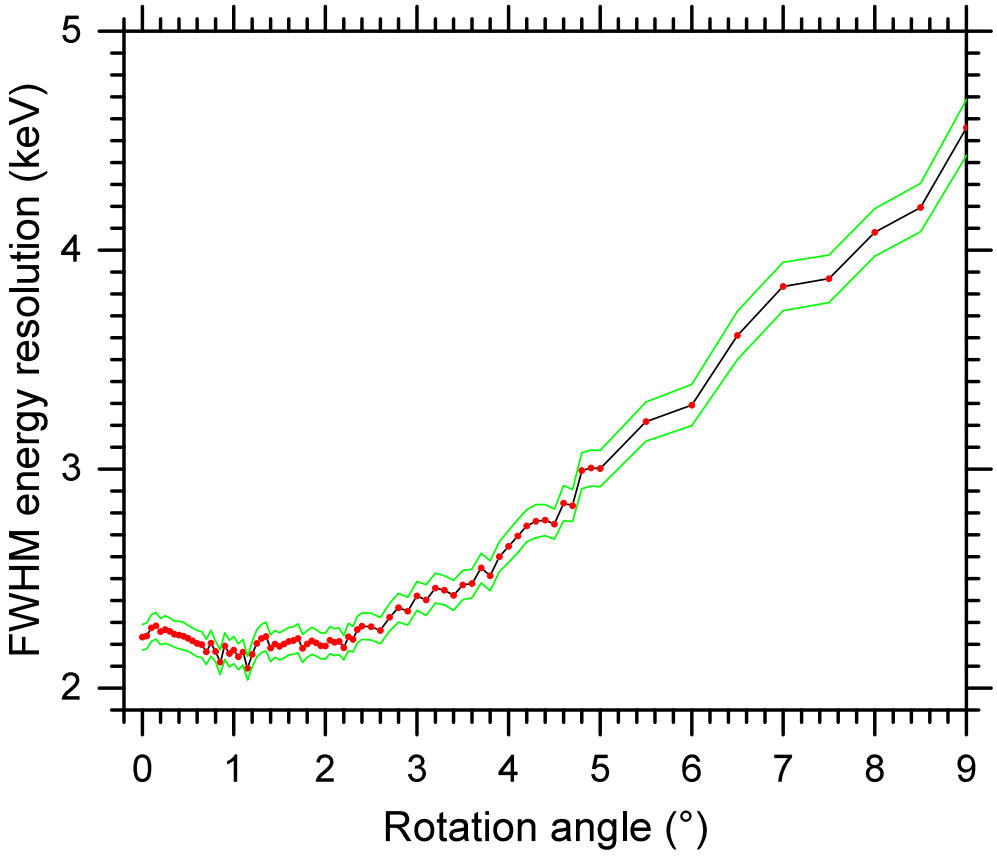

Figure 4.18: FWHM energy resolution in the Phonon$_\theta$ axis versus the rotation angle θ in the CPSD module with $CaWO_4$ as the absorber. The red dots represent the sampling points, and the black lines between the red dots are just for guidance. The green lines on the upper and lower sides represent the statistical error of the FWHM energy resolution.

the ^{57}Co γ-source is distributed around one. Because no neutron source has been deployed in this experiment, there are no events in the nuclear recoil band in this light yield plot. The lines show the 90% confidence level upper bound and lower bound for the electron recoil event population, which means 80% of the electron recoil events are expected between these two lines. Because the light channel has an energy resolution that is one order of magnitude worse than that in the phonon channel, these two 90% confidence lines are mainly decided by the light channel performance, which means the light channel performance decides the discrimination power between electron recoils and nuclear recoils in the CPSD. Compared to a cryogenic calorimeter-based light detector, there is minimal baseline noise in the low-temperature PMT as a light detector because photon counting of the PMT is a digital readout. The digital readout scheme means that, even though the light detector based on a PMT in this work has a slightly inferior energy resolution compared to the best light detector based on cryogenic calorimeter at the energy of 122.1 keV_{ee}, its energy resolution could become more competitive in the low-energy region. As shown in Figure 4.19, below 40 keV, the lower bound for the electron recoil events in this work is tighter than the CRESST 2015 result, which implies that better discrimination between nuclear and electron recoils could be achieved. For WIMP searches, the region of interest for energy deposits in $CaWO_4$ is below 40 keV [45]. It should be noted that the tighter constraint on electron recoil band compared to the CRESST 2015 result is partly due to not taking the non-proportionality of the $CaWO_4$ scintillation into account because not enough low energy events exist in this data set. In contrast, the non-proportionality effects are included in the CRESST 2015 result. Also, the energy resolution of the light detector in this work is not verified in the low-energy region. The extrapolation of energy resolution to the low-energy region in this work uses $\sigma_{E_L} = A\sqrt{E_L}$ relation (σ_{E_L} is the energy resolution of the light detector, A is a factor, E_L is the

energy detected by the light detector), but this relation has not been verified. In contrast, the CRESST light detector follows $\sigma_{E_L} = \sqrt{A_0 + A_1 E_L + A_2 E_L^2}$, where A_0, A_1 and A_2 are different factors [169].

The tighter boundaries of the electron recoil band below 40 keV shown in Figure 4.19 demonstrates the CPSD with a PMT as the light detector can be better than the existing CRESST detectors in terms of discrimination power, while the performance of PMTs is much more consistent and reliable than the cryogenic calorimeter-based light detectors. These features make the cold PMT in this thesis a very attractive alternative solution to the scintillation light detection in CPSD experiments for rare event searches. The cold PMT can potentially revolutionise the CPSD experiments for rare event searches, as the performance consistency issue make it difficult for those experiments to scale up as quickly as the liquid noble gas experiments do. However, the intrinsic radioactivity of PMTs (detailed discussion in Section 4.6) causes more concerns than the cryogenic calorimeter-based light detectors, which needs to be evaluated before they can be applied in CPSD rare event searches.

4.5 PMT characterisation results

4.5.1 Dark count rate result

The upper limit of the dark count rate is found to be (4.97 ± 0.04) Hz (statistical), as shown in Table 4.3. This rate is relatively low and it is important for the application of the cold PMT as a light channel readout in a rare-event search experiment. For the application of the cold PMT in CPSD in dark matter searches, or as the light detector to detect Cherenkov light for the purpose of an alpha veto in a TeO_2 cryogenic experiment in neutrinoless double-beta decay (Section 5.2.2), the number of photons detected for a signal will be only a few, so low

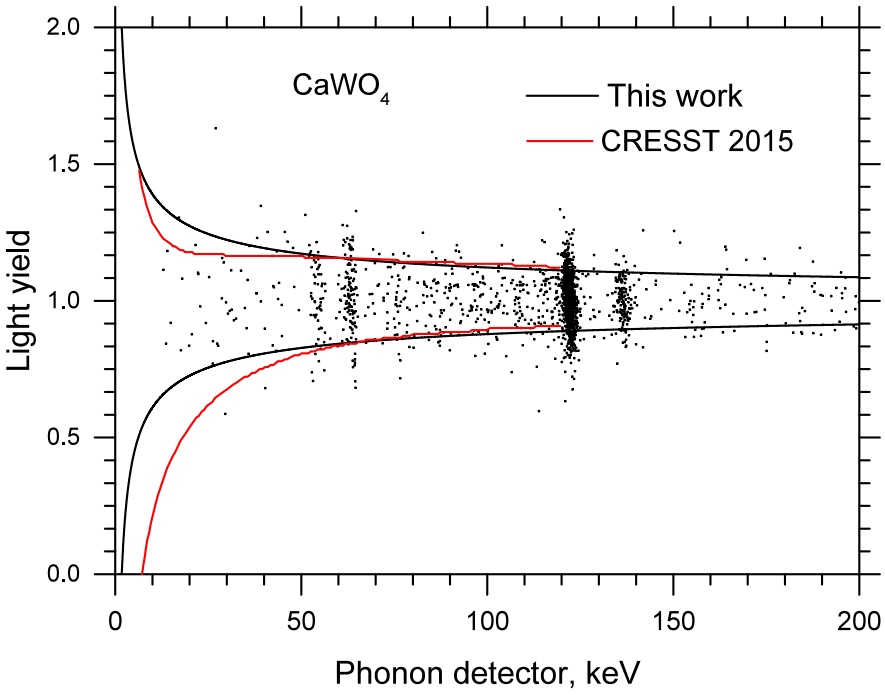

Figure 4.19: Scatter plot of light yield (vertical axis) versus the energy measured by the phonon channel (horizontal axis) in the CPSD module with $CaWO_4$ as the absorber, exposed to a ^{57}Co γ-source. No neutron source was applied, thus there is no nuclear recoil population. The upper and lower 90% confidence level lines are shown in black, which means 80% of the electron recoil events are expected between these two lines. For comparison, the upper and lower 90% confidence level lines from the CRESST 2015 results are shown in red [45]. No effects from scintillator non-proportionality are included in the light yield analysis of this work, while the CRESST 2015 result takes into account the scintillator non-proportionality effect. Also, the energy resolution of the light detector in the low-energy region in this work is not verified.

Table 4.3: The parameters in the dark count rate estimation. Because the veto efficiency by the phonon channel in not proven to be 100%, only an upper limit of the dark count rate can be determined.

	Number of pulses	Duration
Whole data file	336,549	3544.3 s
Veto period	320,807	376.8 s
Dark period	15,742	3167.5 s
Dark count rate	4.97(4) Hz	

dark count rate would ensure high efficiency and good rejection power in particle identification.

4.5.2 Single electron response result and gain of the PMT

As shown in Figure 4.20, the single electron response (SER) peak centred at $x \approx 0.2\,\mathrm{V\,ns}$ is well separated from the pedestal region centred at $x = 0$ by electronic noise. After fitting a Gaussian function to the SER region of the histogram, the voltage integral from the single photoelectron pulse is found to be 0.196 V ns, with a width (σ) of 0.081 V ns. This corresponds to a single photoelectron resolution (σ) of 41%. After taking into account the input impedance and the gain of the readout electronics, the gain of the PMT is determined to be 3.3×10^6. This demonstrates that the PMT and the readout electronics in this work have the capabilities to detect the majority of single photoelectron pulses above the electronic noise.

4.6 PMT intrinsic radioactive background

4.6.1 Radioactivity comparison

As discussed in Section 1.5, the components used to construct the detector need to be low in radioactivity, as the expected signal from dark matter is rare (generally speaking, $<0.1\ \mathrm{count\,kg^{-1}\,keV^{-1}\,year^{-1}}$). Even though the radioactive contaminations in the scintillation crystals have been the dominating factor in the

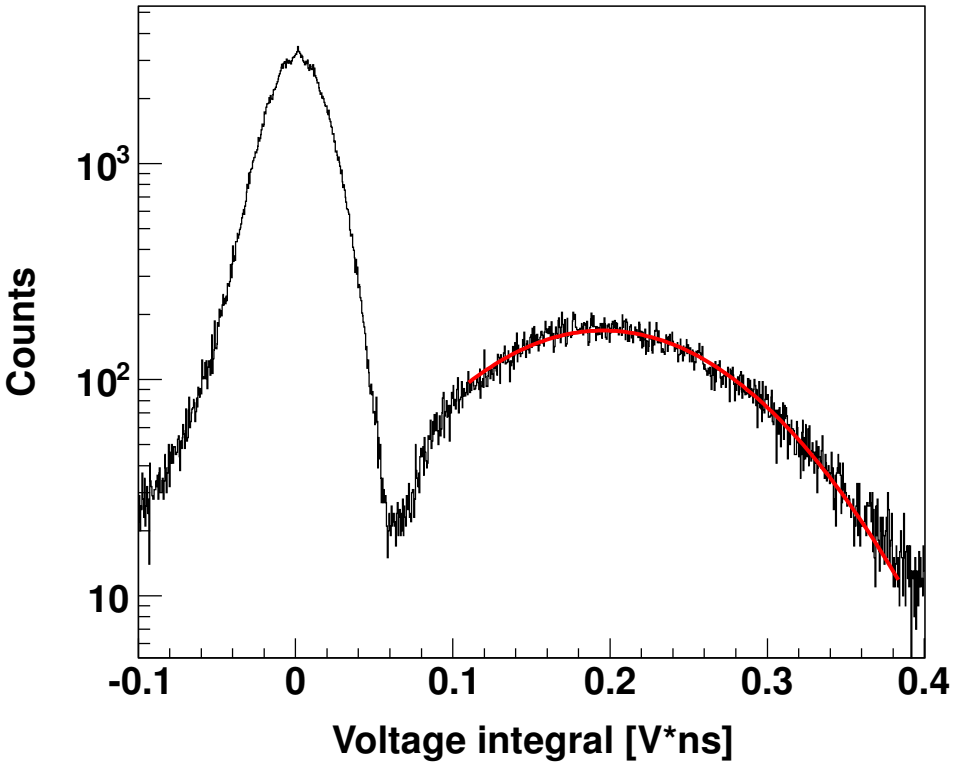

Figure 4.20: Histogram of the voltage integral in the photoelectron pulse region and the pre-trigger baseline region in the records at milli-Kelvin temperatures. The entries in the pedestal region around zero in the horizontal axis are from the voltage integral over the pre-trigger baseline regions. The entries with higher voltage integral (centred at $x \approx 0.2\,\mathrm{V\,ns}$) are from the photoelectron pulses. The red curve shows a Gaussian function fitted to the data. A low-pass filter with 50 ns time constant was applied to the signal trace at the firmware level of the DAQ. This signal includes readout electronics gain (~11).

radioactivity in CPSD [164], the latest development in the purification of scintillation crystal during the crystal growth process and the proposal to reduce the size of the scintillation crystal could change this [170, 171]. Also, the introduction of PMTs into CPSD technology is a new concept, thus the radioactivity contribution from the PMT needs to be evaluated. The radioactivity of a similar PMT model (Hamamatsu R8520-06-Al) has been measured by the XENON100 collaboration [172, 173]. Even though the PMT model in the XENON100 experiment has Al strips rather than the Pt underlay in the PMT used in this thesis, the radioactivity of XENON100 PMTs is used as a first approximation for the evaluation here. The average contaminations of ^{238}U, ^{232}Th, ^{40}K, ^{60}Co and ^{137}Cs for the R8520-06-Al PMTs installed in XENON100 are (0.25 ± 0.04), (0.5 ± 0.1), (8.1 ± 0.9), (0.75 ± 0.08) and 0.17 mBq/PMT, respectively. The intrinsic radioactivity of the most radiopure $CaWO_4$ crystal ever published — TUM40, and that of R8520-06-Al PMTs are shown in Table 4.4. Note that unlike the conventional ways of using γ-ray spectroscopy or ICP-MS to measure the radioactivity, TUM40 was instrumented and operated as a calorimeter at the CRESST cryostat, so its dark matter search data is also used to measure the α-events (> 2 MeV) from the U/Th chains. Because α-particles cannot travel far from the source, practically all the measured α-particles are from the internal contamination of the crystal. The calorimeter directly measures the radioactivity of all the α-emitters inside the crystal. With this information, the intrinsic radioactivity of the β-emitters in the U/Th chains can be deduced. The intrinsic radioactivity of the TUM40 crystal, combined with the cosmogenic activation of W isotopes, accounts for ~50% of the total ER background in the energy region for WIMP search (below 40 keV) in CRESST [171]. Table 4.4 shows that, compared to the TUM40 crystal, the R8520-06-Al PMT has similar radioactivity levels in the ^{238}U early chain and in the ^{235}U chain. The ^{235}U activity of the PMT is deduced from the measured contamination of ^{238}U,

assuming a 0.72% natural abundance of ^{235}U. The PMT has a much higher activity in the ^{238}U late chain (a factor of ~10) and the ^{232}Th chain (a factor of ~100). The amount of radioactivity in the ^{238}U early chain of the crystal is of the same order of magnitude as that of the ^{232}Th chain of the PMT. Consequently, comparing the sum of the radioactivity of isotopes in the U/Th chains, the PMT is only a factor of ~6 larger than that of the crystal, much smaller than the factor of ~100 difference in the activity of the ^{232}Th chain. Even though the PMT has higher intrinsic radioactivity than the TUM40 crystal, the following section confirms that the PMT contributes only a relatively small proportion of radioactive backgrounds in the energy range for WIMP search (below 40 keV) compared to the total ER background measured in CRESST, mainly due to the fact that PMT is an external component relative to the crystal.

4.6.2 Monte Carlo simulation

To assess how much the R8520-06-Al PMT radioactive contaminations contribute to the background of WIMP searches with a CPSD module, a Geant4 Monte Carlo simulation (version 10.2) [70] is carried out. The radioactivity of the PMT in Table 4.4 is taken as input to the simulation. As shown in Figure 4.21, the geometry model in the simulation includes a $CaWO_4$ crystal with the dimensions of $32 \times 32 \times 40$ mm^3 (~249 g, TUM40 dimensions [170]), placed at a distance of 9 mm from the window of the R8520-06 PMT with the 32×32 mm^2 side of the crystal facing the PMT. The PMT model in the simulation includes a synthetic silica window, an Al seal ring, a Kovar alloy body and stem, ten stainless steel dynode electrodes, and a borosilicate glass stem (PMT mass model from Reference [173]). The model also includes an outer copper shielding structure with 10 mm thickness and a gap of ~5 mm to the PMT and the crystal. The space that is not crystal, PMT structures or copper shielding in the simulation is modelled as

Chain	Isotope	decay mode	TUM40 unit activity (μBq/kg)	TUM40 249 g activity (μBq)	R8520 PMT activity (μBq/PMT)
^{238}U	^{238}U	α	$(1.01 \pm 0.02) \times 10^3$	251 ± 5	250 ± 40
	^{234}Th	β	(a)	(a)	(b)
	^{234m}Pa	β	(a)	(a)	(b)
	^{234}U	α	$(1.08 \pm 0.03) \times 10^3$	269 ± 7	(b)
	^{230}Th	α	55.8 ± 5.4	13.9 ± 1.3	(b)
	^{226}Ra	α	43.0 ± 9.9	10.7 ± 2.5	(b)
	^{222}Rn	α	38.1 ± 4.9	9.5 ± 1.2	(b)
	^{218}Po	α	43.1 ± 9.9	10.7 ± 2.5	(b)
	^{214}Pb	β	(a)	(a)	(b)
	^{214}Bi	β	47.4 ± 4.9	11.8 ± 1.2	(b)
	^{214}Po	α			(b)
	^{210}Pb	β	7^{+36}_{-7}	$1.7^{+9.0}_{-1.7}$	(b)
	^{210}Bi	β	(a)	(a)	(b)
	^{210}Po	α	17.8 ± 4.0	4.4 ± 1.0	(b)
^{235}U	^{235}U	α	39.5 ± 4.4	9.8 ± 1.1	11.5 ± 1.8
	^{231}Th	β	(a)	(a)	(b)
	^{231}Pa	α	23.2 ± 4.4	5.8 ± 1.1	(b)
	^{227}Ac	β	98 ± 20	24 ± 5	(b)
	^{227}Th	α	105 ± 19	26.1 ± 4.7	(b)
	^{223}Ra	α	104 ± 7	25.9 ± 1.7	(b)
	^{219}Rn	α	107 ± 7	26.6 ± 1.7	(b)
	^{215}Po	α			(b)
	^{211}Pb	β	(a)	(a)	(b)
	^{211}Bi	α	105 ± 7	26.1 ± 1.7	(b)
	^{207}Tl	β	(a)	(a)	(b)
^{232}Th	^{232}Th	α	9.2 ± 2.3	2.3 ± 0.6	500 ± 100
	^{228}Ra	β	(a)	(a)	(b)
	^{228}Ac	β	(a)	(a)	(b)
	^{228}Th	α	15.2 ± 4.1	3.8 ± 1.0	(b)
	^{224}Ra	α	19.8 ± 8.1	4.9 ± 2.0	(b)
	^{220}Rn	α	8.4 ± 3.4	2.0 ± 0.8	(b)
	^{216}Po	α	Not measured	Not measured	(b)
	^{212}Pb	β	(a)	(a)	(b)
	^{212}Bi	α	$7.7^{+8.9}_{-7.7}$	$1.9^{+2.2}_{-1.9}$	(b)
		β	15.8 ± 2.8	3.9 ± 0.7	(b)
	^{212}Po	α			(b)
	^{208}Tl	β	(a)	(a)	(b)

Table 4.4: The radioactivity of U/Th chains of TUM40 $CaWO_4$ crystal and R8520-06-Al PMTs. The symbol (a) means the β-decay cannot be identified individually but it is in equilibrium with the short-lived α-decay. The symbol (b) means the radioactivity of the isotope is in secular equilibrium of the head isotope in the decay chain. (Adapted from Refs. [171, 172, 173])

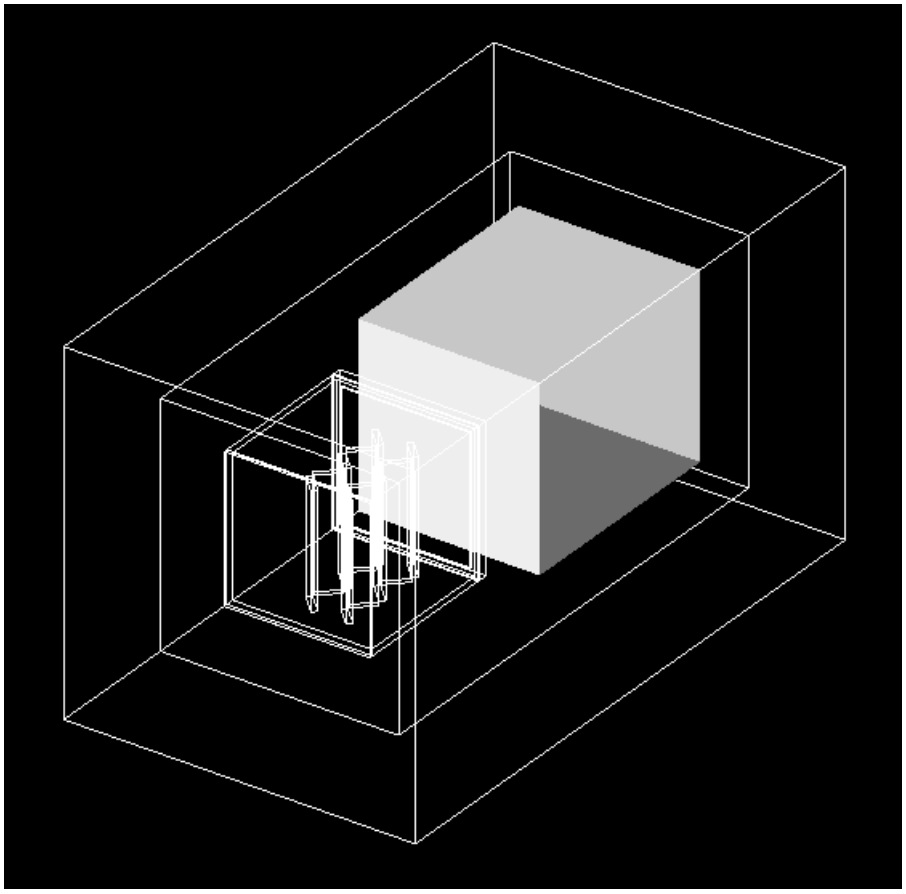

Figure 4.21: The geometry model in the Geant4 simulation. The grey shaded cuboid shows the $CaWO_4$ crystal. The PMT with dynode electrodes inside is shown on the lower left side of the figure. The crystal and PMT are surrounded by an outer copper shield.

vacuum, as would be the case inside a dilution refrigerator and inside a PMT.

To investigate the electron recoil backgrounds, three million decays for each relevant radioactive isotope in the PMT are simulated, with the exception of 30 million decays for ^{40}K. To simulate the nuclear recoil backgrounds, three million neutrons are emitted from the PMT in the simulation. The corresponding statistical uncertainty is roughly 1% for the number of particles ending up in the energy region for dark matter search.

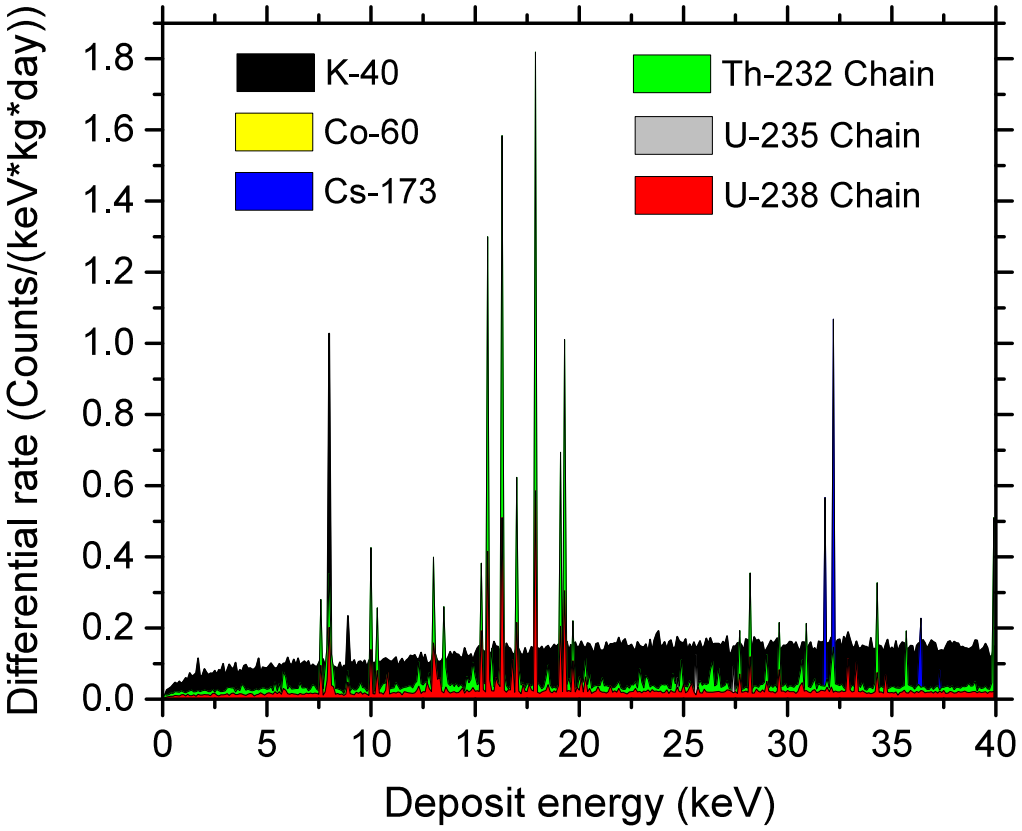

Figure 4.22: The electron recoil backgrounds from an R8520-06-Al PMT deposited in the $CaWO_4$ crystal in the energy range for WIMP search. The backgrounds are classified with their origin isotopes or decay chains, and different proportions are stacked in the figure. The contributions from isotopes in the ^{235}U decay chain and ^{60}Co are too small to be visible in the figure.

4.6.2.1 Electron recoil backgrounds

The Livermore low-energy electromagnetic models were employed to simulate the production, propagation and absorption of electrons and γ-rays in the detector, down to the energy of 250 eV. Physics processes including Compton scattering, photoelectric effect, Rayleigh scattering, electron-positron pair conversion, ionisation, and bremsstrahlung production are implemented in the electromagnetic model. The ER background results of the simulation are shown in Figure 4.22 and Figure 4.23.

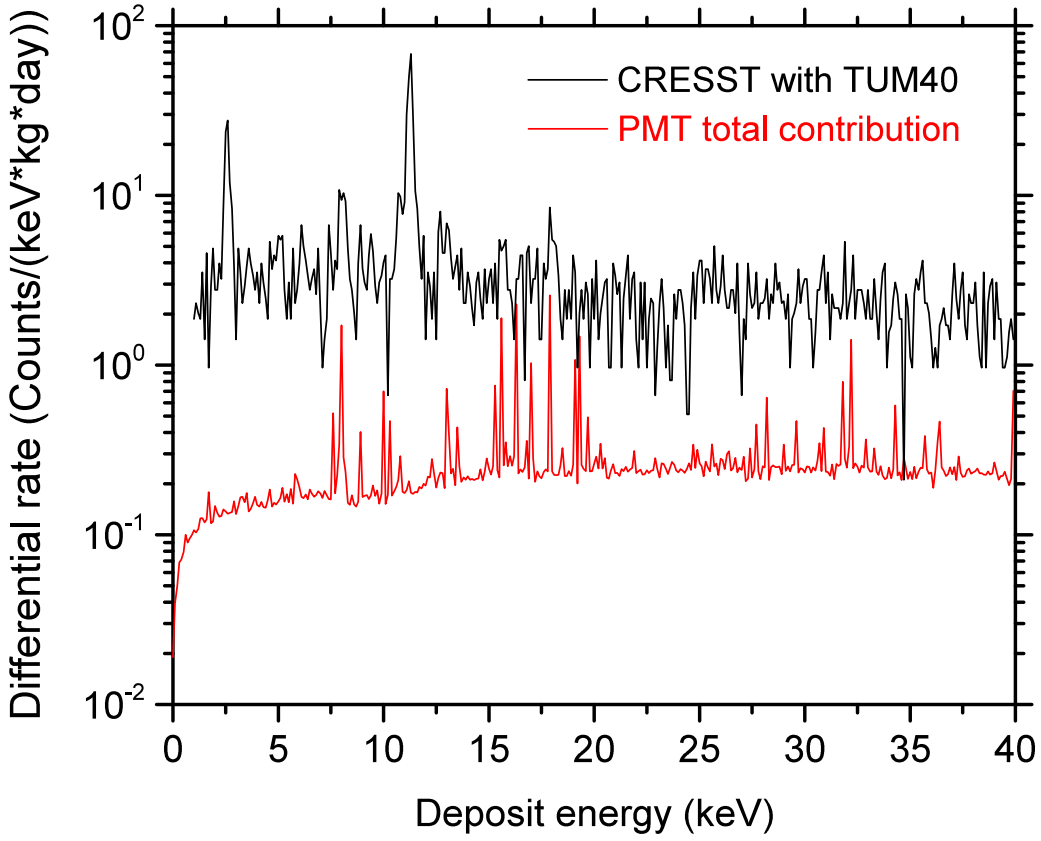

Figure 4.23: The electron recoil backgrounds in the energy range for WIMP search of a $CaWO_4$ crystal. The curve for the CRESST experiment with TUM40 as the target crystal is the measured total ER backgrounds in the detector module [171]. The PMT total contribution is from the Geant4 simulation in this thesis.

Figure 4.22 shows that the major contribution from the PMT to the ER backgrounds in the energy range for WIMP search is from ^{40}K contamination (~50%). Smaller contributions are from isotopes in ^{232}U (~26%) and ^{232}Th (~8%) decay chains. ^{40}K is mainly found in the borosilicate glass and the Kovar alloy of the PMT.

Figure 4.23 shows that the ER background in the energy range for WIMP search contributed by the R8520-06-Al PMT is one order of magnitude smaller than the total ER rate measured in the CRESST experiment with TUM40 as the target crystal [171]. The average ER rate for CRESST with the TUM40

crystal is (3.51 ± 0.09) DRU in the energy range for WIMP search (1–40 keV), while the average rate originating from the R8520-06-Al PMT is (0.26 ± 0.03) DRU (statistical). In the energy range for WIMP search, the ER background contributed from the PMT is only ~7.5% relative to the total ER background in CRESST with TUM40 crystal. As a conclusion, the introduction of a PMT to CPSD only causes a minor increase of ER background in the energy range for WIMP search, with TUM40 as the target crystal.

4.6.2.2 Nuclear recoil backgrounds

As discussed in Section 1.5, neutrons originating from the detector components can be produced through (α,n) reactions and spontaneous fissions. The neutron production rates and energy spectra from the R8520-06-Al PMTs in the XENON100 experiment has been simulated with the SOURCES-4A code in Refs. [174, 175]. As shown in Table 4.5, the neutron production rate for one PMT is calculated to be $(1.14\pm0.14)\times10^{-8}$ neutrons per second (equal to ~0.36 neutrons per year), with inputs from the measured radioactivity and the mass model. Even though the aluminium seal weighs only 0.1 g, it is calculated to account for ~53% of the total neutron production because of its high ^{232}Th contamination and large (α,n) cross-section.

Figure 4.24 shows the simulated differential rate of nuclear rate neutrons originating from the PMT, deposited in the ROI of the $CaWO_4$ crystal. The average NR rate originating from the PMT in the ROI is $(1.53 \pm 0.19) \times 10^{-6}$ DRU (statistical), which is 6 orders of magnitude smaller than the ER rate in the CRESST experiment with TUM40. Information about the neutron background in the CRESST experiment could not be found.

PMT component	^{238}U contamination (mBq/PMT)	Neutrons produced per ^{238}U (incl. ^{235}U) disintegration	Neutron rate from ^{238}U (incl. ^{235}U) chain (n/s) per PMT	^{232}Th contamination (mBq/PMT)	Neutrons produced per ^{232}Th disintegration	Neutron rate from ^{232}Th chain (n/s) per PMT
Kovar alloy	0.0446 ±0.016	(1.2±0.2) $\times10^{-6}$	(5.4±2.1) $\times10^{-11}$	0.1	(1.0±0.2) $\times10^{-6}$	(1.0±0.2) $\times10^{-10}$
Borosilicate glass	0.173 ±0.004	(1.1±0.2) $\times10^{-5}$	(1.91±0.35) $\times10^{-9}$	0.20 ±0.01	(1.5±0.3) $\times10^{-5}$	(3.0±0.6) $\times10^{-9}$
Aluminium seal	0.00030 ±0.00014	(1.4±0.2) $\times10^{-5}$	(4.3±2.1) $\times10^{-12}$	0.218 ±0.012	(2.8±0.5) $\times10^{-5}$	(6.1±1.1) $\times10^{-9}$
SS electrodes	0.023 ±0.009	(1.5±0.3) $\times10^{-6}$	(3.5±1.5) $\times10^{-11}$	0.077 ±0.04	(2.3±0.4) $\times10^{-6}$	(1.8±0.9) $\times10^{-10}$
Synthetic silica	0.000178	(2.2±0.4) $\times10^{-6}$	(3.9±0.7) $\times10^{-13}$	0.00212	(2.1±0.4) $\times10^{-6}$	(4.5±0.8) $\times10^{-12}$
Whole PMT	Subtotal from ^{238}U chain (incl. ^{235}U)		(2.0±0.4) $\times10^{-9}$	Subtotal from ^{232}Th chain		(9.4±1.3) $\times10^{-9}$
	Total neutron rate (n/s) per PMT		(1.14±0.14)$\times10^{-8}$			

Table 4.5: Neutron production rates from different components of the R8520-06-Al PMT. The radioactive contamination and the neutron production rate are from Refs. [172, 174]. The natural abundance of ^{235}U (0.72%) is used. In the screening results [172], the sum of the radioactivity of different components in PMTs before production is larger than the PMT finally produced, by a factor of 5.6 for the ^{238}U chain and a factor of 1.7 for the ^{232}Th chain. Consequently, for the calculations in the table, the contamination from the component screening result is scaled down proportionally to produce the measured average radioactivity of the PMTs. Using the measured radioactivity from components (without scaling down), the neutron rate would be (2.71±0.30)$\times10^{-8}$ (n/s) per PMT.

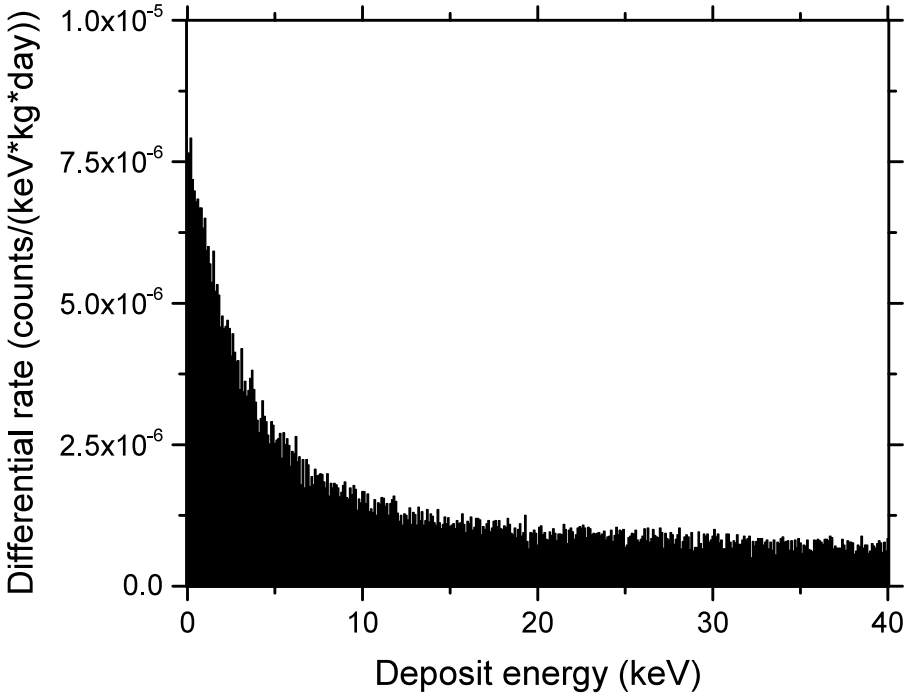

Figure 4.24: The differential nuclear recoil rate spectrum in the ROI (region of interest) of the $CaWO_4$ crystal for the neutrons originating from the R8520-06-Al PMT.

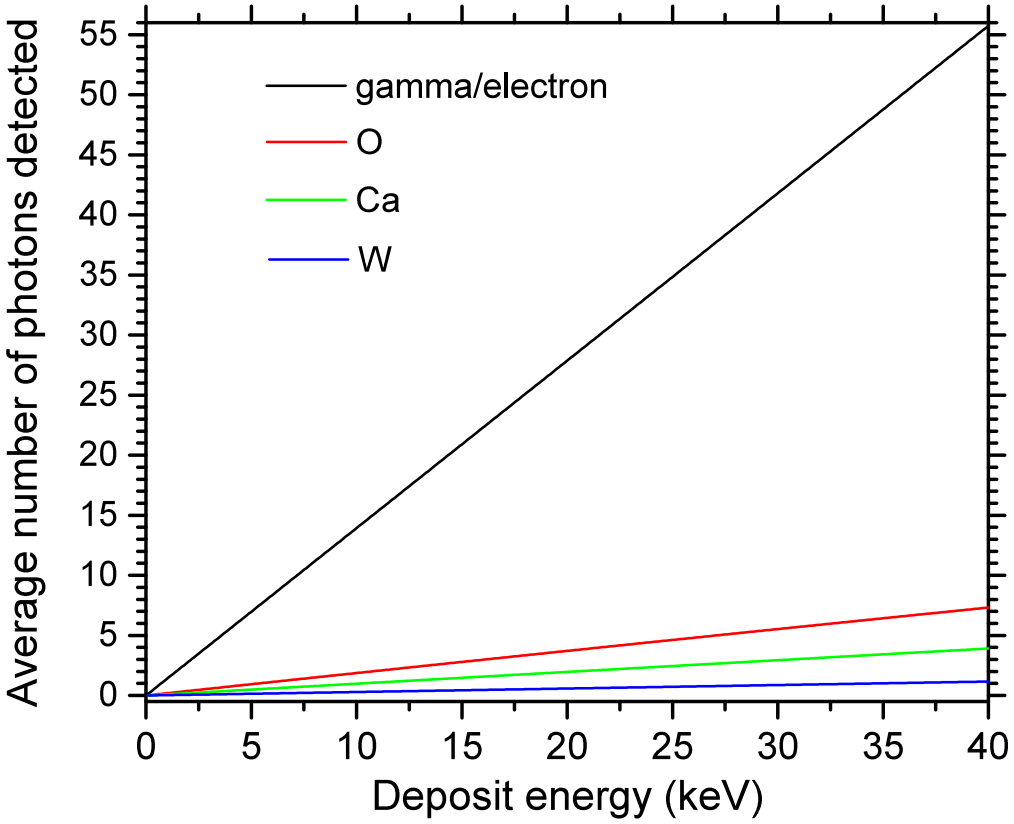

Figure 4.25: The average numbers of photons detected from electron recoil and nuclear recoil off different nuclei in $CaWO_4$, in the energy region of WIMP search. The light detection efficiency measured in this thesis (~1.39 photoelectrons per keV_{ee}) and the light quenching factors measured in Reference [176] are used.

4.6.3 Electron recoil leakage

To compare the electron recoil background and the nuclear recoil background, this section discusses the electron recoil discrimination and leakage, and the corresponding nuclear recoil acceptance. Using the light detection efficiency in this thesis (~1.39 photoelectrons per keV_{ee}) and the light quenching factors for $CaWO_4$ measured in Reference [176], the average numbers of photons detected from electron recoil and nuclear recoil off different nuclei in $CaWO_4$ are shown in Figure 4.25.

Because the number of detected photons is discreet, Poisson Statistics is used. The CRESST experiment uses 50% acceptance in the oxygen nuclear recoil band to define the ROI [116, 45]. However, this is not always possible with PMT readout because of the discreet nature of the detected photons. As a simplification, the acceptance rule used in this calculation is to keep the nuclear acceptance close to but above 50% of the oxygen band. Figure 4.26 shows the resulting ER leakage integrated over the ROI, in comparison to the NR background. The ER rate before discrimination is the sum of the ER rate measured in CRESST with TUM40 and that contributed by the PMT resulted from the Geant4 simulation. It is shown that in the low energy region, the ER leakage is high, which is due to the small number of detected photons and the resulting difficulty to perform discrimination. As a result, the ER backgrounds, mainly from the $CaWO_4$ crystal, is the dominating factor throughout the different analysis threshold scenarios.

In conclusion, from the radioactivity measurement of a similar PMT model as input to a Geant4 simulation, ER background originating from the PMT is only ~7.5% relative to the total ER background in CRESST with TUM40 crystal, in the energy range for WIMP search with $CaWO_4$ as the target material. The NR background originating from the PMT is several orders of magnitude smaller than the ER leakage after discrimination, depending on the analysis threshold. The ER backgrounds originating from the $CaWO_4$ crystal is still the dominating contribution factor to the background of WIMP search with CPSD, even with the current most radiopure crystal.

4.6.4 Potential improvement of PMT radioactivity

The latest Hamamatsu R11410 3-inch PMTs have lower normalised activity (mBq per cm^2 photo-sensitive area) than the R8520 PMTs, with a factor of five reduction of the ^{40}K and ^{60}Co normalised activities [130]. Also, active scintillation shielding

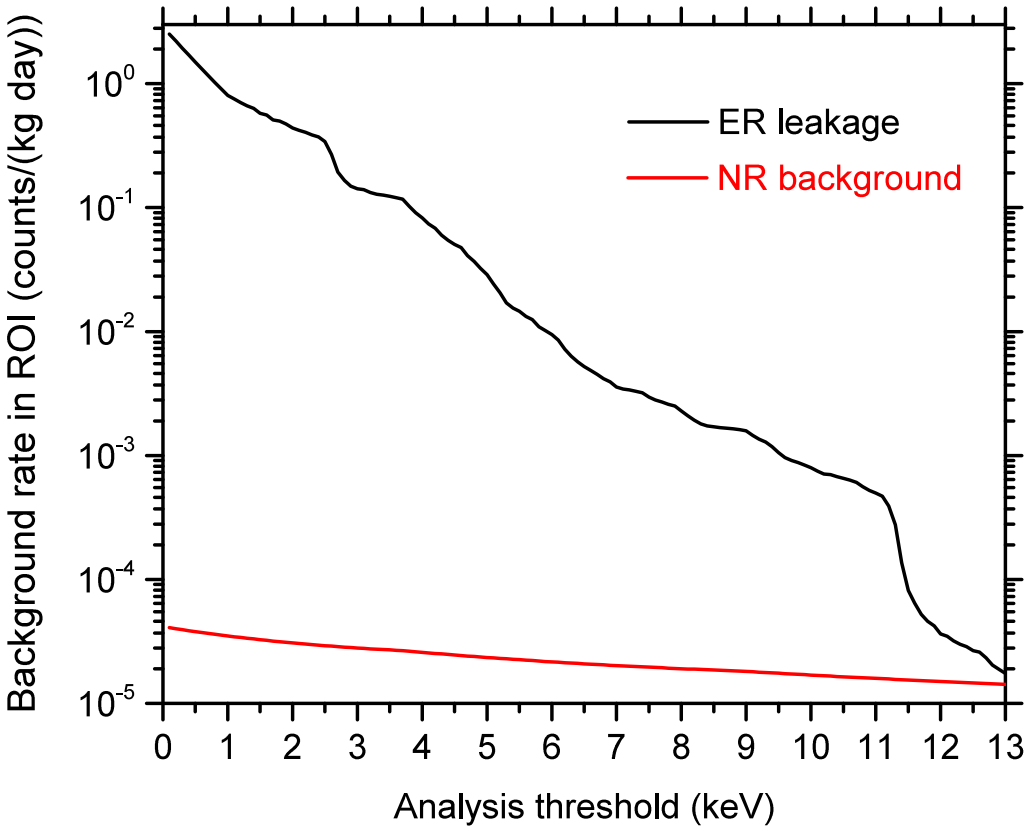

Figure 4.26: The ER leakage and NR background rates integrated over the ROI (from the analysis threshold to 40 keV) versus the analysis threshold. The kinks at ~2.5 keV and ~11.5 keV of the ER leakage curve are caused by cosmogenic activation of W [171].

is possible to alleviate the effect of the PMT radioactivity further [177]. Finally, coincidence between crystals can also alleviate the effect of PMT radioactivity, as dark matter interacts only once in a time with the detector due to its small interaction cross-section, but radioactive backgrounds could interact multiple times.

Chapter 5

Outlook and conclusions

5.1 Future improvement

5.1.1 Light detection

As discussed in Section 2.6, the number of photons detected by the PMT is critical to the performance of the discrimination power of the CPSD. The number of photons detected is the product of the number of photons scintillated from the crystal, the light collection efficiency and the quantum efficiency of the PMT.

To generate a larger number of scintillation photons from the crystal, the scintillation light yield of the crystal needs to be optimised. Heating up the $CaWO_4$ crystal in an oxygen-rich atmosphere is demonstrated to improve the light yield by decreasing the absorption of scintillation light [178].

To improve the light collection efficiency, the geometry of the detector setup may be optimised. A crystal in triangular prism shape with the surfaces roughened in a configuration with truncated cone reflector is demonstrated to have as high as 57% light collection efficiency [151]. The VM2002 reflecting foil used in the CRESST experiment has a higher reflectivity than the VM2000 reflecting foil used in this experiment [179]. Currently, the calorimeter is suspended inside

the detector housing with Nylon fibres. There is very little information about the reflectivity of Nylon for the 420-nm light. PTFE shows a good reflectivity for light near this wavelength [180], so it may be beneficial to use PTFE fibres to suspend the calorimeter. Finally, two PMTs sandwiching the scintillating crystal may help to increase the light collection efficiency, as adopted in several NaI experiments [181, 182], but cautions are needed about the radioactive background from PMTs.

The most significant improvement potential in light detection is likely to be in the PMT quantum efficiency, given the estimated low quantum efficiency (15%) of the PMT in this study. The platinum underlay in this PMT is a thin layer on the photocathode made from Bialkali and this is the main difference between this PMT and those with thin aluminium strips in a cross shape attached to the cathode. The PMTs with Al strips show a higher quantum efficiency of around 30% [143]. It should be explored whether the PMTs made for higher temperatures work at milli-Kelvin temperatures as well.

5.1.2 Powering multiple PMTs

Powering multiple PMTs with a single CWG has yet to be demonstrated, but it is important to the deployment of CSPD with the PMT as the light channel readout for the next-generation rare-event search experiments. Different PMTs in the same model, even in the same production batch, have different gains. Biasing those PMTs with the same potentials will generate different single photoelectron responses. Considering that a photon counting method is used and the PMT in this study was already biased to a voltage around 3 times the voltage recommended by the manufacturer without breakdown, it is possible to have a voltage so that even the PMT with the lowest gain in the group can have a good single photoelectron response. Also, assigning PMTs with similar gains to the same CWG could alleviate the issue. The number of PMTs that could be powered by

a CWG is determined by the size of the capacitors in the CWG.

5.2 Potential applications

5.2.1 CRESST upgrade

For the CRESST experiment, the possibility of replacing the cryogenic calorimeter-based light detectors with low-temperature PMTs demonstrated in this work would not only provide light detectors with consistent and stable performance, which can be better than the existing light detectors in CRESST (demonstrated in Section 4.4), but it would also free up half of the readout SQUID channels originally used for the cryogenic calorimeter-based light channels. These available SQUID channels could then be deployed to accommodate more phonon channels, subsequently the number of detector modules thus the exposure rate of the dark matter search could be doubled without major effort in upgrading the SQUID readout systems. Even though the CRESST 2015 result already set the world best limit for WIMPs with masses smaller than 1.5 GeV c^{-2}, the result only based on the exposure from a single detector module [45]. This highlights the difficulties in obtaining consistent and reliable performance in cryogenic detectors. As a result, combining the possibility of doubling the number of detector modules and the consistent and reliable performance from PMTs, replacing the cryogenic calorimeter-based light detector with PMTs can potentially improve the science reach of CRESST significantly.

5.2.2 TeO_2 neutrinoless double-beta decay experiment

TeO_2 $0\nu\beta\beta$ experiments use cryogenic detectors operated at milli-Kelvin temperatures to measure the electron energy in $\beta\beta$ decay. For the next-generation of a TeO_2 neutrinoless double-beta decay experiment, it is necessary to suppress or

discriminate the background to probe down to the inverse neutrino mass hierarchy [51]. The main background in such TeO_2 experiments is alpha particles, and the signal of double-beta decay is electrons. Because an alpha particle has a much larger mass than an electron, for the same kinematic energy around the Q value (~2.53 MeV for ^{130}Te), the electron emits Cherenkov light in the TeO_2 crystal while the alpha particle does not. TeO_2 crystals only emit a relatively small amount of scintillation photons than Cherenkov light, especially with light quenching effect for the alpha particles [183]. Consequently, the detection of Cherenkov light could be deployed in background discrimination, as demonstrated in Refs. [184, 185]. TeO_2 neutrinoless double-beta decay experiments operate phonon detectors with NTD-Ge as the thermistor at milli-Kelvin temperatures, and the current generation experiment CUORE already has 988 channels installed [51]. It requires light detectors that are scalable and can detect a small number of Cherenkov photons (~130 emitted) between 350 nm to 600 nm at milli-Kelvin temperatures [186]. PMTs demonstrated in this work have the right characteristics for this application. Additionally, the fast response of a PMT is one of the advantages over the cryogenic calorimeter-based light detector in this application. The dark count rate of PMTs needs attention, as the dark pulses could mistake an alpha background event as a beta signal. An increase of the average number of photons detected for beta events could alleviate this concern, as the number of photons resulting from dark pulses of the PMT is typically low. However, the radioactivity of PMT is a big concern for this application.

5.3 Conclusions

Cryogenic detectors with capabilities of simultaneously detecting phonon and light signals from particle interactions in a scintillating absorber may be a good tech-

nical route for rare-event search experiments, including dark matter search and neutrinoless double-beta decay search experiments. In this thesis, CPSD modules with a PMT as the light detector for scintillation photons is tested. Two modules with $CaMoO_4$ and $CaWO_4$ scintillators are characterised respectively and they demonstrated promising performance characteristics for CPSD with an NTD-Ge as the phonon sensor, and a PMT to detect scintillation photons. With excitation from a ^{57}Co source, the data show that the detector modules in this study compares competitively with other CPSDs currently deployed in experiments for rare-event searches, especially in the energy region of interest for dark matter direct detection. The detector module in this thesis maintains the major features of conventional CPSD, i.e. resolving power, high sensitivity, and particle discrimination ability. With the photon counting and grouping algorithm, the energy resolutions (FWHM) for 122.1 keV excitation for the light channel based on a PMT readout are 29.7% and 19.9% for $CaMoO_4$ and $CaWO_4$ respectively. With pulse height estimation from the template fit after a high-pass filter is applied to the data, the energy resolutions for excitation with 122.1 keV for the phonon channel of the CPSD are 0.97 keV (0.79%) and 2.17 keV (1.8%) for $CaMoO_4$ and $CaWO_4$ respectively,. The use of a PMT as the light detector offers hugh improvement of time resolution of the CPSD, compared to the cryogenic calorimeter-based light detector. The PMT is able to perform single-photon counting and consequently the detection module can determine the start time of the event by the response time in the PMT, typically in ~ns scale. The duration in the light channel is determined by the slow scintillation decay time constant of the crystal in use. The slow scintillation decay time constant were found to be (3410 ± 30) µs in $CaMoO_4$ and (382 ± 2) µs in $CaWO_4$. Furthermore, the ionisation density affects the time profile recorded by the PMT, thus there are additional possibilities for discrimination between electron and nuclear recoils with pulse shape analysis, which can

be used for particle identification and rejection.

The dark count rate of the PMT in this study is determined to be below 5 Hz while the gain of the PMT is 3.3×10^6 at milli-Kelvin temperatures, which demonstrates that the PMT remains as an effective light detector for photon counting purpose at milli-Kelvin temperatures.

The cold PMT in this thesis could also potentially be applied to TeO_2 neutrinoless double-beta decay experiment, as veto detectors for alpha particles by detecting the Cherenkov light in beta events. However, the radioactivity of the PMT in this application needs to be evaluated and addressed.

The cold PMT in this thesis can potentially revolutionise the CPSD experiments in rare event searches, by offering an attractive alternative solution to detect the scintillation light in CPSD, as the PMT is easy to use, scalable, consistent in performance and its performance can already be better than the existing cryogenic calorimeter-based light detectors in CPSD experiments, especially in the low energy range.

The simulation results indicate that the radioactive backgrounds originating from a similar PMT model increase the total radioactive backgrounds for WIMP search with CPSD only minorly (<10%), and the crystal of the CPSD is still the dominating contribution factor in the total background budget.

In summary, this thesis presented a novel cryogenic phonon-scintillation detector, with a PMT working at milli-Kelvin temperatures as the light detector, and demonstrated this technology is promising for future cryogenic rare-event search experiments.

Appendix A

R8520-06-Pt PMT room-temperature properties

The single electron response, gain, dark count rate of the R8520-06-PT PMT at room temperature are discussed in this appendix.

A.1 Single electron response and dark count rate at room temperature

Similar to the single electron response (SER) at milli-Kelvin temperatures, the SER at room temperature is shown in Figure A.1. This set of data was taken during the room-temperature verification of the optical modelling, as mentioned in Section 2.6, with a $CaWO_4$ crystal as the scintillator excited by gamma quanta from an external ^{57}Co source. The bias voltage was set at 788 V. The SER peak at room temperature centres at $x \approx 0.12\,\mathrm{V\,ns}$, while the pedestal region centred at $x \approx 0$ is caused by electronic noise. After fitting a Gaussian function to the SER region of the histogram, the voltage integral from the single photoelectron pulse is found to be 0.123 V ns, with a width (σ) of 0.057 V ns. This corresponds

to a single photoelectron resolution (σ) of 46%. After taking into account the input impedance and the gain of the readout electronics, the gain of the PMT is determined to be 2.1×10^6. The histogram shows, in addition to the SER peak, a satellite feature at $x > 0.25$ V ns, roughly at twice the value of the centre of the Gaussian for the single electron peak, indicating they are caused by double photoelectrons.

Because of lacking the phonon channel as veto at room temperature and the constant presence of scintillation light from the $CaWO_4$ crystal, no dark count rate is estimated from data at room temperature. This is because it was a delicate setup and removing the scintillator crystal would have been too risky. Also, from the application viewpoint of this low-temperature PMT technology, the dark count rate at room temperature is not as important as that at low temperature.

The manufacturer gives gain$\approx 3 \times 10^6$ at 800 V, dark count rate$\approx$ 1000 Hz at 800 V at room temperature for this model of PMT [187].

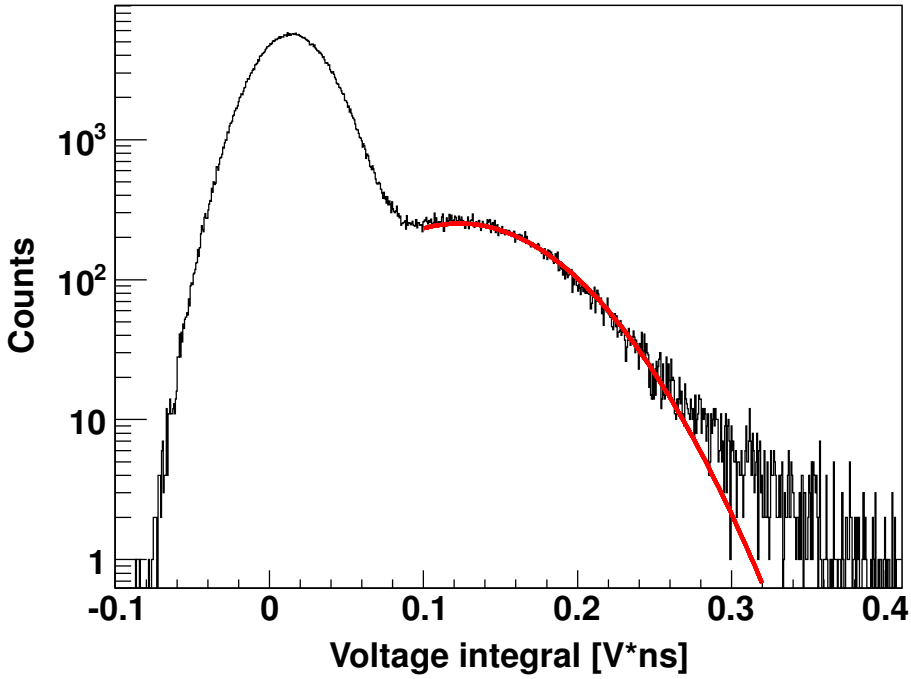

Figure A.1: Histogram of the voltage integral in the photoelectron pulse region and the pre-trigger baseline for recordings at room temperature. The entries in the pedestal region around zero in the horizontal axis are from the voltage integral over the pre-trigger baseline regions. The entries with higher voltage integral (centred at $x \approx 0.12\,\mathrm{V\,ns}$) are from the single photoelectron pulses. The red curve shows a Gaussian function fitted to the data. This signal includes the readout electronics gain (~11).

Bibliography

[1] P. A. R. Ade *et al.*, Astronomy and Astrophysics **594**, A13 (2016).

[2] W. H. Furry, Phys. Rev. **56**, 1184 (1939).

[3] A. Giuliani and A. Poves, Advances in High Energy Physics **2012**, 1 (2012).

[4] W. K. Ford, Astronomical Uses of Cascade Intensifies, in *Photo-Electronic Image Devices*, edited by J. D. McGee, D. McMullan, and E. Kahan, , Advances in Electronics and Electron Physics Vol. 22, pp. 697–704, Academic Press, 1966.

[5] V. C. Rubin and J. Ford, W. Kent, The Astrophysical Journal **159**, 379 (1970).

[6] M. S. Roberts and R. N. Whitehurst, The Astrophysical Journal **201**, 327 (1975).

[7] E. Holmberg, Meddelanden fran Lunds Astronomiska Observatorium Serie II **136**, 1 (1958).

[8] J. Jałocha, Ł. Bratek, and M. Kutschera, The Astrophysical Journal **679**, 373 (2008).

[9] K. G. Begeman, A. H. Broeils, and R. H. Sanders, Monthly Notices of the Royal Astronomical Society **249**, 523 (1991).

[10] F. Zwicky, Helv. Phys. Acta **6**, 110 (1933).

[11] F. Zwicky, General Relativity and Gravitation **41**, 207 (2009).

[12] F. Zwicky, The Astrophysical Journal **86**, 217 (1937), 1937ApJ....86..217Z.

[13] D. Clowe *et al.*, The Astrophysical Journal **648**, L109 (2006).

[14] D. Harvey, R. Massey, T. Kitching, A. Taylor, and E. Tittley, Science **347**, 1462 (2015), arXiv:1203.1166v3.

[15] M. Markevitch *et al.*, The Astrophysical Journal **567**, L27 (2002).

[16] V. Belokurov *et al.*, The Astrophysical Journal **671**, L9 (2007), 0706.2326.

[17] P. Schneider, J. Ehlers, and E. E. Falco, *Gravitational Lenses*, 1 ed. (Springer-Verlag Berlin Heidelberg, 1992).

[18] A. Bergmann, V. Petrosian, and R. Lynds, Astrophysical Journal **350 p. 23-** (1990).

[19] A. Jenkins *et al.*, The Astrophysical Journal **499**, 20 (1998).

[20] P. J. E. Peebles, Astrophys. J. **263**, L1 (1982).

[21] C. S. Frenk and S. D. M. White, Annalen der Physik **524**, 507 (2012), 1210.0544.

[22] V. Springel, C. Frenk, and S. White, Nature **440**, 1137 (2006).

[23] C. Patrignani and P. D. Group, Chinese Physics C **40**, 100001 (2016).

[24] L. Bergström, Reports on Progress in Physics **63**, 793 (2000), 0002126.

[25] C. Alcock *et al.*, The Astrophysical Journal **550**, L169 (2001), 0011506.

[26] T. D. Brandt, The Astrophysical Journal **824**, L31 (2016).

[27] J. Mather *et al.*, The Astrophysical Journal **420**, 439 (1994).

[28] G. F. Smoot *et al.*, The Astrophysical Journal **396**, L1 (1992).

[29] W. Hu and S. Dodelson, Annual Review of Astronomy and Astrophysics **40**, 171 (2002), 0110414.

[30] A. H. Guth, Physical Review D **23**, 347 (1981).

[31] G. Duda and K. Garrett, Advances in Astronomy **2011** (2011), 1006.2483.

[32] R. D. Peccei and H. R. Quinn, Phys. Rev. Lett. **38**, 1440 (1977).

[33] P. W. Graham, I. G. Irastorza, S. K. Lamoreaux, A. Lindner, and K. A. van Bibber, Annual Review of Nuclear and Particle Science **65**, 485 (2015).

[34] G. Jungman, M. Kamionkowski, and K. Griest, Physics Reports **267**, 195 (1996), 9506380.

[35] J. L. Feng, Annual Review of Astronomy and Astrophysics **48**, 495 (2010).

[36] J. D. Lewin and P. F. Smith, Astroparticle Physics **6**, 87 (1996).

[37] R. H. Helm, Physical Review **104**, 1466 (1956).

[38] S. R. Golwala, *Exclusion Limits on the WIMP-Nucleon Elastic-Scattering Cross Section from the Cryogenic Dark Matter Search*, PhD thesis, University of California, Berkeley, 2000.

[39] M. Weber and W. de Boer, Astronomy and Astrophysics **509**, A25 (2009), 0910.4272.

[40] C. Savage, G. Gelmini, P. Gondolo, and K. Freese, Journal of Cosmology and Astroparticle Physics **2009**, 036 (2009), 0808.3607.

[41] F. J. Kerr and D. Lynden-Bell, Monthly Notices of the Royal Astronomical Society **221**, 1023 (1986).

[42] T. Piffl *et al.*, Astronomy and Astrophysics **562**, A91 (2014).

[43] A. K. Drukier, K. Freese, and D. N. Spergel, Physical Review D **33**, 3495 (1986).

[44] M. Kuhlen *et al.*, Journal of Cosmology and Astroparticle Physics **2010**, 030 (2010), 0912.2358.

[45] G. Angloher *et al.*, European Physical Journal C **76**, 1 (2016), 1509.01515.

[46] P. Agnes *et al.*, Physical Review D - Particles, Fields, Gravitation and Cosmology **93**, 1 (2016), 1510.00702.

[47] R. Agnese *et al.*, Physical Review D - Particles, Fields, Gravitation and Cosmology **92**, 1 (2015), 1504.0587.

[48] D. S. Akerib *et al.*, (2016), arXiv:1608.07648.

[49] M. Redshaw, B. J. Mount, E. G. Myers, and F. T. Avignone, Physical review letters **102**, 212502 (2009).

[50] S. Dell'Oro, S. Marcocci, M. Viel, and F. Vissani, Advances in High Energy Physics **2016**, 2162659 (2016).

[51] D. Artusa *et al.*, Physics Procedia **61**, 241 (2015).

[52] W. Maneschg, Nuclear and Particle Physics Proceedings **260**, 188 (2015).

[53] J. Gómez-Cadenas *et al.*, Journal of Cosmology and Astroparticle Physics **2011**, 007 (2011).

[54] F. Boehm and P. Vogel, *Physics of Massive Neutrinos*, 2 ed. (Cambridge University Press, Cambridge, 1992).

[55] J. Barea, J. Kotila, and F. Iachello, Physical Review C **87**, 014315 (2013).

[56] Z. Maki, M. Nakagawa, and S. Sakata, Progress of Theoretical Physics **28**, 870 (1962).

[57] R. Henning, Reviews in Physics **1**, 29 (2016).

[58] D. M. Mei and A. Hime, Physical Review D - Particles, Fields, Gravitation and Cosmology **73**, 1 (2006), 0512125.

[59] D. S. Akerib *et al.*, Astroparticle Physics **62**, 33 (2015), 1403.1299.

[60] G. Angloher *et al.*, The European Physical Journal C **72**, 1971 (2012).

[61] M. J. Berger and S. M. Seltzer, NASA Report SP-3036 (1966).

[62] R. Strauss *et al.*, The European Physical Journal C **75**, 352 (2015).

[63] D. C. Malling *et al.*, (2013), arXiv:1305.5183.

[64] National Nuclear Data Center - Chart of Nuclides http://www.nndc.bnl.gov/chart/, 2016.

[65] D. Reilly, N. Ensslin, H. J. Smith, and S. Kreiner, NRC Report NuREG/cR-5550 LA-UR-90-732 (1991).

[66] A. Navarrete E, R. Kouzes, J. Orrell, T. Berguson, and A. Greene, Pacific Northwest National Laboratory Report No. PNNL-21696, 2012 (unpublished).

[67] V. A. Kudryavtsev, AIP Conf. Proc. **1672**, 60003 (2015).

[68] A. J. Anderson, J. M. Conrad, E. Figueroa-Feliciano, K. Scholberg, and J. Spitz, Physical Review D - Particles, Fields, Gravitation and Cosmology **84**, 1 (2011), 1103.4894.

[69] J. Monroe and P. Fisher, Physical Review D - Particles, Fields, Gravitation and Cosmology **76**, 1 (2007), 0706.3019.

[70] S. Agostinelli *et al.*, Nuclear Instruments and Methods in Physics Research, Section A: Accelerators, Spectrometers, Detectors and Associated Equipment **506**, 250 (2003), 1005.0727v1.

[71] T. M. Undagoitia and L. Rauch, Journal of Physics G: Nuclear and Particle Physics **43**, 013001 (2016).

[72] M. Szydagis *et al.*, Journal of Instrumentation **6**, P10002 (2011), 1106.1613.

[73] J. Jortner, L. Meyer, S. A. Rice, and E. G. Wilson, The Journal of Chemical Physics **42** (1965).

[74] L. S. Miller, S. Howe, and W. E. Spear, Phys. Rev. **166**, 871 (1968).

[75] A. Hitachi *et al.*, Phys. Rev. B **27**, 5279 (1983).

[76] D. Acosta-Kane *et al.*, Nuclear Instruments and Methods in Physics Research, Section A: Accelerators, Spectrometers, Detectors and Associated Equipment **587**, 46 (2008), 0712.0381.

[77] E. Aprile and T. Doke, Rev. Mod. Phys. **82**, 2053 (2010).

[78] V. Chepel and H. Araújo, Journal of Instrumentation **8**, R04001 (2013), 1207.2292.

[79] D. S. Akerib *et al.*, Nuclear Instruments and Methods in Physics Research, Section A: Accelerators, Spectrometers, Detectors and Associated Equipment **818**, 57 (2016).

[80] D. Akerib *et al.*, Nuclear Instruments and Methods in Physics Research Section A: Accelerators, Spectrometers, Detectors and Associated Equipment **704**, 111 (2013).

[81] D. S. Akerib *et al.*, Phys. Rev. Lett. **116**, 161301 (2016).

[82] D. S. Akerib *et al.*, Phys. Rev. D **93**, 72009 (2016).

[83] D. S. Akerib *et al.*, Physical Review D - Particles, Fields, Gravitation and Cosmology **93**, 23 (2016), 1608.05381.

[84] D. S. Akerib *et al.*, (2015), arXiv:1509.02910.

[85] E. Aprile and XENON1T-Collaboration, (2012), 1206.6288.

[86] L. Grandi, XENON1t status, in *Identification of Dark Matter 2016*, 2016.

[87] A. Tan *et al.*, (2016), arXiv:1607.07400.

[88] J. Aalbers *et al.*, (2016), arXiv:1606.07001.

[89] J. Calvo *et al.*, (2015), arXiv:1505.02443.

[90] S. Catalanotti *et al.*, Journal of Instrumentation **10**, P08013 (2015).

[91] K. Abe *et al.*, Nuclear Instruments and Methods in Physics Research Section A: Accelerators, Spectrometers, Detectors and Associated Equipment **716**, 78 (2013).

[92] H. Uchida *et al.*, Progress of Theoretical and Experimental Physics **2014**, 1 (2014), 1401.4737.

[93] K. Abe *et al.*, Physical Review Letters **113**, 1 (2014), 1406.0502.

[94] A. Takeda, Proceedings of Science **ICRC2015**, 1222 (2016).

[95] K. Ueshima *et al.*, Nuclear Instruments and Methods in Physics Research, Section A: Accelerators, Spectrometers, Detectors and Associated Equipment **659**, 161 (2011), arXiv:1106.2209v1.

[96] M. Kuzniak *et al.*, Nuclear and Particle Physics Proceedings **273**, 340 (2016).

[97] Z. Ahmed *et al.*, Science **327**, 1619 LP (2010).

[98] D. S. Akerib *et al.*, Phys. Rev. Lett. **112**, 91303 (2014).

[99] R. Agnese *et al.*, Physical Review Letters **116**, 1 (2016), 1509.02448.

[100] C. Enss and D. McCammon, Journal of Low Temperature Physics **151**, 5 (2008).

[101] G. Angloher, Nuclear Instruments and Methods in Physics Research Section A: Accelerators, Spectrometers, Detectors and Associated Equipment **512**, 401 (2003).

[102] A. Münster, S. Schönert, and M. Willers, Nuclear Instruments and Methods in Physics Research Section A: Accelerators, Spectrometers, Detectors and Associated Equipment , (2016).

[103] J. Billard, M. De Jesus, A. Juillard, and E. Queguiner, Journal of Low Temperature Physics **184**, 299 (2016).

[104] S. Scorza, Journal of Physics: Conference Series **375**, 012021 (2012).

[105] E. Armengaud *et al.*, Journal of Cosmology and Astroparticle Physics **05** (2016), 1603.05120.

[106] S. Marnieros *et al.*, Journal of Low Temperature Physics **176**, 182 (2014).

[107] E. Armengaud *et al.*, Astroparticle Physics **47**, 1 (2013), 1305.3628.

[108] R. Agnese *et al.*, Physical Review Letters **112**, 1 (2014), 1402.7137.

[109] T. Aramaki, Journal of Low Temperature Physics **184**, 885 (2016).

[110] K. Eitel, EDELWEISS: RI&D and perspectives for 2017 and beyond, in *Identification of Dark Matter 2016*, 2016.

[111] A. Broniatowski *et al.*, Journal of Low Temperature Physics **184**, 330 (2016).

[112] R. Agnese *et al.*, Phys. Rev. Lett. **112**, 41302 (2014).

[113] G. Angloher *et al.*, (2015), arXiv:1503.08065.

[114] A. Alessandrello *et al.*, Physics Letters B **420**, 109 (1998).

[115] P. Meunier *et al.*, Applied Physics Letters **75** (1999).

[116] G. Angloher *et al.*, European Physical Journal C **74**, 1 (2014), 1407.3146.

[117] V. B. Mikhailik and H. Kraus, physica status solidi (b) **247**, 1583 (2010).

[118] C. Arnaboldi *et al.*, Astroparticle Physics **34**, 143 (2010).

[119] D. Rosenberg, A. E. Lita, A. J. Miller, and S. W. Nam, Phys. Rev. A **71**, 61803 (2005).

[120] F. Petricca *et al.*, Nuclear Instruments and Methods in Physics Research Section A: Accelerators, Spectrometers, Detectors and Associated Equipment **520**, 193 (2004).

[121] P. C. F. Di Stefano *et al.*, Journal of Applied Physics **94**, 6887 (2003).

[122] N. Coron, P. de Marcillac, J. Leblanc, G. Dambier, and J.-P. Moalic, Optical Engineering **43**, 1568 (2004).

[123] A. Calleja *et al.*, Journal of Low Temperature Physics **151**, 848 (2008).

[124] J. W. Beeman *et al.*, Journal of Instrumentation **8**, P07021 (2013).

[125] C. Isaila *et al.*, Physics Letters B **716**, 160 (2012).

[126] L. Pattavina *et al.*, Journal of Low Temperature Physics **184**, 286 (2016).

[127] H. J. Lee *et al.*, Nuclear Instruments and Methods in Physics Research Section A: Accelerators, Spectrometers, Detectors and Associated Equipment **784**, 508 (2015).

[128] L. Cardani *et al.*, Applied Physics Letters **107**, 093508 (2015).

[129] S. Fukuda *et al.*, Nuclear Instruments and Methods in Physics Research, Section A: Accelerators, Spectrometers, Detectors and Associated Equipment **501**, 418 (2003).

[130] E. Aprile *et al.*, European Physical Journal C **75**, 1 (2015), 1503.07698.

[131] D. S. Akerib *et al.*, Nuclear Instruments and Methods in Physics Research, Section A: Accelerators, Spectrometers, Detectors and Associated Equipment **703**, 1 (2013), arXiv:1205.2272v1.

[132] P. K. Lightfoot, G. J. Barker, K. Mavrokoridis, Y. A. Ramachers, and N. J. C. Spooner, Journal of Instrumentation **3**, P10001 (2008).

[133] F. Carbonara, A. G. Cocco, G. Fiorillo, and V. S. Gallo, Nuclear Instruments and Methods in Physics Research Section A: Accelerators, Spectrometers, Detectors and Associated Equipment **610**, 271 (2009).

[134] A. Falcone *et al.*, Nuclear Instruments and Methods in Physics Research Section A: Accelerators, Spectrometers, Detectors and Associated Equipment **787**, 55 (2015).

[135] L. Baudis, Physics of the Dark Universe **4**, 50 (2014).

[136] H. Kraus and V. B. Mikhailik, Nuclear Instruments and Methods in Physics Research Section A: Accelerators, Spectrometers, Detectors and Associated Equipment **621**, 395 (2010).

[137] H. O. Meyer, Nuclear Instruments and Methods in Physics Research Section A: Accelerators, Spectrometers, Detectors and Associated Equipment **621**, 437 (2010).

[138] T. M. Ito *et al.*, Phys. Rev. A **85**, 42718 (2012).

[139] G. S. Buller and R. J. Collins, Measurement Science and Technology **21**, 12002 (2010).

[140] X. Zhang, J. Lin, V. B. Mikhailik, and H. Kraus, Astroparticle Physics **79**, 31 (2016).

[141] X. Zhang, J. Lin, V. B. Mikhailik, and H. Kraus, Applied Physics Letters **106**, 241904 (2015).

[142] P. Coulter, *Cryogenic Phonon-scintillation Detectors with NTD Germanium Readout*, Ph.d. thesis, University of Oxford, 2014.

[143] E. Aprile *et al.*, Journal of Instrumentation **7**, P10005 (2012).

[144] X. Zhang, *A Novel Phonon-Scintillation Cryogenic Detector and Cabling Solution for Dark Matter Direct Detection*, Ph.d. thesis, University of Oxford, 2015.

[145] Hamamastu Photonics, R8520-406 PMT manual (2013).

[146] S. Henry *et al.*, Journal of Instrumentation **2**, P11003 (2007).

[147] F. Pobell, *Matter and Methods at Low Temperatures* (Springer-Verlag, 1992).

[148] M. F. Weber, C. A. Stover, L. R. Gilbert, T. J. Nevitt, and A. J. Ouderkirk, Science **287**, 2451 (2000).

[149] D. Strul, J. Sutcliffe-Goulden, P. Halstead, and P. K. Marsden, IEEE Trans. Nucl. Sci. **49**, 619 (2002).

[150] M. Janecek, IEEE Transactions on Nuclear Science **59**, 490 (2012).

[151] F. Danevich *et al.*, Nuclear Instruments and Methods in Physics Research Section B: Beam Interactions with Materials and Atoms **336**, 26 (2014).

[152] O. S. Kushnir, Journal of Optics A: Pure and Applied Optics **5**, 478 (2003).

[153] H. Kraus, V. Mikhailik, and D. Wahl, Nuclear Instruments and Methods in Physics Research Section A: Accelerators, Spectrometers, Detectors and Associated Equipment **553**, 522 (2005).

[154] J. E. SHELBY, Journal of the American Ceramic Society **55**, 61 (1972).

[155] V. O. Altemose, Journal of Applied Physics **32** (1961).

[156] S. Hyodo and A. Nagai, Journal of the Faculty of Engineering, University of Tokyo, Series A **18** (1980).

[157] M. R. Bhat, Nuclear Data Sheets **85**, 415 (1998).

[158] R. McGowan, *Data Analysis and Results of the Upgraded CRESST Dark Matter Search*, PhD thesis, University of Oxford, 2008.

[159] H. O. Meyer, EPL (Europhysics Letters) **89**, 58001 (2010).

[160] D. Wahl, *Optimisation of light collection in inorganic scintillators for rare event searches*, PhD thesis, University of Oxford, 2005.

[161] F. Pröbst *et al.*, Journal of Low Temperature Physics **100**, 69 (1995).

[162] R. Strauss *et al.*, Journal of Low Temperature Physics **176**, 905 (2014).

[163] R. F. Lang *et al.*, (2009), arXiv:0910.4414.

[164] R. F. Lang *et al.*, Astroparticle Physics **32**, 318 (2010).

[165] S. J. Lee *et al.*, Astroparticle Physics **34**, 732 (2011).

[166] M. Moszynski *et al.*, Nuclear Instruments and Methods in Physics Research Section A: Accelerators, Spectrometers, Detectors and Associated Equipment **553**, 578 (2005).

[167] R. F. Lang and W. Seidel, New Journal of Physics **11**, 105017 (2009).

[168] V. B. Mikhailik, H. Kraus, S. Henry, and A. J. B. Tolhurst, Phys. Rev. B **75**, 184308 (2007).

[169] M. Kiefer, *Improving the Light Channel of the CRESST-II-Dark Matter Detectors*, PhD thesis, Technischen Universität München, 2012.

[170] A. Münster *et al.*, Journal of Cosmology and Astroparticle Physics **2014**, 18 (2014), 1403.5114.

[171] R. Strauss *et al.*, Journal of Cosmology and Astroparticle Physics **2015**, 030 (2015), arXiv:1410.4188v1.

[172] E. Aprile *et al.*, Astroparticle Physics **35**, 43 (2011), 1103.5831.

[173] E. Aprile *et al.*, Physical Review D - Particles, Fields, Gravitation and Cosmology **83**, 1 (2011), 1101.3866.

[174] E. Aprile *et al.*, Journal of Physics G: Nuclear and Particle Physics **40**, 115201 (2013), 1306.2303.

[175] A. Kish, *Dark Matter Search with the XENON100 Experiment*, Phd thesis, University of Zurich, 2011.

[176] R. Strauss *et al.*, The European Physical Journal C **74**, 1 (2014).

[177] F. A. Danevich *et al.*, Nuclear Instruments and Methods in Physics Research, Section A: Accelerators, Spectrometers, Detectors and Associated Equipment **556**, 259 (2006).

[178] A. Erb and J.-C. J.-C. Lanfranchi, CrystEngComm **15**, 2301 (2013).

[179] M. Janecek and W. W. Moses, IEEE Transactions on Nuclear Science **55**, 2432 (2008).

[180] V. R. Weidner and J. J. Hsia, J. Opt. Soc. Am. **71**, 856 (1981).

[181] J. Cherwinka *et al.*, Phys. Rev. D **90**, 92005 (2014).

[182] R. Bernabei *et al.*, Il Nuovo Cimento A (1971-1996) **112**, 545 (1999).

[183] N. Coron *et al.*, Nuclear Instruments and Methods in Physics Research Section A: Accelerators, Spectrometers, Detectors and Associated Equipment **520**, 159 (2004).

[184] M. Willers *et al.*, Journal of Instrumentation **10**, P03003 (2015).

[185] K. Schäffner *et al.*, Astroparticle Physics **69**, 30 (2015).

[186] T. T. de Fatis, European Physical Journal C **65**, 359 (2010).

[187] Private communication with Hamamatsu Corporation.